

https://dspace.org/

Probing heavy-quark production vs charged-particle multiplicity in pp collisions at s = 5.02 TeV with ALICE

Mdhluli, Joyful Elma

2024

https://hdl.handle.net/10539/37489

Downloaded from a DSpace repository. https://dspace.org/



Probing heavy-quark production vs charged-particle multiplicity in pp collisions at $\sqrt{s} = 5.02$ TeV with ALICE

by

Joyful Elma Mdhluli

(537099)

Thesis

submitted to the Faculty of Science, University of the Witwatersrand, Johannesburg, in fulfilment of the requirements for the degree of

Doctor of Philosophy

in

High Energy Physics

Supervisor:
Prof. Zinhle Buthelezi

Co-Supervisors:
Dr. Siegfried Förtsch
Prof. Deepak Kar

February 28, 2023

Declaration

I declare that this thesis is my own, unaided work. It is being submitted for the Degree of Doctor of Philosophy at the University of the Witwatersrand, Johannesburg. It has not been submitted before for any degree or examination at any other University.



(Joyful Elma Mdhluli)

Student Number: 537099

Date: February 28, 2023

Place: University of the Witwatersrand

Abstract

The differential heavy-flavour (charm and beauty quark) production as a function of the charged-particle multiplicity is investigated in pp collisions at $\sqrt{s} = 5.02$ TeV. The heavy-quark production cross section as a function of transverse momentum (p_{T}) and pseudorapidity (η) is also evaluated. The measurement of the inclusive yield of heavy quarks via the single-muon (μ) decay channel is done in the muon spectrometer at forward pseudorapidity ($-4 < \eta < -2.5$) and the charged-particle multiplicity using the Silicon Pixel Detector at central pseudorapidity ($|\eta| < 1$). These measurements are important in order to gain more insight into which processes are involved in the collision at a partonic level as well as provide information on the interplay between hard and soft mechanisms during particle production.

Reference data taken during Run 2 in 2015 and 2017 in pp collisions at $\sqrt{s} = 5.02$ TeV are analyzed for measurements of the inclusive heavy-flavour decay muon differential cross-section and heavy-flavour decay muon yield as a function of the charged-particle multiplicity. A total number of 102.7 M (21.34 M) events for the single muon low (high)-p_{T} triggers are analyzed for both measurements. Minimum bias triggered events with multiplicity tracklets > 0 are used for multiplicity estimation. Two methodologies are utilized, the data-driven method and the "Official Framework".

Results of inclusive heavy-flavour decay muon differential cross-section measured as a function of p_{T} are compared with the theoretical model FONLL, the data and theoretical model are in agreement within systematic uncertainties. The results are also compared with measurements in pp collisions at $\sqrt{s} = 7$ TeV, an energy dependence is observed. Results of inclusive heavy-flavour decay muon yield as a function of the charged-particle multiplicity indicated an approximately faster than linear correlation. Comparisons with other heavy-quark measurements vs charged-particle multiplicity is made and the measurements are in agreement at low charged-particle multiplicities.

This thesis also reports on the Service Task work done. This entailed tests performed on detector elements of the Muon Chambers (MCH) that suffered high-voltage trips that were repaired during the long shutdown (LS2). The detector elements were successfully repaired and are currently stored as spares for the Run 3 data-taking period.

Dedicated

to

Ellen Mdhluli, Yvonne Mthembi and Sbongile Mathumba

Acknowledgements

To my supervisor, Associate Professor Zinhle Buthelezi, thank you for the opportunity to be able to have been part of your research group. I have gained an enormous amount of knowledge and this would not have been possible if you did not believe in me. Thank you for being patient with me while I was adjusting into the group and taking me as a student so late into my PhD. Words cannot describe how grateful I am. To my co-supervisor Dr Siegfried Förtsch, thank you for invaluable contribution towards the analysis and writing of this thesis. To Professor Deepak Kar, thank you for agreeing to co-supervise me.

I would also like to extend my gratitude to Dr Bharati Naik and Dr Sibaliso Mhlanga for all the help with the analysis, it was a difficult transition into analysis and I wouldn't have been able to adjust as quickly without your help. A special thank you to the conveners of the Heavy-Flavour Muon Physics Analysis Group for their valuable input to the analysis. I would to extend my gratitude to the NRF for the sponsorship throughout my PhD and SA-CERN for sponsoring all my trips to CERN.

To my pillars of strength, the women who get angry and frustrated with me without asking questions; to my three amazing mothers, Ellen Mdhluli, Yvonne Mthembi and Sbongile Mathumba, thank you for all the support you have given me all these years. Thank you for being patient with me all these years, for allowing me to be my own person and dream big. To my amazing grandmother, thank you for patiently waiting for me to finish school so I can finally spoil you ... I can't make any promises but we will see what we can do.

A special thank you to my amazing friend and housemate Tokologo Rathupetsane, you gave me my first PhD and made me endless cups of coffee when I was writing my thesis. To all my friends, thank you for all the support and encouragement - especially my thesis buddy throughout the writing process.

"Last but not least, I wanna thank me
I wanna thank me for believing in me
I wanna thank me for doing all this hard work
I wanna thank me for having no days off
I wanna thank me for, for never quitting."

Contents

Abstract i

List of Figures vii

List of Tables xvii

1 Introduction 1

1.1 Standard Model (SM) and Quantum ChromoDynamics (QCD) 1

1.1.1 Standard Model 1

1.1.2 Quantum Chromodynamics (QCD) 4

1.2 Heavy-flavour production 9

1.2.1 Heavy flavour 10

1.2.2 Heavy-flavour production cross section in pp collisions 12

1.2.3 Heavy-flavour production cross section in LHC experiments 13

1.3 Charged-particle multiplicity 18

1.3.1 Multiple Parton Interactions 21

1.4 Heavy-flavour production as a function of charged-particle multiplicity in pp collisions 23

1.5 Heavy-flavour production as a function of charged-particle multiplicity in pp and p-Pb collisions 26

1.6 Aims of this study 28

1.6.1 Muon sources 29

1.7 Thesis Outline 31

2 Experimental set up **33**
2.1 The Large Hadron Collider (LHC) . . . 33
2.2 ALICE Detector . . . 36
2.2.1 Detector Layout . . . 37
2.2.2 Central Barrel Detectors . . . 37
2.2.3 Global Detectors . . . 40
2.2.4 Forward Muon Spectrometer . . . 42
2.2.4.1 Detector Layout . . . 42
2.2.4.2 Absorbers . . . 43
2.2.4.3 Dipole Magnet . . . 44
2.2.4.4 Muon tracking system . . . 44
2.2.4.4.1 Alignment of the Muon Tracking Chambers . . . 48
2.2.4.5 Muon trigger chambers . . . 49
2.2.5 Summary . . . 52
2.3 The ALICE Online System . . . 54
2.3.1 The Central Trigger Processor . . . 55
2.3.2 Data Acquisition System . . . 57
2.3.3 High-Level Trigger . . . 58
2.3.4 Detector Control System . . . 59
2.4 Data taking conditions . . . 60

3 Analysis Details **69**
3.1 The ALICE Offline Framework . . . 70
3.2 Data sample for the analysis . . . 71
3.2.1 Data Sample . . . 71
3.2.2 Event Selection . . . 72
3.3 Multiplicity Measurements . . . 73
3.3.1 Data-driven method . . . 73
3.3.1.1 Multiplicity Estimation . . . 75
3.3.2 Official Framework . . . 99
3.3.2.1 Multiplicity Estimation . . . 100
3.4 Heavy-flavour decay muon yield determination . . . 103
3.4.1 Muon Track Cuts . . . 103
3.4.1.1 Muon yields in different multiplicity bins . . . 104
3.4.2 Normalization Factor . . . 109
3.4.2.1 Scaler Method (Online Method) . . . 109
3.4.2.2 Offline Method . . . 110
3.4.2.3 Normalization factor results . . . 113
3.4.2.4 Normalization factor as function of multiplicity . . . 116

3.4.2.5 Luminosity Determination . . . 117
3.4.3 Normalization to inelastic collisions . . . 117
3.5 Acceptance times Efficiency ($A \times \epsilon$) . . . 119
3.5.1 FONLL Parameterizations . . . 120
3.5.2 Final results of $A \times \epsilon$ . . . 127
3.5.3 $A \times \epsilon$ as a function of multiplicity . . . 127
3.6 Corrected inclusive muon yield . . . 128
3.7 Background Subtraction . . . 133
3.7.1 Contributions of muons from primary charged pion and kaon decays 134
3.7.1.1 Muon contribution from pion and kaon decays as a function of multiplicity . . . 136
3.7.2 Contribution from secondary decay muons . . . 141
3.7.2.1 Contribution from secondary decay muons as a function of multiplicity . . . 143
3.7.3 Contribution from W and Z/γ^*-decay muons . . . 145
3.7.4 Contribution from J/ψ . . . 148
3.7.4.1 Contribution from J/ψ as a function of multiplicity . . . 152
3.8 Systematic Uncertainties . . . 154
3.9 Heavy-flavour decay differential cross-section . . . 157

4 Discussion of results **159**
4.1 Heavy-flavour decay muon differential production cross-section . . . 159
4.1.1 Comparison with other measurements in pp collisions . . . 163
4.2 Self-normalized yield as a function of charged-particle multiplicity . . . 165
4.2.1 Self-normalized yield as a function of self-normalized charged-particle multiplicity . . . 166
4.2.2 Comparison with other heavy-flavour measurements at mid- and forward rapidity in pp collisions . . . 168
4.2.3 Comparison of pp and p-Pb measurements . . . 173

5 Conclusion and outlook **176**
5.1 Conclusion . . . 176
5.2 Outlook . . . 182

References **184**

Appendix Appendix **201**

Appendix A Data Selection **201**
A.1 Run Lists . . . 201

A.2 Event Selection 201

Appendix B Multiplicity Estimation **203**
B.0.1 Optimization of the reference value. 203

Appendix C Muon Yield **207**
C.0.1 Muon yield in different multiplicity percentile bins 207
C.0.2 Normalization factor 207

Appendix D Acceptance times Efficiency ($A \times \epsilon$) **212**

Appendix E Background subtraction **213**
E.1 Charged primary pion and kaon 213
E.2 Secondary decay muons 213
E.3 Electroweak Bosons 213
E.4 J/ψ background contribution 217

Appendix F Service Work **220**
F.1 Testing of the detection elements 220
F.1.1 Experimental procedure 222
F.1.2 Results and Discussion 223

List of Figures

1 Coordinate system in a pp collision xxii
2 Psuedorapidity values shown on a polar plot xxiii
3 The ALICE coordinate system xxiv

1.1 Standard Model of Particle Physics 2
1.2 The strong-coupling constant α_s as a function of energy energy scale 5
1.3 Overview of the CTEQ6M parton distribution functions at Q = 100 GeV where x is the Bjorken-x discussed in the text and $xf(x)$ is the distribution function. 8
1.4 Born diagrams in QCD for heavy quark (Q) and heavy anti-quark ($\bar{Q}$) production 9
1.5 Topologies of decay channels of charm (D) meson via the hadronic decay channel (left) and decay channels of charm and beauty meson via semileptonic decay channel (right) 11
1.6 Hard partonic scattering process 12
1.7 Charm (left) and beauty (right) differential cross section measured in pp collisions as a function of center-of-mass energy. 14
1.8 Bjorken-x as a function of M^2 for particle production in nucleon-nucleon collisions at the SPS, RHIC and LHC (left) and the accessible Bjorken-x range for heavy flavours in pp collisions at $\sqrt{s}$ = 14 TeV (right) in the rapidity range that can be measured with ALICE at the LHC. The area circled in red is the forward rapidity where the LHC can reach that other experiments cannot. 15

1.9 Invariant double differential production cross sections of electrons from heavy-flavour decays measured by ALICE and ATLAS in pp collisions at $\sqrt{s}$ = 7 TeV in different rapidity intervals. FONLL pQCD calculations with the same rapidity selections are shown for comparison. The dashed lines show the statistical uncertainties of the calculations. 16
1.10 The heavy-flavour differential production cross section as a function of transverse momentum and rapidity measured in pp collisions at $\sqrt{s} = 5.02$ TeV. 17
1.11 Charged-particle pseudorapidity density (upper panels) and the same scaled by $1/(dN_{ch}/d\eta)_{\rm incl.}$ (lower panels) for the 0–0.01% (high multiplicity) to 70–100% (low multiplicity) multiplicity classes measured with the forward multiplicity estimator ($-3.7 < \eta < -1.7$ and $2.8 < \eta < 5.1$) in pp collisions at $\sqrt{s} = 5.02$, 7 and 13 TeV. The multiplicity classes are determined by finding the ratio of the total cross-section (σ) and the minimum-bias cross-section (σ_{MB}). 19
1.12 Schematic diagrams of a) elastic scattering, diffractive processes with b) single diffractive dissociation (SD), c) double diffractive dissociation (DD), d) central diffractive dissociation (CD); and non-diffractive processes e) . . 20
1.13 Multiple Parton Interaction in a pp collision. 21
1.14 Relative J/ψ yield as a function of the relative charged-particle density measured at forward rapidity in pp collisions at $\sqrt{s} = 5.02$ (INEL>0), 7 (INEL) and 13 (INEL>0) TeV (left) and comparison with similar measurements at midrapidity at $\sqrt{s} = 13$ TeV (right). 24
1.15 Comparison of data and theoretical model PYTHIA (left) and self-normalized yield vs charged-particle multiplicity for HF electron decay (right) 25
1.16 Comparison of the self-normalized yields vs charged-particle multiplicity of D meson with non-prompt J/ψ measurements (left) and D meson and prompt J/ψ measurements (right) 26
1.17 Average relative D-meson yields in $|y_{lab}| <0.5$ as a function of the relative charged-particle multiplicity at mid-rapidity $|\eta| < 1.0$. The relative yields are presented in the top panels with their statistical (vertical bars) and systematic (boxes) uncertainties, apart from the uncertainty on the B feed-down fraction, which is drawn separately in the bottom panels 27
1.18 Relative yield of inclusive J/ψ mesons as a function of relative charged-particle pseudorapidity density, measured at mid-rapidity, in comparison to average D mesons, for the $p_{\rm T}$ interval 2–4 GeV/c. The error bars show the statistical uncertainties, and the boxes the systematic ones. 28
1.19 Transverse momentum distribution of reconstructed tracks in the muon spectrometer in pp collisions at $\sqrt{s} = 7$ TeV using PTHIA 30

2.1 LHC luminosity plan from 2010 to 2024, the red dots showing the peak luminosity for each year and the blue line showing the integrated luminosity, the main shutdown periods are indicated by the shaded blocks 34
2.2 CERN's Accelerator Complex, showing the different accelerators involved in particle acceleration 35
2.3 3D ALICE Schematic Run 2 38
2.4 The performance during the LHC Run 2 period of the ALICE central barrel detectors used for PID measurements 39
2.5 Inner Tracking System (ITS) 40
2.6 Beam-gas interactions and pp collisions as measured on the V0A and V0C detectors 41
2.7 Schematic of the V0 timing used for event selection 41
2.8 Schematic diagram of the ALICE muon spectrometer 43
2.9 Layout of the front absorber of the Muon Spectrometer 44
2.10 Muon tracking chamber quadrant 45
2.11 Basic geometry of the Cathode Pad Chamber 46
2.12 Cathode Pad Chamber layout 47
2.13 Muon Tracking Chamber electronics 48
2.14 Schematic view of the ALICE MTR (left) and detector composition of a half plane (right) 50
2.15 MTR Resistive Plate Chamber layout 51
2.16 The Muon Spectrometer trigger principle 52
2.17 Schematic of the ALICE online systems 54
2.18 Schematic of the CTP functions 56
2.19 Overview of the ALICE DAQ 58
2.20 Overview of the ALICE online architecture in Run 2 with focus on the C-RORCs 59
2.21 ALICE DCS Monitoring page during the 2015 data taking period 60
2.22 The LHC beam modes showing the MB current and magnetic field as a function of time 62
2.23 The LHC Page 1, gives information of LHC operations in real time. 65
2.24 Intergrated luminosity during Run 2 for pp collisions at $\sqrt{s} = 5.02$ TeV . . 68

3.1 Illustration of the event selection cuts for the MB trigger of the LHC17p data sample. 74
3.2 Schematic diagram of tracklet reconstruction approaches 76
3.3 Number of active SPD modules 78
3.4 Raw tracklet (3.4a) and average tracklet (3.4b) distributions. 80

3.5 2D Distributions of multiplicity vs SPD z-vertex for the LHC17p (3.5a) and LHC17q (3.5b) data samples. 81
3.6 2D Distribution of multiplicity vs SPD z-vertex for the LHC15n data sample. 82
3.7 Comparison of corrected tracklets (3.7a) and corrected average tracklets (3.7b) for LHC17p data sample. 84
3.8 Comparison of corrected tracklets (3.8a) and corrected average tracklets (3.8b) for LHC15n data sample. 85
3.9 Comparison of the tracklet distributions (3.9a) and mean tracklet distributions (3.9b) for the EPOS generator (LHC20a2). 87
3.10 Comparison of the tracklet distributions (3.10a) and mean tracklet distributions (3.10b) for the PYTHIA generator (LHC17i7b). 88
3.11 Comparison of raw tracklet distributions from data and MC production (3.11a) and the average tracklet distributions (3.11b). 89
3.12 Comparison of raw tracklet distributions from data and MC production (3.12a) and the average tracklet distribution (3.12b). 90
3.13 $N_{gen}-N_{trkl}^{corr}$ is fitted with a linear function in different colors for the different multiplicity bins demarcated by the vertical red lines. 93
3.14 Ratio of the mean number of generated charged particles and the mean number of corrected tracklets further corrected by α_{global} (3.14a) and α_i (3.14b). 94
3.15 Mean of N_{ch} distribution in N_{trkl} intervals anchored to the LHC17p and q data sample 95
3.16 Mean of N_{ch} distribution in N_{trkl} intervals anchored to the LHC15n data sample 96
3.17 DCA vs momentum of muons measured in pp collisions at $\sqrt{s} = 5.02$ TeV. The distributions before (3.17a) and after (3.17b) all muon track cuts are applied. 105
3.18 Evolution of MSL (3.18a) and MSH (3.18b) p_{T} distributions after each muon track cut. 106
3.19 Muon yields in different multiplicity bins for MSL (3.19a) and MSH (3.19b) triggers for LHC17p+q data sample. The horizontal lines represent the bin width and the vertical lines represent the statistical errors. 107
3.20 Muon yields in different multiplicity bins for MSL (3.20a) and MSH (3.20b) triggers for LHC15n data sample. The horizontal lines represent the bin width and the vertical lines represent the statistical errors. 108
3.21 Purity (3.21a) and L0brates (3.21b) as a function of run number. 111
3.22 Number of interacting bunches (3.22a) and Pile-up (3.22b) as function of run number. 112

3.23 Normalization factors for MSL (3.23a) and MSH (3.23b) as a function of run number for the LHC17p data sample. . . . 114
3.24 Normalization factors for MSL (3.24a) and MSH (3.24b) as a function of run number for the LHC17q data sample. . . . 115
3.25 Differential p_{T} (3.25a) and rapidity (3.25b) cross-sections from FONLL simulations. . . . 121
3.26 p_{T}-differential (3.26a) and η (3.26b) cross-sections fitted with functions expressed by equation 3.27 and 3.28, respectively. . . . 123
3.27 Reconstructed and generated yields (3.27a) and $A \times \epsilon$ (3.27b) as a function of p_{T} for MSL and MSH triggers. . . . 124
3.28 Statistical error evolution for the MSL trigger (3.28a) and MSH trigger (3.28b) for LHC17p data sample. . . . 125
3.29 $A \times \epsilon$ as a function of p_{T} in different η bins for MSL (3.29a) and MSH (3.29b). 126
3.30 $A \times \epsilon$ for MSL and MSH triggers as a function of p_{T} for the LHC17p data sample. The vertical lines are the statistical uncertainties associated with the results. . . . 128
3.31 2D Distribution of the $A \times \epsilon$ as a function of p_{T} and η for MSL (3.31a) and MSH (3.31b). . . . 129
3.32 $A \times \epsilon$ as a function of corrected SPD tracklet multiplicity from embedding production. . . . 130
3.33 Comparison of the p_{T}-distributions (3.33a) and ratio (3.33b) of the MSL and MSH triggered events. . . . 132
3.34 Differential inclusive single muon cross-section. Statistical errors are smaller than the symbols. . . . 133
3.35 Inclusive p_{T} distribution (3.35a) and background fraction (3.35b) of single decay muons from primary charged π and K at forward rapidity in pp collisions at $\sqrt{s} = 5.02$ TeV. . . . 135
3.36 p_{T} distributions of primary charged π (left) and K (right) decays in different multiplicity classes in pp collisions at $\sqrt{s} = 5.02$ TeV measured at midrapidity 136
3.37 Pseudorapidity density ($dN_{ch}/d\eta$) distributions at $\sqrt{s} = 5.02$ and 7 TeV (left) and the ratio (right) . . . 137
3.38 Extrapolated p_{T} distributions of primary charged pion decays in different multiplicity classes in pp collisions at $\sqrt{s} = 5.02$ TeV measured at midrapidity. 138
3.39 Extrapolated p_{T} distributions of primary charged kaon decays in different multiplicity classes in pp collisions at $\sqrt{s} = 5.02$ TeV measured at midrapidity. 139
3.40 Estimated background fraction in different multiplicity percentile bins of primary charged π and K at forward rapidity in pp collisions at $\sqrt{s} = 5.02$ TeV. . . . 140

3.41 p_{T} distributions of single decay muons from various sources (3.41a) and background fraction of secondary decay muons (3.41b) associated with the LHC17p and q data sample. 142
3.42 Background fractions of secondary muons in different multiplicity bins associated with the LHC17p and q (3.42a) and LHC15n (3.42b) data samples. 144
3.43 Cross-sections for each decay process using POWHEG simulations. 146
3.44 Differential cross-sections of inclusive muons and electroweak boson single-muon decay (3.44a) and background fraction of electroweak bosons decays (3.44b) for the LHC17p and q data samples. 147
3.45 p_{T}- (left) and (right) y-cross-sections of J/ψ in pp collisions at $\sqrt{s} = 5.02$ TeV 149
3.46 Extrapolated p_{T} (3.46a) and (3.46b) y differential cross-sections of J/ψ in pp collisions at $\sqrt{s} = 5.02$ TeV. The error bars are the statistical and systematic uncertainties added in quadrature. 150
3.47 Differential cross-section distributions of the inclusive muons and J/ψ dimuon differential cross-section (3.47a) and background fraction of J/ψ (3.47b) in pp collisions at $\sqrt{s} = 5.02$ TeV for the LHC17p and q data samples. 151
3.48 The relative J/ψ yield as a function of the relative charged-particle density measured at forward rapidity in pp collisions at $\sqrt{s} = 5.02$ TeV. The red solid line is the pol1 fit. 152
3.49 Inclusive differential single muon cross-section and heavy-flavour decay muon differential cross-section (top panel). Ratio of the inclusive differential single muon cross-section and heavy-flavour decay muon differential cross-section (bottom panel). The boxes are the systematic uncertainties. . 158

4.1 Heavy-flavour decay muon production cross-section as a function of η for integrated p_{T} ($2 < p_{\mathrm{T}} < 20$ GeV/c) in pp collisions at $\sqrt{s} = 5.02$ TeV compared with theoretical calculations from FONLL, the solid curves are the central values and the dotted curves are the systematic uncertainty. The vertical lines are statistical errors and boxes around the data points represent the systematic uncertainties. 161
4.2 Heavy-flavour decay muon production cross-section in pp collisions at $\sqrt{s} = 5.02$ TeV in different η intervals compared with theoretical calculations from FONLL. The horizontal lines are the bin width and the vertical lines are statistical errors. 162
4.3 Ratio of the heavy-flavour decay muon production cross-section and theoretical calculations from FONLL in pp collisions at $\sqrt{s} = 5.02$ TeV in different η intervals. 163

4.4 Comparison of the heavy-flavour decay muon production cross-section in pp collisions at $\sqrt{s} = 5.02$ with published data (4.4a) and 7 TeV (4.4b). The bottom panels show the ratios of the comparison in the top panel. The vertical lines are statistical uncertainties. 164
4.5 Comparison of the self-normalized yield as a function of charged-particle multiplicity using the data-driven method, SPD and V0M estimators of the "Official Framework" method. Ratio between the the heavy-flavour yield and self-normalized charged-particle multiplicity. The solid line is y=x and the boxes represent the systematic uncertainties. 167
4.6 Self-normalized yield as a function of charged-particle multiplicity in different p_{T} intervals. The solid line is y=x and the boxes represent the systematic uncertainties (top panel). Ratio of the relative muon yields in p_{T} intervals as a function of the relative charged-particle multiplicity, p_{T} interval $2 < p_{\mathrm{T}} < 4$ GeV/c is chosen as reference. The horizontal solid line represents unity and the boxes represent the systematic uncertainties (bottom panel). 169
4.7 Self-normalized yield as a function of charged-particle multiplicity in two different p_{T} intervals. The solid line is y=x and the boxes represent the systematic uncertainties. Top: low-p_{T} interval $2 < p_{\mathrm{T}} < 4$ GeV/c. Bottom: high-p_{T} interval $14 < p_{\mathrm{T}} < 20$ GeV/c 170
4.8 Comparison of J/ψ (green data points) and the differential heavy-flavour (red and blue data points) muon decay as a function of charged-particle multiplicity in pp collisions at $\sqrt{s} = 5.02$ at forward rapidity. The solid line is y=x and the boxes represent the systematic uncertainties. 172
4.9 Self-normalized yield as a function of charged-particle multiplicity measured in midrapidity for the average D-meson and J/ψ measurements and at forward rapidity for this study. The solid line is y=x and the boxes represent the systematic uncertainties. 173
4.10 Comparison of average D-meson and relative J/ψ measurements in p-Pb at $\sqrt{s_{NN}} = 5.02$ TeV and the differential heavy-flavour muon decay in pp at $\sqrt{s} = 5.02$ TeV as a function of charged-particle multiplicity at midrapidity and forward rapidity, as indicated. The solid line is y=x and the boxes represent the systematic uncertainties. 174

B.1 Correlation between the corrected number of tracklets and the generated charged particles for the different bins, bottom right panel shows the correlation factor for all 8 bins anchored to the LHC17p and q data samples. . 205

B.2 Correlation between the corrected number of tracklets and the generated charged particles for the different bins, bottom right panel shows the correlation factor for all 8 bins anchored to the LHC17p and q data samples. . 206

C.1 MSL (top) and MSH (bottom) p_{T} distribution in different multiplicity percentile bins for LHC17p+q. 208
C.2 MSL (top) and MSH (bottom) p_{T} distribution in different multiplicity percentile bins for LHC15n. 209

D.1 $A \times \epsilon$ of MSL and MSH triggers as a function of p_T for LHC17q (left) and LHC15n (right) data samples 212

E.2 Background fraction of secondary muons in different multiplicity percentile bins associated with the LHC17p and q (top) and LHC15n (bottom) data samples. 215
E.3 Electroweak bosons and inclusive muon differential cross sections (top) and background fraction of electroweak bosons (bottom) for the LHC15n data sample. 216
E.4 Differential cross section distributions of the inclusive muons and J/ψ (E.4a) and background fraction of J/ψ (E.4b) for the LHC15n data samples. 218

F.1 Outside the buffer zone where the control PC, gas bottle and HVPS are located. 221
F.2 Inside the buffer zone where the gas distribution rack, X-ray source and slat are located. 221
F.3 Amptex Mini-X controller software used to control the X-ray source safely from outside the buffer zone. 222
F.4 Slat 144 SR2 04 measurements when it was tested in 2019 224
F.5 Slat 144 SR2 04 measurements when it was tested in 2022 224

List of Tables

1.1 Properties of quarks . . . 3
1.2 Properties of leptons. . . . 3
1.3 Summary of open heavy-flavour particles and their properties . . . 10
1.4 Properties of the pions and kaons . . . 30

2.1 Summary of the different beam species and energies of the LHC for Run 2 as reported by CERN . . . 36
2.2 Summary of the the center-of-mass energies achieved by the LHC . . . 36
2.3 Summary of the ALICE detector subsystems . . . 53
2.4 Trigger capabilities of the ALICE trigger detectors . . . 56
2.5 Summary of the LHC operator modes . . . 61

3.1 Quality Assurance (QA) criteria . . . 72
3.2 Summary of runs MSL, MSH and MB triggered events for data samples being analysed . . . 72
3.3 Summary of Event Selection . . . 73
3.4 Summary of number of active SPD modules in the inner and outer layers during data-taking. . . . 77
3.5 Summary of the minimum and maximum reference values for the different data samples . . . 83
3.6 Summary of MC productions available on the ALICE Grid, in brackets is the data-taking period these are anchored to. . . . 86
3.7 Comparison of $\frac{dN_{ch}}{d\eta}$ for method 1 and 2 for data samples LHC17p+q. . . . 98
3.8 Comparison of $\frac{dN_{ch}}{d\eta}$ for method 1 and 2 for LHC15n data sample. . . . 98

3.9 Multiplicity axis that will be used in the final result for data samples LHC17p+q and LHC15n. . . . 99
3.10 Pseudorapidity density $dN/d\eta$ and the charged-particle multiplicity $\frac{dN_{ch}/d\eta}{\langle dN/d\eta \rangle}$ in pp collisions at $\sqrt{s} = 5.02$ TeV. . . . 101
3.11 Values of the charged-particle multiplicity ($\frac{dN_{ch}/d\eta}{\langle dN/d\eta \rangle}$) for LHC17p (second column) and LHC15n (fourth column). The corresponding systematic uncertainty is given in the third and fifth columns for LHC17p and LHC15n, respectively. . . . 102
3.12 Normalization factors determined using scaler and offline methods for MSL and MSH data sample. . . . 116
3.13 Normalization factor per multiplicity bin for the different data samples for both the MSL and MSH triggers, used for the data-driven method analysis. 118
3.14 Integrated luminosity for MSL and MSH data sample. . . . 119
3.15 Summary of the statistical uncertainties at $p_{\mathrm{T}} = 20$ GeV/c. . . . 127
3.16 Summary of the F_{norm}, $N_{MSL/MSH}$ and σ_{MB} . . . 131
3.17 Summary of MC productions . . . 141
3.18 Summary of the total POWHEG cross-section values and $nTrials$ for each process. . . . 145
3.19 Self-normalized J/ψ yields as a function of charged-particle multiplicity for the data-driven method. . . . 153
3.20 Systematic uncertainties considered in the measurement of muons from heavy-flavour decays in $2.5 < y < 4$. . . . 156
3.21 Systematic uncertainties considered in the measurement of muons from heavy-flavour decays as a function of charged-particle multiplicity. . . . 157

4.1 Self-normalized charged-particle multiplicity and self-normalized yield for the different multiplicity estimation methods. . . . 166

A.1 Summary of LHC17p event selection . . . 202
A.2 Summary of LHC17q event selection . . . 202
A.3 Summary of LHC15n event selection . . . 202

C.1 Normalization factor per multiplicity percentile for the different data samples for both the MSL and MSH triggers, used for the SPD estimator analysis. 210
C.2 Normalization factor per multiplicity percentile for the different data samples for both the MSL and MSH triggers, used for the V0M estimator analysis. . . . 211

E.1 Self-normalized J/ψ yields as a function of charged particle multiplicity for the V0M and SPD multiplicity estimators for the "Official Framework". . . 219

F.1 Summary of all slats tested in the period of the Service Task in May -June 2022. 225

List of Abbreviations

ACORDE	Array of Scintillators
ALICE	A Large Ion Collider Experiment
BR	Branching Ratio
CPC	Cathode Pad Chamber
CTP	Central Trigger Processor
DAQ	Data Acquisition
DCS	Detector Control System
ECS	Experiment Control System
EmCal	Electromagnetic Calorimeter
EPOS	Energy Shielding, Parton Multiple Scattering, Outshell remnants, and Screening, Shadowing and Strings
FMD	Forward Multiplicity Detector
FONLL	Fixed Order plus Next-to-Leading Logarithms
HF	Heavy-flavour
HFE	Heavy-flavour Electron
HFM	Heavy-flavour Muon
HLT	High-Level Trigger
HMPID	High Momentum Particle Identification Detector
IP	Interaction Point
ITS	Inner Tracking System
LHC	Large Hadron Collider
LTU	Local Trigger Units

MB Minimum Bias

MC Monte Carlo

MCH Muon Tracking Chambers

MPI Multiple Parton Interactions

MSH Muon Single High

MSL Muon Single Low

MTR Muon Trigger System

Pb-Pb Lead-Lead

PDF Patron Distribution Function

PHOS Photon Spectrometer

PID Particle Identification

PMD Photon Multiplicity Detector

pp proton-proton

pQCD Perturbative Quantum Chromodynamics

QCD Quantum Chromdynamics

QGP Quark Gluon Plasma

RPC Resistive Plate Chamber

RF Radiofrequency

SDD Silicon Drift Detector

SPD Silicon Pixel Detector

SSD Silicon Strip Detector

TOF Time-of-Flight

TPC Time Projection Chamber

TRD Transition Radiation Detector

Nomenclature

VARIABLES

In particle physics detectors, the origin of the coordinate system is fixed at the collision point. The positive z-axis lies along the incident proton beam direction, the polar angle θ_{cm} is in the xz plane and the azimuthal angle (ϕ) is around the beam axis in the xy plane, this is illustrated in Fig.1. The momentum (p) of the particle consists of three components along the x, y and z axes, p_x, p_y and pz, respectively. The transverse momentum p_{T} of the particle is given as:

$$p_{\mathrm{T}} = \sqrt{p_x^2 + p_y^2}. \tag{1}$$

Using particle kinematics, the rapidity (y) relative to a beam axis is given as:

$$y = \frac{1}{2} ln(\frac{E + p_z c}{E - p_z c}), \tag{2}$$

where E is the energy of the particle and c is the speed of light.

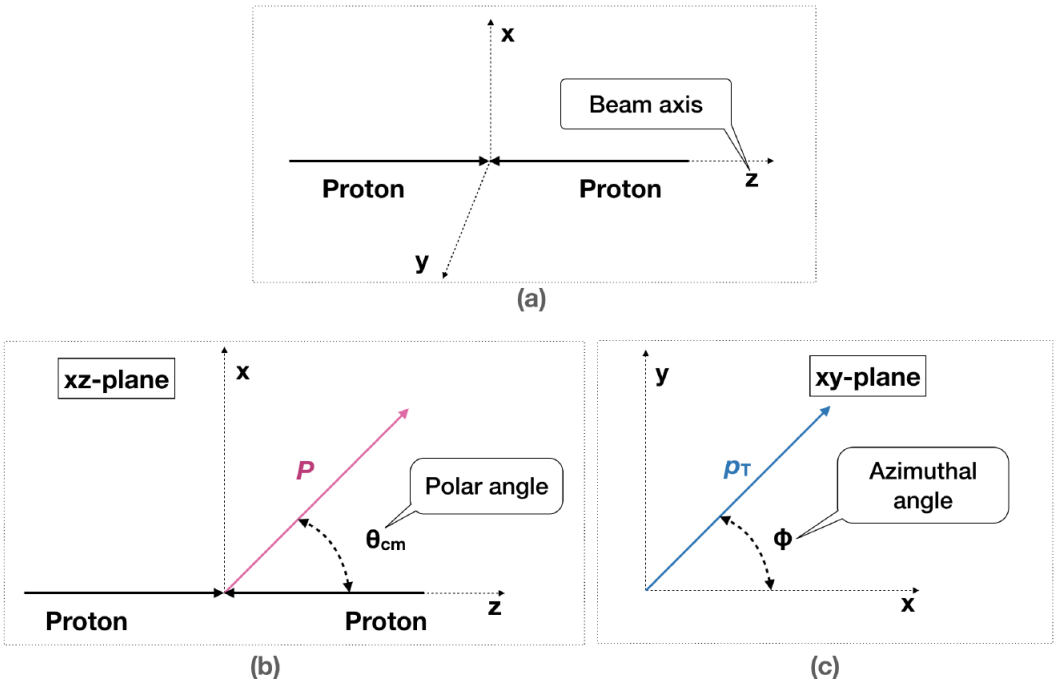

Fig. 1 Coordinate system in a pp collision [1].

The position of a particle in the detector can be expressed in terms of the azimuthal angle, rapidity (y) or the pseudorapidity (η). Rapidity is a dimensionless variable that is related to velocity, it describes the rate at which a particle is moving with

respect to a chosen point of reference that is situated in a line of motion. For highly relativistic particles, the rapidity is hard to measure as both the energy and the total momentum are required. It is difficult to get the total momentum vector of a particle at high values of the rapidity where the z component of the momentum is large, and the beam pipe can be in the way of measuring it precisely. In order to overcome this, a more simple concept was introduced known as pseudorapidity. Pseudorapidity is a useful variable as it does not require the energy and momentum of the particle but merely the polar angle as shown in Fig. 2.

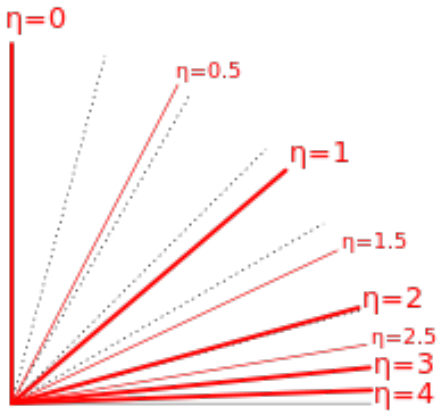

Fig. 2 Psuedorapidity values shown on a polar plot [2]

η is a spatial coordinate used to describe the angle of a particle relative to the axis of the beam. It can be defined as:

$$\eta \equiv -\ln\left[\tan\left(\frac{\theta}{2}\right)\right] \tag{3}$$

where θ is the angle between the particle three-momentum p and the positive direction of the beam axis. The center-of-mass energy is all the energy that is available to create new particles or to explore the internal structure of particles. Since the energy is measured at the center of mass reference of the system, the energy does not change the internal properties of the system [3].

For highly relativistic particles, $y \simeq \eta$. Starting with the definition of y,

$$y = \frac{1}{2} ln(\frac{E + p_x c}{E - p_x c}), \tag{4}$$

In the case of highly relativistic particles, y is then defined as:

$$y \simeq -\ln\left[\tan\left(\frac{\theta}{2}\right)\right] \tag{5}$$

ALICE coordinate system

A right-handed orthogonal coordinate cartesian system, shown in Fig. 3, is used for the ALICE detector. The point of origin is $x, y, z = 0$, is the interaction point (IP) of the two beams. The axes, azimuthal angle ϕ and polar angle θ are defined as follows [4]:

- **x-axis** is perpendicular to the beam direction that is aligned with the local horizontal, i.e. parallel to the ground;
- **y-axis** is perpendicular to the x axis and the mean local beam direction which is pointing upward from the IP;
- **z-axis** is parallel to the mean beam direction. In ALICE, the muon spectrometer is at negative z;
- **azimuthal angle (ϕ)** increases counter-clockwise from $x(\phi = 0)$ to $y(\phi = \frac{\pi}{2})$ with the observer standing at the positive z and looking in the direction of the muon spectrometer;
- **polar angle (θ)** increases from $z(\theta = 0)$ to the x, y plane $(\theta = \frac{\pi}{2})$ to $-z(\theta = 0)$.

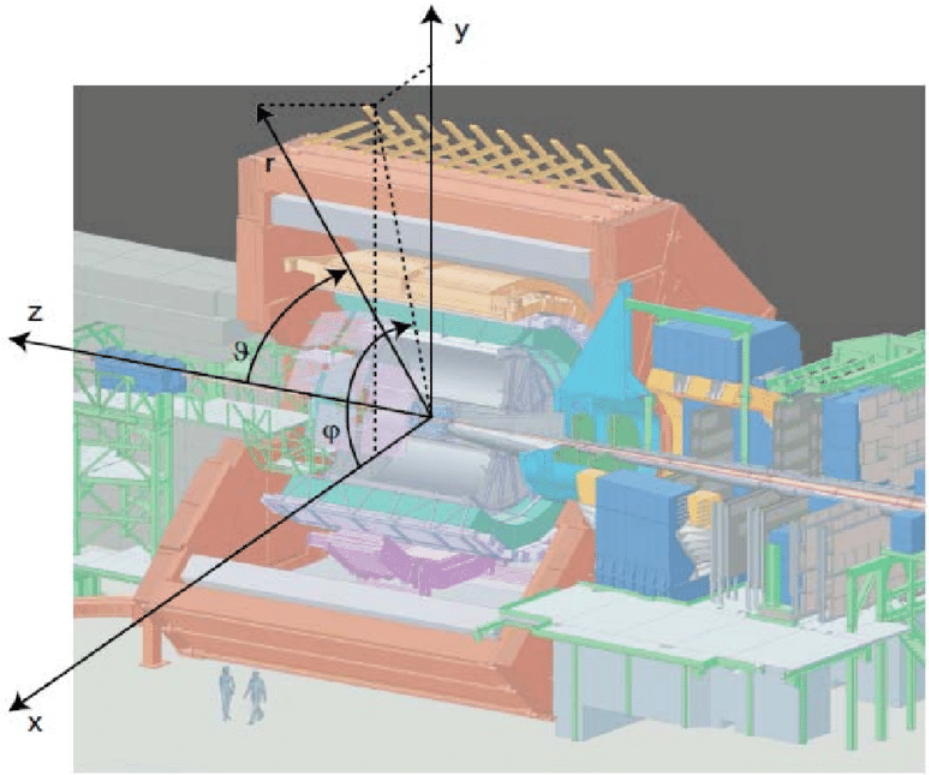

Fig. 3 The ALICE coordinate system [5].

CHAPTER 1

Introduction

1.1 Standard Model (SM) and Quantum ChromoDynamics (QCD)

1.1.1 Standard Model

The Standard Model (SM) of particle physics is a model based on gauge theories. The first of the theories was quantum electrodynamics which describes the interactions of electrons with light. The model was later incorporated into the electroweak theory that describes the electromagnetic and weak nuclear interactions. It also includes quantum chromodynamics which is the theory of the strong nuclear interactions [6]. It is the modern-day framework used to describe particle physics. In the Standard Model, nucleons are no longer considered the fundamental building blocks of matter, instead they are composite particles that consist of three valence quarks that are held together by the strong force.

The model divides all the fundamental particles into two classes, fermions and bosons. Fermions and bosons are characterized by their mass, electric charge and spin. Considering the spin[1] of the particles, fermions and bosons are differentiated with their spin numbers;

[1] A permanent angular momentum possessed by all particles in quantum theory, even when they are at rest.

particles with half-integer spin are fermions while those with integer spin are bosons. All matter is made up of fermions while bosons mediate the interactions that happen at the fundamental particle level. Fermions are further divided into two groups, leptons and quarks. The force responsible for the interaction of leptons is the second fundamental force, the weak interaction, while quarks interact via the strong interaction [7]. Quarks are in a bound state while leptons can exist as free particles. For every particle of nature, there exists an associated particle, called an antiparticle that has the same mass as the corresponding particle. The SM is summarized in Fig. 1.1.

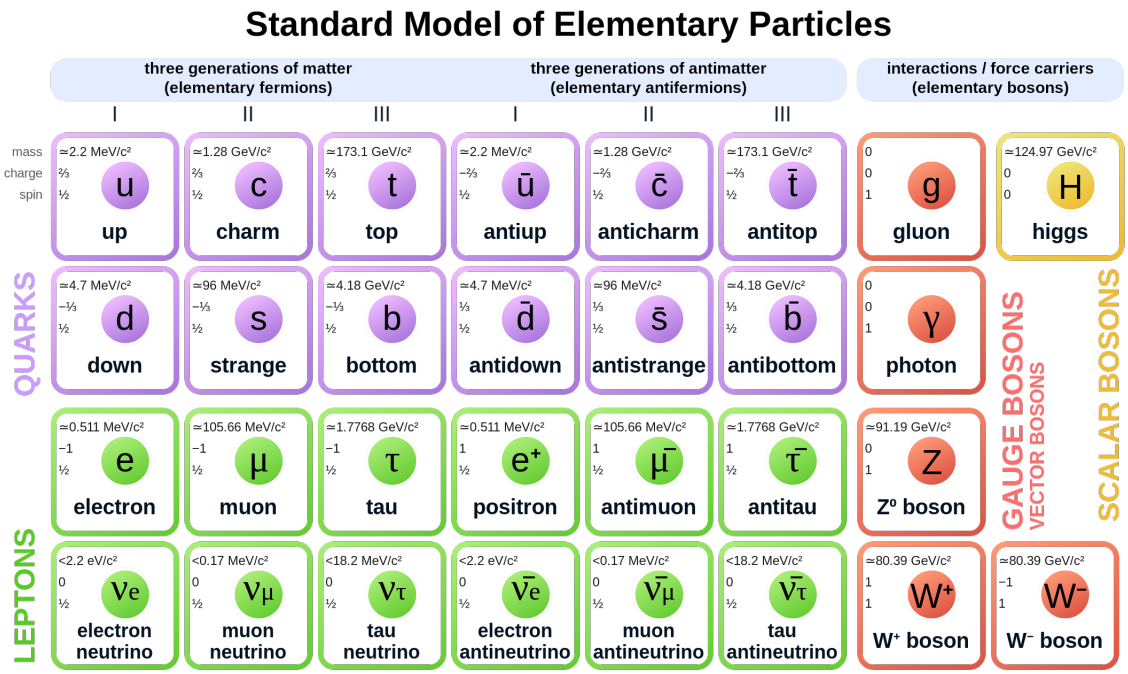

Fig. 1.1 Standard Model of Particle Physics [8]

There are six "flavours" of quarks, flavour refers to the species of an elementary particle. Quarks are bound together by the strong interaction force, which will be discussed in the next section, to make up hadrons such as protons and neutrons. A summary of their properties is given in Table 1.1. The first three quarks as listed in the table have very small masses in contrast to the other three quarks that are much heavier. The charm, bottom and top quarks are referred to as heavy quarks, with the charm and bottom quarks having a notably smaller mass than the top quark. Hadrons that contain the charm (c) or beauty (b) quarks or their anti-quarks are referred to as heavy flavoured particles or simply heavy-flavour particles.

There are also six "flavours" of leptons; the electron, muon, tau and their associated neutrinos. There are three negatively electrically charged leptons, and three electrically neutral leptons. The electrically neutral leptons are neutrinos. A summary of the prop-

Quark (anti-quark)	**Symbol**	**Mass (MeV/c^2)**	**Charge**
up	u($\bar{u}$)	1.5 - 4.0	$+\frac{2}{3}$ ($-\frac{2}{3}$)
down	d($\bar{d}$)	4 - 8	$-\frac{1}{3}$ ($+\frac{1}{3}$)
strange	s($\bar{s}$)	80 -130	$-\frac{1}{3}$ ($+\frac{1}{3}$)
charm	c($\bar{c}$)	1150 - 1350	$+\frac{2}{3}$ ($-\frac{2}{3}$)
bottom	b($\bar{b}$)	4100 - 4400	$-\frac{1}{3}$ ($+\frac{1}{3}$)
top	t($\bar{t}$)	171 400 - 210 000	$+\frac{2}{3}$ ($-\frac{2}{3}$)

Table 1.1 Properties of quarks [9]

erties of the leptons is given in Table 1.2.

Particle (Anti-particle)	Symbol	Mass (MeV/c^2)	Charge
Electron	e^- (e^+)	0.511	-1
Electron neutrino	v_e ($\bar{v_e}$)	$0(< 7 \times 10^{-6})$	0
Muon	μ^- (μ^+)	105.7	-1
Muon neutrino	v_μ ($\bar{v_\mu}$)	$0(< 0.27)$	-0
Tau	τ^- (τ^+)	1777	-1
Tau neutrino	v_τ ($\bar{v_\tau}$)	$0(< 31)$	0

Table 1.2 Properties of leptons[9, 10].

The interactions that happen at the fundamental particle level are mediated by bosons. These forces include the strong force which is mediated by the gluon, the electromagnetic force which is mediated by the photon and the weak force mediated by the electroweak bosons. Electroweak bosons, W and Z bosons, are short-lived bosons that do not interact strongly. They interact with each other as well as with all quarks and leptons through the weak interaction. These bosons are created at a very early stage of hard parton[2]-parton interactions. The W boson can be split into two types, the W^- with a negative electric charge and the W^+ with a positive electric charge. Each W boson has a mass of 80 GeV/c^2. The Z boson is neutral and has a mass of 90 GeV/c^2.

The other two bosons are the gluon and photon. Gluons are the force carriers of the strong interaction, there are eight glouns in total that all have zero mass and are all electrically neutral. Photons are quanta of electromagnetic radiation, commonly known as gamma (γ) rays.

[2]A parton is a constituent of hadrons, an example of this are quarks and gluons

1.1.2 Quantum Chromodynamics (QCD)

The interaction between the quarks through the strong force and its force carrier, the gluon, is described by the theory of quantum chromodynamics (QCD). Quarks and gluons are color-charged particles; each quark has a certain color charge: red, blue or green and their respective anti-colors. Gluons carry a color and an anti-color charge at any time. As the quarks exchange gluons with other quarks, the color charge of the quarks changes; the exchange of these color charges creates a very strong color force field that binds the quarks together. Quarks and gluons can only be found in confined colorless composites; e.g. in protons and neutrons which are color neutral.

In QCD, gluons do not only interact with quarks to "glue" them together but they also interact with themselves. The gluon-gluon interaction leads to the reduction of the coupling constant, α_s, as the energy increases. The gluon-gluon interaction is responsible for the confinement of quarks within composite particles. The interaction between gluons leads to the quarks being closely bounded to each other. The strong coupling constant (α_s) is a free parameter of the Langrangian of QCD; this is only if the masses of quarks are fixed [11]. The coupling constant varies as a function of the energy scale or the momentum transfer (Q) for a specific process. The theory of strong interaction in QCD is studied using the fact that $\alpha_s(Q^2)$ decreases for increasing energy scale. A small α_s is within the perturbative regime of QCD, the so-called pQCD. The dependence of the coupling constant to the energy scale is shown in Fig. 1.2 [12].

The property of gluons being able to interact with themselves implies that the closer the quarks come to each other, the weaker the quark colour charge will be and hence resulting in the interaction being weaker. The gluon-gluon interaction constrains color fields to string-like objects referred to as flux tubes; these tubes exert a force when stretched. As the quarks move closer together, the flux tubes are less stretched and thus resulting in the force binding the quarks to decrease. The property of the energy increasing while the interaction strength decreases is known as asymptotic freedom and simply implies that the beta (β) function is negative [13]. The β function encodes the dependence of a coupling constant, α_s, on the energy scale, μ, of a given physical process that is described by quantum field theory. The function is a logarithmic derivative defined as [14]:

$$\beta(\alpha_s) = \frac{\partial \alpha_s}{\partial log(\mu)} \tag{1.1}$$

Due to the underlying re-normalization group, there is no explicit dependence on μ, so the β function only depends on μ implicitly through the coupling constant α_s. The dependence on the energy scale makes the β function known as the running of the coupling constant.

At high energies (Q), up to 200 GeV, quarks and gluons behave as almost free particles as a result of the asymptotic relationship between the strong coupling constant and energy.

The asymptotic freedom allows for calculations of the small distance interaction of quarks and gluons. The logarithmic decrease of the coupling constant depends on the QCD energy-scale parameter, Λ. Since Λ is the scale of confinement and all other typical processes of pure QCD which are independent on the masses of quarks, it controls the predictions of pQCD at short distances [15]. Experiments at SLAC [16], DESY [17], CERN's Large Electron−Positron (LEP) collider [18] and Fermilab Tevatron [19] have measured the decrease of the QCD coupling constant as shown in Fig. 1.2.

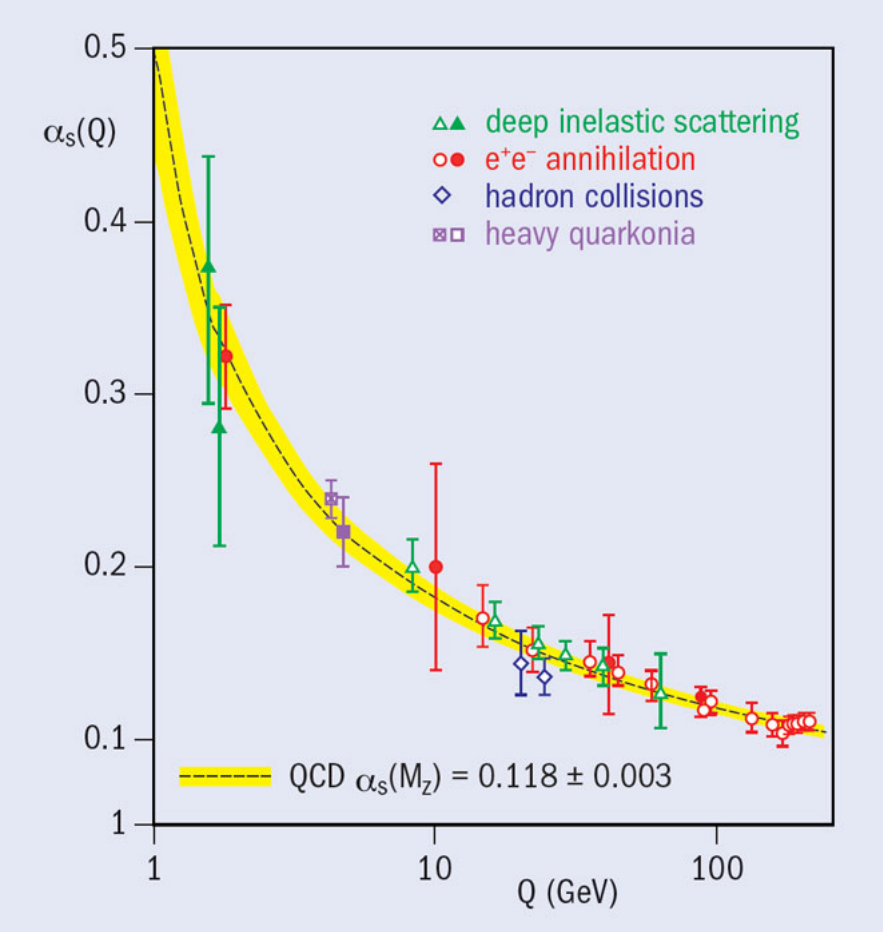

Fig. 1.2 The strong-coupling constant α_s as a function of energy scale [12].

The energy-scale parameter Λ arises when solving the differential equation, a β function, of α_s as defined below,

$$\beta(\alpha_s) \equiv \frac{\mu}{2}\frac{\delta\alpha_s}{\delta\mu} = -\frac{\beta_0}{4\pi}\alpha_s^2 - \frac{\beta_1}{8\pi^2}\alpha_s^3 - .... \tag{1.2}$$

where

$$\beta_0 = 11 - \frac{2}{3}n_f,\ \beta_1 = 102 - \frac{38}{3}n_f \tag{1.3}$$

and n_f is the number of quarks with a mass less than μ (number of degrees of freedom), the energy scale. β_0 and β_1 correspond to the number of loops (will be discussed in the

next section) with β_0 and β_1 being one loop and two loops, respectively. These terms are also independent of the renormalization scheme[3] [15].

A first order approximation (this will be discussed later) can be made for equation 1.2 and can be expressed as:

$$\alpha_s(\mu^2) = \frac{\alpha_s(\Lambda^2)}{1 + \frac{\alpha_s(\Lambda^2)}{12\pi}\beta_0 ln\frac{\mu^2}{\Lambda^2}} \tag{1.4}$$

Figure 1.2 illustrates the case when asymptotic freedom is achieved, when $\mu \to \infty$, the coupling constant decreases with an increase in energy. QCD is divided into two regions in Fig. 1.2; pQCD (> 100 GeV) and non-perturbative (< 100 GeV) QCD. An example where pQCD is successfully implemented is in the e^+e^- annihilation leading to the production of the Z^0 boson. The Z^0 boson has a final state that consists of quarks and gluon jets. This allows for the use of the mass of the Z^0 (M_Z) boson, to determine the coupling constant [21] $\alpha_s(M_Z) = 0.118 \pm 0.003$.

Non-perturbative QCD is an approach used in QCD to formulate the theory of a finite space-time lattice. By preventing the space-time from being continuous, the number of degrees of freedom are reduced to a finite number. This allows for the theory to be applied in a computer program and a calculation can be performed. Non-perturbative QCD is especially useful in cases like quark confinement which is not treated by pQCD theories [22]. Non-perturbative interactions are indispensible for understanding heavy flavor quenching and flow at low and intermediate transverse momentum.

The results from pQCD calculations of the hard scattering process cross section, will be discussed later in the chapter, depend on the strong coupling constant, α_s and its renormalization scale μ_F as shown in equation 1.5. The renormalization scale of the coupling constant is responsible for summing all the terms that are involved in the β function expressed in equation 1.2. In order to sum up all the non-conformal terms ($\beta \neq 0$) in the perturbative expansion that arise from the renormalization, μ_F has to be set accordingly. When μ_F is set accordingly, the remaining terms in the perturbative series correspond with the $\beta = 0$ theory [23].The hard scattering process cross section is given by [24]:

$$d\sigma^{hard}_{AB\to C} = \sum_{a,b} f_{a|A(x_a,Q^2)} \bigotimes f_{b|B(x_b,Q^2)} \bigotimes d\sigma^{hard}_{ab\to C}(x_a, x_b, q^2) \bigotimes D_{c\to C}(z, Q^2) \tag{1.5}$$

Equation 1.5 embodies an important assumption made in the parton model factorization. The summation is a product of three factors: two probability densities (the red and green

[3]Renormalizing is the process of limiting an infinite frame of group into a finite frame or group. Renormalizing is confining potentially infinite quantum complications into relativistic unit frames [20].

terms) and a subprocess cross section (blue term). The probability densities are assumed to be universal, process-independent properties of the incident hadrons [25].

From equation 1.5, it can be concluded that pQCD calculations are based on:

- A factorization approach and computed as a convolution of the hard parton scattering cross section,
- Evaluated as a perturbative series of the coupling constant of the strong interaction,
- The parton distribution function (PDF) of the colliding protons, and;
- The fragmentation function of heavy quarks to heavy-flavour hadrons.

PDFs were introduced in the parton model to explain the Bjorken scaling[4] in deep inelastic scattering data. They are usually interpreted as probability distributions, giving the probability of finding a parton with a certain momentum fraction (x) at some momentum transfer Q^2 that defines the energy scale of the process [24]. PDFs can be obtained by first choosing a factorization scheme, a perturbation theory order (LO, NLO, etc) and a starting scale (Q_0) where pQCD applies.

The next step is to parametrize the quark and gluon distributions at Q_0, where pQCD is applicable. Thereafter, the Dokshitzer–Gribov–Lipatov–Altarelli–Parisi (DGLAP) evolution equations are solved to obtain the PDFs at any value of x and scale $Q > Q_0$. DGLAP equations are used in QCD to describe the variation of PDFs with varying energy scales. After solving the DGLAP equations, the solutions are fitted to data to obtain the parameters as illustrated in Fig. 1.3 [27]. The data are obtained from various experiments like SLAC [16], CDF [19], D0 [19], etc.

There are many groups that extract PDFs from global data analyses like CTEQ [28], NNPDF [29], HERAPDF [30], MSTW [31], etc. There is a broad agreement overall with a few differences introduced by the input distributions, the treatment of data errors, heavy quarks, order of the perturbation theory and parameterization at Q_0. Some groups include theoretical assumptions about the flavour symmetries and the behaviour of the PDF at Bjorken-x $(x) \to 0.1$.

Bjorken-x values, x_1 and x_2, are identified to be the fraction of the proton momentum carried by a struck quark in a frame where the proton has very high energy.

$$x_{1,2} = \frac{Me^{\pm y}}{\sqrt{s}} \tag{1.6}$$

where M is the mass of a heavy quark, y is the rapidity and $\sqrt{s}$ is the center-of-mass

[4] scaling of a large class of dimensionless physical quantities in elementary particles [26]

energy. Figure 1.3 shows that up and down quarks contribute to the quantum numbers of protons, they form valence quarks and therefore carry a large fraction of the momentum. Parton momentum distributions depend on the momentum transfer of the interaction, Q^2. At large Q^2, the interacting particles see the short-distance structure of the proton. As a consequence, PDF's are shifted towards small Bjorken-x values.

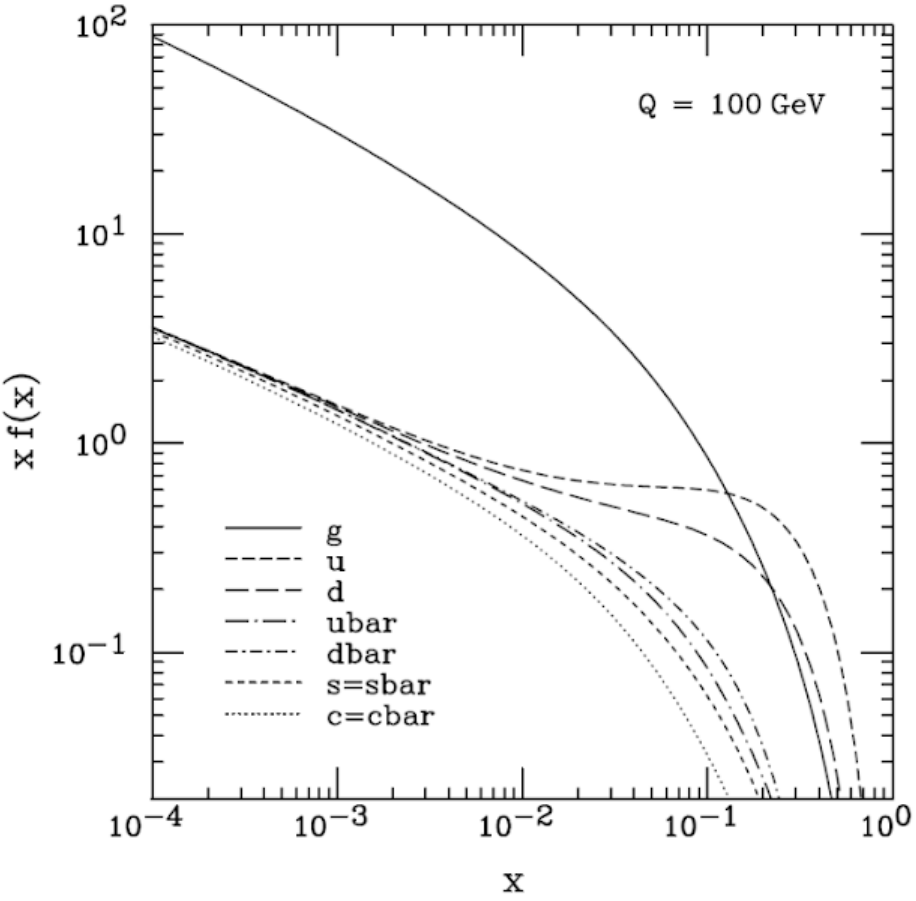

Fig. 1.3 Overview of the CTEQ6M parton distribution functions at Q = 100 GeV where x is the Bjorken-x discussed in the text and $xf(x)$ is the distribution function [27].

To summarize, in pQCD the strong coupling constant is small at high energy and short distance interactions. In the majority of pQCD application, the cross sections are separated into two parts, namely, (i) process dependent pQCD calculable short-distance parton cross section and (ii) the universal long-distance functions measured with global fits to experimental data to obtain a partly calculable prediction to particle reaction processes. In the next section, the heavy flavour production process is discussed.

1.2 Heavy-flavour production

In pQCD, heavy-flavour production can be expressed with the lowest-order Born diagrams as illustrated in Fig. 1.4. A heavy quark (Q) and heavy anti-quark ($\bar{Q}$) are produced from two-parton to two-parton processes whereby either two gluons fuse together (gg) or a light quark (q) annihilates with a light anti-quark ($\bar{q}$). The constituents of the incident interacting hadrons are the initial partons; i.e. quark, anti-quark and gluon. Taking the proton as an example, it is made up of two up quarks and a down quark bound together by the gluons; in the case should a proton be a carrier anti-quarks, then the proton would be referred to as an antiproton. The cross sections of the subprocess associated with the diagrams in Fig. 1.4 are proportional to the strong coupling constant (this is discussed in the next section) [25].

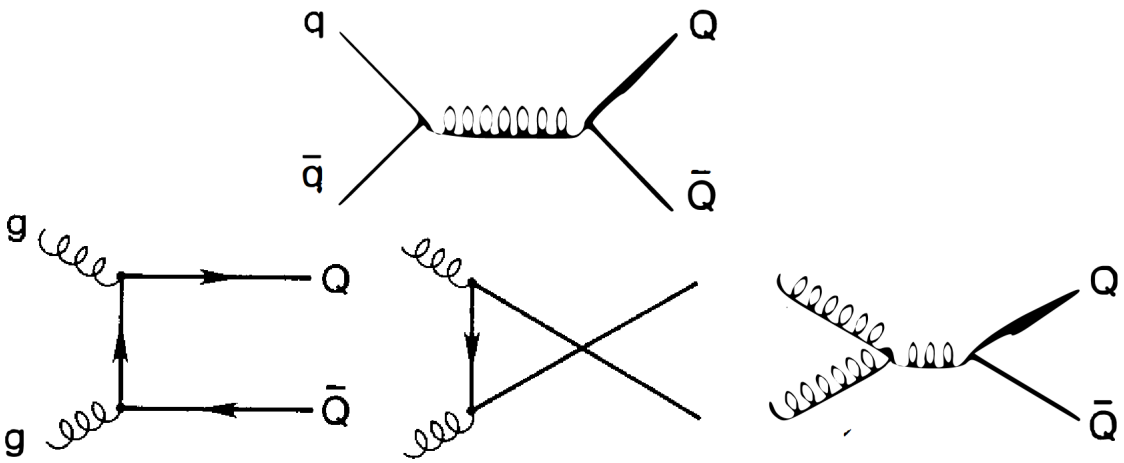

Fig. 1.4 Born diagrams in QCD for heavy quark (Q) and heavy anti-quark ($\bar{Q}$) production [25].

The two-parton to two-parton (2-to-2) processes shown in Fig. 1.4 are leading order (LO) production processes, $O(\alpha_s^2)$. The processes can be summarized as:

$$q + \bar{q} \rightarrow Q + \bar{Q} \tag{1.7}$$

$$g + g \rightarrow Q + \bar{Q} \tag{1.8}$$

The internal gluon and/or heavy quark lines shown in Fig. 1.4 are off-mass-shell by m_Q^2 where m_Q denotes the mass of the heavy quark. Off-shell refers to fields that do not have to obey the equations of motion and are virtual particles while on-shell are fields that obey the equations of motion and are real particles. For large values of m_Q, from the mass of charm or beauty to the mass of the top quark, Next-to-Leading (NLO)

production processes ($O(\alpha_s^3)$) involve QCD radiation, which is the gluon-gluon interaction that results in gluon radiation. The gluon is either in the initial or final state of the process as illustrated in equations 1.9, 1.10 and 1.11 [32]; these are the processes of interest in this study.

$$q + \bar{q} \rightarrow Q + \bar{Q} + g \tag{1.9}$$

$$g + g \rightarrow Q + \bar{Q} + g \tag{1.10}$$

$$q(\bar{q}) + g \rightarrow Q + \bar{Q} + g \tag{1.11}$$

NLO calculations are necessary since LO calculations can only describe the mass and rapidity distributions for single-inclusive distributions. The p_{T} and azimuthal doube-differential distributions cannot be calculated at Born level since the $Q\bar{Q}$ pairs are produced back-to-back in LO. The importance of these Born diagrams and what dynamical features are observed are discussed in more detail in [25].

A discussion on heavy-flavour will follow in the next subsection.

1.2.1 Heavy flavour

In this thesis, inclusive measurements will be done via the semileptonic (the muon in this case) decay channel; this simply means that muons from both charm and beauty quarks will be measured with no distinct separation since the Run 2 ALICE muon spectrometer capabilities cannot distinguish them in the rapidity region of interest.

Heavy-flavour particles can be divided into two groups, namely: open heavy flavour and quarkonia. Open heavy flavour are hadrons that contain at least a heavy quark or antiquark and a light quark. Quarkonia are defined as bound states of a heavy quark-antiquark pairs.

Particle	**Quark content**	**Mass** (MeV/c^2)	**Decay time** τ ($\times 10^{-15}$ s)	**Decay length** $c\tau$ (μm)
$\mathrm{D}^{\pm}$	$c\bar{d}$	1869.65 ± 0.05	1040 ± 7	311.8
D^{0}	$c\bar{u}$	1864.83 ± 0.05	410.1 ± 1.5	122.9
$\mathrm{B}^{\pm}$	$u\bar{b}$	5279.32 ± 0.14	1.638 ± 0.004	491.1
B^{0}	$d\bar{b}$	5279.63 ± 0.15	1.520 ± 0.004	455.7

Table 1.3 Summary of open heavy-flavour particles and their properties [33].

Open heavy flavour can further be divided into the hadronic decay channel and the semileptonic decay channel [34]. Examples of the decay channels and their respective

branching ratios (BR) are given below. A branching ratio is the fraction of particles that decay through a certain decay mode with respect to the total number of particles that decay.

- Examples of the hadronic decay channel:
  1. $D^0 \rightarrow \pi^- K^+$ $(D^0(c\bar{u}))$ $BR \approx 3.93\%$
  2. $D^+ \rightarrow K^- \pi^- \pi^+$ $(D^0(c\bar{d}))$ $BR \approx 9.46\%$
- Examples of semileptonic decay channel:
  1. Charm $\rightarrow$ lepton (e/μ) $BR \approx 10\%$
  2. Beauty $\rightarrow$ lepton (e/μ) $BR \approx 10\%$
  3. Beauty $\rightarrow$ charm $\rightarrow$ lepton (e/μ) $BR \approx 9\%$

The respective topologies of the decay channels are illustrated in Fig. 1.5. In the hadronic decay channel (left in Fig. 1.5), the V_{prim} is the primary vertex where the D meson is produced and the V_{sec} is the secondary vertex where the D^0 decays into a kaon (K) and a pion (π). In the semileptonic decay channel (right in Fig. 1.5), the B or D meson decays into an electron or muon and something else.

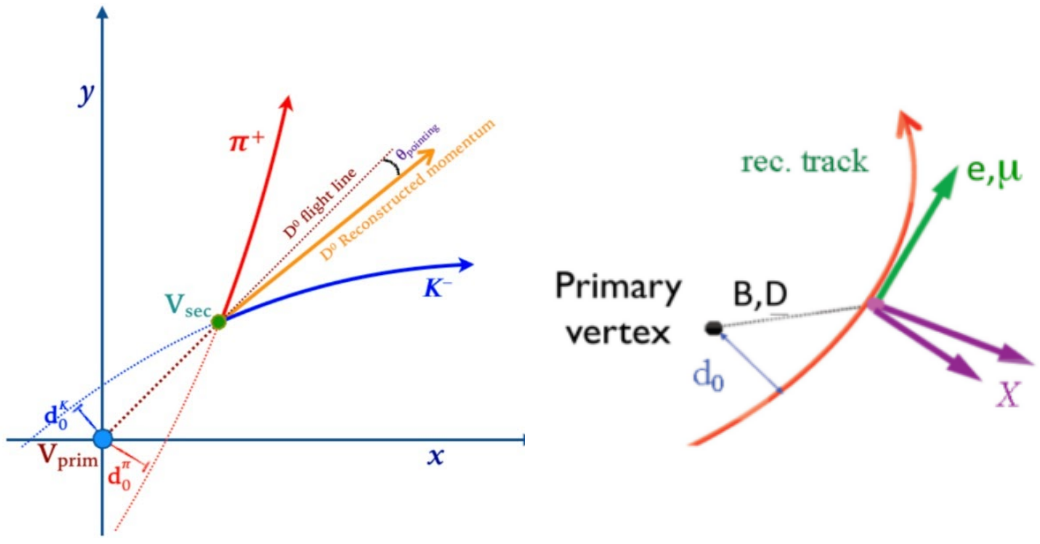

Fig. 1.5 Topologies of decay channels of charm (D) meson via the hadronic decay channel (left) and decay channels of charm and beauty meson via semileptonic decay channel (right) [35]

The production cross section in pp collisions will be discussed in the next section.

1.2.2 Heavy-flavour production cross section in pp collisions

Heavy quarks are products of hard-scattering processes - those that involve momentum transfer larger than the mass of protons - between constituent partons. Figure 1.6 is an illustration of hard partonic scattering process where it shows the probability of finding a parton $f_{a|A(x_a,Q^2)}$) and $f_{b|B(x_b,Q^2)}$ in a hadron A and B with a momentum fraction x_a and x_b at the energy μ_F^2. $f_{a|A(x_a,Q^2)}$ and $f_{b|B(x_b,Q^2)}$ are parton distribution functions (PDF) of hadrons A and B.

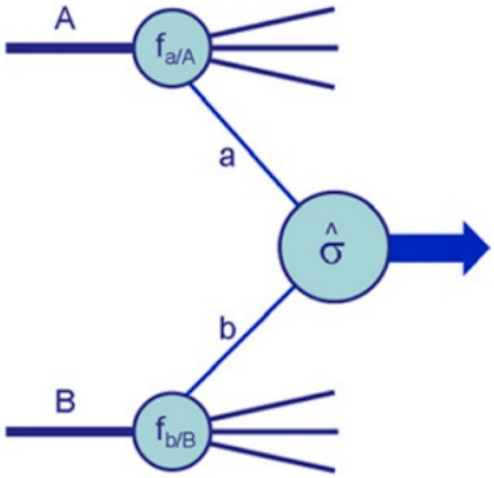

Fig. 1.6 Hard partonic scattering process[24].

The LHC is the most abundant source of heavy-flavour particles [36], this is illustrated in Fig. 1.7 where the production cross sections of the charm and beauty quarks in pp collisions as a function of center-of-mass ($\sqrt{s}$) energy are shown. In Fig. 1.7 on the left, it is clear that all the LHC experiments measure a higher production cross section as compared to other experiments, which is attributed to the higher collision energies at the LHC. The production cross section is pseudorapidity-dependent and peaks at $|\eta| \approx 3$ and increases as a function of $\sqrt{s}$ [36].

Figure 1.7 on the left shows the dependence of the total charm production cross section at midrapidity per unit of rapidity as a function of the collision energy. Results from other experiments are also shown. The curves show theoretical calculations from pQCD calculations based on Fixed Order plus Next-to-Leading Logarithms (FONLL) [37] and Next-to-Next-to-Leading order (NNLO) [38] with the corresponding uncertainties.

The FONLL code is used to calculate the total or single inclusive differential cross sections for heavy-quark (charm or bottom) production at $\overline{p}$ or pp colliders, with cuts on p_{T} and y or η [39]. FONLL merges the massive Next-to-Leading Order (NLO) calculations based on QCD with the Next-to-Leading Logarithms resummation (NLL) of terms of

collinear origin. Next-to-Leading Logarithms (NLL) are of the type $log(p_T/m)$, where p_T is the transverse mometum and m is the mass of a quark; they appear when $p_T >> m$, limiting the NLO $O(\alpha_s^3)$ calculations and require to be resummed to all orders. NLO terms $\alpha_s^3 log(p_T/m)$ are related to the mass singularities that originate from collinear configurations when $m \to 0$ for fixed p_T [39].

Some of the advantages of the FONLL framework are:

- The pertubative uncertainty does not increase when $p_T >> m$.
- The non-pertubative input describing the quark-to-meson hadronization can be extracted from e^+e^- data and included in predictions for hadronic collisions.
- It predicts the total heavy-quark production rates according to NLO QCD which is not always the case for other frameworks.

The FONLL code is available for anyone to use [40], it gives the user options to choose the collider (for a high p_T^{max} reach) and center-of-mass energy, the PDFs, perturbative order (option between FONLL and NLO), heavy quark, hadronic final state, further decay and cross section type. The user is also given the option to input the transvere momentum and rapidity range. The Parton Distribution Functions (PDFs) available for the FONLL code include CTEQ6.6 and NNPDF30nlo_as0118 [40].

In Fig. 1.7, the dependence on the collision energy is described by the pQCD calculations where the data points populate the upper band of the theoretical prediction however still fall within statistical uncertainties [41]. On the right is the dependence of the total beauty production per unit rapidity as a function of the collision energy. Results from other experiments are also shown. The curves show theoretical calculations from pQCD calulations FONLL and NNLO with the corresponding uncertainties. The dependence on the collision energy is described by the pQCD calculations where the theory describes the data [42].

1.2.3 Heavy-flavour production cross section in LHC experiments

The previous section highlighted some of the experiments from low energies [43, 44, 45] to LHC energies [41, 42] involved in measurements of heavy-quark production cross sections also at lower energies . In this section, the discussion is narrowed down to measurements performed in LHC experiments with the special focus on the ALICE experiment. The forward rapidity range of the ALICE experiment allows us to test pQCD predictions in the region of small $O(10^{-4})$ Bjorken-x. The forward rapidity is the region closest to the beam axis.

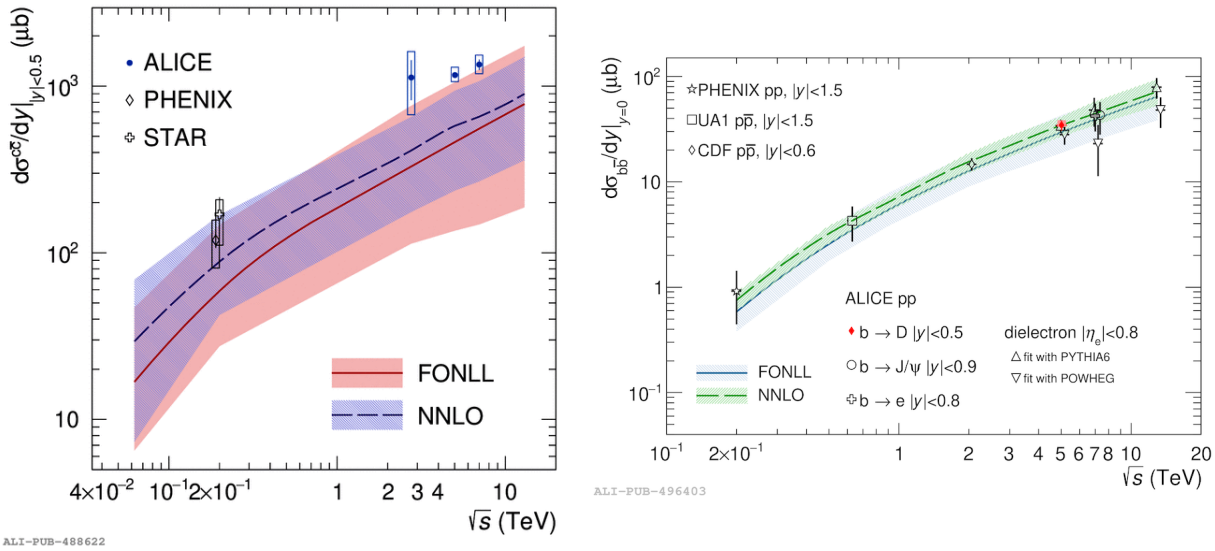

Fig. 1.7 Charm (left) [41] and beauty (right) [42] differential cross section measured in pp collisions as a function of center-of-mass energy.

The Bjorken-x regime relevant for charm and beauty production at the LHC, $O(10^{-4})$, is about two and three orders of magnitude lower than that at RHIC and SPS, respectively. On the left of Fig. 1.8, Bjorken-x as a function of M^2 - M is the mass of a heavy quark - for particle production in nucleon-nucleon collisions at the SPS, RHIC and LHC is shown. The lines correspond to constant rapidity at corresponding energies, it can be noted that as the rapidity increases, lower Bjorken-x values can be investigated[46].

On the right of Fig. 1.8, the regions in the (x_1, x_2)[5] plane covered by charm and beauty in the ALICE acceptance in pp collisions at $\sqrt{s} = 14$ TeV. It is worth noting that in the acceptance of the ALICE forward muon spectrometer, the accessible Bjorken-x range is of the order two times lower than that measured in the central barrel. Heavy-flavour measurements in the forward rapidity therefore offer a unique opportunity to measure PDFs down to extremely low, $O(10^{-6})$, Bjorken-x values [46].

At unprecedented LHC energies, a large amount of heavy quarks are produced in pp collisions. The production cross-sections for $c\bar{c}$ and $b\bar{b}$ quark−antiquark pairs show an increase of $\approx 5/50$ [41] and $\approx 10/100$ [42] from RHIC to LHC, respectively. The 4 major experiments at the LHC are complementary to each other in terms of kinematic region coverage, there is a coverage of entire rapidity range when comparing results from the experiments. This complementarity is also explored in heavy-flavour measurements.

Figure 1.9 shows the invariant double differential production cross sections of electrons

[5]The fraction of the proton momentum carried by a struck quark in a frame where the proton energy is very high

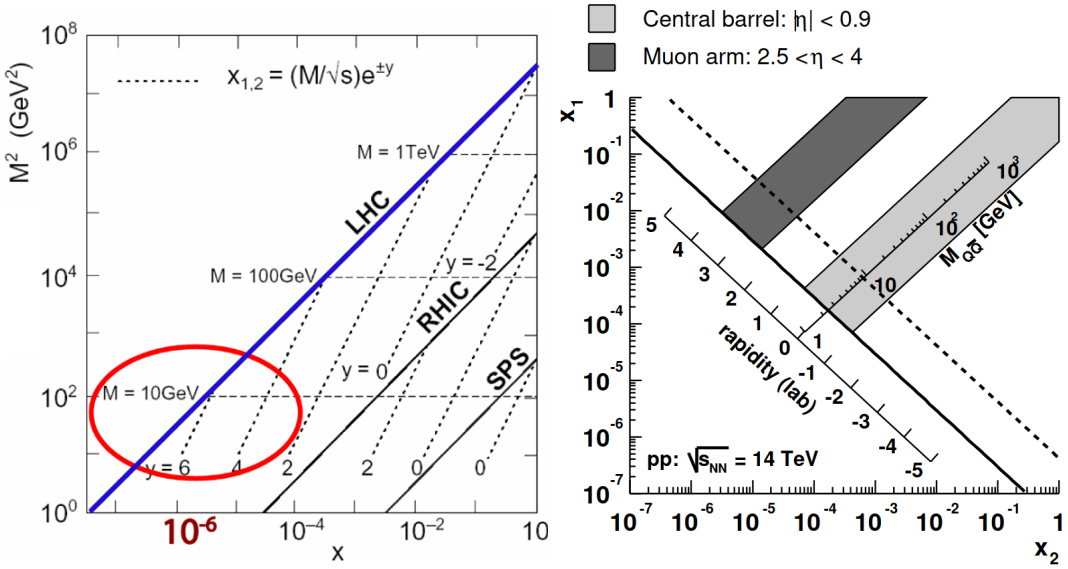

Fig. 1.8 Bjorken-x as a function of M^2 for particle production in nucleon-nucleon collisions at the SPS, RHIC and LHC (left) [46] and the accessible Bjorken$-x$ range for heavy flavours in pp collisions at $\sqrt{s} = 14$ TeV (right) in the rapidity range that can be measured with ALICE at the LHC [47]. The area circled in red is the forward rapidity where the LHC can reach that other experiments cannot.

from heavy-flavour decays measured at midrapidity by ALICE and ATLAS at midrapidity in pp collisions at $\sqrt{s} = 7$ TeV. The ALICE experiments shows results up to $p_{\mathrm{T}} < 8$ GeV/c while the ATLAS experiment shows results for $p_{\mathrm{T}} > 8$ GeV/c. FONLL pQCD calculations with the same rapidity selections are shown for comparison. The error bars depict the statistical uncertainty while boxes show the total systematic uncertainty of the measurements [48].

The ratio of the measured cross section and FONLL calculations is shown in the lower panel of Fig. 1.9. The error bars and boxes indicate the statistical and systematic uncertainties of the electron spectrum from heavy-flavor decays, respectively [48]. The results show that the production cross section of electrons from charm and beauty decays decreases with an increase in p_{T}. The ALICE and ATLAS experiments compliment each other where the ALICE experiment measures at low p_{T}, $p_{\mathrm{T}} < 8$ GeV/c and the ATLAS experiment at high p_{T}, $p_{\mathrm{T}} = 8$ GeV/c.

Heavy-flavour decay muon (HFM) measurements with the Muon Spectrometer of the ALICE detector at forward rapidity ($-4.0 < y < -2.5$) were published for the production cross section as a function of transverse momentum and rapidity in pp collisions at $\sqrt{s} = 5.02$ [49]. In the 5.02 TeV publication [49] as shown in Fig. 1.10, the results obtained were extended to the transverse momentum interval of $2 < p_{\mathrm{T}} < 20$ GeV/c as compared

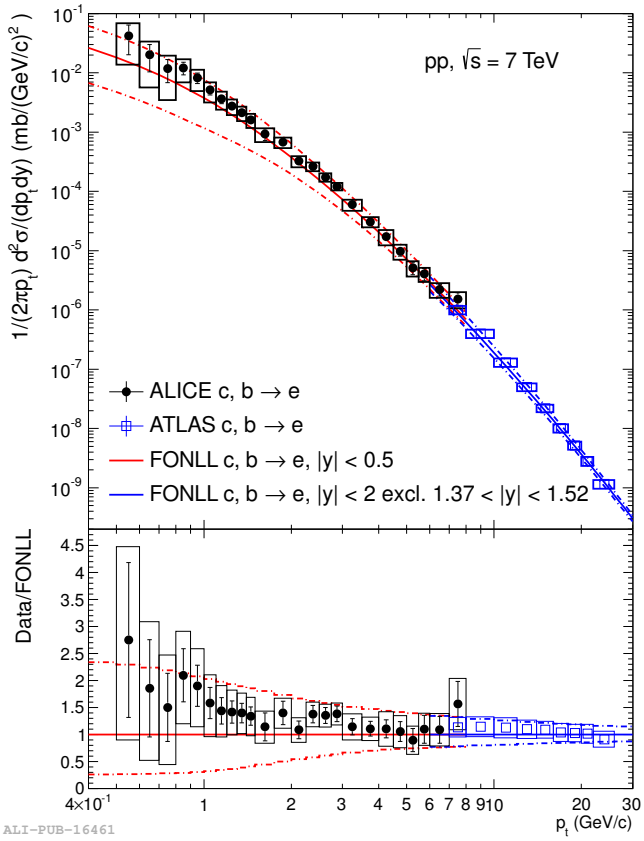

Fig. 1.9 Invariant double differential production cross sections of electrons from heavy-flavour decays measured by ALICE and ATLAS in pp collisions at $\sqrt{s} = 7$ TeV in different rapidity intervals. FONLL pQCD calculations with the same rapidity selections are shown for comparison. The dashed lines show the statistical uncertainties of the calculations [48].

to the results for the decay electrons in Fig. 1.9. A comparison of the results was made for different center-of-mass energies ($\sqrt{s} = 2.76$ and 7 TeV). Predictions made by models based on pQCD calculations describe the data within the experimental and theoretical uncertainties for the p_{T}- and y-differential production cross sections; as well as the p_{T}-differential production cross section ratios between different centre-of-mass energies and different rapidity intervals [49].

In summary, measurements of heavy-quark production cross sections in pp collisions are important in testing theoretical predictions as well as being a reference for p-Pb and Pb-Pb collision systems [50]. In a p-Pb collision system, the production of heavy quarks can be influenced by the dense environment found within the Pb nucleus. This effect is known as cold nuclear matter (CNM) effects [51, 52]. Signatures of such effects can be observed and distinguished by using measurements from pp collision system as a reference for which CNM effects are absent. In a Pb-Pb collision system, a hot dense state of matter is formed

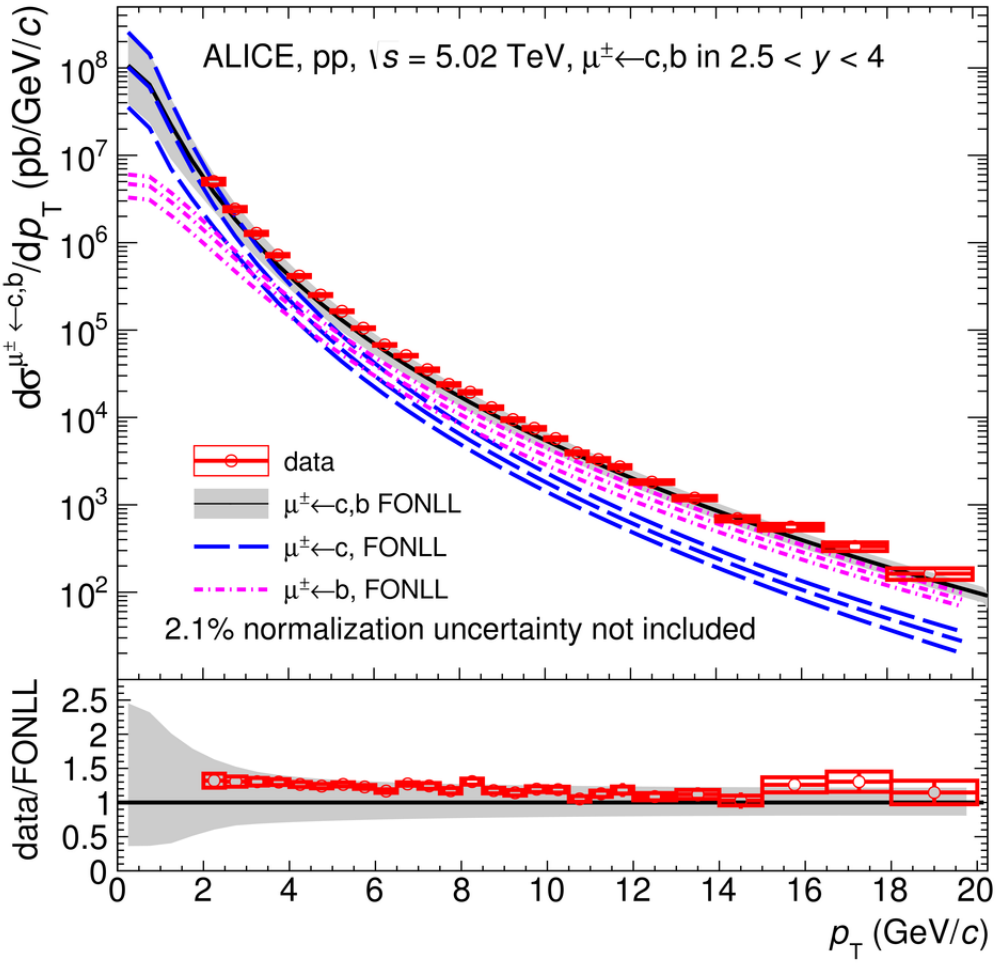

Fig. 1.10 The heavy-favour differential production cross section as a function of transverse momentum and rapidity measured in pp collisions at $\sqrt{s} = 5.02$ TeV [49].

known as the quark-gluon plasma (QGP). It is known that heavy quarks are produced earlier in the collision before the formation of the QGP. The presence of this medium can be observed through the measurement of the production cross section of heavy quarks by using measurements from a pp collision system. In principle, more heavy quarks are formed in a Pb-Pb system however, since these heavy quarks traverse the medium, they lose energy. A comparison of measurements in pp and Pb-Pb at the same center-of-mass energy is used to confirm the presence of the QGP [53].

Differential measurements of heavy-flavour production in proton-proton (pp) collisions as a function of the charged-particle multiplicity are important in order to gain more insight into processes involved in the collision at a partonic (quark and gluon) level. These measurements also provide information on the interplay between hard (high momentum transfer) and soft (low momentum transfer) mechanisms during particle production. It is reported that the relationship is expected to depend on the energy and the impact

parameter of the pp collision. The impact parameter is the distance of closest approach that occurs in colliding particles should they follow their initial straight-line trajectories [54]. The impact parameter is used to characterize a collision. In the next section, charged-particle multiplicity and the processes involved therein will be discussed.

1.3 Charged-particle multiplicity

Multiplicity is a basic yet fundamental measurement for event characterization. An event is the result of an interaction between two subatomic particles, in the case of this study, an event is the result of the interaction between two protons (pp collision). Charged-particle multiplicity is the number of charged particles created in a single event. Primary charged particles are defined as prompt charged particles that are emerging from the interaction point after a collision for a given event [55]. The background is classified with decaying particles coming from strangeness and secondary particles. The spectrum of charged particles in pseudorapidity is expressed as:

$$\frac{1}{N_{event}}\frac{dN_{ch}}{d\eta} \approx \frac{1}{N_{event}}\frac{\Delta N_{ch}}{\Delta\eta}, \tag{1.12}$$

where N_{ch} is the number of primary charged particle tracks and N_{event} is the number of selected events. It is a spectrum of charged particles for a given $\Delta\eta$ bin per event. Reducing the width of the η bin to $\Delta\eta = 0.2$ results in the right term above to be expressed as:

$$\frac{1}{N_{event}}\frac{\Delta N_{ch}}{\Delta\eta} = \frac{dN_{ch}}{d\eta} \tag{1.13}$$

The resulting charged particles spectrum can be approximated to:

$$\frac{1}{N_{event}}\frac{dN_{ch}}{d\eta} \equiv \frac{dN_{ch}}{d\eta}, \tag{1.14}$$

The data sample can be normalized for three event classes:

- INEL - Inelastic events,
- NSD - Non-single diffractive events, and;
- INEL$>$ 0 - Inelastic events with at least one charged particle generated in the pseudorapidity interval $|\eta| < 1$.

Measuring multiplicity allows for the study of the dependence between $\langle\frac{dN_{ch}}{d\eta}\rangle$ and the center-of-mass energy. $\langle\frac{dN_{ch}}{d\eta}\rangle$ is the pseudorapidity density distribution of a primary charged particle and is defined as the average number of primary charged-particles produced in an interaction per pseudorapidity unit. This depedence is shown in Fig. 1.11, the figure shows the pseudorapidity density measurements in pp collisions at $\sqrt{s} = 5.02$,

7 and 13 TeV for different multiplicity classes measured at forward rapidity. The upper panel shows the absolute scale of the pseudorapidity density and the lower panel shows the self-normalized charged-particle pseudorapidity density. The highest multiplicity classes are 5 times larger than the inclusive ones. Similar measurements at midrapidity are shown in [56].

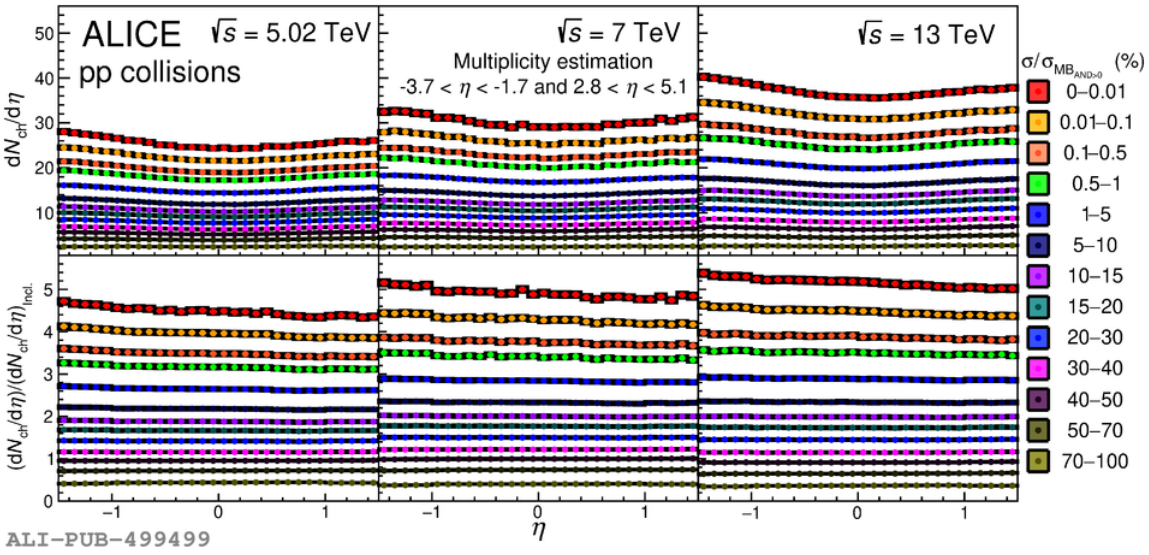

Fig. 1.11 Charged-particle pseudorapidity density (upper panels) and the same scaled by $1/(dN_{ch}/d\eta)_{\text{incl.}}$ (lower panels) for the 0–0.01% (high multiplicity) to 70–100% (low multilicity) multiplicity classes measured with the forward multiplicity estimator ($-3.7 < \eta < -1.7$ and $2.8 < \eta < 5.1$) in pp collisions at $\sqrt{s} = 5.02$, 7 and 13 TeV. The multiplicity classes are determined by finding the ratio of the total cross-section (σ) and the minimum-bias cross-section (σ_{MB}) [56].

The global property of a medium produced in a collision can be fixed by the charged-particle multiplicity and/or the average number of charged particles. The charged-particle multiplicity is related to the energy density reached in a collision and is considered in many calculations of other observables in high-energy collisions. The accuracy at which many of the observables are measured is determined by the charged-particle multiplicity. Multiplicity measurements are dominated by low momentum transfer QCD processes. This is also referred to as soft non-pertubartive QCD [57]. As a result, the variable cannot be derived from the QCD Lagrangian, this leads to the relevant processes being modelled. Models that describe particle production based on Monte Carlo (MC) generators are therefore tested and can be constrained [58].

In hadron collisions, the multiplicity is normally reported for inelastic collisions and/or the sample of non-single diffractive interactions. Inelastic collisions can be classified as either diffractive or non-diffractive. An interaction is said to be diffractive when there is an interaction between a proton and a Pomeron that produces a system of particles.

A Pomeron is the colour singlet exchange carrying vacuum quantum numbers that mediate soft interactions. A Pomeron is regarded as a colourless and flavourless multiple gluon/glueball in QCD [59]. Figure 1.12 shows the schematic diagram of different interactions.

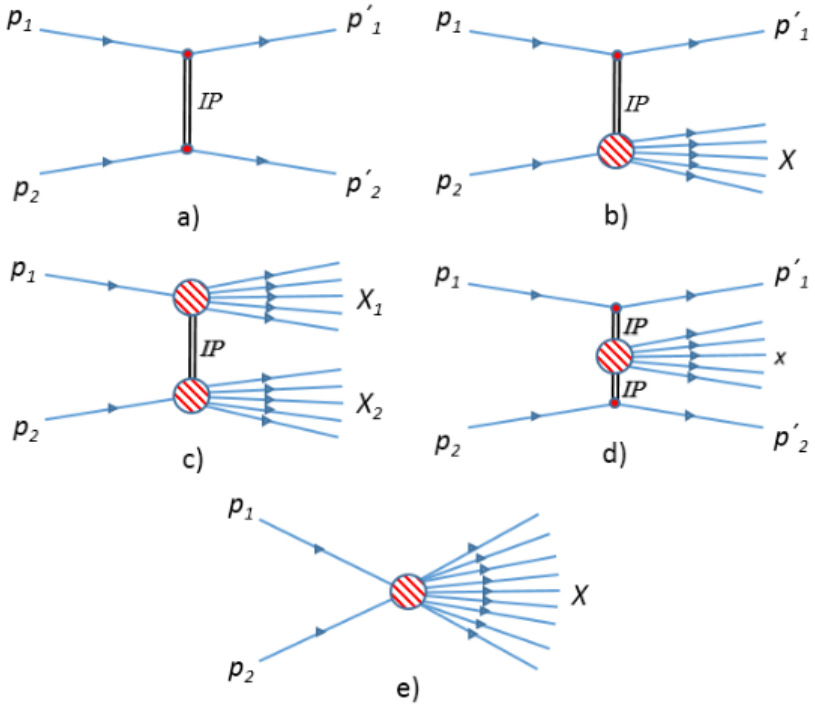

Fig. 1.12 Schematic diagrams of a) elastic scattering, diffractive processes with b) single diffractive dissociation (SD), c) double diffractive dissociation (DD), d) central diffractive dissociation (CD); and non-diffractive processes e) [59].

For diffractive systems, although there is minimum energy transfer between the interacting protons, one or both the protons will dissociate into multi-particle final states with the quantum numbers remaining constant throughout the process. b), c) and d) in Fig. 1.12 are showing different diffractive processes. b) is illustrating a Single Diffractive (SD) process where only one proton dissociates, c) is illustrating a Double Diffractive (DD) process where both the protons dissociate and d) is illustrating a Central Diffractive (CD) process where there is an interaction between two Pomerons and the protons remain intact in the final state. In a non-diffractive interaction as illustrated by e), there is an exchange of colour charge which leads to more hadrons being produced [59].

At LHC energies, there are two additional contributions that are considered in the case of heavy-quark production. The first contribution is from the larger amount of radiation from gluons that is associated with the short distance production processes at larger energies and the transverse momenta of particles. The second contribution is from the number of hard partonic interactions that occur in a single event, this is also commonly

known as multiple-parton interactions (MPI) [60, 61, 62]. Charged-particle multiplicity measurements are used to constrain MPI-based models (by making comparisons between data and the models) where pQCD is not applicable which gives a deep insight into microscopic mechanisms. In the next section, MPIs are discussed.

1.3.1 Multiple Parton Interactions

Several methods (PYTHIA [63]), HERWIG/JIMMY [64] and SHERPA [65]) that are able to describe qualitatively some of the observed features in collisions, are based on MPIs. Multiple parton hard scatterings are events in which two or more distinct hard parton interactions occur simultaneously in a single hadron-hadron collision. They generally take place at high center-of-mass energies where there are several interactions with high momentum transfer processes.

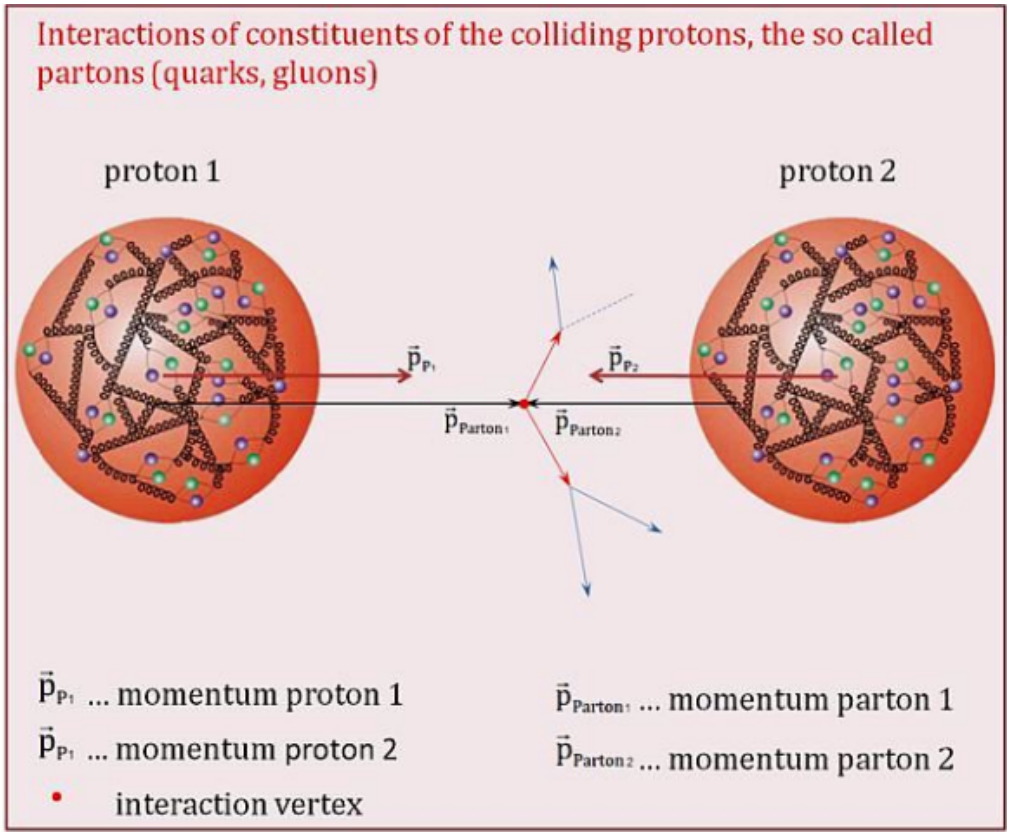

Fig. 1.13 Multiple Parton Interaction in a pp collision [66].

MPIs are split into two groups: soft (low p_{T}) and hard (high p_{T}) MPIs. Hard MPIs are rare to find while soft MPIs are very frequent. Due to several interactions occurring at the parton level in a collision, particle production becomes dependent on the total charged-particle multiplicity.

Monte Carlo (MC) generators like PYTHIA [63] and EPOS [67] that are perturbative quantum chromodynamics (pQCD)-based models of MPIs are used as the theoretical models to compare data with. PYTHIA [63] is a C++ based standard tool used by LHC experimentalists among others to generate events in high energy collisions between elementary particle physics that comprise of a set of physics models for the evolution of a few-body hard-scattering processes to a complex multi-particle final state. The physics models contained in PYTHIA are complex, with a multitude of different processes that are implemented at different stages of the collisions. While some parts of the physics has been derived from theory in the PYTHIA code, there are other parts that are based on phenomenological models with parameters that are determined from the data under study.

Some of the physics models considered in the code are not limited to but include: hard processes, soft processes, multiparton interactions, beam remnants and colour reconnection, hardronisation, and resonance and particle decays. The main use of the code includes the exploration of experimental consequences of theoretical models, the development of search strategies, the interpretation of experimental data and the study of detector performance. Its capabilities allows it to span throughout the lifetime of an experiment, starting from the detector design all the way to the analysis of the data [63].

EPOS[67] is another MPI-based MC generator that can be used to compare data with. It is a parton model with many binary parton-parton interactions, with each one creating a parton ladder. The EPOS model consists of **E**nergy Shielding, **P**arton Multiple Scattering (MPI), **O**utshell remnants, and **S**creening, Shadowing and Strings . EPOS can be used for minimum bias[6] hadronic interaction generation from 100 GeV to 1000 TeV. The parton ladder can be divided into a soft and a hard part. The soft part is a phenomenological object that is parameterised in Regge pole fashion. The Regge theory allows for multiple interactions to happen in parallel with the "Pomeron" which represents an elementary interaction [69]. In addition to the parton ladder, there are two off-shell remnants (the interacting partons leave behind a projectile and a target remnant - both of which are excited) that are also responsible for particle production.

For hadronic interactions, EPOS consistently treats for all kinds of systems with the final state depending on the energy used for each event (multiplicity) and not only on the energy available. This clearly indicates that EPOS is a consistent quantum mechanical multiple scattering approach that is based on partons and strings. The cross section and particle production are calculated consistently taking into account energy conservation for both

[6]Events collected with a trigger that is not very restrictive are referred to as minimum bias events (MB)[68]. They are inelastic events which are selected with the minimum possible requirement necessary to ensure that an inelastic collision occurred.

cross section and particle production calculations. The model takes into account nuclear effects that are related to Cronin transverse momentum broadening, parton saturation, screening, and high density effects that lead to a collective behaviour in heavy-ion collisions [67].

1.4 Heavy-flavour production as a function of charged-particle multiplicity in pp collisions

The study of HF production vs charged-particle multiplicity is important as it contributes towards understanding:

- The interplay between soft and hard partonic interactions,
- Events that contain MPIs are expected to have higher multiplicity, and
- The role of the collision geometry as well as the final-state effects.

Published results of heavy quarks versus charged-particle multiplicity in pp collisions at LHC energies [70, 71, 72, 73, 74] show a stronger than linear increase of the yield of heavy quarks with the charged-particle multiplicity. The trend is reproduced by theoretical models involving the contribution of MPI. The following discussion will focus on some of the results, in particular, from the heavy-flavour sector measured in ALICE.

For the ALICE forward rapidity region, measurements of heavy-flavour production via the single muon decay channel vs charged-particle multiplicity are currently unavailable. However, the analysis of data taken during the LHC Run 1 2012 proton-proton data at $\sqrt{s}$ = 8 TeV of heavy-flavour production via single muon decay channel vs charged-particle multiplicity at forward rapidity ($2.5 < y < 4$) is currently ongoing. Preliminary results obtained from ongoing study are shown in Fig. 1.15 - will be discussed later in the section.

Other measurements at forward rapidity have been reported for J/ψ via the muonic decay channel. Measurements of forward rapidity J/ψ production as a function of charged-particle multiplicity in pp collisions at $\sqrt{s}$ = 5.02, 7 and 13 TeV are shown in the left of Fig. 1.14. On the right of Fig. 1.14 is a comparison of the results with midrapidity measurements of the relative J/ψ yield [75].

On the left of Fig. 1.14, it is observed in all three energies that the relative J/ψ yield shows approximately linear increase with midrapidity relative charged-particle multiplicity. The similarity of the results suggests that the production of J/ψ has no dependence on $\sqrt{s}$ in the same final state multiplicity domain. The ratio of the relative yield of J/ψ is taken to better assess deviations from the linear behavior and this is shown in the bottom panel

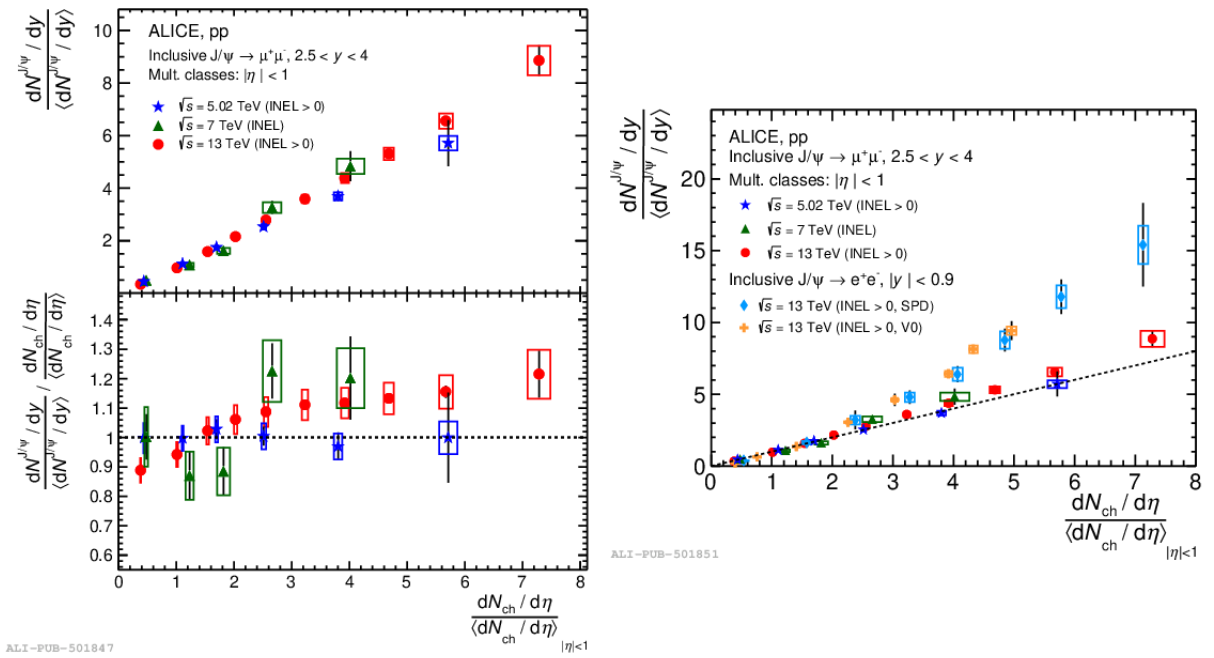

Fig. 1.14 Relative J/ψ yield as a function of the relative charged-particle density measured at forward rapidity in pp collisions at $\sqrt{s}$ = 5.02 (INEL>0), 7 (INEL) and 13 (INEL>0) TeV (left) and comparison with similar measurements at midrapidity at $\sqrt{s}$ = 13 TeV (right) [75].

[75].

On the right of Fig. 1.14, the results are compared with midrapidity measurements at $\sqrt{s}$ = 13 TeV. There is a faster than linear increase as a function of charged-particle multiplicity in the midrapidity measurements. For the midrapidity measurements, the forward and midrapidity multiplicity selection estimators were used. Both estimators are compatible within uncertainties. This comparison is important as it confirms that the difference in trends for forward and midrapidity is not due to the possible auto-correlation bias that arises from the multiplicity selection [75].

Measurements of charm and beauty production at central rapidity versus charged-particle multiplicity in proton-proton collisions at $\sqrt{s}$ = 7 TeV is reported in [76], a comparison between the average D-meson measurement, J/ψ via the semi-leptonic decay channel and J/ψ via the muonic decay channel is made. A similar trend is observed between the forward and midrapidity measurements as shown on the right of Fig. 1.14.

Heavy-flavour electron (HFE) decay production ($c, b \to e + X$ with BR $\approx 10\%$) meaurements as a function of charged-particle multiplicity in pp collisions at $\sqrt{s}$ = 13 TeV [70] are shown in Fig. 1.15. There is a faster than linear increase as the multiplicity increases. The theoretical model PYTHIA [63] is in fair agreement with the data as shown on the

left of Fig. 1.15. On the right of Fig. 1.15, a comparison of the HF electron decay production (blue data points) and HF muon decay production (green data points - these are $\sqrt{s} = 8$ TeV data) at midrapidity and forward rapidity, respectively is shown. There is a faster than linear trend observed for both rapidity ranges with some differences at low multiplicity at midrapidity as compared to the forward rapidity [70].

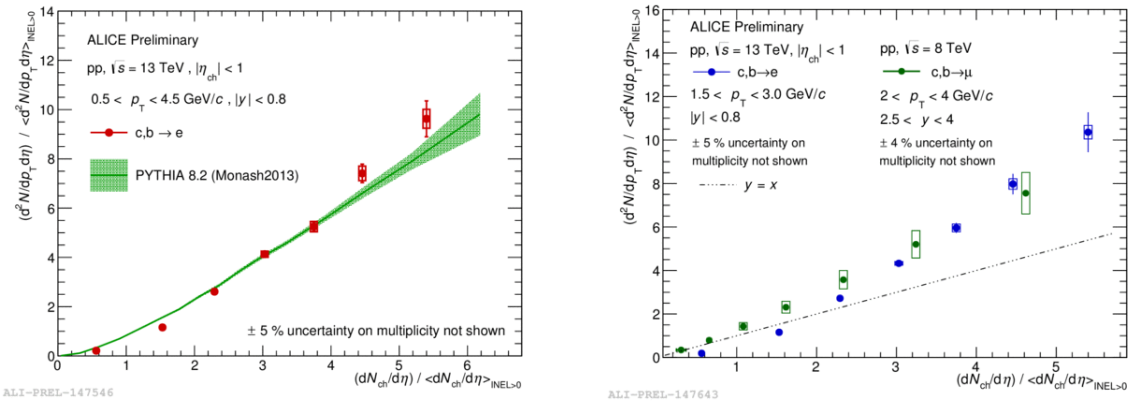

Fig. 1.15 Comparison of data and theoretical model PYTHIA (left) and self-normalized yield vs charged-particle multiplicity for HF electron decay (right)[70].

A faster than linear relationship was observed for both cases. However, there are some differences that are observed at low multiplicity. Since the measurement for HFE was done at midrapidity, there could be possible "auto-correlation" effects due to the overlap between pseudorapidity regions of HF measurements and the multiplicity estimator.

In [70], a comparison is also made between prompt[7] and non-prompt[8] J/ψ data with HF measurements of charm production at central rapidity vs charged-particle multiplicity in pp collisions at $\sqrt{s} = 7$ TeV. Figure 1.16 on the left shows this comparison between prompt J/ψ and D-meson measurements while on the right, a comparison between non-prompt J/ψ and D-meson is shown. It is concluded that the charm hadron relative yields exhibit a similar increase with increasing charged-particle multiplicity. It is also observed that the relative yield of the D meson seems to increase faster than the prompt J/ψ at higher multiplicity. In contrast, the relative yield of the D meson and non-prompt J/ψ are comparable within statistical uncertainties. The D-meson measurements also have a higher multiplicity reach as compared to the J/ψ measurements [70].

Open charm, beauty and hidden charm hadron relative yields all present a similar trend of a faster than linear increase as a function of charged-particle multiplicty. The compatibility of these comparsions is related to the production processes of $c\bar{c}$ and $b\bar{b}$ and not

[7] A prompt lepton is a lepton originating from the main collision taking place in the event, as a direct product of the particular decay

[8] Non-prompt leptons come later, through the decay of the hadronized quarks

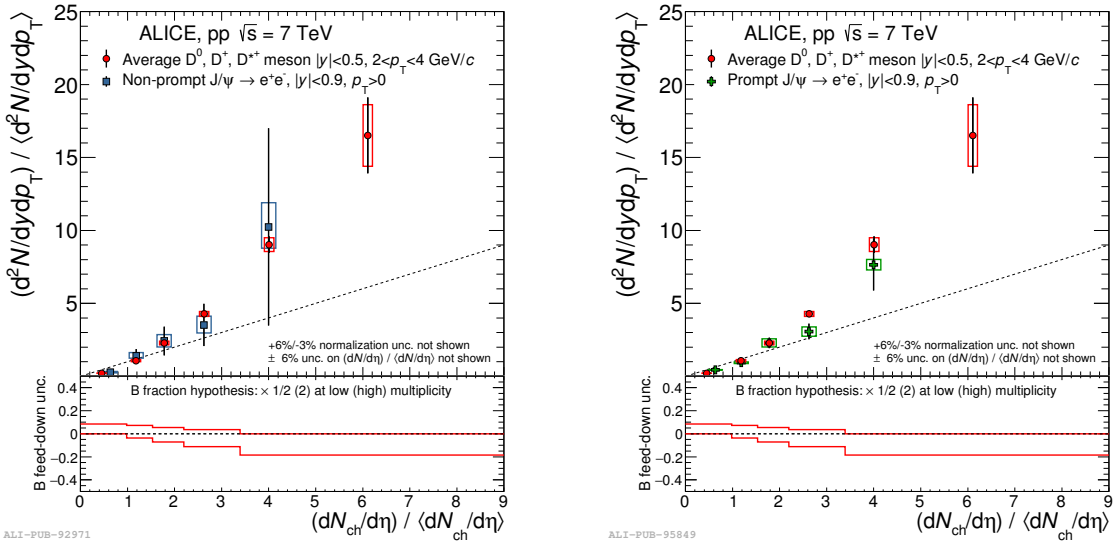

Fig. 1.16 Comparison of the self-normalized yields vs charged-particle multiplicity of D meson with non-prompt J/ψ measurements (left) and D meson and prompt J/ψ measurements (right) [70].

necessarily influenced by hadronisation according to Ref. [70].

Recent LHC studies [77] indicate that pp and proton-lead (p-Pb) collisions with high charged-particle multiplicities exhibit features (e.g. collective effects such as elliptic flow and strangeness enhancement) traditionally associated only with heavy-ion collisions (e.g. Pb-Pb) where a strongly-interacting quark-gluon plasma (QGP) is formed. One such study is the measurement of strange quark production as a function of charged-particle multiplicity [77]. Whether or not a small drop of strongly-interacting QGP is formed in pp and p-Pb collisions, is still a pending question, particularly, since jet quenching signals have not been observed so far in small-collision pp and p-Pb collisions systems. However, these results are a clear indication that, for high charged-particle multiplicities, pp and p-A collisions offer interesting physics studies in their own right.

1.5 Heavy-flavour production as a function of charged-particle multiplicity in pp and p-Pb collisions

As already mentioned, in a p-Pb collision system, the heavy-flavour production yield can be affected by the CNM effects. Heavy-flavour production yields as a function of charged-particle multiplicity measurements can give additional insight into these effects.

Figure 1.17 shows a comparison of p-Pb data at $\sqrt{s_{NN}} = 5.02$ TeV with pp at $\sqrt{s} = 7$ TeV results of the relative D-meson yield as function of charged-particle multiplicity at

midrapidity is made in [78]. Both collision systems have a relative similar faster than linear increase, this is shown in Fig. 1.17. It is observed that the D-meson yields increase faster in pp than in p-Pb, this difference can be attributed to the initial condition of the collision that are affected by the presence of the Pb nucleus in a p-Pb collision [78].

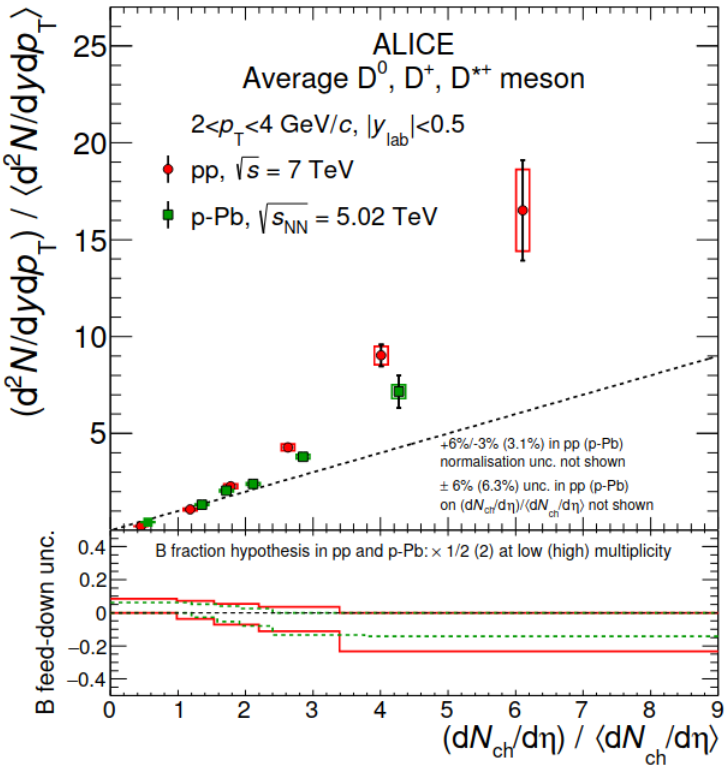

Fig. 1.17 Average relative D-meson yields in $|y_{lab}|$ <0.5 as a function of the relative charged-particle multiplicity at mid-rapidity $|\eta| < 1.0$. The relative yields are presented in the top panels with their statistical (vertical bars) and systematic (boxes) uncertainties, apart from the uncertainty on the B feed-down fraction, which is drawn separately in the bottom panels [78].

It is important to note that this comparison is made between p-Pb collisions at $\sqrt{s_{NN}}$ = 5.02 TeV and pp at $\sqrt{s}$= 7 TeV; measurements of heavy-flavour production versus charged-particle in pp at $\sqrt{s}$ = 5.02 TeV are therefore important to make such comparisons at the same center-of-mass energies for a more complete understanding.

The dependence of the relative J/ψ measurement on the relative charged-particle multiplicity is compared to measurements for prompt D meson at midrapidity in p-Pb collisions at $\sqrt{s_{NN}}$ = 5.02 TeV in [79]. Figure 1.18 shows the comparison of the two measurements, the D mesons are measured in the p_{T} range 2-4 GeV/c. Both measurements display an increase of the relative yield with charged-particle multiplicity. A similar trend was observed in pp collisions [70] as discussed in section 1.4.

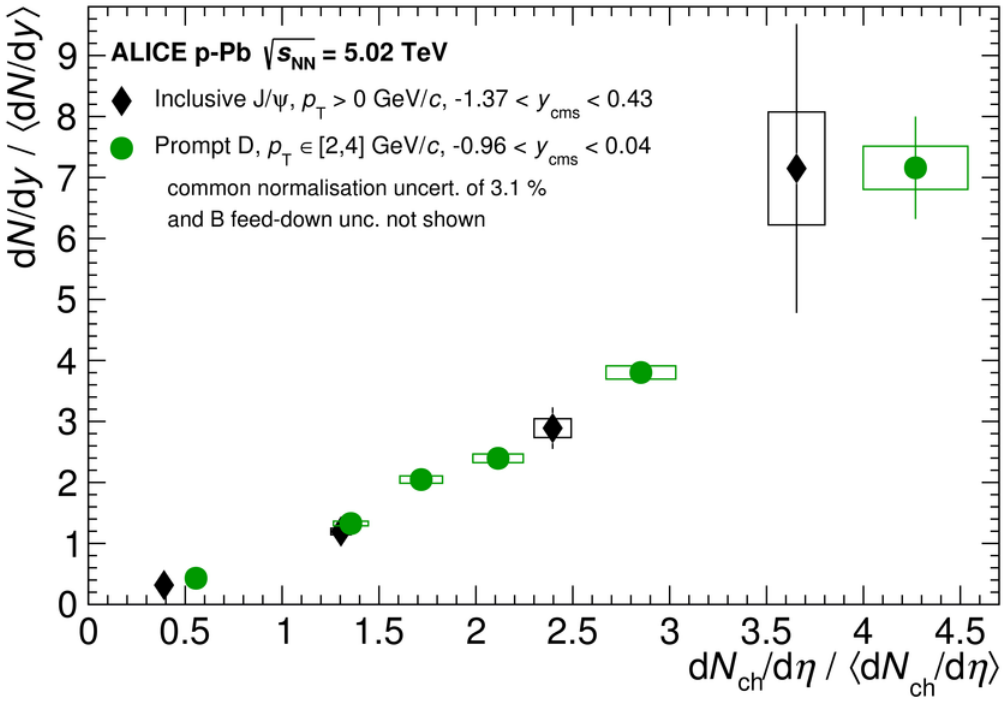

Fig. 1.18 Relative yield of inclusive J/ψ mesons as a function of relative charged-particle pseudorapidity density, measured at mid-rapidity, in comparison to average D mesons, for the p_{T} interval 2–4 GeV/c. The error bars show the statistical uncertainties, and the boxes the systematic ones [79].

1.6 Aims of this study

Due to the low p_{T}-threshold and excellent particle identification capabilities in the central barrel of the ALICE detector, the physics programme in pp collisions is complementary to other LHC experiments. The analysis of minimum-bias (MB) pp collisions allows for the understanding of soft QCD processes such as particle and multiple particle production in the non-perturbative QCD regime. In addition, pp collisions provide a reference for p-Pb and Pb-Pb collisions. Measurements in pp collisions at $\sqrt{s} = 5.02$ TeV are especially relevant as this is the only common center-of-mass energy for all three collision systems available at the LHC [80].

In this study, heavy-quark production as a function of the charged-particle multiplicity is investigated by using data collected in pp collisions with the ALICE detector during the LHC Run 2 (2015-2018) at $\sqrt{s} = 5.02$ TeV. In this context, the heavy-quark production cross section as a function of transverse momentum and pseudorapidity as well as the heavy-flavour decay muon yield as a function of the charged-particle multiplicity are

determined. These experimental results will be compared to measurements from other heavy quark vs multiplicity studies at LHC energies. This measurement will include pp reference data collected in 2015 and 2017 in order to profit from increased statistics as compared to the published cross section results at the same energy [49]. Moreover, the measurement of heavy-flavour decay muon yield vs charged-particle multiplicity will be a new result in pp at this collision energy.

The objective is to measure the inclusive yield of heavy quarks via the single-muon (μ) decay channel in the muon spectrometer at forward pseudorapidity ($-4 < \eta < -2.5$) and the charged-particle multiplicity using the Silicon Pixel Detector at central pseudorapidity ($|\eta| < 1$) in pp collisions at $\sqrt{s} = 5.02$ TeV. Two techniques will be explored and compared for the multiplicity measurement in this study. What makes ALICE a suitable detector for such research is the fact that the forward pseudorapidity range accessibility ($-4 < \eta < -2.5$) allows to test pQCD predictions in a region of small Bjorken x down to about 10^{-5}. These measurements are important as they offer unique opportunities to measure PDFs that are considered in theoretical models like FONLL.

A comparison with other available heavy-quark measurements vs multiplicity at mid-rapidity in pp at LHC energies will be made to address the interplay between soft and hard partonic interactions and understanding the role of the collision geometry as well as the final-state effects. It will also address heavy-quark production vs charged-particle multiplicity at forward vs mid rapidity. Whereas, the comparison with p-Pb collisions at the same collision energy of $\sqrt{s_{NN}} = 5.02$ TeV at midrapidity will be done to test the influence of initial conditions of the collisions that are affected by the presence of the Pb nucleus.

1.6.1 Muon sources

It is important to note that the muon spectrometer measures the inclusive decay muons, i.e. all muons from different sources and not exclusively from charm and beauty quarks. It is therefore important to take into account the different sources and remove contributions from them to have a clean signal from heavy quarks. There are four contributions that are considered in this study, each decay process dominates in a specific region of the total transverse momentum. The p_{T}-distributions of the various sources are shown in Fig. 1.19. The different muon source contributions also results in the choice of considering the p_{T} region $2 < p_{\mathrm{T}} < 20$ GeV/c, this region is chosen since this is where HF muons dominate.

Decay muons from the free decay of pions and K produced in the primary collision, have a significant contribution at low p_{T} (i.e. $p_{\mathrm{T}} < 2$ GeV/c). Other contributions at low p_{T} come from secondary muon, which are muons from the decay of pions (π) and kaons (K) produced inside the front absorber due to multiple scatterings. Pions and kaons can

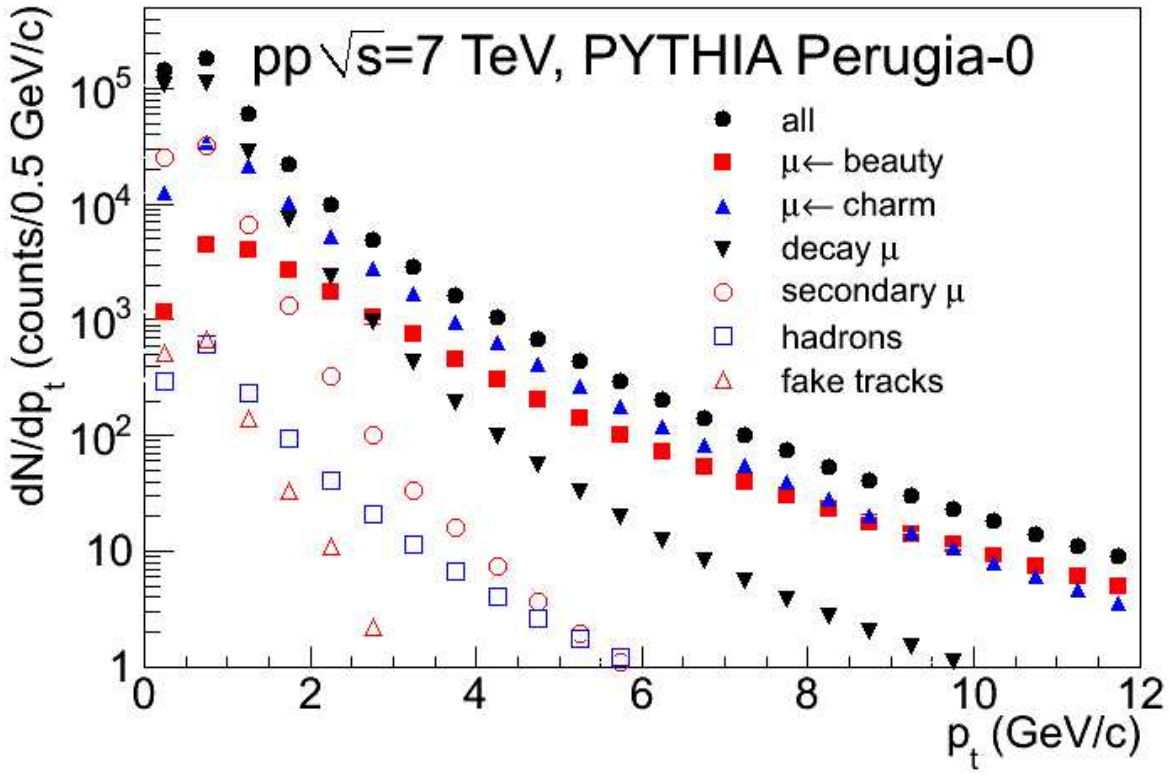

Fig. 1.19 Transverse momentum distribution of reconstructed tracks in the muon spectrometer in pp collisions at $\sqrt{s} = 7$ TeV using PYTHIA [81].

be neutral, positively or negatively charged. In this thesis, only charged π and K are considered. The π-meson is the lightest meson and is made up of $u\bar{d}$ for the π^+ and $\bar{u}d$ for the π^-. The K meson is made up of $u\bar{s}$ for the K^+ and $\bar{u}s$ for the K^-. A summary of the properties of the π- and K mesons is given in Table 1.4.

Particle	Symbol	Rest Mass (MeV/c^2)	Lifetime (s)	Decay modes (Branching ratio)	Decay length (c_τ - m)
Pion	$\pi^\pm$	139.6	2.60×10^{-8}	$\mu^+ v_\mu$ (99.98770%)	7.8045
Kaon	$K^\pm$	493.7	1.24×10^{-8}	$\mu^+ v_\mu$, $\pi^+\pi^0$ (63.56%)	3.711

Table 1.4 Properties of the pions and kaons [82].

At higher p_T ($p_\mathrm{T} >= 20$ GeVc [49]), the electroweak bosons dominate. The electroweak boson productions can be measured via their leptonic decay channels [83]. The Z boson decays into a charged lepton-antilepton pair; the lepton pairs can either be an electron-positron pair, a muon-antimuon pair or a tau-antitau pair. The muonic decay channel for the Z boson has a 3.3% branching ratio [84]. The W boson decays into an electron, a muon or a neutrino. The branching ratio of the muonic decay for the W boson is 10%

[85]. The decay channels of the bosons are shown in equation 1.15.

$$W^+ \rightarrow \mu^+ v_\mu,\ W^- \rightarrow \mu^- \bar{v}_\mu,\ Z^0 \rightarrow \mu^+ \mu^- \tag{1.15}$$

The J/ψ meson is a good example of a quarkonium called a charmonium, which consists of a $c\bar{c}$ pair. The J/ψ also contributes to the background. It has a mass of 3096.900 ± 0.005 MeV/c^2 and long lifetime compared to the lifetime of the strong interaction [34],

$$\tau_{J/\psi} \sim 10^{-20} > \tau_s \sim 10^{-23}\ s \tag{1.16}$$

A possible decay of the J/ψ is:

$$J\psi \rightarrow \mu^+ + \mu^- \tag{1.17}$$

The BR of a J/ψ undergoing a muonic decay is $5.961 \pm 0.033\%$ [34].

1.7 Thesis Outline

This thesis is divided into five chapters. In this chapter; Chapter 1; an overview of the theoretical and experimental aspects are discussed to give context to why this study is necessary. Chapter 1 is the introduction chapter that is divided into 6 sections. The first section is a discussion on the Standard Model and quantum chromodynamics. A discussion on heavy-flavour production follows where the production of heavy flavour is discussed as well as heavy-flavour production cross-section in pp collisions and in LHC experiments. Charged-particle multiplicity is discussed thereafter. Results of heavy-flavour production as a function of charged-particle multiplicity in pp collisions and p-Pb collisions are discussed and the chapter is concluded by a section on the aims of this study.

Chapter 2 gives an outline of the ALICE Detector with special emphasis on the muon spectrometer as it plays a key role in the measurement of the inclusive muons. Details on the service task; which a requirement for all PhD students to complete for the ALICE collaboration; are also given in under the muon spectrometer section as the project contributed towards the muon arm project. The ALICE Online system is discussed following the outline of the ALICE detector. The chapter is concluded with a discussion of the data taking conditions of the ALICE experiment.

Chapter 3 gives details on the ALICE Offline Framework and is thereafter followed by the discussion of the analysis procedure. Details on the data sample being analyzed and event selection are given. This is followed by a discussion of the methods used for the multiplicity estimation and the procedure followed to obtain the charged-particle multiplicity. The procedure for the muon analysis follows; in order to obtain the heavy-flavour decay muon signal,a number of things need to be considered. These include the background

contribution, the efficiency corrections as well as normalization procedures to minimum bias events as well as the systematic uncertainties associated with the measurements. A detailed discussion of how these factors are accounted for is given in this chapter.

Chapter 4 is dedicated to the discussion of the final results obtained from the study of heavy-flavour decay muons as a function of charged-particle multiplicity. A comparison of the results to other multiplicity measurements is also presented. In addition to the charged-particle multiplicity, the differential production cross-section is also shown for this study. The differential production cross-section measurements are compared to published data.

The thesis is concluded with Chapter 5 that consists of the conclusion and the outlook.

CHAPTER 2

Experimental set up

In this chapter, the experimental setup is discussed. This thesis reports on the experimental conditions during the Run 2 data taking period from 2015 to 2018 as shown in Fig. 2.1. The figure shows the LHC luminosity[1] plan from 2010 to 2024, the red dots showing the peak luminosity for each year and the blue line showing the integrated luminosity[2], the main shutdown periods are indicated by the shaded blocks [87].

The chapter starts with a discussion of the Large Hadron Collider. This section gives details on the LHC and all the experiments involved. Thereafter, details on the experiment of interest, the ALICE experiment, is discussed. This section is followed by a section on the ALICE online system, in which more information on how the online system operates is given and highlighting some of the key components of the system. The section that follows describes the steps required and procedures taken by the LHC operators to provide stable beams that are presented and for data taking.

2.1 The Large Hadron Collider (LHC)

The Large Hadron Collider (LHC) [88], is a particle accelerator which is part of the Conseil Européen pour la Recherche Nucléaire (CERN) that is used in high energy physics

[1] Luminosity is the measure of how many collisions occur in a particle accelerator over a given fraction of phase space in a given time

[2] The integral of the luminosity with respect to time [86]

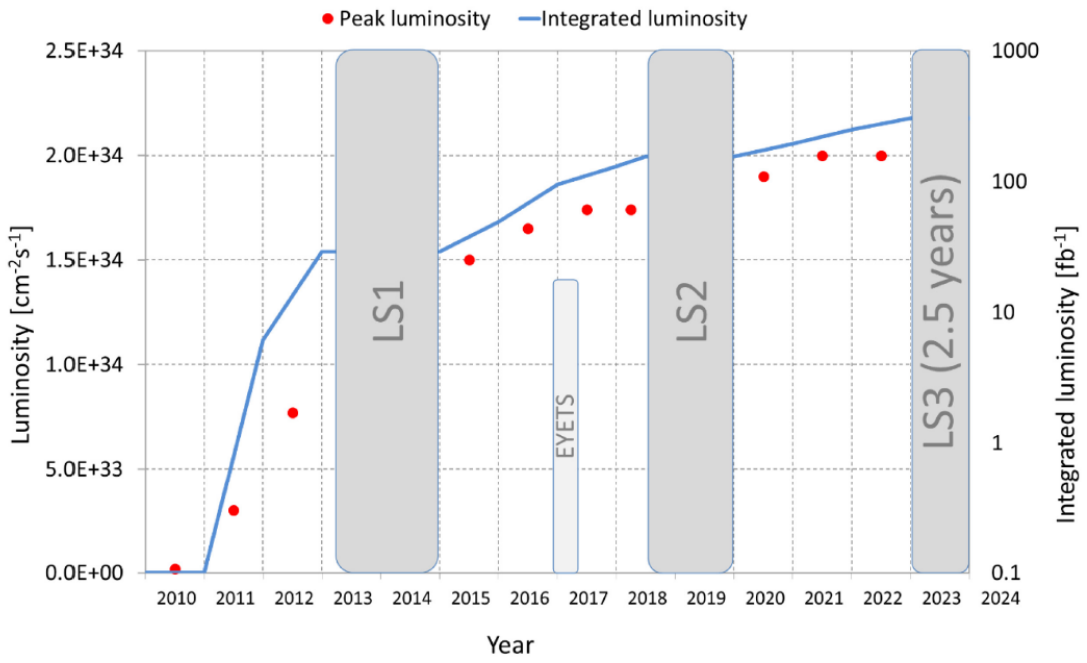

Fig. 2.1 LHC plan from 2010 to 2024, the red dots showing the peak luminosity for each year and the blue line showing the integrated luminosity, the main shutdown periods are indicated by the shaded blocks [87].

experiments in search of dark matter, dark energy, supersymmetry; and studies the quark-gluon plasma, matter and antimatter. The LHC is the largest particle accelerator and started working in 2009, it is located near Geneva on the French-Swiss border. It is located in a circular tunnel 50 to 175 m below the ground, it consists of a 27 km ring of superconducting magnets and number of accelerating structures that boost the energy of the particles along the way [89]. The diameter of the tunnel is 3.8 m [90].

The CERN accelerator complex comprises of different accelerators that are needed in producing and delivering particle beams at ultrarelativistic energies with the LHC. These different accelerators are shown in Fig. 2.2.

A bottle of hydrogen gas is connected to the ion source, a duoplasmotron machine that feeds the Linear accelerator 2 (Linac2). The duoplasmotron is used to strip the hydrogen gas of its electrons; resulting in a plasma of protons, electrons and molecular ions. A proton beam is formed and ready for acceleration after passing through the extraction electrodes. Linac2 accelerates the protons to a maximum energy of 50 MeV, ready for injections into the booster. Here the beam is further accelerated to 1.4 GeV before it is transmitted to the Proton Synchrotron (PS). The PS is a pre-accelerator of the Super Proton Synchrotron (SPS), accelerating the beam up to 25 GeV. The SPS accelerates the beam up to 450 GeV and is the final stage before the beam is transferred into the LHC

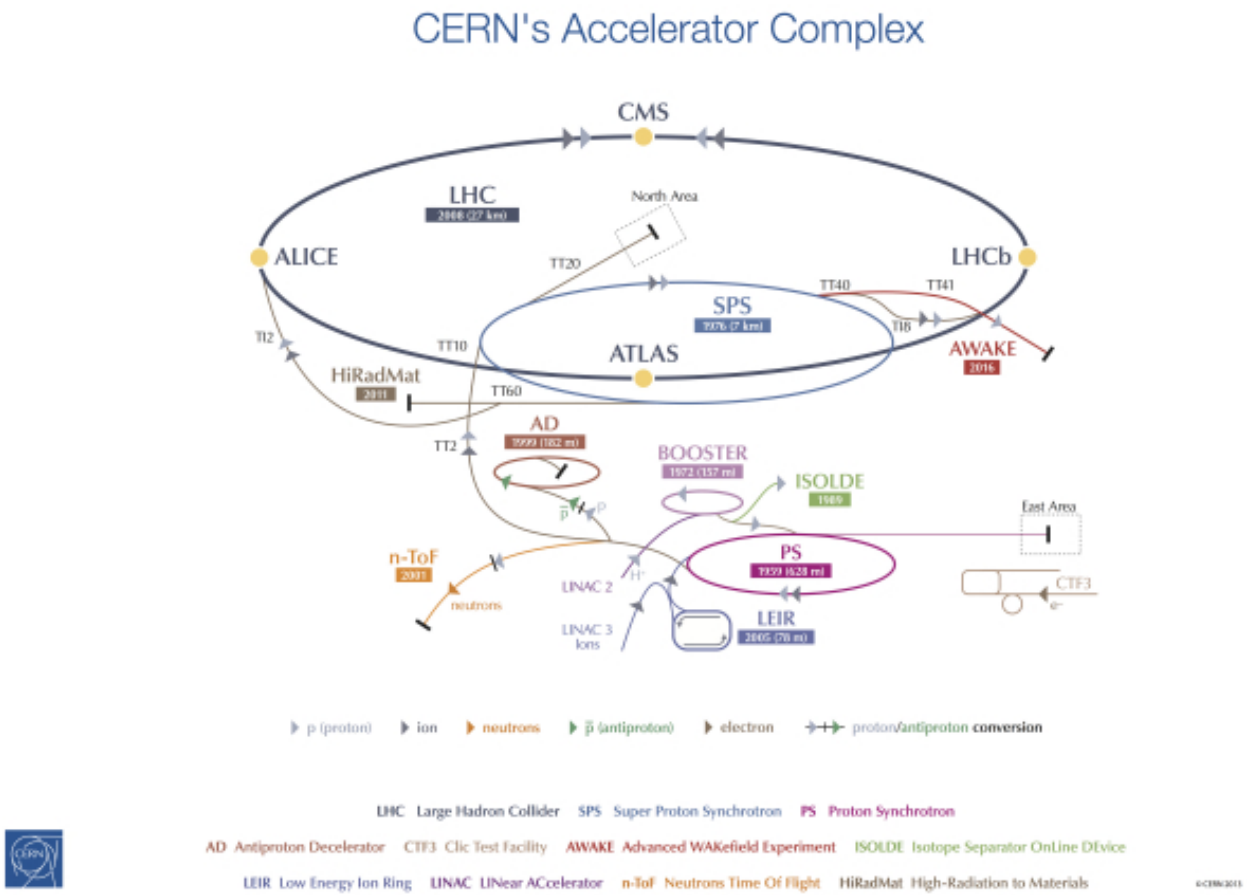

Fig. 2.2 CERN's Accelerator Complex, showing the different accelerators involved in particle acceleration [91].

[92].

The particle beams travel in clockwise and anti-clockwise directions inside the beam pipes. The transferred beam with an energy of 450 GeV is accelerated inside the beam pipes with the aid of radiofrequency (RF) cavities. The RF cavities can accelerate the beam up to a maximum of 6.5 TeV in pp collisions, this is achieved by oscillating the field of the RF cavity at a given frequency. This process is discussed in more details in section 2.4. The LHC ring takes 4 minutes and 20 seconds to fill each ring and 20 minutes to accelerate the protons to a maximum energy of 6.5 TeV. The time it takes to accelerate each beam to 2.51 TeV can be approximated to $\sim$ 13.9 minutes [93]. There are four collision points in the LHC ring, namely: ATLAS [94], ALICE [95], CMS [96] and LHCb [97] as shown in Fig. 2.2. A summary of the different beam species and energies of the LHC for Run 2 as reported by CERN is given in Table 2.1 [98].

A summary of the the energies achieved by the LHC is shown in Table 2.2.

Quantity	Number
Nominal energy, protons	2.51 and 6.5 TeV
Nominal energy, ions	2.56 TeV/u (energy per nucleon)
Nominal energy, proton collisions	5.02 and 13 TeV
No. of bunches per proton beam	2808
No. of protons per bunch (at start)	1.2×10^{11}
No. of turns per second	11245
No. of collisions per second	1 Billion

Table 2.1 Summary of the different beam species and energies of the LHC for Run 2 as reported by CERN [98]

Beam Energy (TeV)	$\sqrt{s}$ (TeV)
1.18	2.36
2.51	5
3.5	7
4	8
6.5	13

Table 2.2 Summary of the the center-of-mass energies achieved by the LHC

ATLAS and CMS experiments are general-purpose detectors at the LHC. They investigate a wide range of physics including studying extra dimensions and particles that could make up dark matter [94, 95]. While they both have the same scientific goals, each experiment uses different detector technologies and a different magnet-system design. The Large Hadron Collider beauty (LHCb) experiment studies the beauty quark, in particular which allows the investigation of the differences between matter and anti-matter.

The experiment of interest in this study is the ALICE experiment. The ALICE experiment is a detector dedicated to heavy-ion physics at the LHC. With its excellent capabilities of particle tracking and particle identification (PID) close to zero transverse momentum, it is designed to study the physics of strongly interacting matter at extreme energy densities, where the QGP is formed. The measurements of particles produced in pp and p-Pb collisions are complementary to the study of the QGP produced in Pb-Pb collisions. Proton-proton (and p-Pb) collisions also offer interesting physics in their own right.

2.2 ALICE Detector

The A Large Ion Collider Experiment (ALICE) detector has dimensions of 16 m $\times$ 16 m $\times$26 m and a total weight of $\approx$ 10 000 t. It is located at point 2 of the LHC ring as

shown in Fig 2.2 and situated in a cavern 56 m below the ground. Point 2 is between the ATLAS (Point 1) and CMS (Point 5) experiments on the French side of the LHC ring, with beams arriving from the A (ATLAS) and C (CMS) side, which is used as a labeling convention of the detector. A schematic diagram of the ALICE detector used during Run 2 is shown in Fig. 2.3.

2.2.1 Detector Layout

The ALICE detector consists of the central barrel that is responsible for measuring hadrons, electrons, photons at midrapidity ($|y| < 1$), and the forward muon spectrometer dedicated to measure muons at forward rapidities ($2.5 < y < 4$).

Within the central barrel there is an Inner Tracking System (ITS), Time Projection Chamber (TPC), Time-of-Flight (TOF) particle identification arrays, a Ring Imaging Cherenkov detector called the High Momentum Particle Identification Detector (HMPID) and Transition Radiation Detector (TRD), the electromagnetic calorimeters (EMCal) and Photon Spectrometer (PHOS) [99]. The L3 solenoid magnet which encapsulates the central barrel detectors, has a radius of 5.93 m, a total length of 11.90 m and a maximum magnetic field of 0.5 T at the nominal power of 4 MW [100].

The detectors contained within the central barrel are responsible for tracking particles by measuring the momentum of particles carrying an electric charge. This is acheived by measuring the curved path inside the magnetic field created by the L3 magnet[101].

There are also several other smaller detectors that are used for global event characterization and triggering located at small angles on either sides of the interaction point. These detectors include the Zero Degree Calorimeters (ZDC), Photon Multiplicity Detector (PMD), Forward Multiplicity Detector (FMD), T0 and V0 as shown in Fig 2.3. An array of scintillators (ACORDE) are mounted on top of the L3 magnet, which are used for cosmic ray tirggering.

All of these detectors play a key role in the ALICE experiment in terms of data taking. In this thesis, however, not all of the detectors will be discussed in detail but focus will only be on the key detectors that were used to obtain the data which were analyzed. For a more detailed description of the ALICE detector, reference [99] among other publications provides detailed discussions.

2.2.2 Central Barrel Detectors

As already mentioned the central barrel consists of a number of detectors, namely the ITS, TPC, TRD, TOF, HMPID, PHOS, EMCal and ACORDE. In this section, the focus

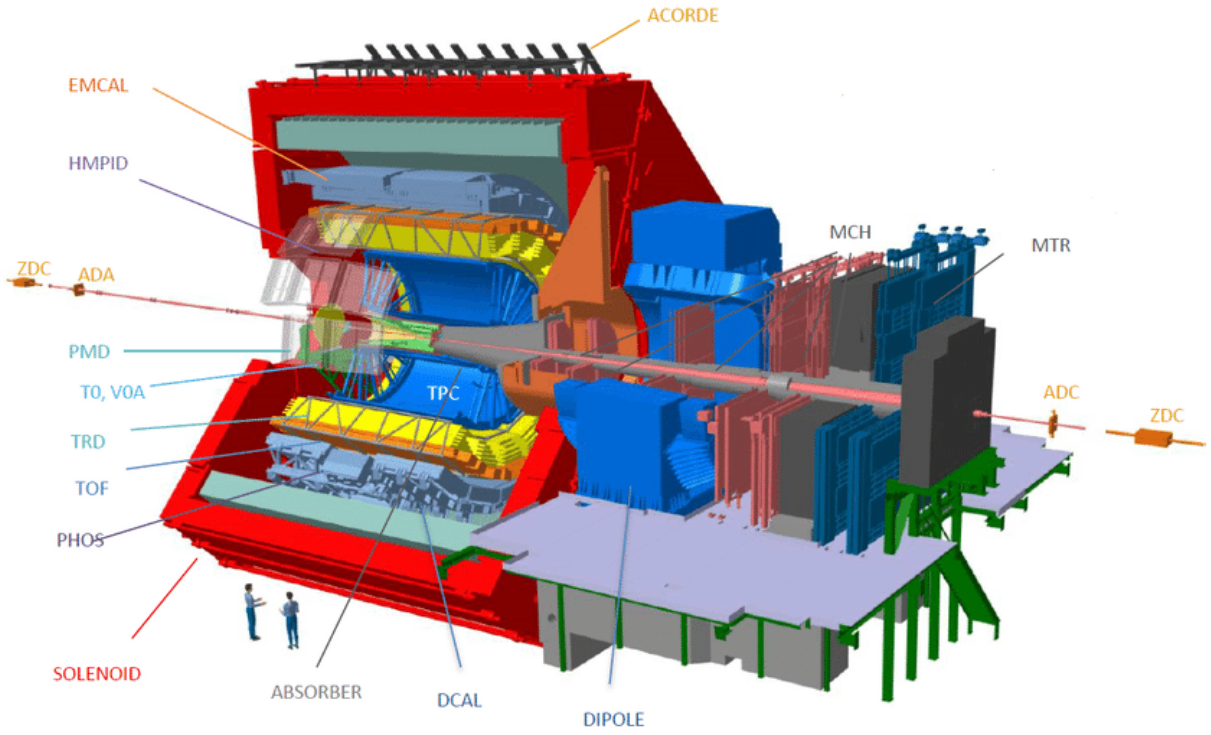

Fig. 2.3 3D ALICE Schematic Run 2 [102].

is on the ITS, more specifically the Silicon Pixel Detector (SPD).

Inner Tracking System (ITS)

The **Inner Tracking System (ITS)** is required for all the physics studies in the ALICE experiment starting from localizing the primary vertex with resolution better than 100 μm to reconstructing the secondary vertices from the decays of hyperons and D and B mesons. The system can also be used to track and identify particles with momentum below 200 MeV/c, improve the momentum and angle resolution for particles that are reconstructed by the Time-Projection Chamber (TPC) and also reconstructs particles traversing dead regions of the TPC [99].

The ITS consists of six cylindrical layers of silicon detectors that are located at radii between 4 and 43 cm and covers the psuedo-rapidity range of $|\eta| < 0.9$. This defines the rapidity range of the central barrel. The Silicon Pixel Detectors (SPD) constitutes the two innermost layers of the ITS. It is used to determine the position of the primary vertex and measure the impact parameter of secondary tracks that originate from the weak decays of strange, beauty and charm particles. Figure 2.5 shows the ITS with the SPD located at the inner barrel and the other 2 layers located in the outer barrel of the ITS [99]. The excellent particle tracking and particle identification (PID) close to zero transerve momentum ($p_{\mathrm{T}} \sim 0.1$ GeV/c) of the ITS is illustrated in Fig. 2.4 [103].

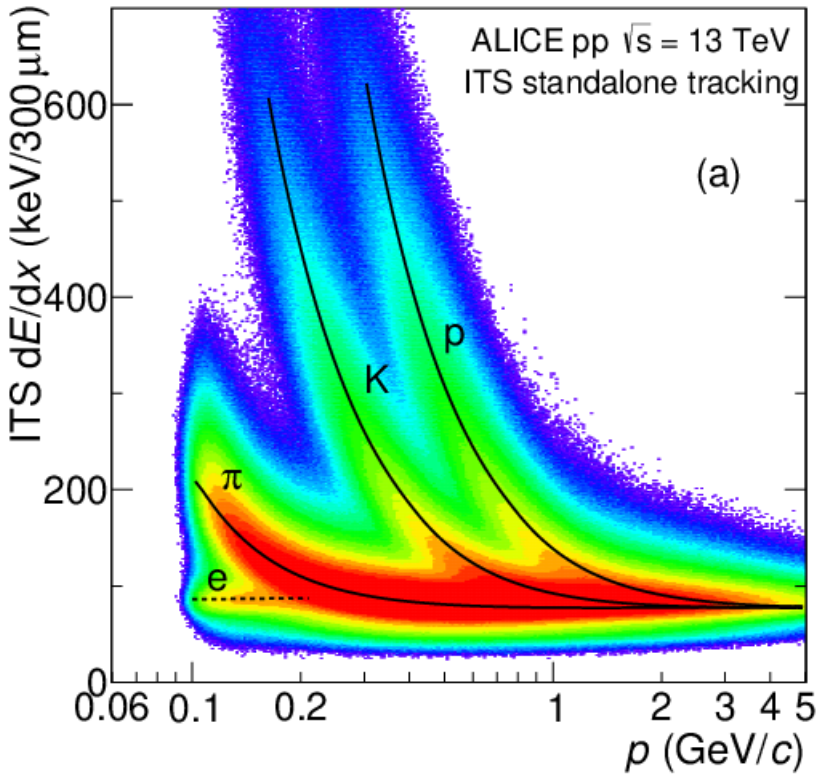

Fig. 2.4 The performance during the LHC Run 2 period of the ALICE central barrel detectors used for PID measurements [103].

The intermediate layers of the ITS are equipped with Silicon Drift Detectors (SDD). These detectors have excellent multi-tracking capabilities and provide the two of the four energy loss ($\mathrm{d}E/\mathrm{d}x$) samples that are needed by the ITS for particle identification. The Silicon Strip Detectors are the outer layers of the ITS system and play a very crucial role in matching the tracks from the TPC to the ITS. They also provide a two dimensional measurement of the track position and provide the other two of the four $\mathrm{d}E/\mathrm{d}x$ samples that are used to identify particles with low-momentum.

Silicon Pixel Detector (SPD)

As already mentioned above, the Silicon Pixel Detector constitutes the innermost layers of the ITS. The physical properties of the detector are summarized in Table 2.3. The detector has capabilities of providing prompt trigger signals called the Fast-OR, these signals contribute to the L0 trigger decision that is discussed later in this chapter [104]. Information obtained from the SPD is used in the analyses of particle production as a function of charged-particle multiplicity and centrality[3].

[3]The degree of overlap between two colliding ions

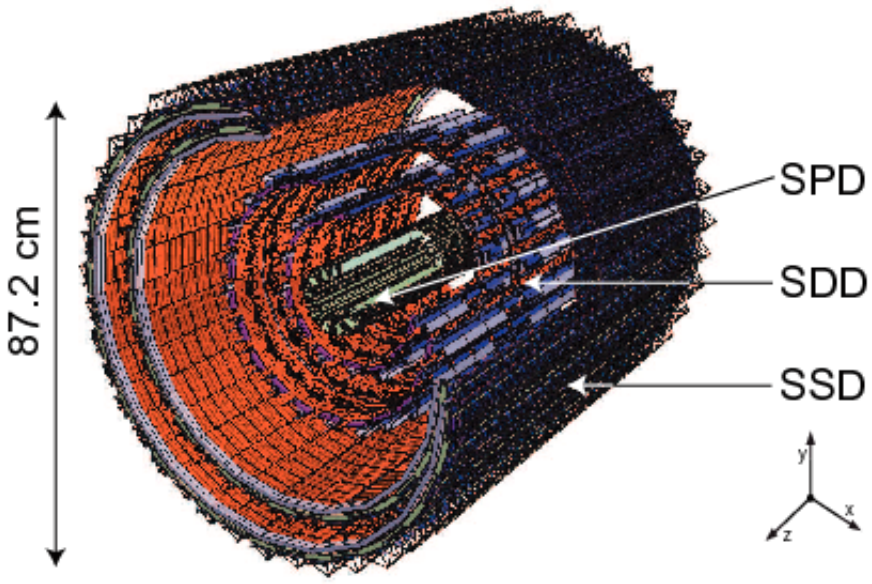

Fig. 2.5 Inner Tracking System (ITS) [105].

2.2.3 Global Detectors

As mentioned the forward detectors include the ZDC, PMD, FMD V0 and T0 detectors. In this section, the focus is on the V0 and T0 detectors.

- V0 detector
  The V0 detector consists of two arrays of scintillator counters, called V0A and V0C, respectively. They are installed on either side of the ALICE interaction point. The V0A covers the pseudorapidity range $2.8 < \eta < 5.1$ and is located at $z = +330$ cm while the V0C covers the pseudorapidity range $-3.7 < \eta < -1.7$ and is located at $z = -90$ cm. The difference in the time response between the two detectors allows for the identification and rejection of beam-gas events. Beam gas interactions are interactions that occur between the beam-particles and the residual gas inside the beam pipe as illustrated in Fig. 2.6 which illustrates how the beam-gas interactions are identified, since the V0A and V0C detectors are not symmetrically located from the IP, the time taken for the particles to reach each detector respectively is different.

  A cut on the V0 timing is applied to reject the background interactions as shown in Fig. 2.7. The cuts applied use the timing information from the V0A and V0C as follows:

$$4 < (t_{V0A} + t_{V0C}) < 12ns$$

$$10 < (t_{V0A} - t_{V0C}) < 18ns$$

  The background events are identified by using the correlation between the number

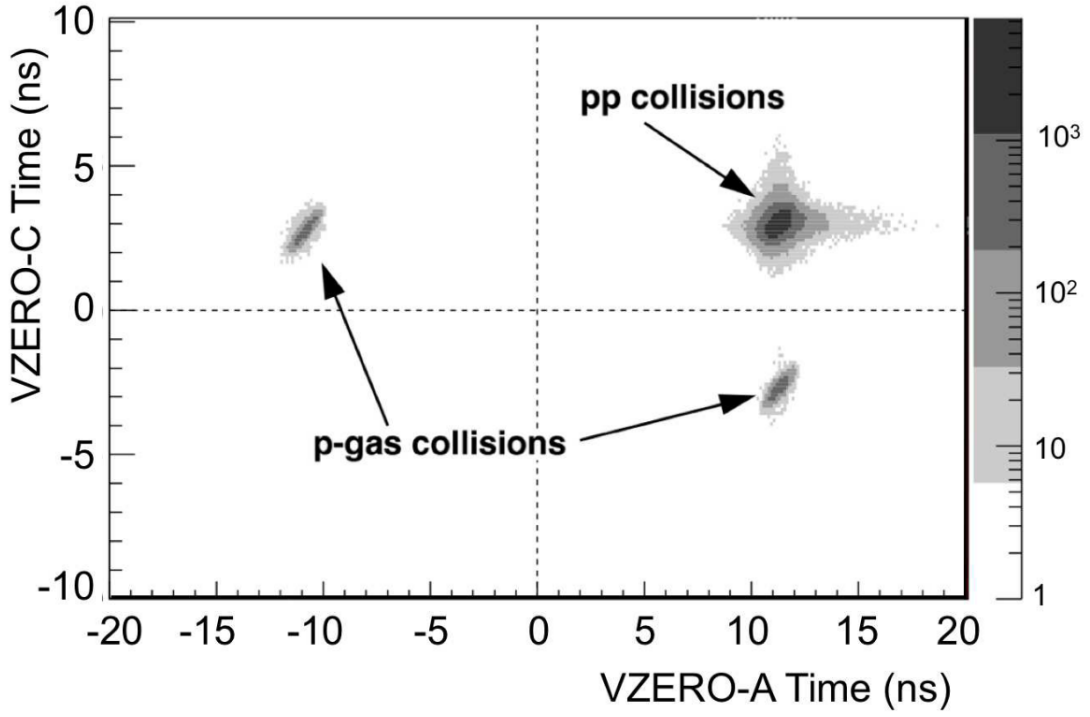

Fig. 2.6 Beam-gas interactions and pp collisions as measured on the V0A and V0C detectors [106].

of tracklets (N_{trkl}) and the number of SPD clusters (N_{cl}). It provides minimum-

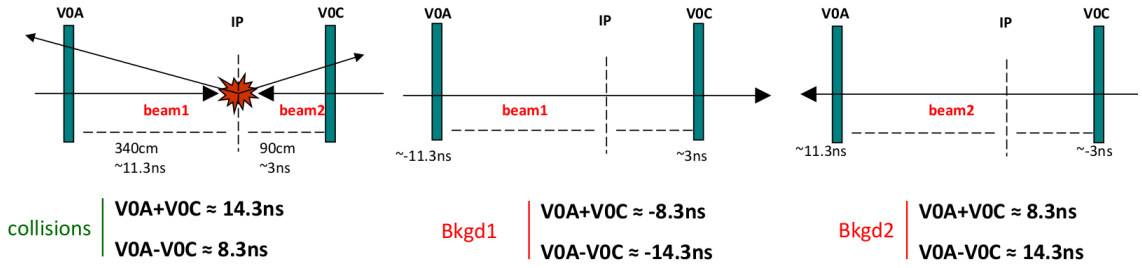

Fig. 2.7 Schematic of the V0 timing used for event selection [106].

bias (MB) triggers for the central barrel detectors in pp, proton-nucleon (p-A) and nucleon-nucleon (A-A) collisions. There are three triggers: the multiplicity, semi-central and central triggers; these triggers are discussed in more detail in section 2.3.1. In pp collisions, there are two types of MB triggers available, MB_{OR} and MB_{AND}. The V0 detector also participates in the measurement of luminosity in pp collisions with a good precision of about 10%.

The MB_{OR} is defined as a coincidence of a signal from the SPD and a signal from either the V0A or the V0C. The MB_{AND} is defined as a coincidence between signals

from both V0A and V0C and the LHC_{bunchx} (LHC bunch crossing[4] signal).

- T0 detector
  The main role of the T0 detector is to provide fast timing signals. The time resolution of the T0 detector is better than 50 *ps* with the triggering efficiency varying from about 50% in pp collisions up to 100% in A-A collisions [108]. It generates the earliest L0 trigger signals that are generated online without the possibility of offline corrections, L0 trigger signals are discussed in more detail in section 2.3.1. The T0 detector also generates the start time (T0) for the Time-of-Flight (TOF) detector. Offline corrections like the time reference for the TOF detector, are applied for non-trigger signals. The pseudorapidity range of T0-C is $-3.28 \leq \eta \leq -2.97$. On the opposite side of the Interaction Point (IP), the T0-A is grouped together with the other forward detectors (FMD, V0, and PMD) and covers the pseudorapidity range of $4.61 \leq \eta \leq 4.92$. In the radial (transverse) direction both T0 arrays are placed as close to the beam pipe as possible to maximize triggering efficiency. The T0 detector is also used for luminosity measurements [99].

2.2.4 Forward Muon Spectrometer

The Muon spectrometer [109] detects muons in the psuedorapidity acceptance $-4.0 < \eta < -2.5$. It allows for the measurement of the complete spectrum of quarkonia and the ϕ meson in the $\mu^+\mu^-$ decay channel. These measurements allow for direct comparison of production rates as a function of transverse momentum and collision centrality amongst the different quarkonia species. The detector also measures unlike-sign dimuon continuum up to masses around 10 GeV/c^2. Measurements of the production of open (heavy) flavour can be studied since at LHC energies, the continuum is dominated by single muons from semileptonic decay of open charm and beauty [41, 42]. The electroweak bosons (W and Z) are also studied with the Muon spectrometer via the single muon decay channel.

2.2.4.1 Detector Layout

The muon spectrometer detects muons in the polar angular range $171° - 178°$, pseudorapidity range of $-4.0 < \eta < -2.5$ and a momentum threshold of $p_{\text{T}} < 1$ GeV/c [110]. The spectrometer consists of:

- A passive front absorber to absorb hadrons, electrons and photons.
- A high-granularity tracking system of 10 detector planes.
- A large dipole magnet.

[4] A bunch is a collection of beam protons captured within one RF bucket [107]

- A passive muon-filter wall.
- Four planes of trigger chambers.
- An inner beam shield to protect the chambers from primary and secondary particles.
- Rear absober.

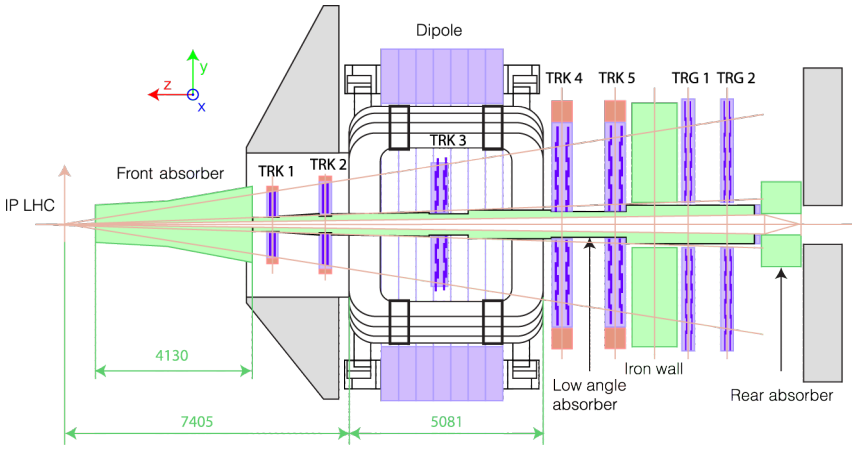

Fig. 2.8 Schematic diagram of the ALICE muon spectrometer [110].

2.2.4.2 Absorbers

The **front absorber** is located inside the solenoid magnet 90 cm away from the interaction point (IP). It has a length of 4.12 m and is made of carbon and concrete. This allows to limit the small-angle scattering and energy loss of traversing muons. In addition, the absorber also protects other ALICE detectors from secondary particles produced within the absorbing material. Figure 2.8 shows where the front absorber is located in the Muon spectrometer. The background from particle interaction along the length of the spectrometer is reduced by having the shape of the front absorber in a conical geometry as illustrated in Fig. 2.9. The layout of the front absorber is shown in Fig. 2.9. The front absorber is located closest to the IP and is made of low atomic number (Z) material, i.e. carbon and concrete.

A dense absorber tube made of tungsten, lead and stainless steel is used to shield the spectrometer throughout its length. This is the **beam shield** and its purpose is to shield the beam pipe along the Muon Spectrometer. The beam shield contributes to reducing the background coming from the interaction of low angle particle. These interactions are either with the beam pipe or are the beam-gas interactions.

The **muon filter** is placed after the last tracking chamber and in front of the first trigger chamber. The filter is made up of a 1.2 m thick iron wall and located 14.6 m away from the IP. Its purpose is to reduce the residual background from hadrons and low p_{T} ($p_{\mathrm{T}} < 0.5$

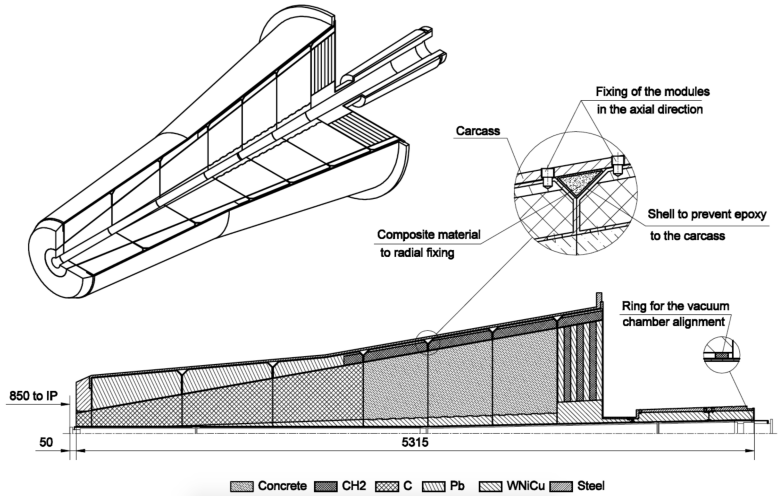

Fig. 2.9 Layout of the front absorber of the Muon Spectrometer [1].

GeV/c) muons in the trigger system. Together with the front absorber, the muon filter is used to prevent muons with momenta (p) below 4 GeV/c to reach the Muon Trigger Chambers (MTR).

Additional shielding is provided by the **rear absorber** at the back end of the MTR. Background originating from beam-gas interactions in the beam pipe is reduced by this absorber. The machine induced background (beam-gas interactions) is proportional to the beam current. The LHC provides high luminosity beams, especially in pp collisions, this results in high machine induced background. The rear absorber plays a key role in reducing the background [111].

2.2.4.3 Dipole Magnet

The dipole magnet is located $\sim$ 7 m from the interaction vertex. A maximum magnetic field of 0.7 T and an integral field of 3 T.m. can be created by this magnet and is used to distinguish between μ^+ and μ^- due to their bent tracks measured with the tracking chambers. The zy plane is defined as the bending plane since the direction of the field is perpendicular to the beam pipe in the horizontal plane. Muons are deviated along the zy plane. The xz plane is referred to as the non-bending.

2.2.4.4 Muon tracking system

The Muon Spectrometer consists of 10 Cathode Pad Chambers (CPC) that are organized in the 5 tracking stations (TRK 1 - TRK 5) as shown in Fig. 2.8. These make up the muon tracking chambers (MCH) of the spectrometer. Two of the five tracking stations (TRK 1 and 2) are placed in front of the dipole magnet (closest to the interaction point), one is inside (TRK 3) and TRK 4 and TRK 5 are placed behind the dipole magnet. TRK 1 and

2 have different detector structure as compared to the TRK 3, 4 and 5. The differences are attributed to the location of the first two stations; they are located closest to the IP and have a small radius but are exposed to a higher particle flux than the other three stations. A higher particle flux results in a higher granuality in the cathode segmentation. To overcome this, the two stations are divided into quadrants as illustrated in Fig. 2.10. TRK 3, 4 and 5 have a slat geometry since they are larger in size.

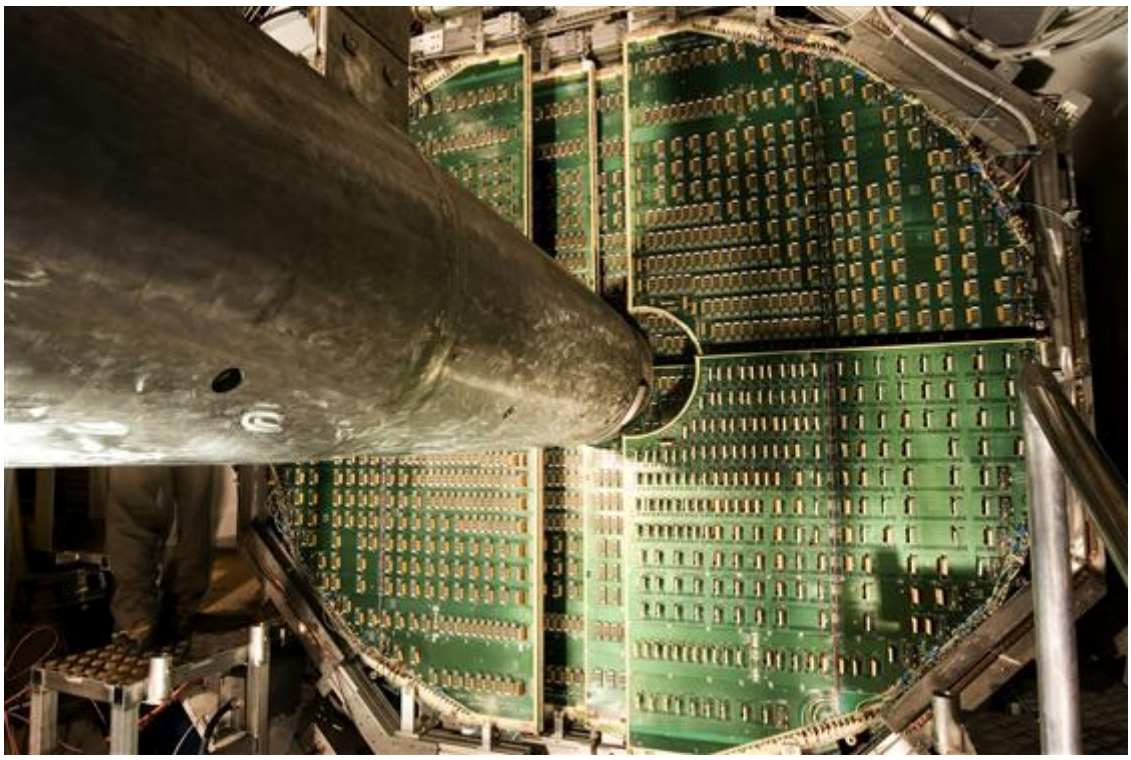

Fig. 2.10 Muon tracking chamber quadrant [112].

Each station contains two chambers called Cathode Pad Chambers; Cathode Pad Chambers (CPC) are multiwire proportional chambers that consists of two cathodes that are segmented on pads. The basic geometry of the CPC is illustrated in Fig. 2.11, the chambers provide two-dimensional hit information in the plane transverse to the beam direction, along the track bending direction and along the non-bending direction [113]. The working principle of the CPC will be discussed in more detail further into this section.

Each chamber consists of two half-chambers that are made up of detection elements. The CPC is made of a plane of thin, parallel anode wires that are equally spaced and placed symmetrically between two cathode planes. The volume is filled with a mixture of argon and carbon dioxide gas (Ar/CO_2) with a ratio of 80%/20%. The choice to use this specific gas is due to the fact that it meets the experimental requirements that include low working voltage, high gain operation, long detector life, etc. The anode wires are made of 20 μm

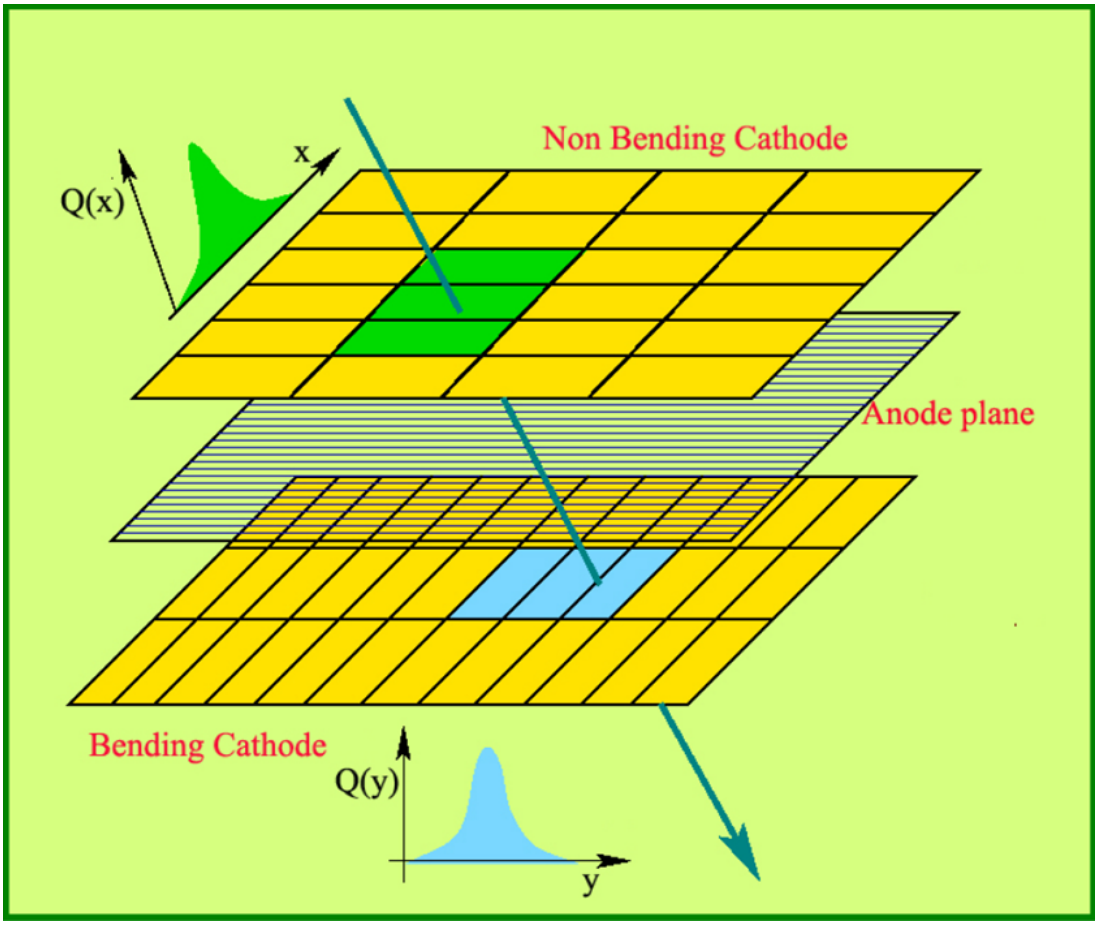

Fig. 2.11 Basic geometry of the Cathode Pad Chamber [114].

wire of tungensten and rhenuim alloy that is gold plated. The scattering and energy loss is reduced by making the chambers transparent and using materials with a low atomic number (Z) [115].

When a positive potential is applied to the anode wire and the cathode planes are grounded, then an electric field is created. The anode potential is given as 1650 V. When a charged particle traverses through the active gas volume within the CPC, the gas is ionized along the trajectory of the charged particle. The primary electrons drift towards the nearest anode, since the electric field is stronger in the region close to the anode, the electrons ionize the gas further, creating an avalanche. This is illustrated Fig. 2.12 that shows the layout of the CPC. A charge distribution is created on the cathode pads close to the avalanche location by captive coupling, this charge distribution is induced by the resulting ion cloud. The position of the charged particle passing through the detector can be determined by using the relative induced charges [114].

The readout of the MCH can be divided into three parts; the front-end boards, the readout system and the interface with the general ALICE trigger. The front-end boards are called

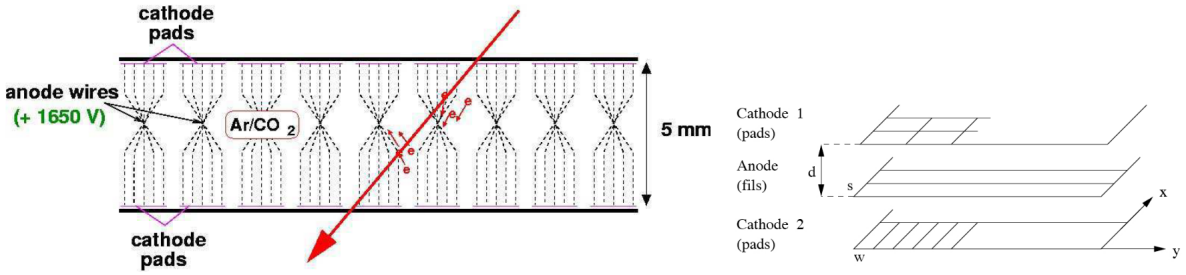

Fig. 2.12 Cathode Pad Chamber layout [116].

the MANU (MAnas NUmérique, they are based on a 16 channel chip called MANAS (Multiplexed ANALogic Signal processor). This chip can act as a charge amplifier, filter, shaper and track & hold. The signal digitization is done on the board. The Muon Arm Readout Chip (MARC) is used to read out the 12-bit Analog Digital Cards (ADCs) that the MANAS chips channels are fed into. There is approximately 17 000 MANU in the tracking system that are treating over a million channels [110].

The readout system is called CROCUS (Cluster Read Out Concetrator Unit System), this system is connected to the MANUs with the PATCH (Protocol for ALICE Tracking Chamber) buses. Each PATCH bus is read out by two CROCUS, this leads to a total number of 20 CROCUS [110].

The interface with the general ALICE trigger is called the TCI (Trigger Crocus Interface). The TCI ditributes the trigger signals coming from the Central Trigger Proccesor (CTP) to the CROCUS. The CTP will be discussed later in this chapter. The TCI decodes the trigger signal and generates a L1 reject in the FFT (Frontal Fan-out Trigger) and also manages the busy signals of all the CROCUS crates [110].

Figure 2.13 shows a layout of how the electronics chain in the tracking system is linked to each other. The front-end boards, readout system and the interface with the general ALICE trigger system is clearly indicated.

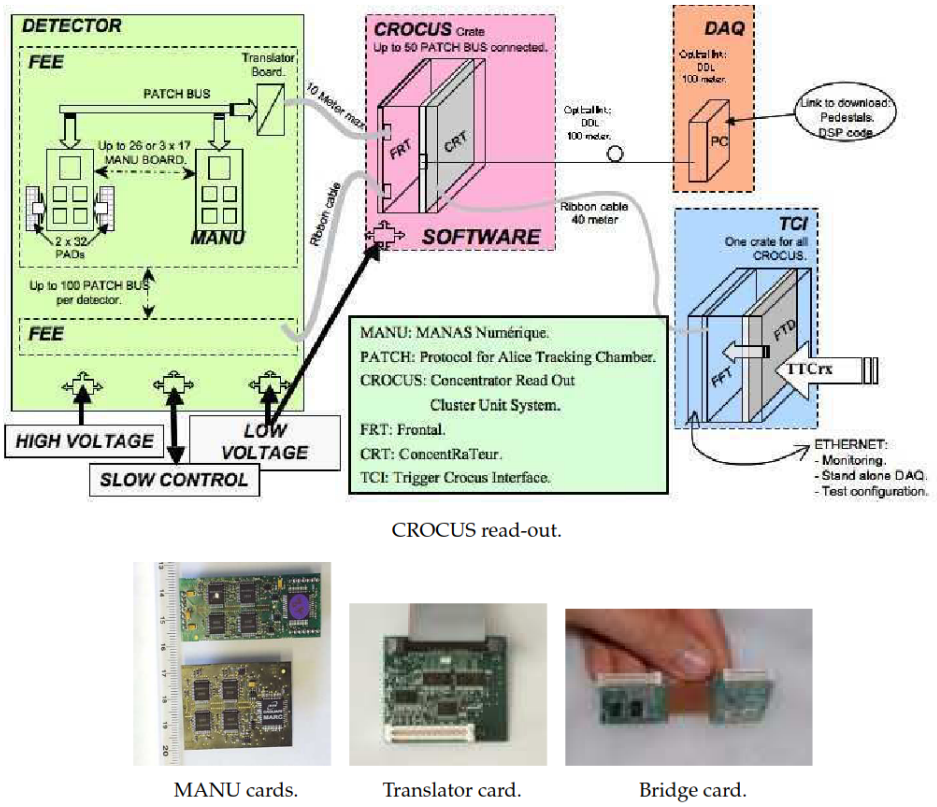

Fig. 2.13 Muon Tracking Chamber electronics [116].

2.2.4.4.1 Alignment of the Muon Tracking Chambers

The mass resolution of the Muon Spectrometer is 100 MeV/c^2, in order for this mass resolution to be maintained, the muon chambers need to be aligned and monitored. During the installation phase, the position of the detection elements can be aligned with the aid of photogrammetric measurements; these measurements give the relative position of each element in an arbitrary coordinate system. However, the initial position of the detection elements changes upon the switching on of the magnetic fields and the electronic power supplies. It is therefore necessary to make special runs to account for misalignment, there are two types of runs that are made for the alignment:

- The first type of run is done using cosmic data. This is the case where the dipole magnet is switched off and the initial position of the chambers is measured using straight muon tracks. These type of runs are known as calibration runs and are done with the magnetic field off.

- The second type of run is done with the dipole magnet switched on. Measurements of the chamber displacements are done with the magnetic field on.

The straight tracks from the run are processed with the Millepede algorithm [117], this

algorithm is utilized for detector alignment and calibration based on track fits. The method solves the linear least squares problem with a simultaneous fit of all global and local parameters, irrespective of the number of local parameters [118].

In addition to the displacement of the detection elements when the magnetic field and electronics are switched on, the detection elements also suffer from thermal expansion and deformations. During data taking, the detection elements are monitored using the Geometry Monitoring System (GMS) [119]. The system consists of an array of 460 optical sensors that are placed on platforms located at the corner of each detection element.

2.2.4.5 Muon trigger chambers

The Muon Trigger Chambers (MTR) are designed to select muon candidates during collisions, more specifically the high p_{T} muons that are produced in heavy quarkonia, open charm and bottom decays. Muons from W and Z decays and low mass vector mesons are also selected by the spectrometer during collisions. The system allows for individual p_{T} trigger level cuts on muons rejecting tracks of $p_{\mathrm{T}} < 0.5$ GeV/c. The system detects both dimuons and single muons for given p_{T} to produce the relevant triggers. The system has two p_{T} cuts available that help to reduce the background for the data analysis of interesting physics events. The p_{T} cuts are ~ 0.5 GeV/c and ~ 4.2 GeV/c for the low and high p_{T}, respectively. For muon data taking, the following trigger inputs are defined:

1. **0MSL** - consists of at least one reconstructed muon that satisfies the low p_{T},
2. **0MSH** - consists of at least one reconstructed muon that satisfies the high p_{T},
3. **0MUL** - consists of at least one reconstructed unlike signed dimuon pair satisfying the low p_{T} and;
4. **0MLL** - consists of at least one reconstructed like signed dimuon pair satisfying the low p_{T} cut.

The MTR is located behind the muon filter at a distance of ~ 16 m from the IP. The MTR consists of 72 Resistive Plate Chamber (RPC) that are grouped into two stations (MT1 and MT2) that are 1 m apart with the first station 16, from the IP. Each station is made up of two detection planes consisting of 18 RPC modules and a total of four single gap RPC detector planes; these are referred to MT11, MT12, MT21 and MT22, respectively. The detection planes are arranged perpendicular to the beam line. Each plane covers an area of 5.5×6.5 m^2 with a central hole for the beam pipe and its shielding of dimension 1.2×1.2 m^2. As a result of the hole made in the detection planes to accommodate the beam pipe, there are three different kinds of detectors with different shapes and segmentation. The different shaped detectors are illustrated in Fig. 2.14 on the right; there is the Long

(L), Cut (C) and Short (S). On the left of Fig. 2.14 is a schematic view of the ALICE MTR with the two stations indicated. Each strip is equipped with readout strips that provide spatial information in the x and y directions, there is a total number of 21 000 strips [120, 121].

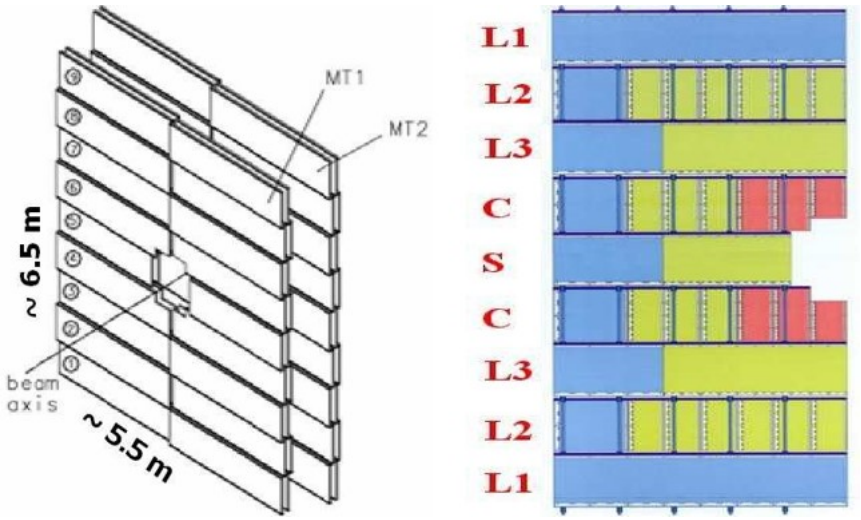

Fig. 2.14 Schematic view of the ALICE MTR (left) and detector composition of a half plane (right)[120].

The strips placed in the horizontal direction are known as the X-strips and are used to measure the y-coordinate. The strips placed in the vertical direction are known as the Y-strips and are used to measure the x-coordinate. The signals from the readout strips are sent to the RPCs front-end electronics, the ADULT (A Dual Threshold). The ADULT sends the digital signals to the local trigger electronics. The aim of the local trigger electronics is to produce a level 0 single muon trigger that implements the p_{T} threshold on the single tracks. The ALICE CTP then reads out the input bit patterns that are stored in a pipe lined memory by the local trigger electronics.

The RPC is composed of two low-resistive electrodes separated by a 2 mm volume gap filled with gas. The gas in the gap is a mixture of $Ar/C_2H_2F_4$/i-butane/SF_6 with ratio 49%/40%/7%/1%. The electrodes are bakelite electrodes and require the relative humidity of the gas mixture to be kept at 37% to prevent any alterations to the electrodes [120].

Figure 2.15 shows the RPC structure; the graphite layer, which is a conductive material, is used to connect the plates to ground and high voltage (HV) on the external surfaces. A minimum of 4-5 kV/mm is required for the RPCs to function. An insulating film is used to cover the graphite electrodes and aluminum "pick-up" strips are placed outside the chamber. The insulating film is Mylar which is a type of polyester film. On the one side of the RPC, it is aligned with the x-axis of the ALICE reference system and measures the

deviation in the bending plane. The other side is aligned with the y-axis and measures the deviation in the non-bending direction. To allow gas flow in and out of the detector at atmospheric pressure, the RPC is surrounded by a frame of polycarbonate equipped with four pipes.

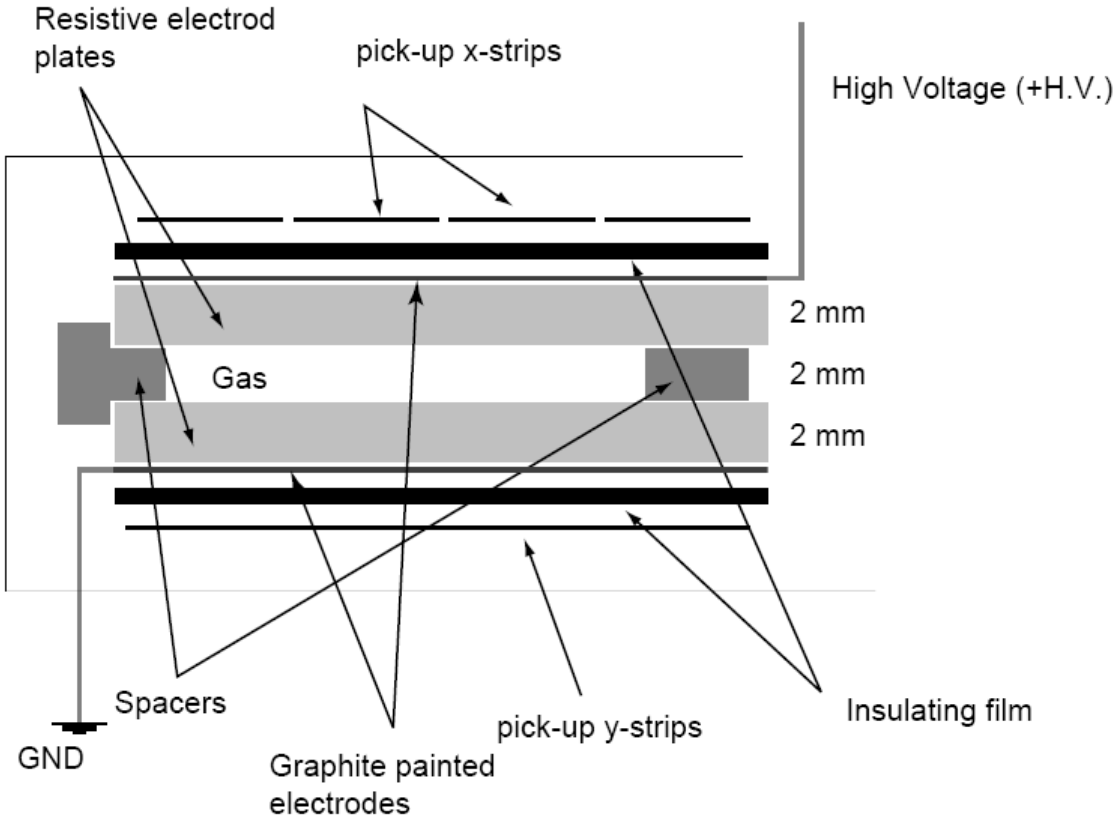

Fig. 2.15 MTR resistive Plate Chamber layout [116].

In pp collisions, an avalanche operating mode is used to reduce the aging effect of the RPC's [116]. Before the avalanche working mode is discussed, the basic working principle of the RPC detector is described. The particle detection in the RPC relies on the ionization of the gas within the RPC. As the particle traverses through the gas, some of the gas atoms are ionized. The electrons move towards the anode while the ions move towards the cathode in the presence of an electric field. The electrons however, have enough energy to ionize more gas molecules as they move towards the anode, this is secondary ionization. The secondary ionization process leads to the amplification of the signals which is then collected by the strips attached on the side of the RPC.

In the avalanche operating mode, the argon (Ar) gas that is part of the gas composition that fills the RPC is substituted with an organic gas ($C_2H_2F_4$). The gas mixture changes from $Ar/C_2H_2F_4$/i-butane/SF_6 to $C_2H_2F_4/C_2H_2F_4$/i-butane/SF_6. The $Ar/C_2H_2F_4$, Freon

($C_2H_2F_4$) and i-butane are quenchers[5] while SF_6 is an electro-negative gas. The organic gas allows for ionization to happen more easily and also possesses better quenching features. The working principle of this mode is the same as mentioned above.

The trigger principle is in the presence of a magnetic field, the trajectory of the muon deviates as shown in Fig. 2.16. The muon interacts with MT1 in Y_1 and MT2 in Y_2, respectively, the transverse momentum of the muon crossing the chamber can be estimated by measuring the deviation caused by the magnetic field of the dipole magnet. The p_T cuts mentioned above are based on the deviation of the muon relative to a straight p_T track shown in Fig. 2.16. The deviation in the bending plane is expected to be smaller than a deviation δy that corresponds to a p_T threshold and a given magnetic field B.

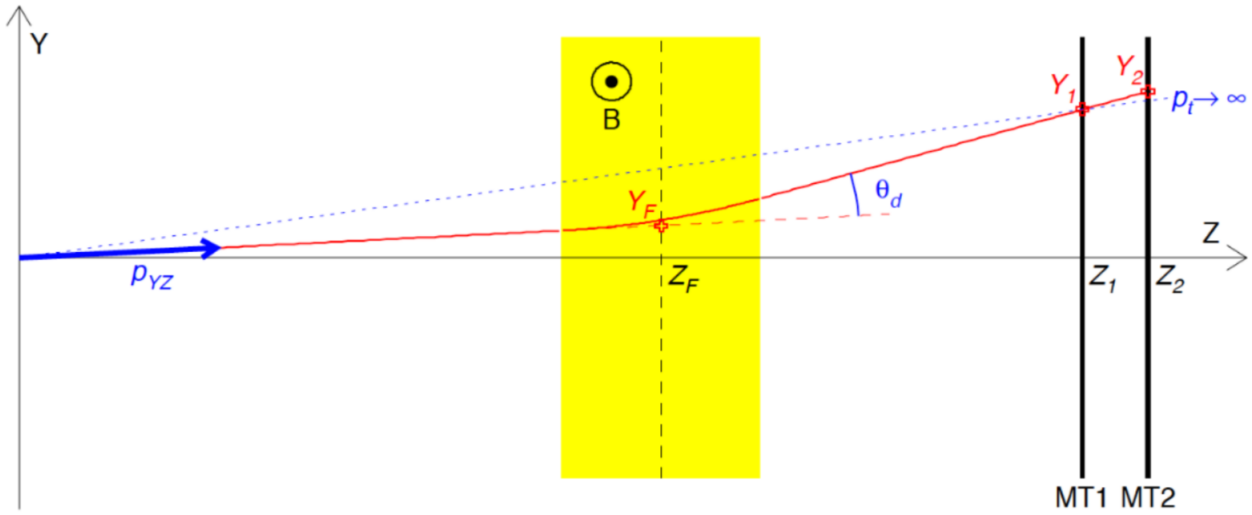

Fig. 2.16 The Muon Spectrometer trigger principle [1].

2.2.5 Summary

A summary of the detector subsystems is given in Table 2.3. It should be noted that the acceptance of η is calculated from the nominal interaction point and it is 360° in azimuth. The position of each detector is the approximate distance from the interaction point to the face of the detector, it corresponds to the radius of the barrel detectors or the position along the beam for the other detectors. The dimension is the total area subtended by each detector component while the "channels" is the total number of the independent electronic readout channels.

[5]Substances that are capable of absorbing energy and re-emitting much of that energy in the form of heat and/or visible light

Detector	Acceptance (η, ϕ)	Position (m)	Surface area (m^2)	Channels
ITS				
Layer 1,2 (SPD)	$\pm 2, \pm 1.4$	0.039, 0.076	0.21	9.8 M
Layer 3,4 (SDD)	$\pm 0.9, \pm 0.9$	0.150, 0.239	1.31	133 000
Layer 5,6 (SSD)	$\pm 0.97, \pm 0.97$	0.380, 0.430	5.0	2.6 M
TPC	± 0.9 at r = 2.8m	0.848, 2.466	readout 32,5	557568
	± 1.5 at r = 1.4m		Vol. $90m^3$	
TRD	± 0.84	2.90, 3.68	71.6	1.2 M
TOF	± 0.9	3.78	141	157 248
HMPID	± 0.6, $1.2° < \phi < 58.8°$	5.0	11	161 280
PHOS	± 0.12, $220° < \phi < 320°$	4.6	8.6	17 920
HMPID	± 0.7, $80° < \phi < 187°$	4.36	44	12 672
HMPID	± 1.3, $-60° < \phi < 60°$	8.5	43	120
Muon Spectrometer				
Tracking Station 1	$-2.5 < \eta < -4.0$	-5.36	4.7	1.08 M
Tracking Station 2		-6.86	7.9	
Tracking Station 3		-9.83	14.4	
Tracking Station 4		-12.92	26.5	
Tracking Station 5		-14.22	41.8	
Trigger Station 1	$-2.5 < \eta < -4.0$	-16.12	64.6	21 000
Trigger Station 2		-17.12	73.1	
PMD	$2.3 < \eta < 3.7$	3.64	2.59	2 221 184
V0A	$2.8 < \eta < 5.1$	3.4	0.548	32
V0C	$-1.7 < \eta < -3.7$	-0.897	0.315	32
T0A	$4.61 < \eta < 4.92$	3.75	0.0038	12
T0C	$-3.28 < \eta < -2.97$	-0.727	0.0038	12

Table 2.3 Summary of the ALICE detector subsystems [99, 122].

2.3 The ALICE Online System

The ALICE online system is made up of five systems: Trigger, Data Acquisition, High-Level Trigger, Detector Control System and Experiment Control System. These systems all play a key role in the data taking operations of the ALICE experiment. A summary of the key functions of each system is given below:

- The Central Trigger Processor (CTP) system is responsible for combining information from all the triggering detectors. It is required to make decisions within microseconds on whether the data from each bunch crossing[6] of the LHC is worth being collected. A sequence of trigger signals is sent by the CTP to all the triggering detectors instructing them to read out the data should the trigger system make a positive decision.

- The Data Acquisition (DAQ) system is responsible for data flow within the experiment. It ensures the data flow from the detector to data storage with the aid of software packages performing data quality and system performance monitoring.

- The High-Level Trigger (HLT) is responsible for reducing the volume of the physics data through data selection and compression.

- The Detector Control System (DCS) is responsible for controlling all the detector services within the experiment. This includes the high and low-voltage power supplies, magnet, cooling, gas, detector operations, etc.

- The Experiment Control System (ECS) is responsible for coordinating the activities of all the online systems.

Figure 2.17 shows the schematic of how the online systems, showing how the ECS is responsible for the four other systems.

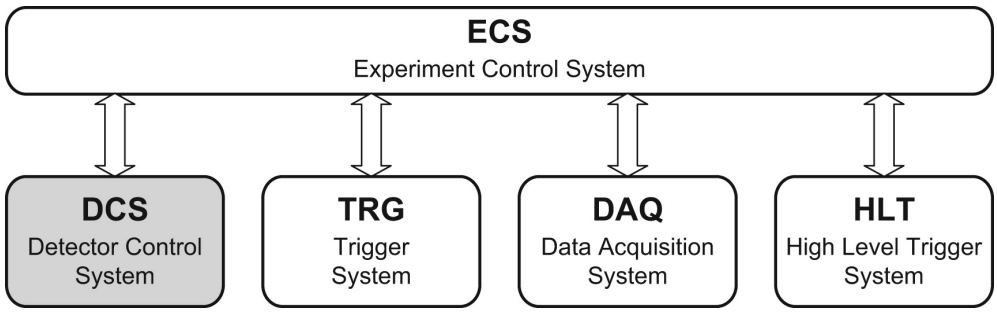

Fig. 2.17 Schematic of the ALICE online systems [123].

[6] A bunch is a collecction of particles captured within one RF bucket [107]

2.3.1 The Central Trigger Processor

The trigger decision of the ALICE detector is generated by the Central Trigger Processor (CTP). The CTP was designed with the intention to combine and align information from all the Local Trigger Units (LTU) in ALICE. There are 24 LTUs altogether that work as a unifrom interface for the front-end electronics. The CTP is responsible for synchronizing information from all the trigger detectors in ALICE, thereafter it sends the detectors a sequence of trigger singals to make them read out correctly. It concurrently sends the trigger information also to the data aquisition (DAQ) which collects it as scaler information and trigger event records [124].

The CTP is controlled by the ALICE run control. Figure 2.18 shows the principal function of the CTP and the relationship between the run control and DAQ. Some of the detectors have significantly different latencies, which results in the ALICE detector trigger system to have three trigger levels; the **L0**, **L1** and **L2**. At any time, the 24 ALICE sub-detectors are dynamically partioned in up to six clusters, the cluster configuration is arbitrary and fully programmable. The clusters can be exclusive but are more likey to overlap in most cases. The **L0** is the fastest trigger level with a latency of 1.2 μs. This trigger level is responsible for providing detectors with fast track-and-hold elecctronics with a strobe as well as to initiate a "BUSY" flag for all the detectors in a specific cluster. The second trigger level **L1** has a latency of 6.5 μs. At this trigger level, there are more trigger inputs available requiring major rate reductions. This level is typically responsible for storing event data in multi-event buffers. The third trigger level, L2, is responsible for waiting for the detector with the longest sensitivity period to determine whether the events should be rejected as a result of pile-up [125].

There are in total 60 trigger inputs used for trigger conditions; 24 L0, 24 L1 and 12 L2. These trigger inputs come from the different trigger detectors in the ALICE detector. Table 2.4 gives a summary of the different trigger detectors and also shows which level each detector is contributing to [126].

Scalers are used to store the information as counts for all the trigger classes at each of the levels before (L0b) and after (L0a) the CTP decision. Whenever the CTP does not generate an L0 signal the CTP might raise a veto flag; this can be triggered either by the cluster if one of the detectors is busy, a mismatch exits between the L0 input and bunch crossing, a downscaling of certain trigger classes needs to be performed to increase the bandwidth of the DAQ for rare events or due to a past-future protection.

For Pb-Pb collisions, the past-future protection monitors the number of interactions that are classified according to the multiplicity[7]. In pp collisions, where there is a lower

[7]Average number of particles produced in a collision at a given center-of-mass energy system

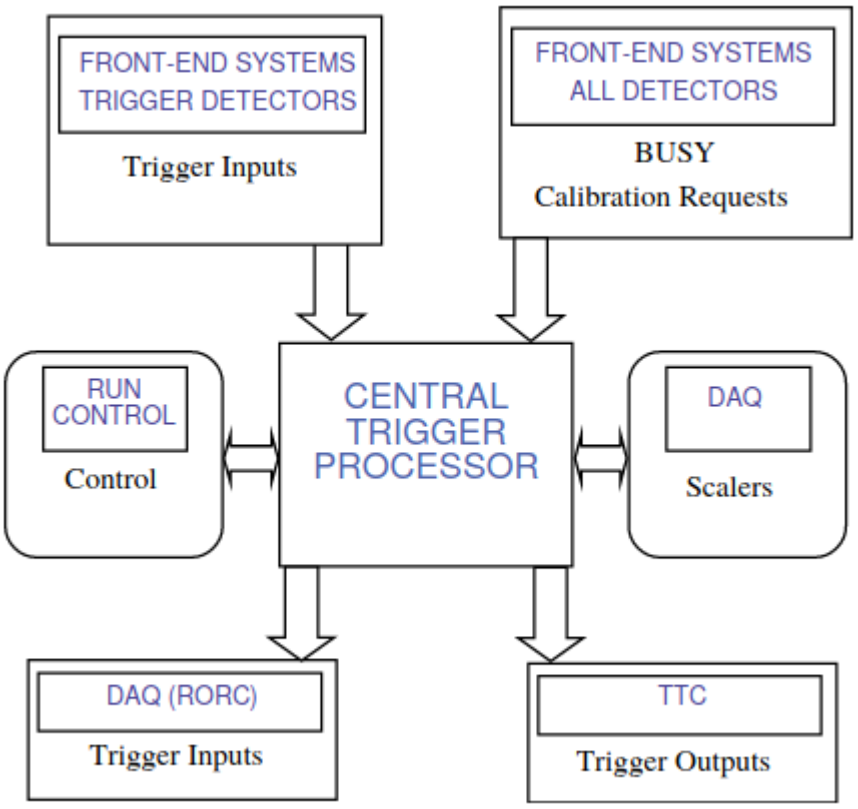

Fig. 2.18 Schematic of the CTP functions [125].

Detector	Function	Level
SPD	hit-multiplicity and hit-topology based trigger	L0
TRD	electron, high-p_{T} particle and charged-jet trigger	L1
TOF	multiplicity, topological (back-to-back) and cosmic-ray trigger	L0
PHOS	photon trigger	L0
EMCal	photon and neutral-jet trigger	L0/L1
ACORDE	cosmic-ray trigger (single and multiple hits)	L0
V0	coincidence based minimum-bias interaction and centrality trigger	L0
T0	event-vertex selection and interaction trigger	L0
ZDC	minimum-bias interaction and electromagnetic-dissociation triggers in Pb-Pb	L1
MTR	single-muon and dimuon trigger	L0

Table 2.4 Trigger capabilities of the ALICE trigger detectors [126].

multiplicity, the number of separate primary vertices resulting from pile-up rather than the number of tracks is monitored [125]. In the absence of CTP vetoes, the sub-detectors are readout after the L2 trigger. The event information is sent to the High Level Trigger

(HLT) where the events are accepted or rejected after the implementation of the trigger criteria.

2.3.2 Data Acquisition System

The Data Acquisition system (DAQ) [127] controls the detector software, infrastructure, data quality monitoring and the overall data-flow and handling of the experiment. The bookkeeping of all the operational activities of the experiment are recorded in the electronic logbook. The logbook is the only software that both the DAQ and ECS systems directly use.

Figure 2.19 shows the overview of the hardware architecture of the ALICE DAQ during Run 1. The data-flow begins with the CTP, see section 2.3.1, which makes a decision for every bunch crossing of the LHC. The decision is communicated to the LTU of all the readout detectors using the L0, L1a and L2a triggers. Selecting interesting physics events, providing efficient access to the events and archiving the data to permanent data storage are some of the tasks taken on by the DAQ system. Decisions to give a fair share of DAQ resources with respect to the DAQ bandwidth for frequent triggers and detector livetime for rare triggers are considered to be positive decisions [99]. Positive decisions are broadcasted by the LTUs over the Trigger, Timing and Control (TTU) network. The Front-End and Readout (FERO) electronics receive the data from the detectors according to the corresponding sequence of the trigger signals. The event fragments produced by the detector electronics are transported by the Detector Data Links (DDL). DDL links are point-to-point optical links that are clocked at 2.1 GB/s with each DDL containing a capacity of 200 MB/s. Almost 500 links are responsible for transporting the data from 100 m underground from the detector to the computing room. The computing room is located close to the surface and is named Counting Room 1 (CR1) [127].

The DAQ Readout Receiver Card (D-RORC) is on the receiving end of the DDL and is repsonsible for transferring the data directly into the memory of the PCS using a Direct-Memory Access (DMA). A copy of the data is sent over to a second DDL by some of the D-RORCs to the HLT farm. These data are received by a HLT ReadOut Receiver Card (H-RORC) that tranfers it to the Front-End Processors (FEP) for online reconstruction, decision making about which data should be recorded and compressed. It is important to note that during the first LHC long shutdown (LS1), the D-RORCs and H-RORCs in the DAQ system were replaced with the Common Readout Receiver Card (C-RORC) for Run 2 [127].

The D-RORC is hosted on detector specific computers called Local Data Concentrators (LDCs). Event fragments are sent to be assembled into sub-events in the LDCs and then sent to a farm of computers called Global Data Concentrators (GDCs). The whole event

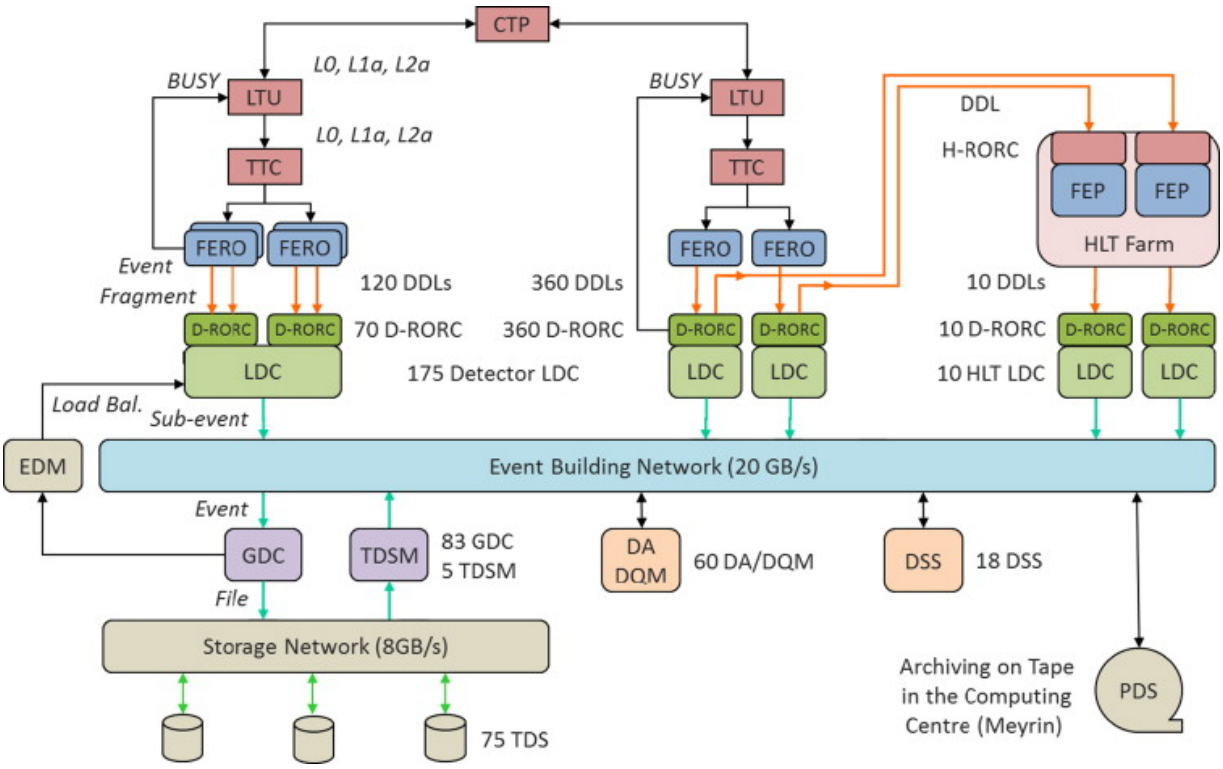

Fig. 2.19 Overview of the ALICE DAQ [127].

is built at the GDCs and subsequently shipped to a Transient Data Storage (TDS). The data from each run is registered on the ALICE Environment (AliEn) that is hosted via the MONitoring Agents using a Large Integrated Services Architecture (MonALISA).The decision to send the event to the TDS or Permanent Data Storage (PDS) is made by the Event Destination Manager, EDM. In the next section, the HLT is discussed in more detail.

2.3.3 High-Level Trigger

The High-Level Trigger (HLT) [128] is responsible for online reconstruction and compression of the data received from the readout detectors. The experimental data received by the DAQ system are also sent to the HLT farm via the DDL. The data are received by the C-RORCs and sent to the computing cluster. Whenever a decision is made by the HLT to record or discard the data, the data are processed. After the data have been processed, they are sent back to the DAQ system using the C-RORCs and DDL. The original data that are stored by the DAQ system are then discarded and only the data accepted and processed by the HLT are stored. This process significantly reduces the volume of the data in the permanent storage. Figure 2.20 shows an overview of the ALICE online architecture in Run 2 with focus on the C-RORCs.

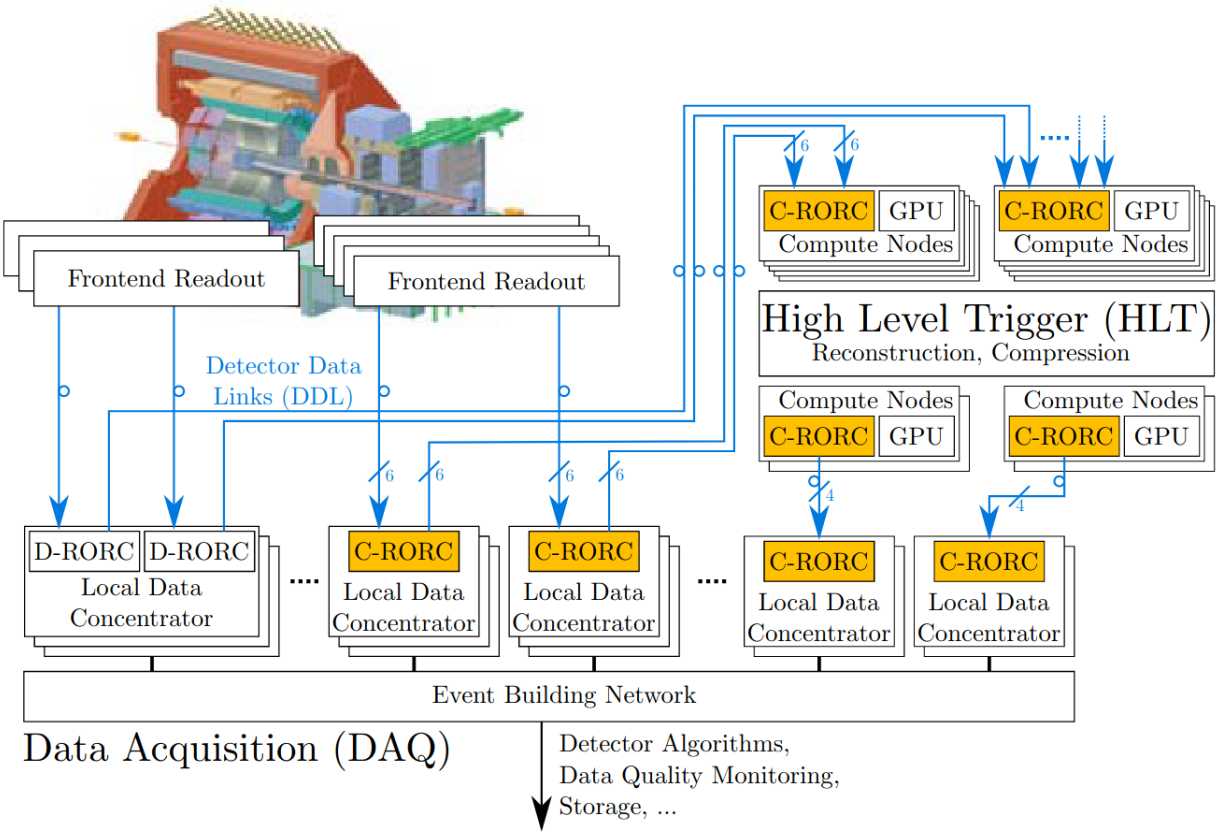

Fig. 2.20 Overview of the ALICE online architecture in Run 2 with focus on the C-RORCs [128].

2.3.4 Detector Control System

The Detector Control System (DCS) is responsible for controlling all the detector services within the experiment. This includes the high and low-voltage power supplies, magnet, cooling, gas, detector operations, etc. The DCS ensures a safe and proper operation of the experiment during all the LHC operations, whether it is during data taking, commissioning or shutdown periods. The experimental equipment can be configured, monitored and remote controlled by the DCS. The DCS is also responsible for monitoring the environmental safety, ensuring that areas that are accessible to personnel are safe from radiation. It is also responsible for collecting and managing alarms, data and commands. The LHC communicates with the experiment by sending "handshakes" to the DCS to inform the experiment on the status of the LHC beam operations.

As an example, Fig. 2.21[8] shows a screenshot of the ALICE DCS Monitoring page during the 2015 data taking period. On the DCS monitoring page, the status of the LHC,

[8]The reference to the image is a link to a real time page and this figure cannot be retrieved from this reference

detectors, magnets, alarms and the overall status of the ALICE experiment are monitored. As shown in Fig. 2.21, both the dipole and solenoid magnets were on and their polarity was negative with the respective currents and magnetic fields printed on the screen. The LHC status is also shown with a "handshake" warning message from the LHC operations indicating an upcoming beam dump (to be discussed in the next section). All the sub-detectors except the PMD were ready for data taking, with the green lock showing that the detectors were available for use by central DCS. Notes from the DCS and the LHC are also printed on the screen.

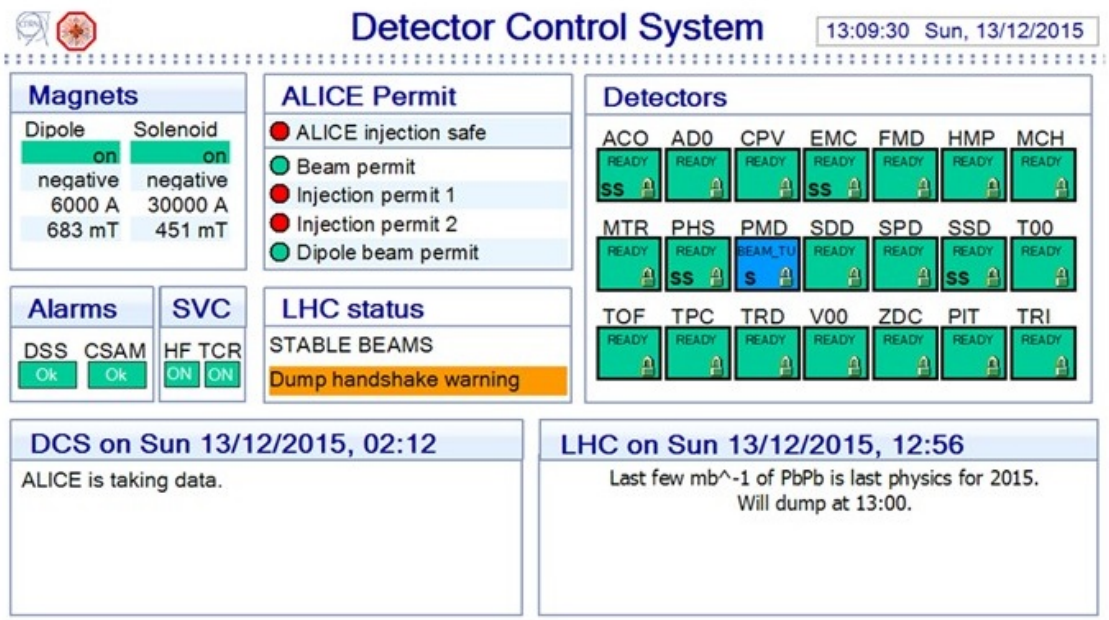

Fig. 2.21 ALICE DCS Monitoring page during the 2015 data taking period [129].

When the DCS receives communication from the LHC in relation to the LHC beam modes, the experiment needs to start preparing to receive the beam by ensuring that the sub-detectors are in a safe state. This is achieved by reducing voltages during the injection, acceleration and the adjusting modes of the LHC beams. These modes are discussed in the next section.

2.4 Data taking conditions

The LHC has to take a number of steps in order to provide stable colliding beams to the experiments. The mode of the accelerator gives information on its current operations. The LHC has two modes: the accelerator mode and the beam mode. In the accelerator mode, information on the activity of the accelerator is given. Such information includes the type of physics, access to the beam lines and experimental caverns and shutdown to

mention a few. The beam mode provides information on the state of the accelerator with regards to its cycle during the delivery of the beams. This includes the injection, ramp, beam dump, etc.

Accelerator Mode:
According to the accelerator mode, there is either beam or no beam in the LHC. Conditions that would require no beam include a shutdown during the winter, machine check-out, access, machine test, calibration, warm-up and recovery. During beam setup, proton physics, ion physics, Totem physics and machine development, a beam is required. Beam setup requires either one or both beams, it includes beam commisioning from the injection phase to the collision phase. More details on the accelerator mode is discussed in [130]. A summary of the accelerator modes is given in Table 2.5

Accelerator mode	**Description**	Status
Shutdown	Usual winter status	No beam
Beam Setup	Beam commissioning from the beam injection phase to the collision phase.	Beam
Proton Physics	Beam based operation for proton physics	Beam
Ion Physics	Beam based operation for ion physics	Beam

Table 2.5 Summary of the LHC accelerator modes, a detailed summary is given in [130].

Beam Mode
In every LHC cycle, there is a sequence of operations that need to be carried out in order for the accelerator to deliver a beam for physics. A summary of these operations is well illustrated in Fig. 2.22.

In preparation of physics beams, the LHC cycle starts with the **SETUP** mode. In this mode the two beams are in the transfer lines ready to be injected into the LHC. There is no beam in the LHC ring during the setup mode.

The **INJECTIONS** mode, as indicated in Fig. 2.22, is divided into 3 types of injections [130]:

1. The injection probe beam is used to perform a number of checks on the accelerator's sub-systems before injecting bunches with higher intensities. The probe beam is used to establish a circulating safe beam for a given time period.

2. The injection setup beam follows the probe beam, this beam allows to make more precise measurements before filling the beam lines with the physics beams. This

beam represents the physics beam that follows with just a few bunches[9] to stay below the damage threshold, this beam is not accelerated in the beam lines.

3. The injection physics beam is only done after the machine has been optimized using the two previous beams. In this mode, the LHC beam lines have been fully optimized and has been proven that the beam lines are able to circulate the beams with the appropriate lifetime. At this stage the beam lines are ready to accept beams with high intensities that are required for physics.

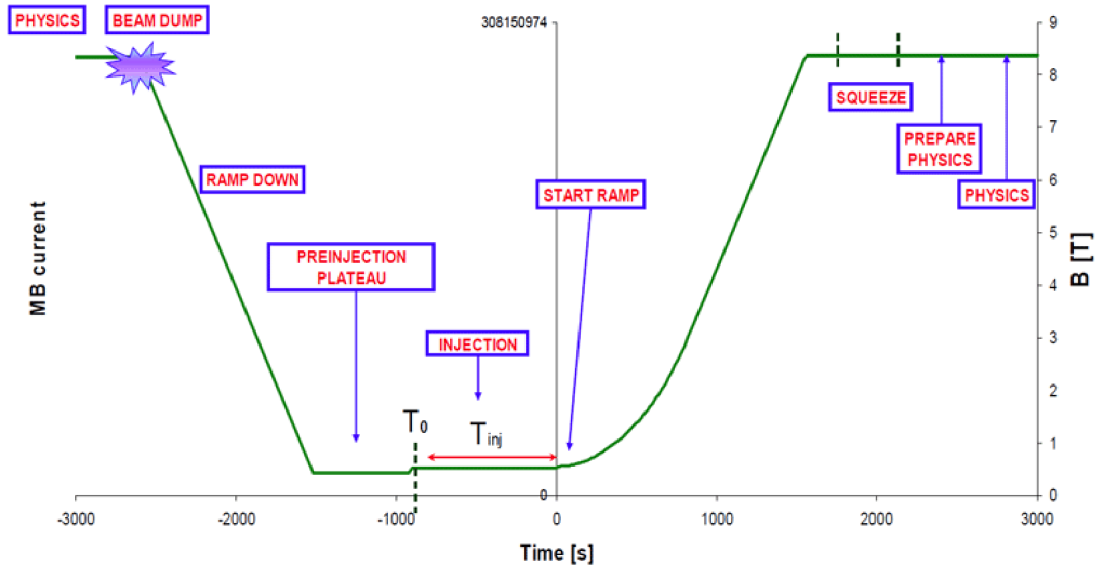

Fig. 2.22 The LHC beam modes showing the MB current and magnetic field as a function of time [131].

The next mode after the injections is the **PREPARE RAMP** mode. Once the injection has been completed, preparations for the ramp are done. The **RAMP** mode is the process where the beam energy is increased to the desired energy. The accelerators in the LHC beam pipes are fitted with metallic chambers that contain an electromagnetic field known as radiofrequency (RF) cavities. The RF cavities create electrical impulses that accelerate charged particles injected into the field. The LHC consists of 16 RF cavities in total that can work in a superconducting state. Each RF cavity is driven by a tube that contains electron beams, this tube is known as a high-power klystron. The electron beams have a frequency of 400 MHz, this corresponds to 400 million oscillations per second. The energy within the tube is directed to the cavity with a waveguide, a rectangular pipe of conducting metal. Each cavity reaches a maximum voltage of 2 megavolts (MV), this corresponds to 16 MV per beam [132].

The particle beam is injected into the LHC with an energy of 450 GeV, the RF cavities

[9]Chunks of particles that are a few centimeters long squeezed down to the size of a human hair.

can accelerate the beam up to a maximum of 6.5 TeV in pp collisions. This acceleration is 14 times more than the injection energy. The maximum energy is reached in 20 minutes, with the beams having passed the RF cavities at least 10 million times. The field of the RF cavity is oscillated by switching the direction at a given frequency. It is important to know the arrival time of the particles in order to oscillate the RF cavity accordingly. The RF cavities in the LHC each oscillate at 400 MHZ, once the beam has reached the desired energy, ideally timed protons will cease to accelerate. The protons that are not ideally timed will either decelerate if they had more energy or accelerate if they have not reached the desired energy [132].

At this stage, the LHC experiments start to prepare their detectors by ensuring that the detectors are brought to and stay in a safe state, e.g. reduced voltages during the injection, acceleration, and adjusting phases of the LHC beams [130].

Once **RAMP** is completed, the machine switches to **FLAT TOP** as demonstrated in Fig. 2.22. Pre-squeeze checks are done in preparation for the **SQUEEZE** mode. In the squeeze mode, the beams are focused to minimize the beam size and maximize the luminosity, resulting in an increase in intensity. The beams are focused using quadrupole magnets that act as lenses by gathering the particles closer together. The charged particles can be focused to one plane or defocused to an orthogonal plane. A system called an inner triplet is created using three quadrupoles, there are eight inner triplets in total at the LHC. Each experiment has two inner triplets. These inner triplets can tighten a beam from 0.2 mm down to 16 μm across, this is making the beam 12.5 times narrower than it was [133]. The squeeze mode is followed by the **ADJUST** mode which is in preparation for collisions. In the **ADJUST** mode, the beams are adjusted and focused to enable collisions. The beams are adjusted by ensuring the quadrupoles are aligned.

The period between the **RAMP** and **ADJUST**, the ALICE sub-detectors are calibrated to get **READY** for collisions. The calibration tasks can be performed directly online while other tasks are operational. There are also certain tasks that are completed offline. For the MCH, calibrations runs are performed in preparation for data taking. The tracking chambers take a pedestal run is taken at ADJUST when MCH is BEAM_TUNING state, where the low voltages (LVs) are switched on at 3 V, and the high voltages (HV) are at an intermediate value typically ∼1200 V [134]. See below under Beam-Tuning for further details about the pedestal run. There are four main states that MCH detector can be in, each state is discussed in short details below [135]:

1. The **STANDBY** state implies that the High Voltages (HV) and Low Voltages (LV) are switched off.

2. The **STANDBY_CONFIGURED** state implies the LV are switched on (±3 V)

and a voltage of ∼600 V is applied to move to the **BEAM_TUNING** state.

3. The **BEAM_TUNING** state involves the LV on and HV being at an intermediate voltage of ∼1200 V. For example, for the MCH; at this voltage, there is no gain resulting from particles crossing the detector. During this run, pedestal are measured and thresholds are computed. These measurements are necessary for the correction of the gain dispersion and noise, in order to be able to accurately determine the collision points of the particles during data taking [136].

4. The last state is the **READY** state, in this state, the LV are on and HV have a maximum voltage of ∼1600 V. The detectors are ready for physics runs and data taking.

STABLE BEAMS mode implies that the machine switches to colliding the beams in the four IP. At the end of data taking or should there be an emergency during operations, the **BEAM DUMP** mode is entered. After the beam dump, the **RAMP DOWN** mode follows. There are more modes discussed in [130].

Since there are different beam energies and species being collided in the LHC, there are different periods that are dedicated for the different types of physics. To keep track of the data taking conditions for the different run periods, the LHC developed a filling scheme (LHC Automatic Filling Scheme - AFS) with all the necessary important information stated. This information is published on LHC page 1 [137][10]. Figure 2.23 shows a snapshot of page one during the Run 2.

In Fig. 2.23, at the bottom left of the image is where the AFS is printed. The basic structure of the filling scheme is:

<spacing> _ <Nb>b_ <IP1/5> _ <IP2> _ <IP8> _ <code>

where:

- <spacing> gives the characteristics of the bunch spacing. The options available are: single, 2025ns, 525ns, 75ns, 50ns, 25ns, etc. Single means that only single bunches are injected into the LHC, more on the bunch spacing is discussed in reference [138].
- <Nb>b is the total number of bunches per beam for a given filling scheme.
- <IP1/5> is the expected number of colliding bunch pairs in IP1 and/or 5 which corresponds to the ATLAS and CMS experiments respectively.

[10]This is a real time page and the information displayed in this thesis will be different should the page be accessed

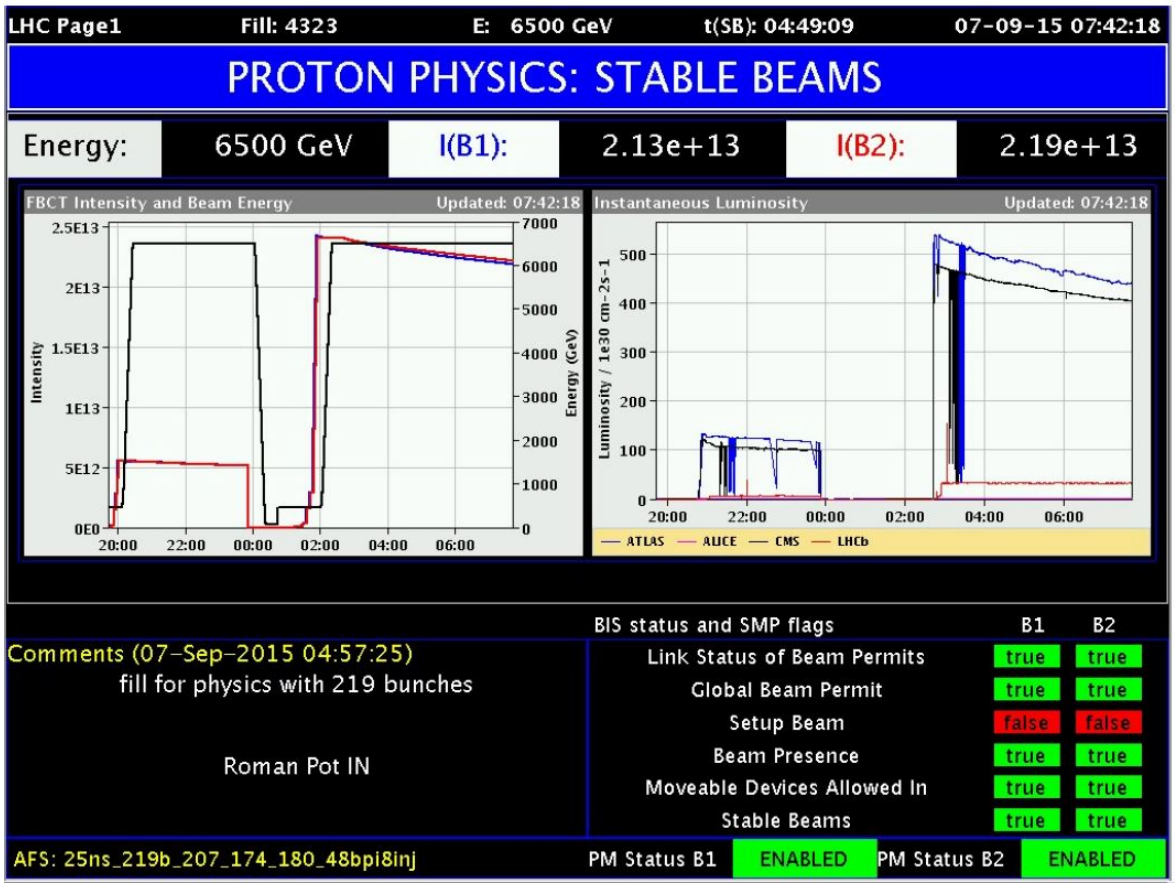

Fig. 2.23 The LHC Page 1, gives information of LHC operations in real time [137].

- <IP2> is the expected number of colliding bunch pairs in IP2 which is the ALICE experiment.
- <IP8> is the expected number of colliding bunch pairs in IP8 which is the LHCb experiment.
- <code> is a free suffix that encodes the variants of a filling scheme.

Other information that can be found in LHC Page 1 is information on beam intensity, beam energy, beam mode, fill number, beam stability time and etc.

The LHC delivers beams according to the requirements of the different experiments to fulfill the physics of interest. The criteria that needs to be satisfied is based on the luminosity and cross sections the experiments require to be able to investigate the physics of interest. For this thesis work, the data sample analysed was collected in 2015 and 2017 in pp collisions at $\sqrt{s} = 5.02$ TeV during the Run 2 data taking period where the LHC provided two beams, each with a center-of-mass energy 2510 GeV. In the 2015 data taking period, the LHC15n run period was dedicated to pp collisions at $\sqrt{s} = 5.02$ TeV. This period lasted 5 days, from November 15th to November 23rd. In the 2017 data taking

period, two more run periods, LHC17p and LHC17q, were dedicated to pp collisions at $\sqrt{s} = 5.02$ TeV. These periods lasted 10 days, from November 11th to November 21st.

Each run period within the ALICE data-taking program is a collection of runs, for which the beam energy, magnetic field and polarity as well as the trigger setup is the same. However, for some run periods, there may be differences in the characteristic bunch spacing or total number of bunches per beam. The filling scheme of one of the periods (282118) considered in this thesis taken from the LHC17p run period, is as follows:

25ns_1836b_1824_1744_1096_128bpi_16i8b4e

The characteristic bunch spacing was 25ns and the total number of beam bunches was 1836. The total number of beam bunches that collided in ATLAS and CMS are 1824, at ALICE there were 1744 beam bunches that collided and LHCb had 1096 beam bunches collide.

In ALICE, different trigger classes are used to distinguish interactions and select physics of interest for different analysis. In this thesis, the physics of interest is the inclusive single muon production from charm and beauty decays. Single muon triggers in the Forward Muon spectrometer were used to select the physics events of interest. The general naming scheme for ALICE trigger classes has the following format [139]:

C<descriptor code> − <bunch crossing mask code> − <past-future protection code> − <detector cluster code> − <rare flag, if needed>

- A descriptor is a logical function of the trigger inputs.
- The bunch crossing mask gives information on which bunch crossings in the orbit of the LHC are activated.
- The past-future protection scheme is used to define the conditions imposed on the presence of trigger in the bunch crossings preceding and following the trigger bunch crossing.
- The detector cluster gives information on which detectors are used for readout.
- A rare flag is a special time interval reserved for classes flagged as rare [139].

The trigger classes of interest in this thesis are listed below:

- CMSL7-B-NOPF-MUFAST is the low p_{T} single muon trigger defined by a coincidence of signals in V0A and V0C detectors with a muon satisfying the low p_{T} threshold in the Muon Spectrometer;

- CMSH7-B-NOPF-MUFAST is the high p_{T} single muon trigger defined by a coincidence of signals in V0A and V0C detectors with a muon satisfying the high p_{T} threshold in the Muon Spectrometer;
- CINT7-B-NOPF-MUFAST is the minimum-bias trigger defined by a coincidence of the V0A and V0C with the SPD.

An example can be made using the first trigger class mentioned above:

CMSL7-B-NOPF-MUFAST

- **CMSL7** means 0MSL input with V0AND.
- **B** indicates bunches from **both** beams on the bunch crossing mask from the LHC.
- **NOPF** means there is no veto applied for past-future protection.
- **MUFAST** is the cluster name that includes the SPD, MCH, MTR, T0, V0 and AD detectors.

The number of recorded triggers in pp collisions at $\sqrt{s} = 5.02$ TeV for the Run 2 data taking period is shown in Fig. 2.24 which shows the integrated luminosity for different triggers, including the triggers of interest in this thesis, i.e. the single μ high$-p_T$, single μ low$-p_T$ and minimum bias (MB). The plateau in the figure shows that no data taking in pp collisions at $\sqrt{s} = 5.02$ TeV was done during certain periods in 2015 and 2017.

In summary, the chapter discussed the Large Hadron Collider, details on the LHC and all the experiments involved were also given. Thereafter, details on the experiment of interest, the ALICE experiment, was discussed. The ALICE online system was also discussed, in which more information on how the online system operates was given and highlighting some of the key components of the system. The steps required and procedures taken by the LHC operators to provide stable beams that are presented and for data taking were discussed. The next chapter will discuss the offline ALICE system and the analysis strategy followed to obtain the results discussed in this thesis.

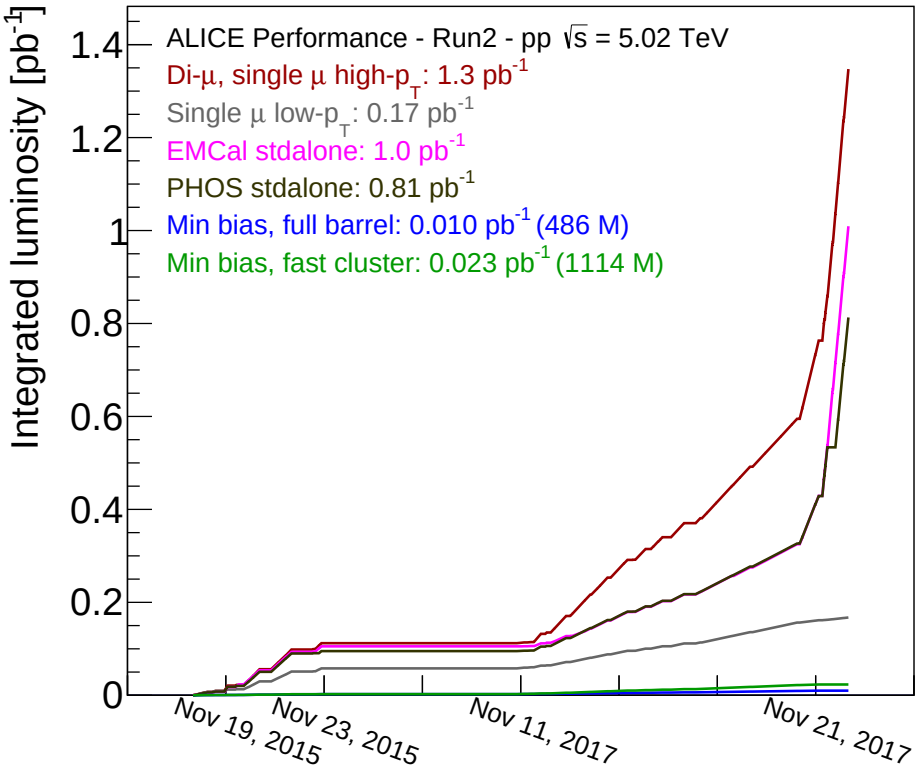

Fig. 2.24 Intergrated luminosity during Run 2 for pp collisions at $\sqrt{s} = 5.02$ TeV [140].

CHAPTER 3

Analysis Details

In this chapter, the analysis details are discussed. This chapter starts with a discussion on the ALICE Offline framework, which includes event simulation and reconstruction. This is followed by a description of the analysis framework and focuses on the selected data sample and associated selection criteria.

In the subsequent section, multiplicity measurements are discussed, based on the two approaches followed, namely, the "Official Framework" developed by the ALICE central multiplicity analysis group [56] and the data-driven method. The section thereafter focuses on the steps taken to obtain the muon yields measured in the spectrometer taking into account all muon sources, i.e. the application of muon track cuts applied on the data sample after event selection and the normalization to minimum bias to eventually get the cross-section. This is necessary since the muon-triggered sample analysed in this study constitute only a fraction of minimum bias events.

The acceptance and efficiency correction of the detector is discussed next. This correction needs to be taken into account as the efficiency of the detector decreases during data taking. This correction factor is used to ensure that the data analyzed relates to the true number of muons measured.

The next-to-last section focuses on the different background contribution sources of single muons for which the corresponding background fractions are determined. Finally, the chapter concludes with a section devoted on a discussion of the different systematic

uncertainties contributing towards the results.

3.1 The ALICE Offline Framework

The ALICE Offline project was developed in 1998 as a simulation tool to be used for the Technical Design Report (TDR) [141] for the ALICE detector. At the start of the development of the project, the object-oriented (OO) programming technique and C++ were used as the implementation language.

It was later decided to use ROOT [142] as the framework and GEANT 3.21 [143] as the simulation code. ROOT is an object-oriented program and library that was designed at CERN to be utilized by particle physicists for data analysis. The program contains several features to be used in the particle-physics field. However it can also be used in astronomy and data mining [142]. GEANT is a Monte Carlo transport code used to simulate the passage of particles through matter. The toolkit is used in high energy, nuclear and accelerator physics.

The ALICE offline framework, known as AliRoot [144], is a framework for simulation, reconstrunction and analysis built on the ROOT framework. For simulations, it utilizes Geant4 [145] or FLUKA [146] packages to perform particle transport simulations through the detector and energy deposition simulations. There is an exception for large existing libraries that remain in the legacy code like PYTHIA [147] and HIJING [148]. AliPhysics contains the analysis code that uses the ROOT system.

Event Simulation and Reconstruction

The simulation framework is responsible for a number of considerations within the ALICE offline framework like simulating the: primary collisions, emerging particles, energy deposition (hits) in the detector components, their individual responses that are stored in summable digits, and the generation of digits from summable digits with optional merging of underlying events and creation of raw data.

Monte Carlo generation is used to reproduce the detector response by generating hits that are then stored as digits from which raw simulated data are created. In the reconstruction phase, the real or simulated data are reconstructed to retrieve information of the particles detected [149].

Analysis Framework

The analysis framework is designed in such a way that it relies directly on the ROOT framework facilities. ROOT tasks are used to implement the analysis train by reading one

event into memory and thereafter passing through different analysis tasks linked to each other like wagons of a train. In Run 1 and 2, ALICE had two different kinds of analysis objects; the Event Summary Data (ESD) and the Analysis Object Data (AOD).

The **Event Summary Data (ESD)** is a data format where data are generated by the ALICE raw data reconstruction software. It contains a list of reconstructed tracks/particles and global event properties. The **Analysis Object Data (AOD)** is produced by the analysis task that is specific to a given set of physics objectives. They are the main source for physics analysis and are smaller in size compared to the ESDs [150]. Files named **AliAOD.Muons.root** are specifically created for the muon analysis. These events are reconstructed specifically for the physics performed with the muon spectrometer. Another type of file that is created is the **AliAOD.root** file. This file is larger in size than the AliAOD.Muons.root file as it contains more information and also event reconstruction in other detectors. Both these files are used in this thesis for the data analysis.

The analysis tasks used in this study can be accessed via https://github.com/Joyful-Elma/Analysis-files

3.2 Data sample for the analysis

For this thesis work, the data sample analyzed was collected in 2015 and 2017 in pp collisions at $\sqrt{s} = 5.02$ TeV. Specific AODs filtered for MUONs from the general purpose reconstructed data were used for the analysis. Events used in this analysis were collected for the following triggers for which a detailed description was given in Chapter 2:

- CMSL7-B-NOPF-MUFAST (MSL) - low-p_{T} single muon trigger
- CMSH7-B-NOPF-MUFAST (MSH) - high-p_{T} single muon trigger
- CINT7-B-NOPF-MUFAST (MB) - Minimum Bias trigger

In this section, details on the data sample and the event selection under study is given.

3.2.1 Data Sample

The runs used in the data analysis all had to pass the Quality Assurance (QA) checks. The criteria for the QA checks are summarized in Table 3.1.

Table 3.2 shows a summary of the total number of runs, total number of MSL, MSH and MB triggered events for each period.

Each raw event sample needs to be refined by applying certain selection cuts to it. There

Period:	LHC17p, LHC17q, LHC15n
Run type:	Physics
Beam mode:	Stable
Trigger detectors:	At least muon trigger
Readout detectors:	At least muon tracking, muon trigger and SPD
Run quality:	Good for readout detectors
Run duration:	$\geq$ 10 minutes

Table 3.1 Quality Assurance (QA) criteria.

Period	Runs	MSL events	MSH events	MB events
LHC17p	38	61.4M	7.7M	11.1M
LHC17q	13	6.5M	11.97M	1.81M
LHC15n	25	34.8M	1.67M	5M

Table 3.2 Summary of runs MSL, MSH and MB triggered events for data samples analysed.

are three offline selection cuts that are applied and these are discussed in detatil in the next subsection.

3.2.2 Event Selection

Offline selection cuts are necessary for selecting interactions with the highest possible efficiency while rejecting any background that is either machine-induced and/or physical. The three offline selection cuts used to refine the event sample are: physics selection, trigger selection and the reconstructed vertex (good vertex).

- **Physics selection** is used to reject machine-induced background caused by the interaction of beam particles with the residual gas or the mechanical structure of the beam-pipe.
- **Reconstructed vertex** considers events originating only from the primary vertex and inside the acceptance of the SPD, $|z| < 10$ cm, which allows for an accurate measurement of the charged-particle density and $\mathbf{N_{contributors}} > 0$ which eliminates tracklets with zero multiplicity. $N_{contributors}$ is the number of events that contribute to the multiplicity tracklets.
- **Trigger selection**, the data sample considered in the analysis consists of MB, MSL and MSH triggered events.

A summary of the total number of events after applying the physics selection, trigger

selection and reconstructed vertex cuts on the data sample is given in Table 3.3. A comparison can be made with Table 3.2 that shows the number of events before event selection. Figure 3.1 shows the evolution of events after each applied cut for the LHC17p data sample, a similar trend is observed in the LHC17q and LHC15n data samples. A summary of how each cut removes non-interesting events is shown in appendix A.2. The number of MB events is expected to be more than the MSL and MSH events, however this is not the case. These differences can be attributed to the physics of interest during data taking. For the LHC17p, LHC17q and LHC15n data samples, there is a downscaling to 0.410%, 0.003% and 0.010% of the MB events, respectively. Moreover, referring back to Fig. 2.24 in the previous chapter, it is evident from the integrated luminosity that the physics of interest was single muon high-p_{T} and then single muon low-p_{T} events.

	MB	**MSH**	**MSL**
LHC17p	9 522 946	6 808 855	5.452467×10^7
LHC17q	1 607 112	1.08007×10^7	6 099 882
LHC15n	485 210	1 495 153	3.1603659×10^7

Table 3.3 Summary of Event Selection.

The next section gives details on the multiplicity measurements, employing two methods to determine the multiplicity axis of the final result of self-normalized yield versus charged-particle multiplicity.

3.3 Multiplicity Measurements

There are two methods that can be used for the analysis of multiplicity; the "Official Framework" method developed by the ALICE central multiplicity analysis group [56] and the data-driven method. In this thesis, both methods will be discussed and the results will be compared to each other. The data-driven method will be discussed first in subsection 3.3.1 while the "Official Framework" for multiplicity measurements will be discussed in subsection 3.3.2.

3.3.1 Data-driven method

In this section, the determination of the charged-particle multiplicity using the estimator at midrapidity is discussed. The goal is to obtain an estimator that allows to classify events that will be used later to study the correlation between HFM production and charged-particle multiplicity. The procedure followed is discussed in previous studies [131]. The acceptance of the SPD is reduced due to dead regions. The data-driven method is used as

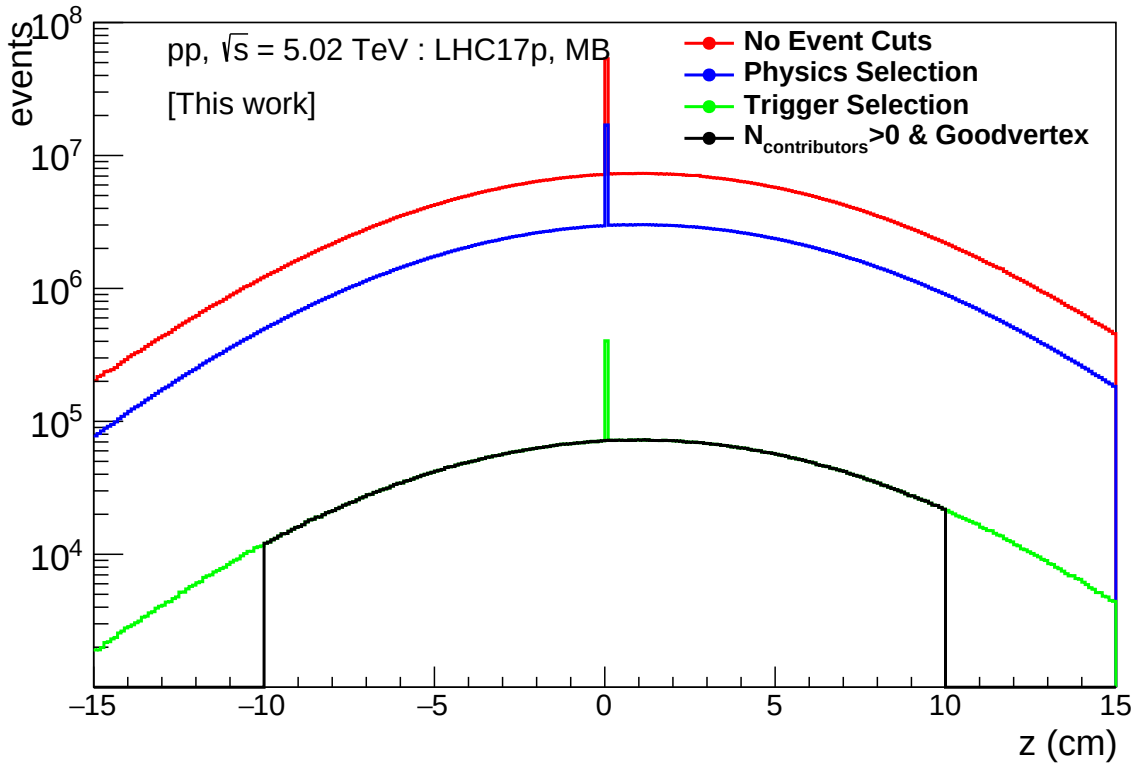

(a) MB Vertex Distribution showing the evolution of the event selection cuts

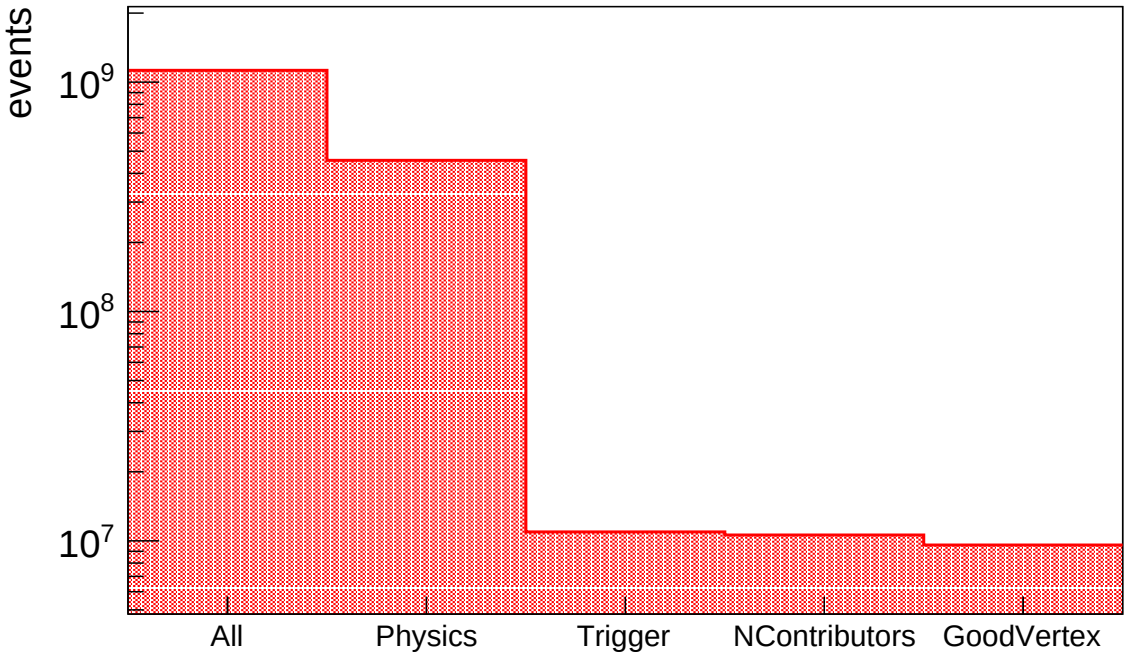

(b) Histogram showing number of events after every event selection cut

Fig. 3.1 Illustration of the event selection cuts for the MB trigger of the LHC17p data sample.

it does not require the use of MC simulations to correct for the dead regions in the SPD. The data-driven method is also used as it takes into account the pile-up factor which is required to account for the detector response during data taking.

As already defined, the pseudorapidity density ($\frac{dN_{ch}}{d\eta}$) is the average number of charged particles produced in a defined η region. The aim of this section is to determine $\frac{dN_{ch}}{d\eta}$ using information obtained from the SPD. The MB trigger is used to obtain the $\frac{dN_{ch}}{d\eta}$ estimator.

3.3.1.1 Multiplicity Estimation

The multiplicity estimation procedure starts with the discussion of the time dependence of the SPD conditions. This is followed by the presentation of the raw tracklet distribution obtained from the SPD. The multiplicity correction is discussed next and thereafter a comparison of the data and Monte Carlo productions is made. A description on the procedure to convert the raw tracklets to charged particles follows and the final results are presented to conclude the section.

The event selection is necessary before the multiplicity estimation procedure. The following multiplicity cuts were applied to the data sample:

- $N_{contributors} > 0$ - this cut eliminates zero multiplicity tracklets.
- $\sigma_z^{SPD} < 0.25$ cm - this is the resolution of the SPD vertex, it ensures an accurate estimation of charged particles measured per event.
- $|Z_{vertex}| < 10$ cm - this is the vertex position from the IP where events of the analysis are selected.
- $|\eta| < 1$ - indicates the kinematic region where only charged particles within this cut are considered.

Time dependence of SPD conditions

The SPD vertex and tracklets are necessary in the muon triggering and reconstruction of muon tracks in the muon spectrometer. There are two approaches that can be used to describe the SPD vertex and tracklet reconstruction [151].

- The first approach is the 3D vertex. This approach involves reconstructing the x, y, and z position of the interaction vertex. This method is dependent on the multiplicity, which in turn results in the resolution increasing with multiplicity. The tracklet candidates are reconstructed by connecting points identified between the two SPD layers. To calculate the coordinates of the pairs with the crossing point in the reference interaction region, a distance of closest approach (DCA) cut is applied on the tracklets. By using the distributions of the coordinates of the individual crossing

points, the coordinates of the vertex are determined. The displaced tracklets from the first vertex reconstruction are removed by performing a second reconstruction. A recomputation of the coordinates of the vertex is performed on the remaining tracklets [124, 151, 152].

- A second approach that can be used is the 1D vertexer. The 1D vertexer uses the z-coordinate of the SPD vertex for reconstruction. The x and y coordinates are measured online and thereafter stored in the Offline Condition Database (OCDB), the stored coordinates are then used to extract the x and y coordinates of the tracklet. For each candidate tracklet i, the intersection point z_i with the beam axis and the corresponding error σ_i are calculated. By assuming that z_i follows a Gaussian distribution, an estimation of the z-vertex coordinate $\langle z \rangle$ from all tracklets N_{trk} is computed around the region of the peak [152].

  The $\langle z \rangle$ vertex is computed using the following expression:

$$\langle z \rangle = \frac{\sum_{i=1}^{N_{trk}} \frac{z_i}{\sigma_i}}{\sum_{i=1}^{N_{trk}} \frac{1}{\sigma_i}} \tag{3.1}$$

  An iteration on the value of $\langle z \rangle$ is performed until all the tracklets considered are coming from a symmetric region around the mean value $\langle z \rangle$.
  By correlating the SPD vertex with a cluster in both layers, the SPD tracklets can be reconstructed. This approach considers drawing a straight line from the vertex to a cluster in the inner layer and a straight line from the vertex to a cluster in the outer layer. From the two lines drawn, as shown in Fig. 3.2, the difference in the azimuthal ($\Delta\varphi$) and polar angles ($\Delta\theta$) is calculated. Only $\Delta\varphi$ and $\Delta\theta$ values that fall within the small azimuthal window from the interaction point are accepted [152].

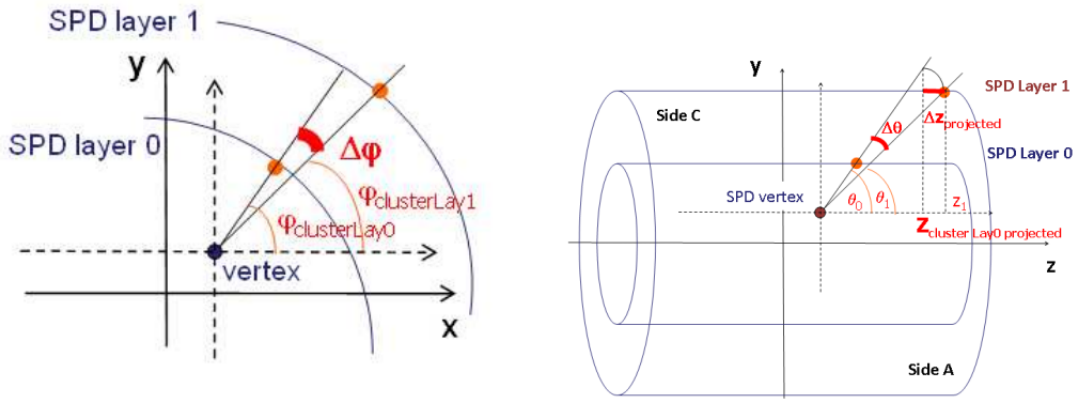

Fig. 3.2 Schematic diagram of tracklet reconstruction approaches [124, 152].

The analysis of SPD tracklets provides the information required to perform multiplicity measurements. To reconstruct the tracklets, information from the two layers (inner and outer layers) of the detector is used in conjunction with the main SPD vertex position. Since the tracklet information is dependent on the inner and outer layer of the SPD, it is important to take the status of the SPD modules during data-taking into consideration. The acceptance and the efficiency of the SPD is reduced by dead regions of the SPD modules. It is therefore important to monitor and consider the number of active SPD modules per run for all of the run periods being considered.

Sub-figures 3.3a, 3.3b and 3.3c show the number of active SPD modules in the inner and outer layers as a function of the run number during the LHC17p, LHC17q and LHC15n run periods, respectively. The number of active modules for the three run periods is summarized in Table 3.4.

Run period	Active modules inner layer	Active modules outer layer
LHC17p	80/80	180/180
LHC17q	80/80	180/180
LHC15n	68/80	168/180

Table 3.4 Summary of number of active SPD modules in the inner and outer layers during data-taking.

There are 80 SPD modules in the inner layer and 180 in the outer layer. A preferred data taking period is one where all the SPD modules are active. For the LHC17p and q periods, this was the case as all the SPD modules were active in both the inner and outer layers. However, for the LHC15n data sample, not all the SPD modules were active during the data-taking period, this could be a result of some of the modules being dead during the data-taking period.

The next section will be devoted to the discussion of the raw tracklet distributions using information obtained from the SPD.

Raw tracklet distributions

With the statistics available during Run 2 in pp collisions at $\sqrt{s} = 5.02$ TeV, the multiplicity of 100 tracklets can be barely reached. Figure 3.4a shows the raw tracklet distributions for the minimum bias (MB) trigger events. In principle, the physical properties of the events are expected to not change with the position where the events need to be reconstructed. As a result, a flat average value is expected for a detector that has no inactive areas and a homogeneous efficiency. As observed in Fig. 3.4b, the distribution is clearly not flat. In fact, there is a drop in the distribution for $|z| \gtrsim 6$ cm. This drop can be

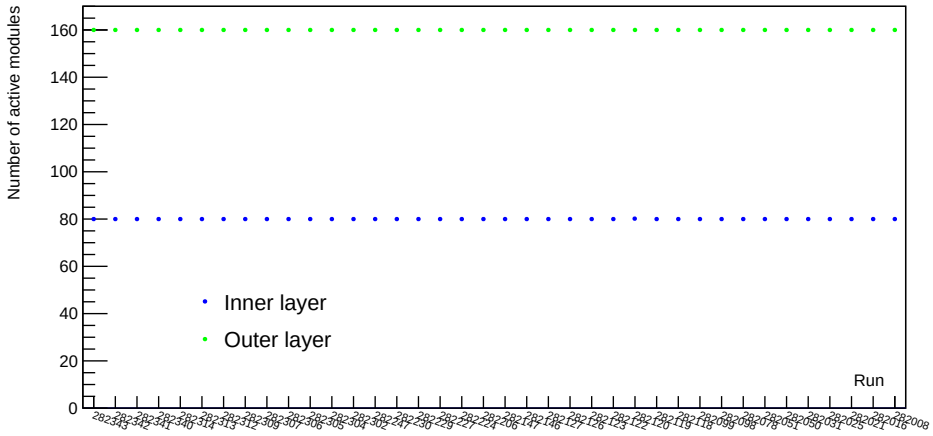

(a) Number of active SPD modules for run period LHC17p.

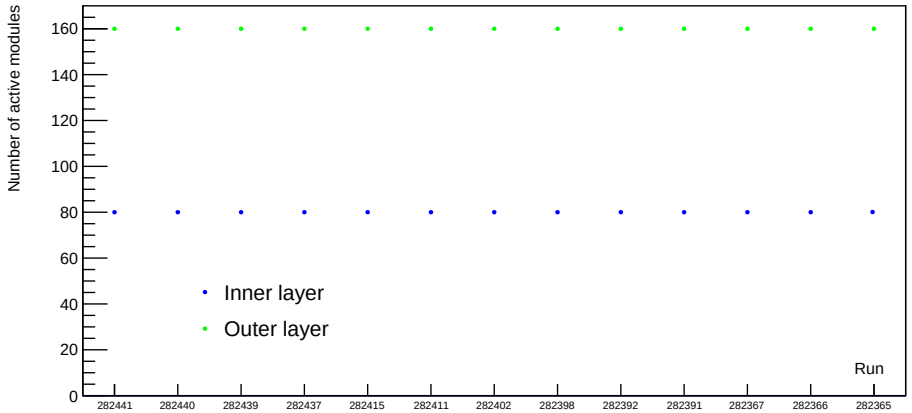

(b) Number of active SPD modules for run period LHC17q.

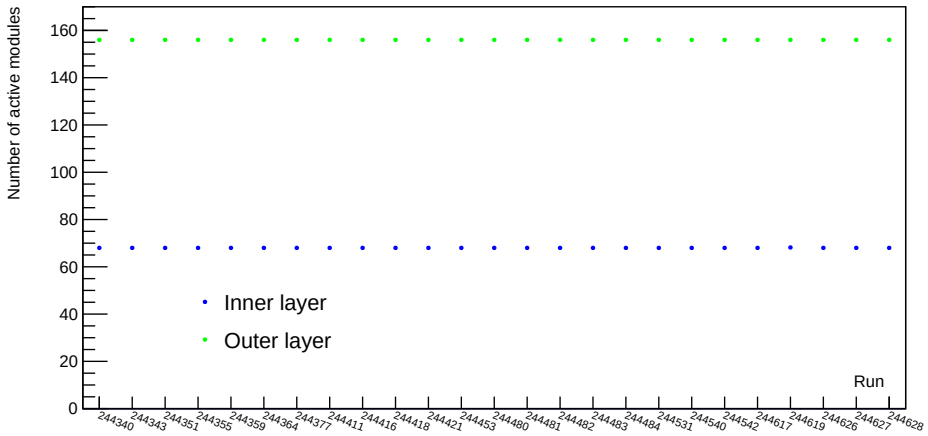

(c) Number of active SPD modules for run period LHC15n.

Fig. 3.3 Number of active SPD modules

attributed to the tracklets at the edge of the acceptance of the SPD. This is observed for all the data samples in this analysis. For the LHC15n data sample, as already indicated in section 3.2.1, due to the lack of statistics, the error bars are visibly large as shown in Fig. 3.4b.

Figures 3.5a, 3.5b and 3.6 show the 2D distribution of the multiplicity versus the SPD z-vertex for the LHC17p, LHC17q and LHC15n data samples, respectively, this gives a visual of the non-uniformity of the average tracklets. This is indicative of the dependency of the tracklets on the SPD z-vertex.

In order to get rid of this dependency, the average tracklet multiplicity will need to be corrected to obtain a flat distribution as expected. The next section will be dedicated to the multiplicity correction.

Multiplicity Correction

As mentioned previously, the average tracklet multiplicity as a function of the SPD vertex shown in Fig. 3.4b is expected to have a flat average, however that is not the case. A correction, which is used in previous measurements is employed [131]. This correction aims to equalize the SPD efficiency along the z-vertex to obtain a flat distribution. The efficiency loss of the detector is corrected for the event multiplicity, which is done with respect to a reference region on an event by event basis. The reference region can be at the edge of the SPD acceptance where the average tracklets is minimum or where the average tracklet is a maximum as shown in Fig. 3.4b.

The correction makes use of ΔN, which is expressed as a product of the value of the raw tracklet multiplicity ($N^{raw}_{trkl}(z)$) and the relative difference of the average multiplicity ($\langle N_{trkl}(z)\rangle$) and the average multiplicity at some reference value $\langle N_{trkl}(ref)\rangle$ [131]. ΔN is expressed as:

$$\Delta N = N^{raw}_{trkl}(z) \cdot \frac{\langle N_{trkl}(z)\rangle - \langle N_{trkl}(ref)\rangle}{\langle N_{trkl}(z)\rangle} \tag{3.2}$$

where:

- $N^{raw}_{trkl}(z)$ is the raw tracklet multiplicity that will be corrected,
- $\langle N_{trkl}(z)\rangle$ is the average multiplicity
- and $\langle N_{trkl}(ref)\rangle$ is the average multiplicity at a reference z-vertex value.

The correction ΔN_{rndm} is generated randomly with a Poissonian distribution centered in ΔN. A Poissonian distribution is chosen because not only does it flatten the N^{corr}_{trkl} but can also equalize the resolution of the SPD along the z-vertex as shown in [153]. The number of missing tracklets with respect to the generated number of charged particles at

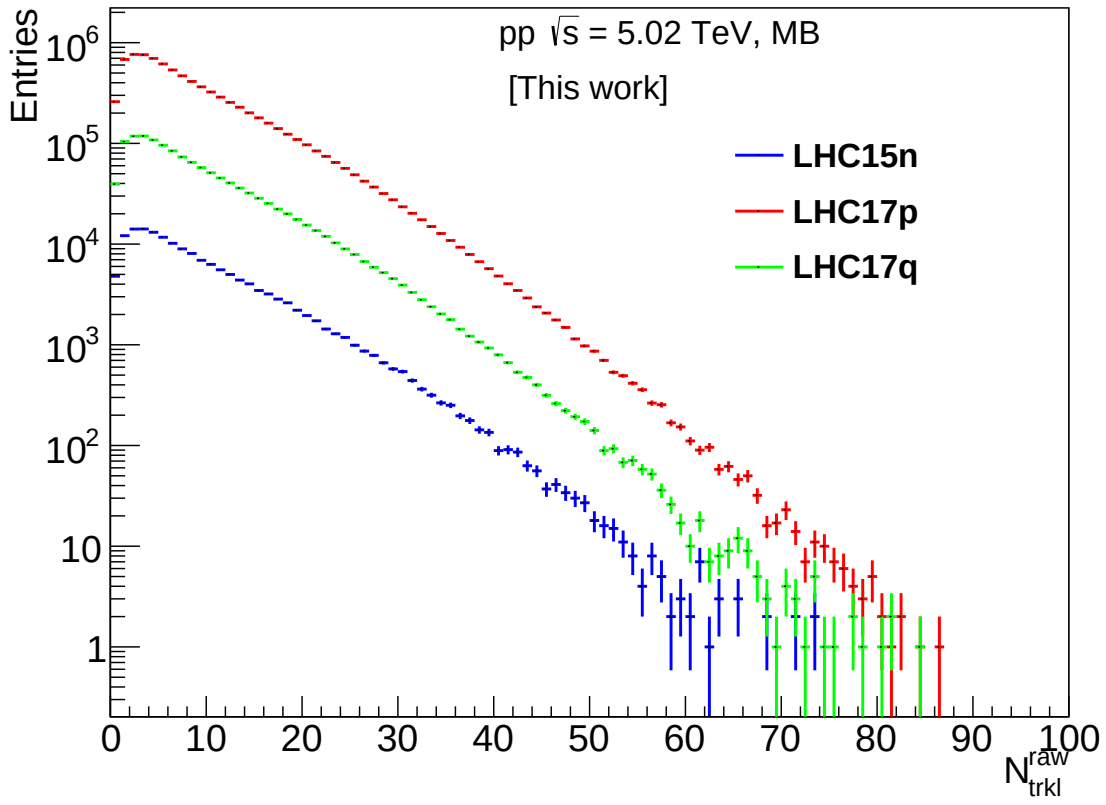

(a) Raw tracklet distributions for all the data samples.

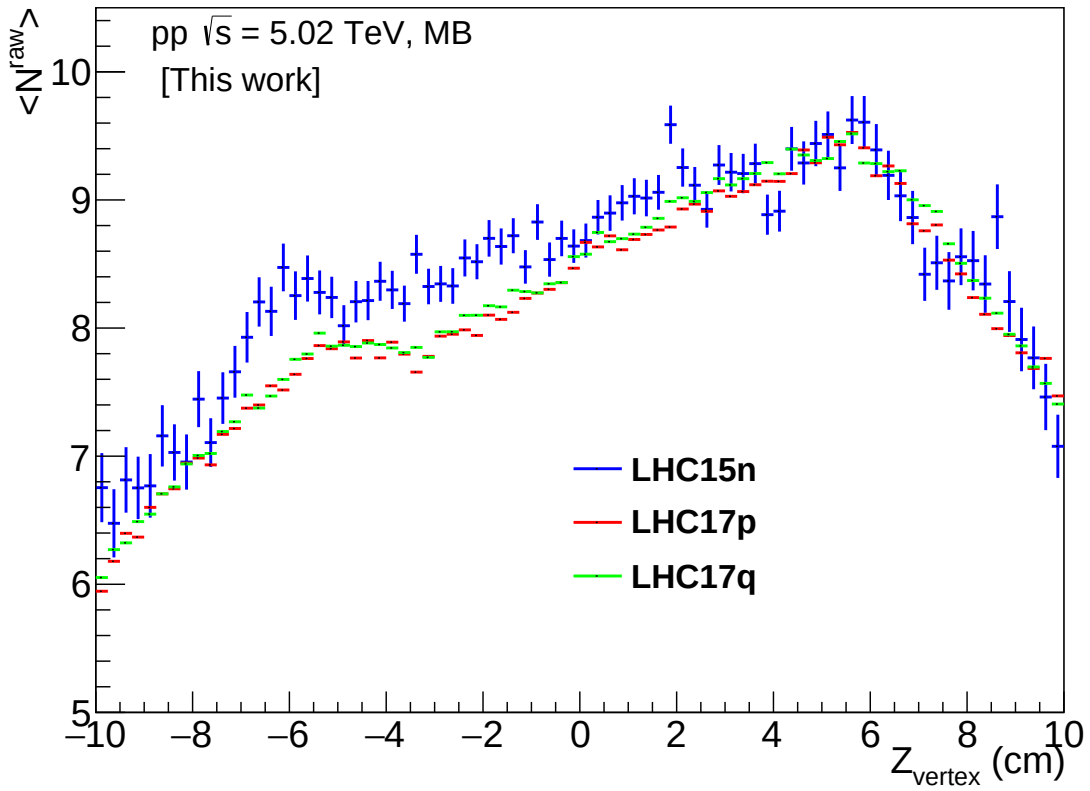

(b) Average tracklet distributions for all the data samples.

Fig. 3.4 Raw tracklet (3.4a) and average tracklet (3.4b) distributions.

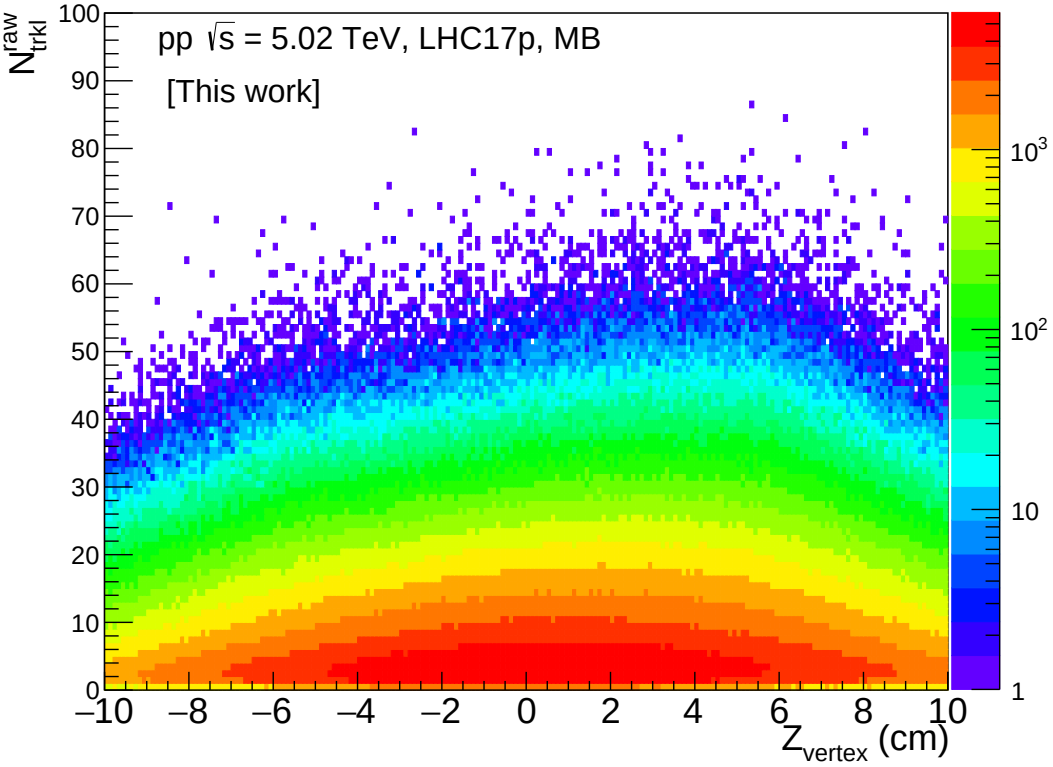

(a) 2D Distribution of multiplicity vs SPD z-vertex for the LHC17p data sample.

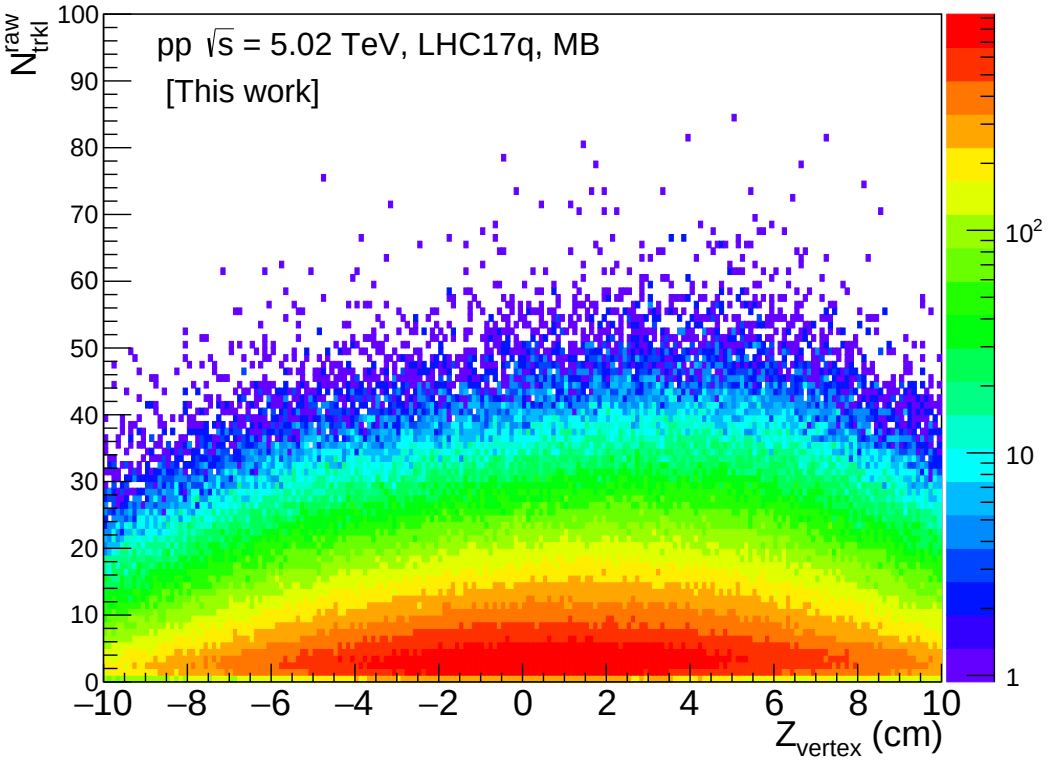

(b) 2D Distribution of multiplicity vs SPD z-vertex for the LHC17q data sample.

Fig. 3.5 2D Distributions of multiplicity vs SPD z-vertex for the LHC17p (3.5a) and LHC17q (3.5b) data samples.

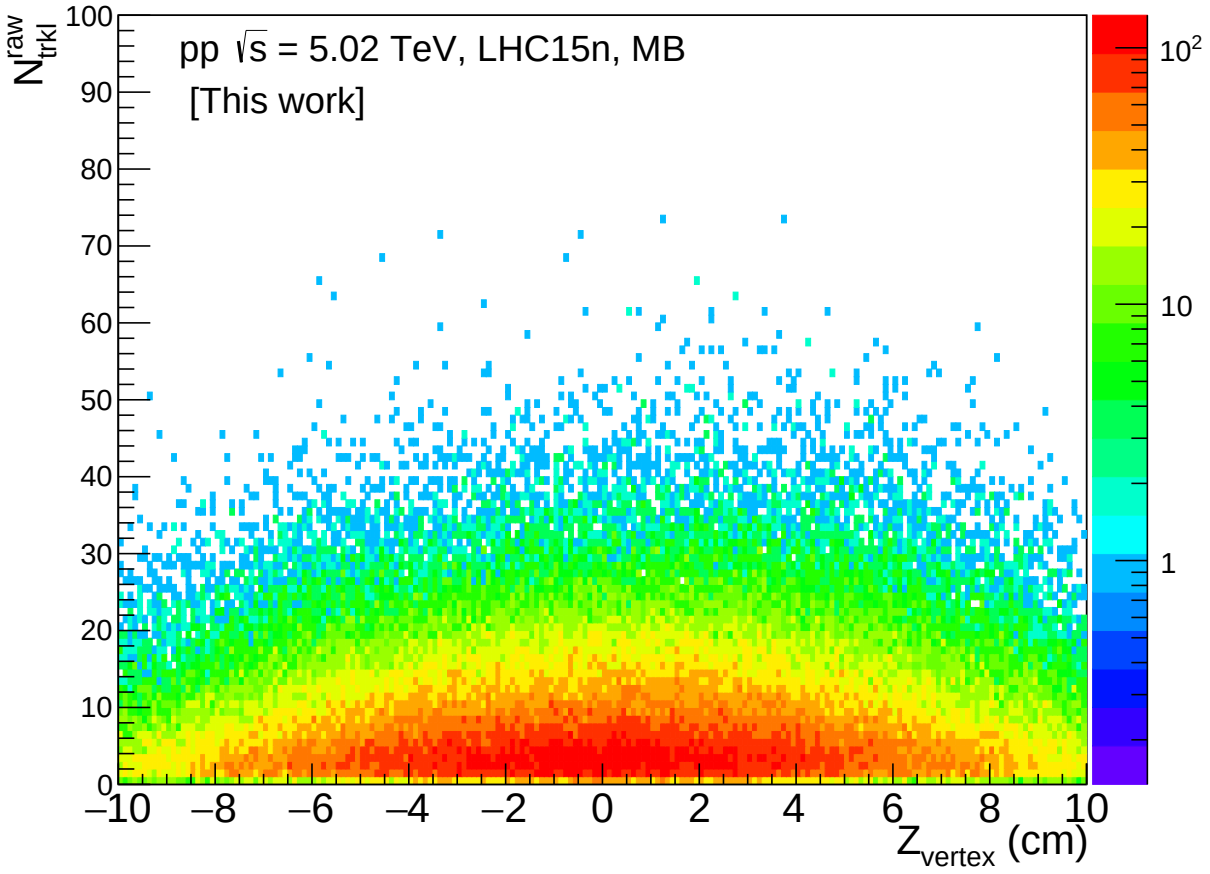

Fig. 3.6 2D Distribution of multiplicity vs SPD z-vertex for the LHC15n data sample.

a given z-vertex can be described by a Poissonian distribution as shown in [153].

The final number of the corrected tracklets is then given using the following expression:

$$N^{corr}_{trkl} = N^{raw}_{trkl}(z) + \Delta N_{rndm} \tag{3.3}$$

A choice of $\langle N_{trkl}(ref)\rangle = min(\langle N_{trkl}(z)\rangle)$ or $max(\langle N_{trkl}(z)\rangle)$ as a reference for the correction can be made. ΔN_{rndm} will be positive if the average multiplicity value is greater than the average multiplicity reference values, i.e. $\langle N_{trkl}(ref)\rangle = min(\langle N_{trkl}(z)\rangle)$; or negative if the average multiplicity value is smaller than the average reference values, i.e. $\langle N_{trkl}(ref)\rangle = max(\langle N_{trkl}(z)\rangle)$. A summary of the minimum and maximum reference values for all the data samples is given in Table 3.5. The minimum value is taken at position $z_{vertex} = -10$ cm and the maximum value at $z_{vertex} = 6$ cm.

In this analysis, $\langle N_{trkl}(ref)\rangle = max(\langle N_{trkl}(z)\rangle)$. This choice is made based on other analyses [131, 152] that use the maximum reference value for the correction; for consistency, the same is done for this analysis. In this study, the LHC17p and q data samples will be added together since they have the same data taking conditions. A discussion on the optimization of the reference value and results thereof is shown in Appendix B.0.1.

	LHC17p	LHC17q	LHC15n
Minimum reference value	6 cm	6 cm	6.5 cm
Maximum reference value	9.6 cm	9.6 cm	9.5 cm

Table 3.5 Summary of the minimum and maximum reference values for the different data samples

In Fig. 3.7 and 3.8, the minimum and maximum reference values were used for the correction of $N_{\text{contributors}} > 0$, which eliminates tracks with zero multiplicity. In figures 3.7a and 3.8a, a comparison of the raw tracklet distribution (red data points) to the corrected tracklet distributions is shown while the green data points are shown for the minimum reference value and blue data points for the maximum reference value. It is observed that the maximum reference value allows for a wider distribution and higher multiplicity reach. Figures 3.7b and 3.8b show the average tracklet distributions as a function of the z-vertex.

The number of SPD tracklets obtained is not the actual number of charged particles. To obtain the number of charged particles, the SPD tracklets need to be corrected by some factor α which will be discussed in the next section.

Comparison of MC productions and data

The number of SPD tracklets obtained is not the actual number of charged particles. However, the SPD tracklets can be approximated to be proportional to the actual number of charged particles [131];

$$N_{ch} = \alpha N_{trkl}, \tag{3.4}$$

where α is the efficiency of the SPD. Monte Carlo (MC) simulations can be used to determine the factor α. MC simulations generate events and count the number of charged particles produced (N_{trkl}^{gen}), for which an ideal detector is considered with a 100% efficiency. The generated events are then processed by a realistic simulation of the SPD and the number of charged particles detected by the SPD are counted. Table 3.6 shows a summary of the MC productions from the central production available on the ALICE Grid [154] used in this analysis. In the table, the MC production name is given with a description of what event generator is used, the number of runs used from data and the number of events generated in the production.

Before a MC production can be used to estimate the α factor, the production has to be checked for compatibility with the data. This is done by analyzing the MC production using the same procedure used for the data, as described in section 3.3.1.1. The LHC20a2 MC production was the only production available that best describes the data from the

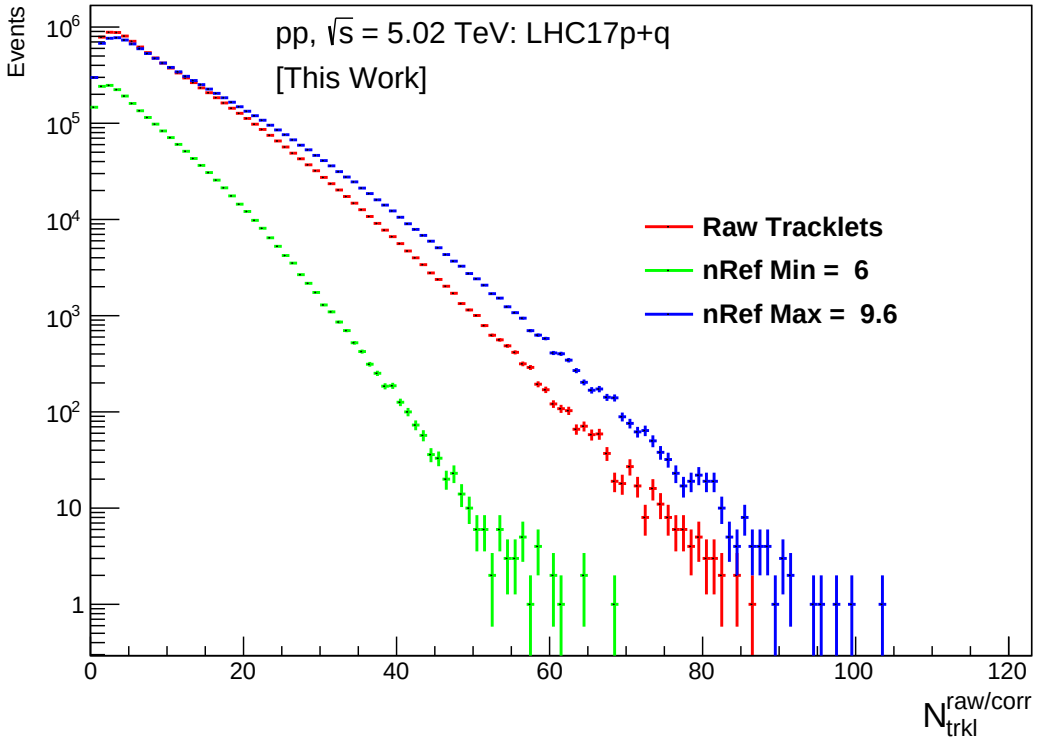

(a) Comparison of corrected tracklets using minimum and maximum reference values.

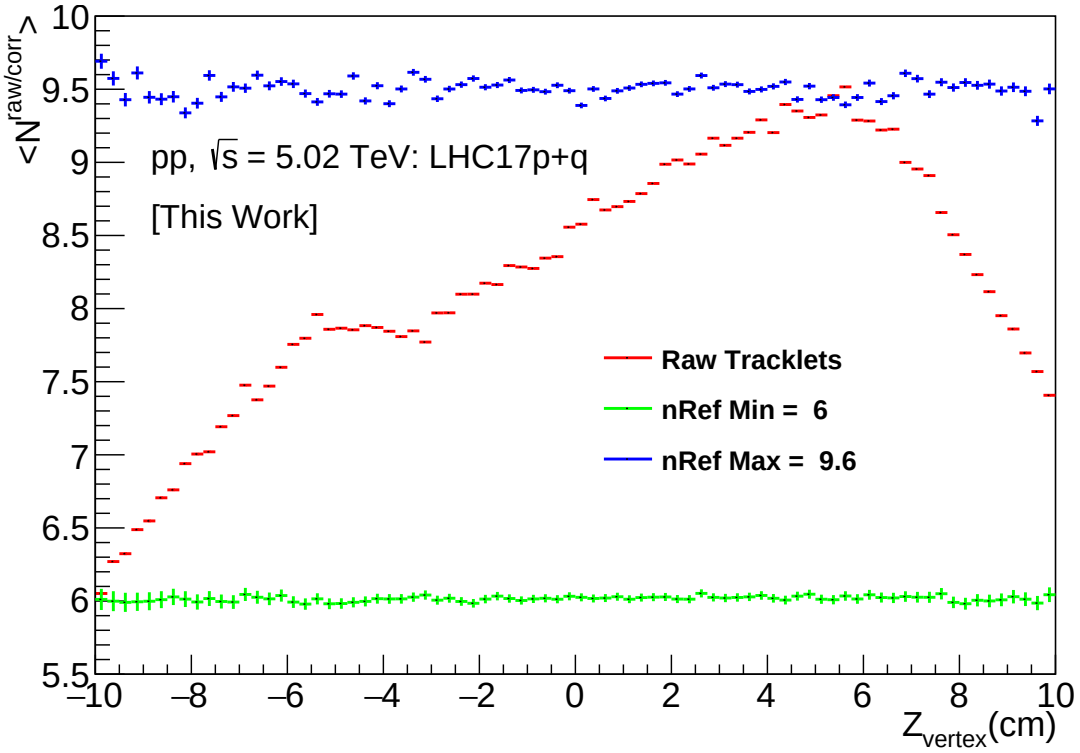

(b) Corrected average tracklets using minimum and maximum reference values.

Fig. 3.7 Comparison of corrected tracklets (3.7a) and corrected average tracklets (3.7b) for LHC17p data sample.

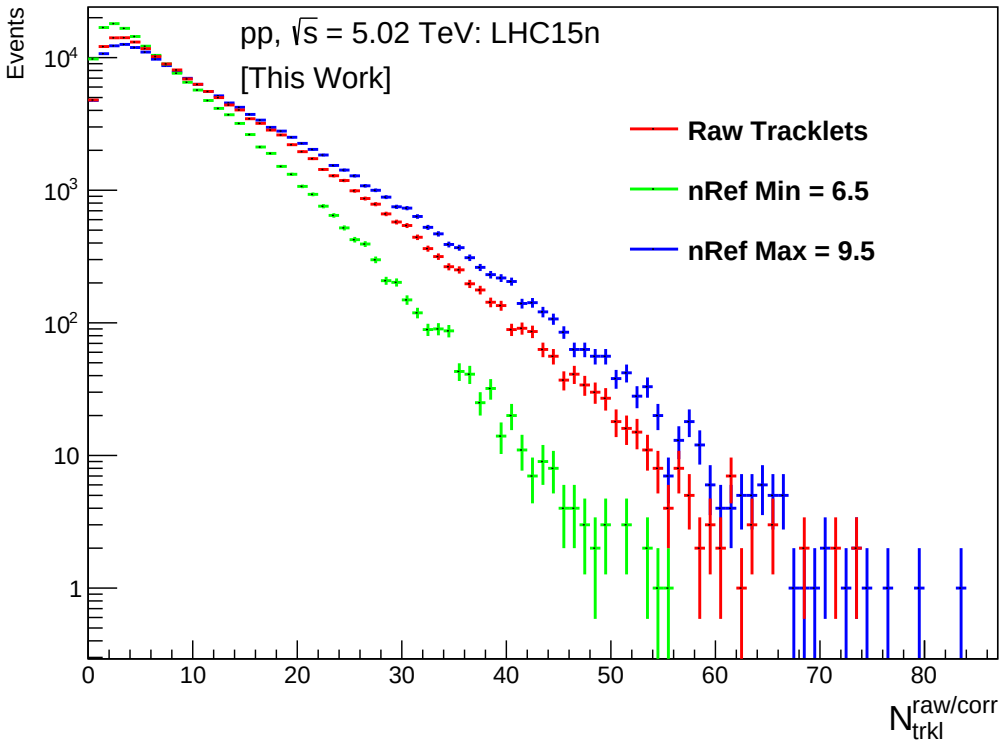

(a) Comparison of corrected tracklets using minimum and maximum reference values.

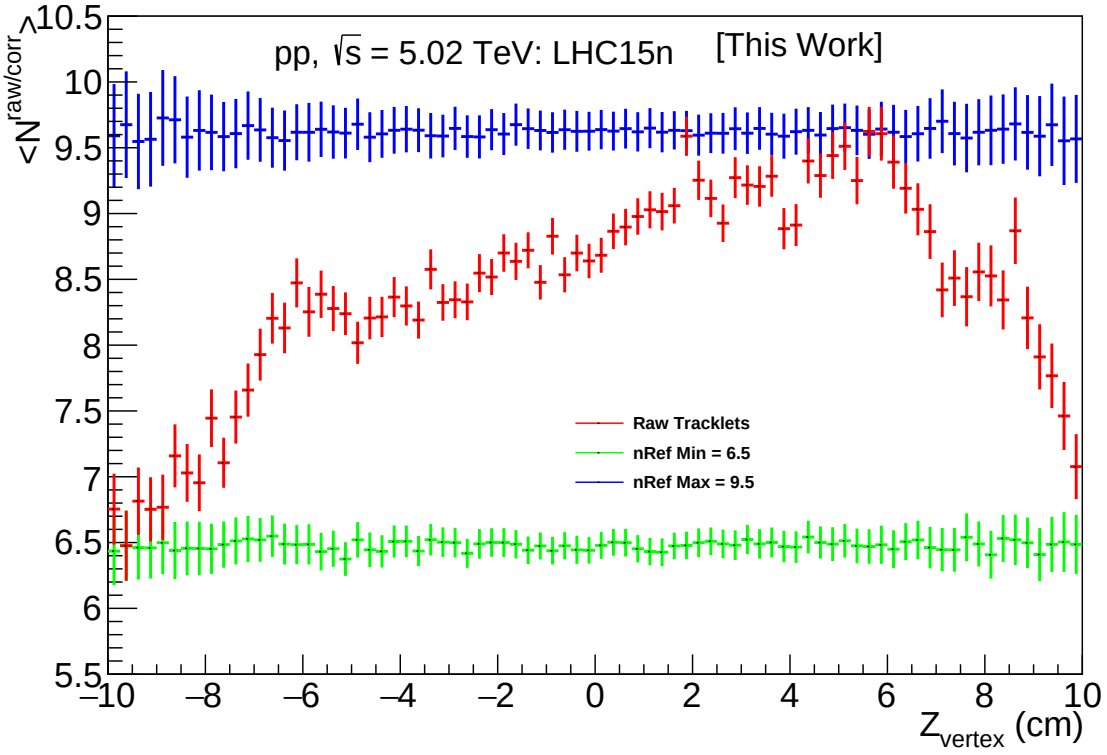

(b) Corrected average tracklets using minimum and maximum reference values.

Fig. 3.8 Comparison of corrected tracklets (3.8a) and corrected average tracklets (3.8b) for LHC15n data sample.

MC Production	Description	Runs	Event Count
LHC20a2 (LHC17p and q)	Muon EPOS	51	27 555 000
LHC17i7b (LHC15n)	PYTHIA8_Monash2013	1	521 600

Table 3.6 Summary of MC productions available on the ALICE Grid [154], in brackets is the data-taking period these are anchored to.

LHC17p and q run periods. This production makes use of the EPOS [67] theoretical model. For the LHC15n data sample, the LHC17i7b MC production was the only production that was the closest to describing the data, this production makes use of the PYTHIA [63] theoretical model.

Figures 3.9 and 3.10 show the correction with the minimum and maximum reference values for the LHC17p+q and LHC15n data samples, respectively. Figures 3.9a and 3.10a is a comparison of the raw tracklet distribution (black data points) to the corrected tracklet distribution shown by the green data points (min reference value) and blue data points (max reference value). Figures 3.9b and 3.10b show the average value of the tracklets as a function of the vertex. The mean profile distribution is shown by the black data points, the corrected average distribution shown by the green data points (min reference value) and blue data points (max reference value).

It is observed that the maximum reference value allows for a wider distribution and higher multiplicity reach as observed in the data. It can be concluded that the correction method described before works well for the MC generated events for both the min and max reference values. Generated tracklets in an ideal detector, represented by MC truth, are shown by the magenta data points for both the tracklet and average tracklet distribution. As expected, the number of generated tracklets are more than the reconstructed tracklets.

The raw tracklet distribution extracted from the MC production is compared with that extracted from the experimental data. The raw tracklet distribution from the MC production is simply the reconstructed tracklets obtained for the realistic simulation that takes into account the conditions of the SPD. A comparison of the N_{trkl}^{raw} between the data (black data points) and that obtained from the MC productions (red data points) is shown in Fig. 3.11 and 3.12 for the LHC17p+q and LHC15n data samples, respectively.

A comparison of the $\langle N_{trkl}^{raw} \rangle$ between the data (black), reconstructed (red) and generated (magenta) from MC productions is also shown in Fig. 3.11 and 3.12, but only the maximum correction is applied to the reconstructed data for the LHC17p+q and LHC15n data samples, respectively. It is observed that EPOS (PYTHIA) underestimates the data, which is especially evident after correcting for the maximum reference value as shown in the average profile in Fig. 3.11b and 3.12b. For these reasons, it is necessary to determine

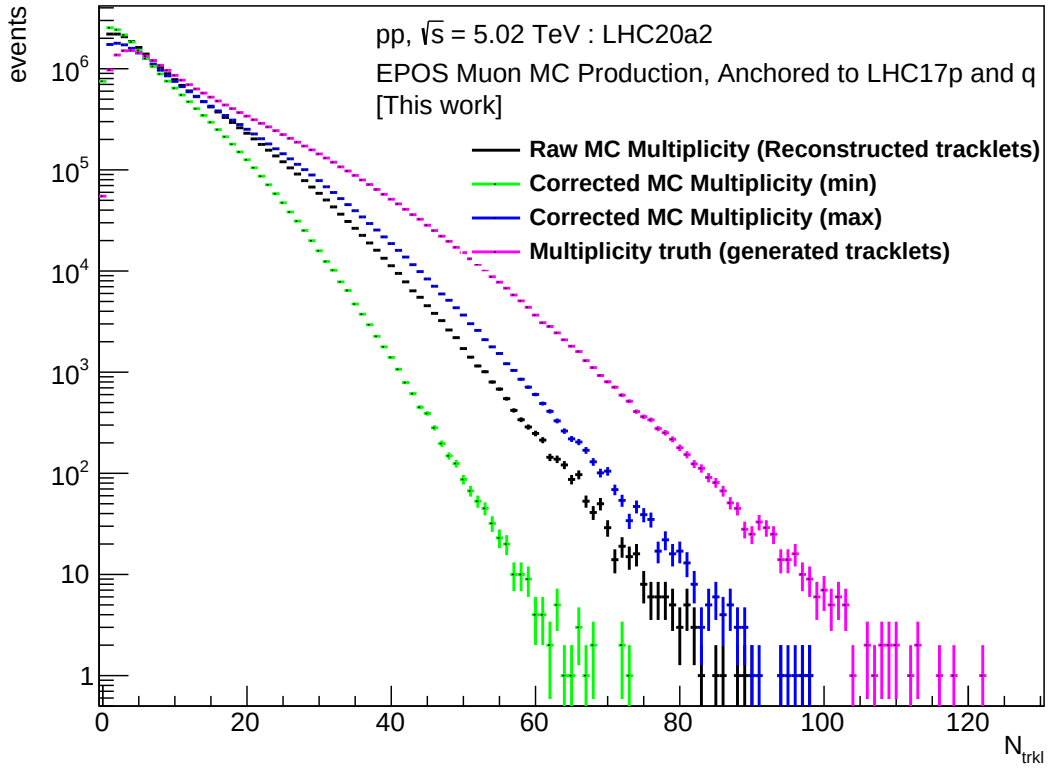

(a) Comparison of the tracklet distributions for the EPOS generator (LHC20a2).

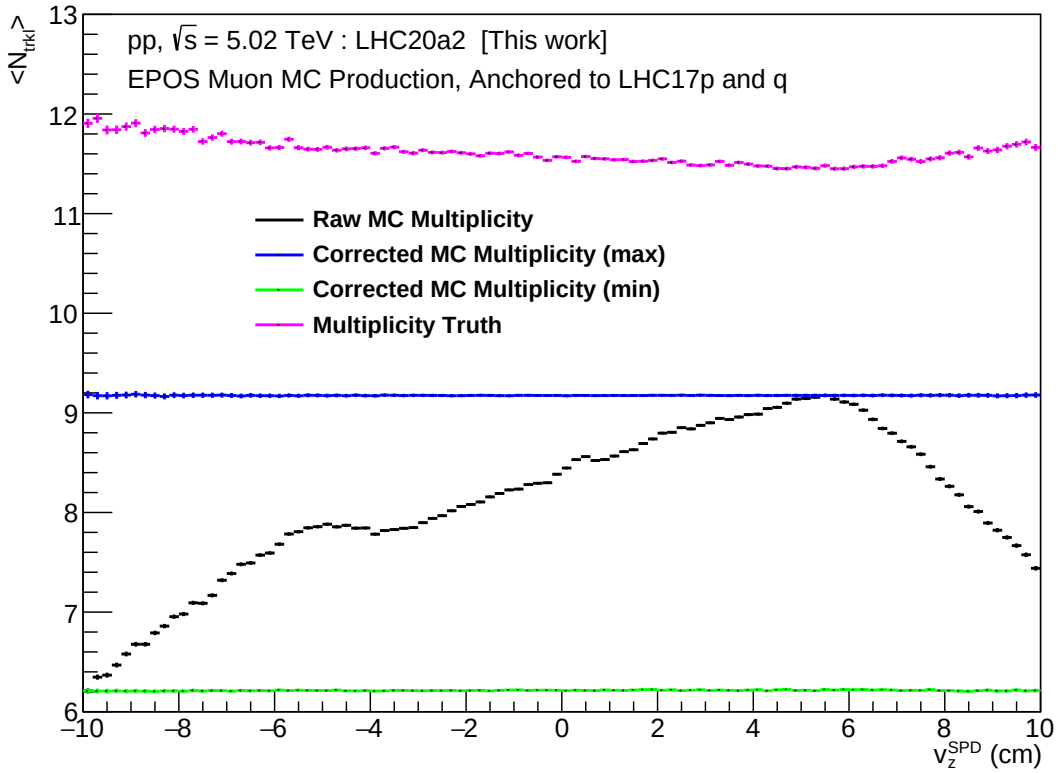

(b) Comparison of the mean tracklet distributions for the EPOS generator (LHC20a2).

Fig. 3.9 Comparison of the tracklet distributions (3.9a) and mean tracklet distributions (3.9b) for the EPOS generator (LHC20a2).

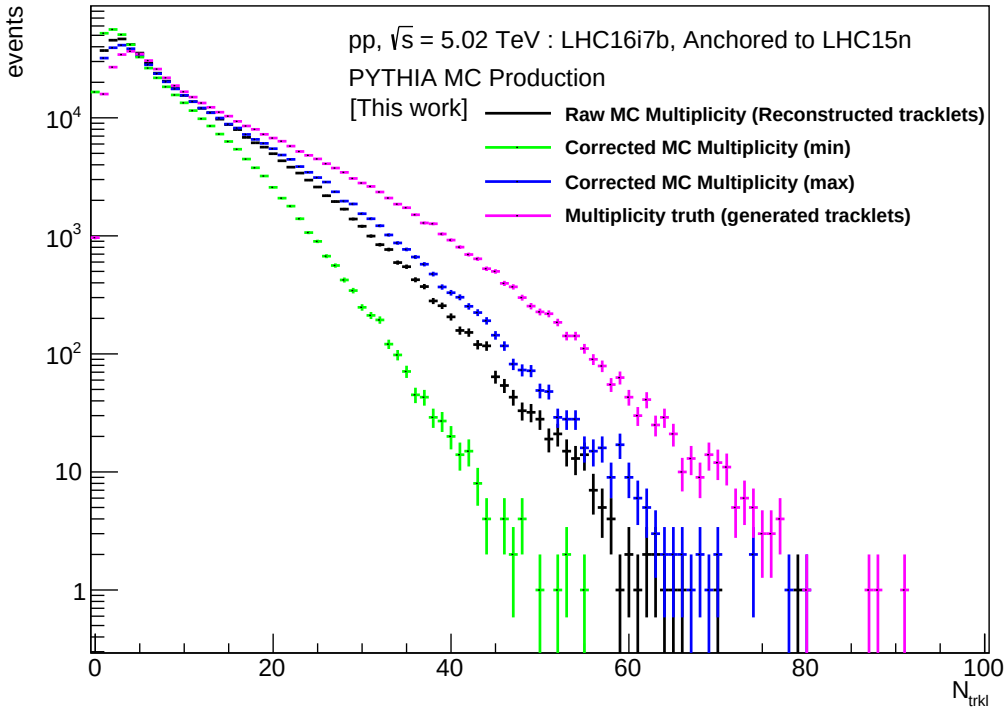

(a) Comparison of the tracklet distributions for the PYTHIA generator (LHC17i7b).

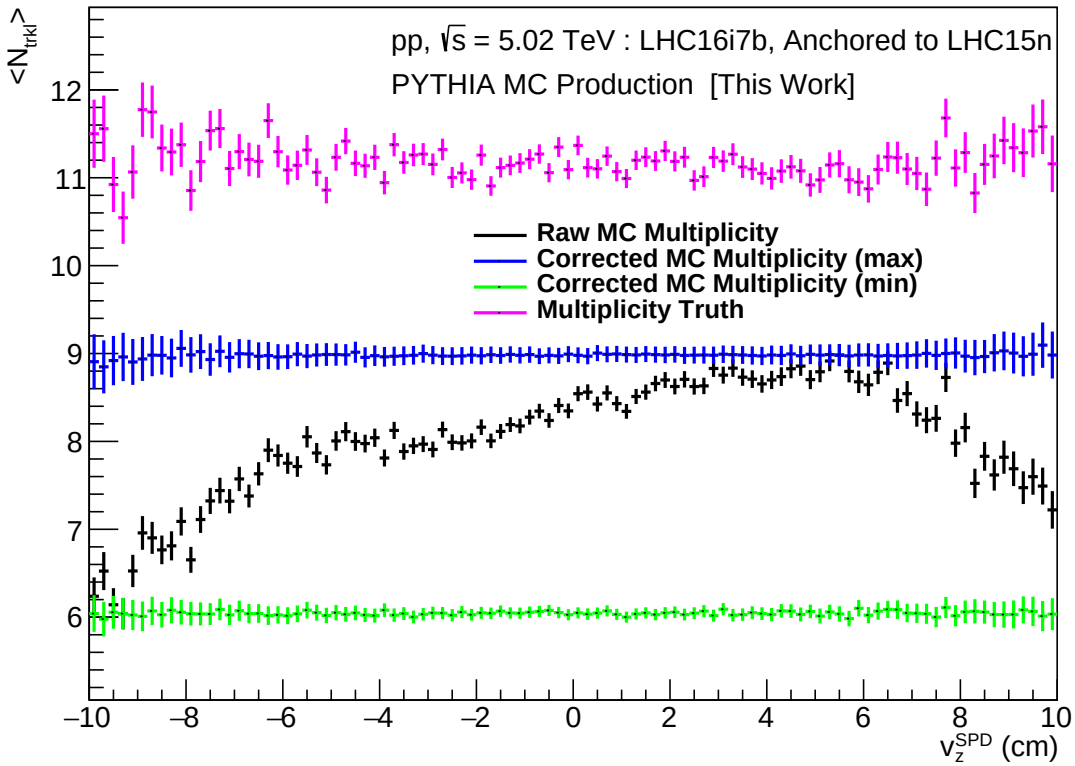

(b) Comparison of the mean tracklet distributions for the PYTHIA generator (LHC17i7b).

Fig. 3.10 Comparison of the tracklet distributions (3.10a) and mean tracklet distributions (3.10b) for the PYTHIA generator (LHC17i7b).

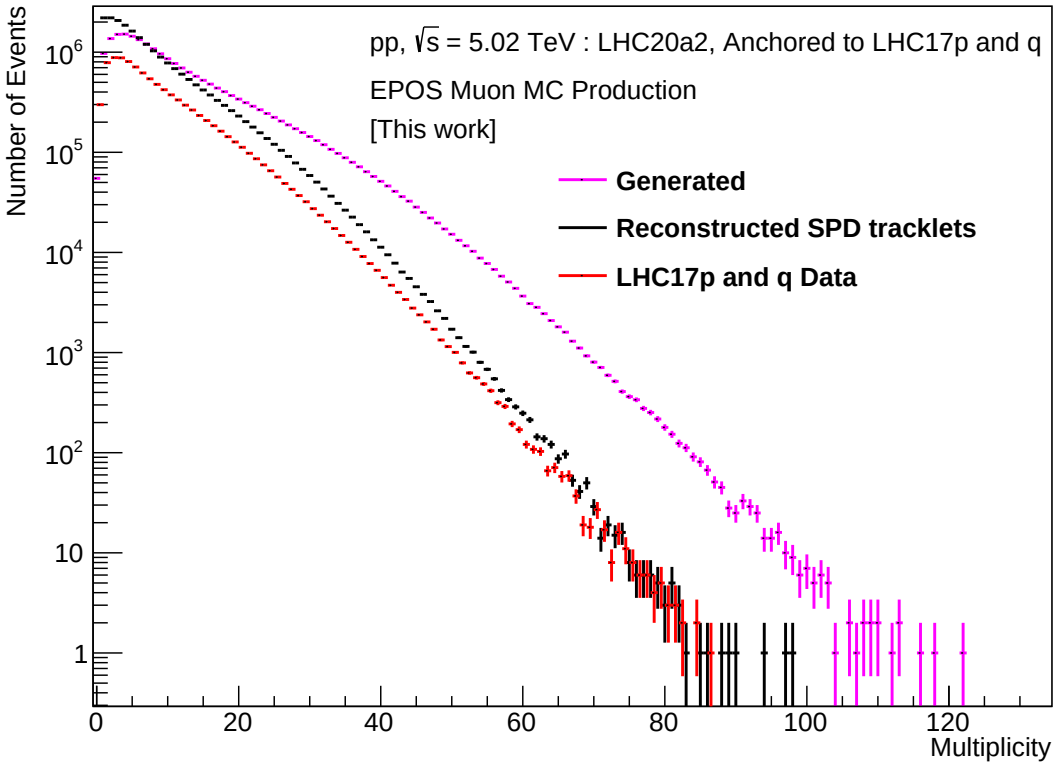

(a) Comparison of raw and tracklet distributions from data and MC production.

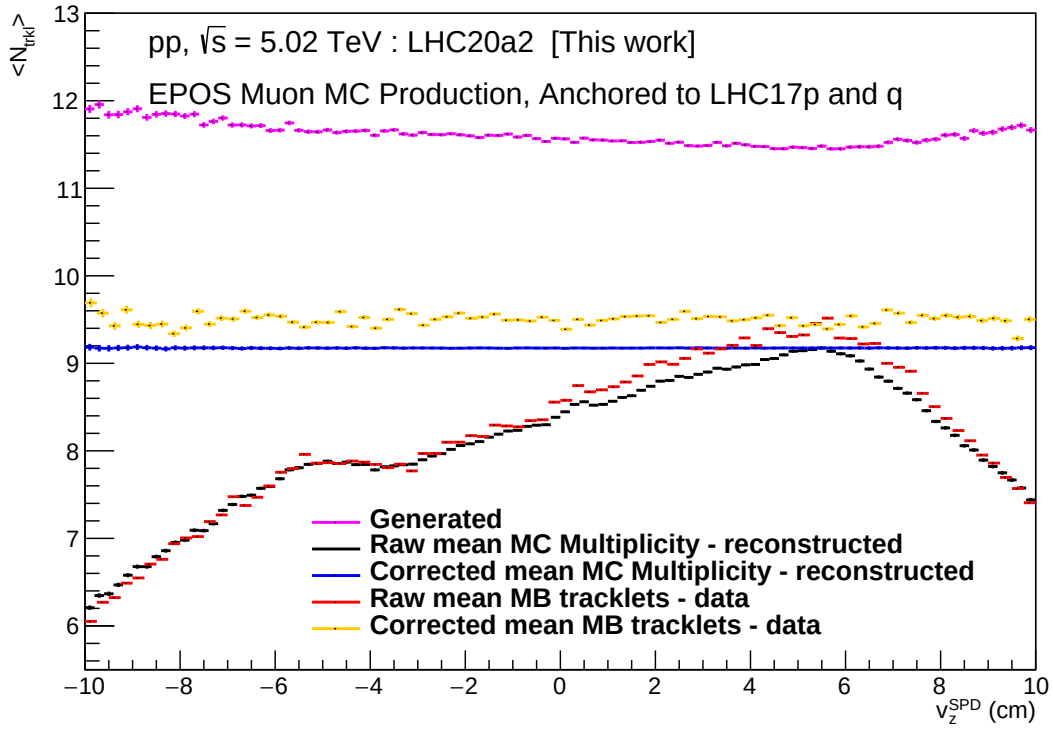

(b) Comparison of the average tracklet distributions for data and MC production.

Fig. 3.11 Comparison of raw tracklet distributions from data and MC production (3.11a) and the average tracklet distributions (3.11b).

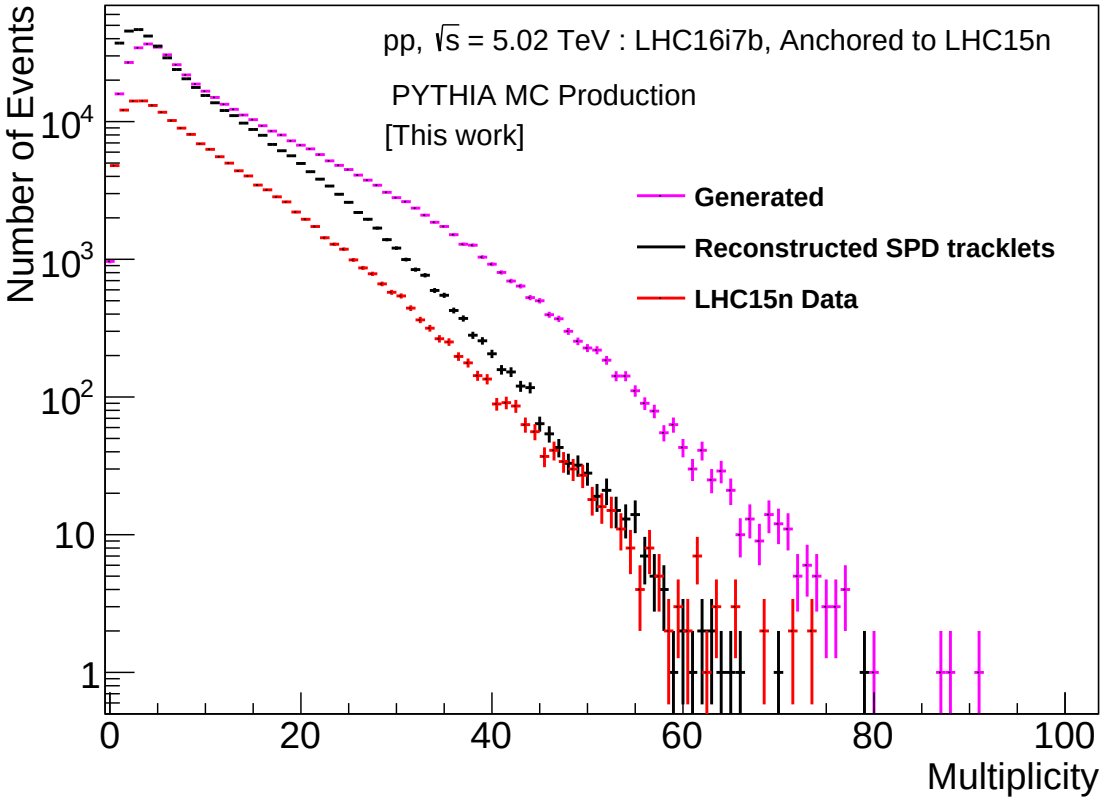

(a) Comparison of raw and tracklet distributions from data and MC production.

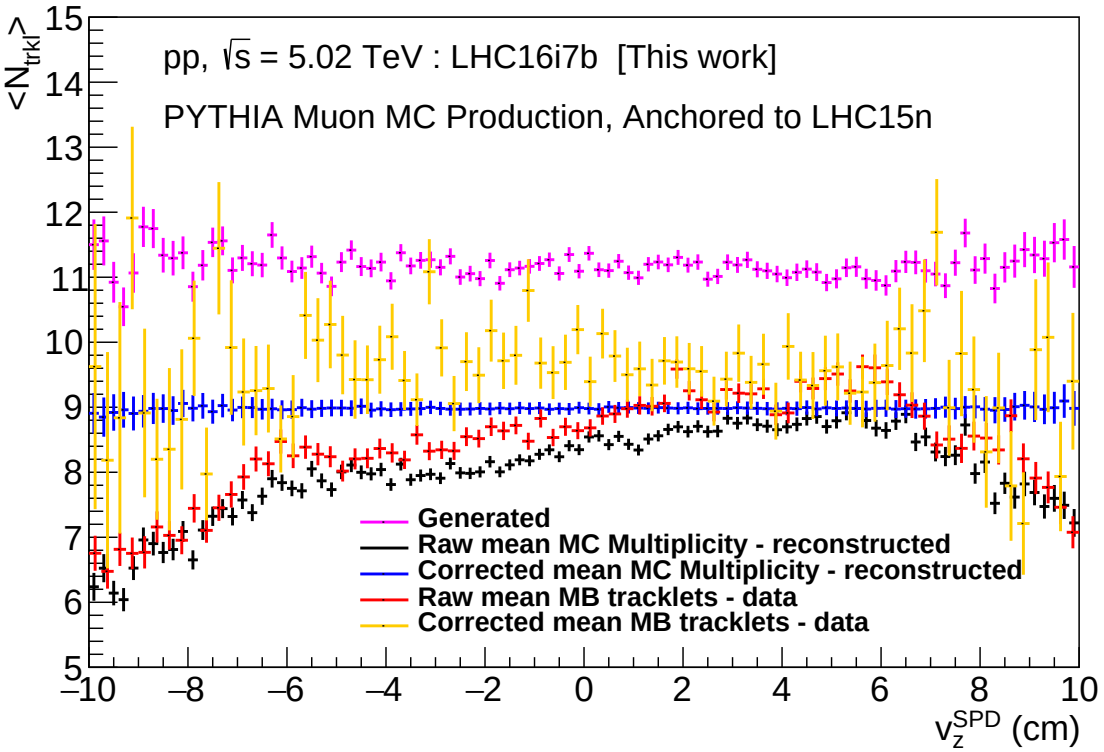

(b) Comparison of the average tracklet distributions for data and MC production.

Fig. 3.12 Comparison of raw tracklet distributions from data and MC production (3.12a) and the average tracklet distribution (3.12b).

the SPD efficiency correction factor to account for these differences.

The conversion from SPD tracklets to charged particles will be discussed in the next section. This is done by determining a factor that correlates tracklets and charged particles.

From SPD tracklets to charged particles

The conversion from tracklets to charged particles can be achieved using two methods. The first method is one that has been implemented in other analyses [131]. The second method was utilised by a different physics group and is adopted from [155]. The first method makes use of determining an α factor as a function of multiplicity bins to correct for the SPD efficiency. The second method involves the direct determination of the mean number of charged particles (N_{ch}) as a function of the number of corrected tracklet intervals (N_{trkl}^{corr}). Both methods will be discussed in this section and a comparison of the two methods will be made.

1. **Method 1 - Evaluating the α factor.** In an ideal experiment, the number of corrected tracklets (N_{trkl}^{corr}) is the same as the number of generated charged particles (N_{trkl}^{gen}). This is however not the case as was shown in the previous section. Due to detector inefficiencies, N_{trkl}^{corr} and N_{trkl}^{gen} are not the same. These inefficiencies are corrected for by evaluating the α factor as expressed in equation 3.4. The $N_{trkl}^{gen} - N_{trkl}^{corr}$ correlation is used to obtain α by fitting it with a linear function. There are two methods that can be used to obtain α:

   (a) α evaluated from the linear fit of the entire distribution:

   $$\alpha_{global} = \frac{\langle N_{ch} \rangle}{\langle N_{corr} \rangle} \tag{3.5}$$

   where $\langle N_{ch} \rangle$ and $\langle N_{corr} \rangle$ are the mean number of generated charged particles and corrected tracklets over the entire distribution, respectively.

   (b) $N_{trkl}^{gen} - N_{trkl}^{corr}$ is fitted with a linear function in different multiplicity bins and α is determined for each bin i:

   $$\alpha_i = \frac{\langle N_{ch} \rangle_i}{\langle N_{corr} \rangle_i} \tag{3.6}$$

   where $\langle N_{ch} \rangle_i$ and $\langle N_{corr} \rangle_i$ are the mean number of generated charged particles and corrected tracklets over the ith multiplicity bin, respectively.

   The statistics were divided into 9 multiplicity bins as quoted in Table 3.7, so that each multiplicity bin consists of $\sim$ 10% of the statistics. Figure 3.13 shows the $N_{trkl}^{gen} - N_{trkl}^{corr}$ correlation fitted with a linear function in different multiplicity bins (shown by the different colored lines) for LHC20a2 MC production anchored to

the LHC17p+q data samples (3.13a) and for LHC16i7b MC production anchored to the LHC15n data samples (3.13b). In Table 3.7, a summary of the obtained α factors anchored to the LHC17p and q data samples is given. For the LHC15n data sample, the statistics are divided into 8 multiplicity bins and the extracted α values are summarized in Table 3.8.

The effectiveness of the two methods used to determine α can be checked by taking the following ratios:

(a) Using α_{global}:

$$\frac{\langle N_{ch}\rangle_i}{\alpha_{global} \times \langle N_{corr}\rangle_i} \tag{3.7}$$

(b) Using α_i:

$$\frac{\langle N_{ch}\rangle_i}{\alpha_i \times \langle N_{corr}\rangle_i} \tag{3.8}$$

The ratio is expected to be consistent with unity if the method is deemed to be good enough. Figure 3.14 shows the plots of the ratios, Fig. 3.14a is the ratio using α_{global} and Fig. 3.14b is the ratio using α_i [131]. It can be seen that the α factor is multiplicity dependent as it is consistent with unity in Fig. 3.14b, where α was determined for different multiplicity bins. This is observed for all the data samples, therefore α_i will be used for the correction.

2. **Method 2**
This method determines the mean number of charged-particles ($\langle N_{ch}\rangle$) as a function of the number of corrected tracklet intervals (N^{corr}_{trkl}). Unlike in the first method where the α factor is used for the correction, in this method, the mean N_{ch} is the charged-particle pseudorapidity ($N_{ch}/d\eta_i$) in the ith multiplicity bin. Figures 3.15 and 3.16 show the N_{ch} distributions in different N^{corr}_{trkl} intervals and the corresponding mean values in each histogram extracted from the same MC productions mentioned in Method 1 anchored to LHC17p+q and LHC15n, respectively.

Final result: self-normalized charged-particle multiplicity

The goal of this section is to obtain the self-normalized charged-particle multiplicity estimator at midrapidity. The self-normalized charged-particle multiplicity or simply referred to as the relative multiplicity is defined as[131]:

$$\frac{dN_{ch}/d\eta_i}{\langle dN_{ch}/d\eta\rangle} = \frac{\langle N^{corr}_{trkl}\rangle_i \cdot \alpha_i}{\Delta\eta \cdot \langle dN_{ch}/d\eta\rangle} \tag{3.9}$$

where

- $dN_{ch}/d\eta_i$ is the charged-particle pseudorapidity in the ith multiplicity bin,

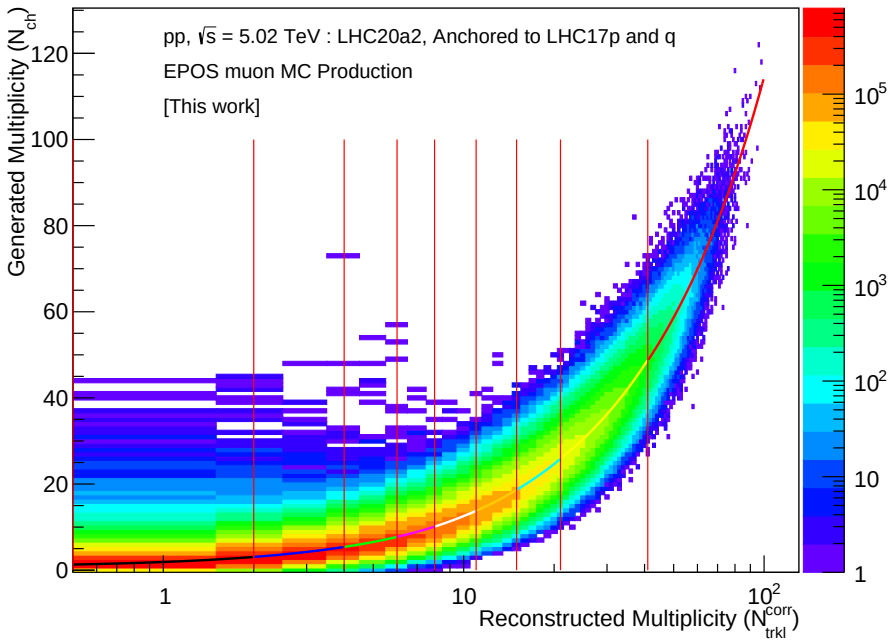

(a) $N_{gen} - N_{trkl}^{corr}$ is fitted with a linear function in different multiplicity bins for LHC20a2 MC production anchored to the LHC17p+q data samples.

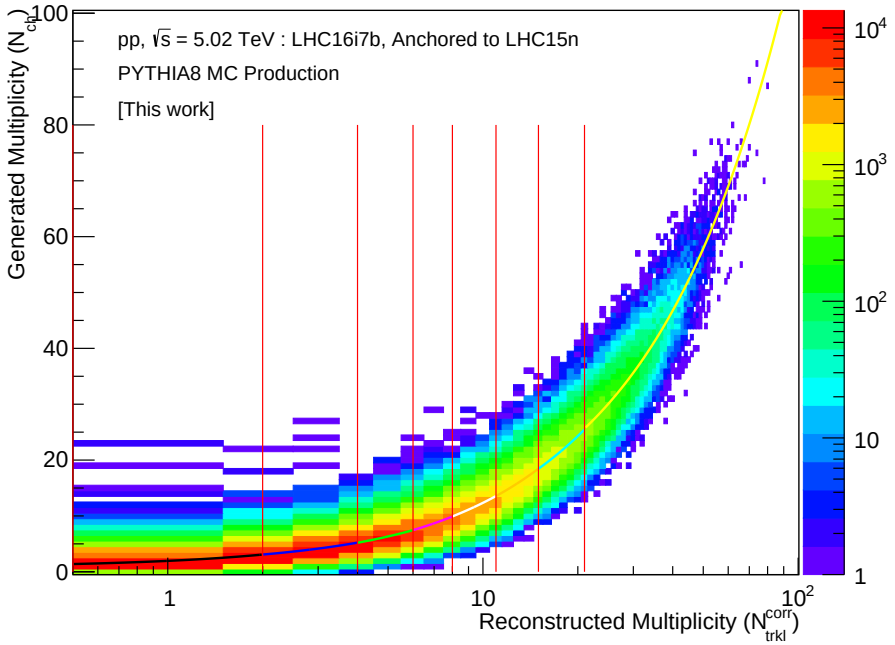

(b) $N_{gen} - N_{trkl}^{corr}$ is fitted with a linear function in different multiplicity bins for LHC16i7b MC production anchored to the LHC15n data samples.

Fig. 3.13 $N_{gen} - N_{trkl}^{corr}$ is fitted with a linear function in different colors for the different multiplicity bins demarcated by the vertical red lines.

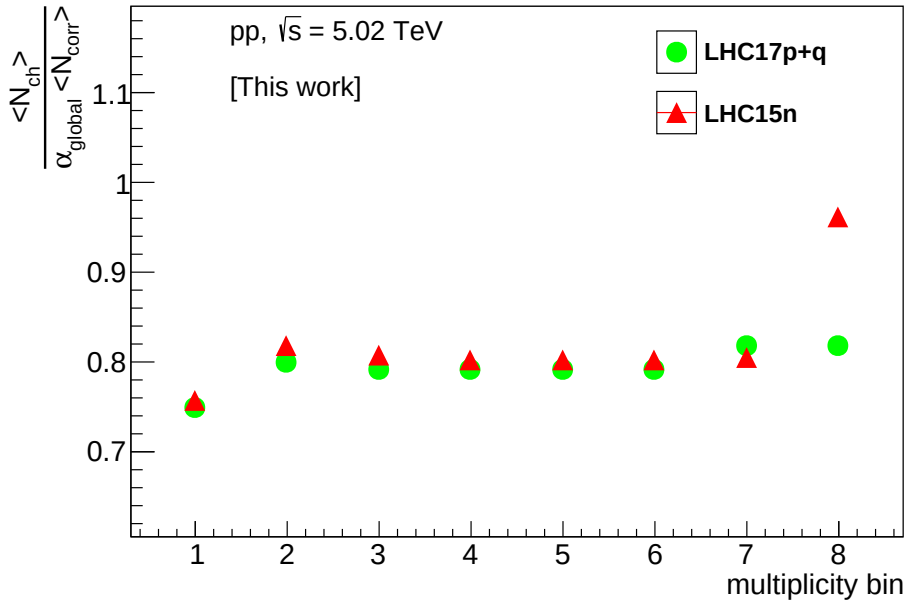

(a) Ratio of the mean number of generated charged particles and the mean number of corrected tracklets further corrected by α_{global}.

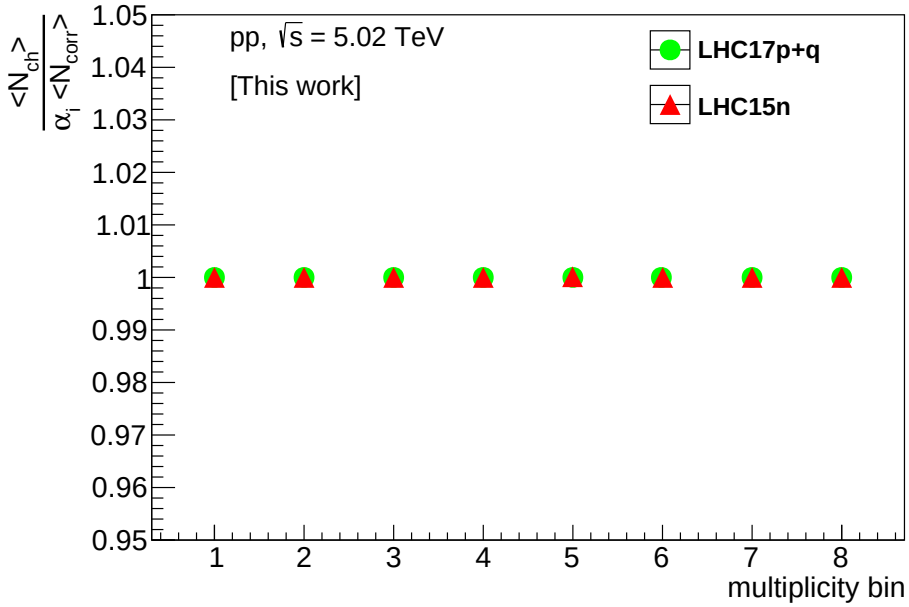

(b) Ratio of the mean number of generated charged particles and the mean number of corrected tracklets further corrected by α_i.

Fig. 3.14 Ratio of the mean number of generated charged particles and the mean number of corrected tracklets further corrected by α_{global} (3.14a) and α_i (3.14b).

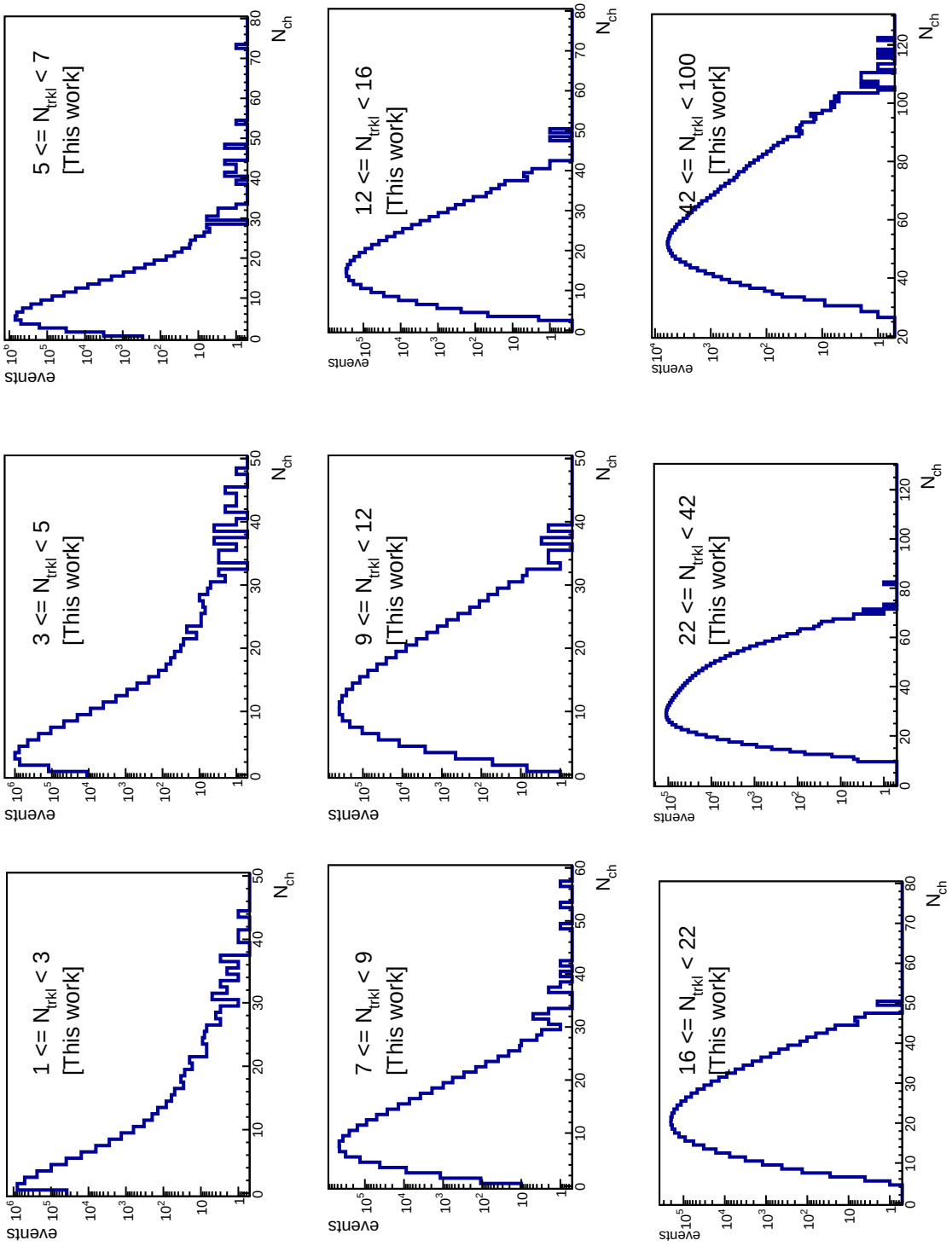

Fig. 3.15 Mean of N_{ch} distribution in N_{trkl} intervals anchored to the LHC17p and q data sample

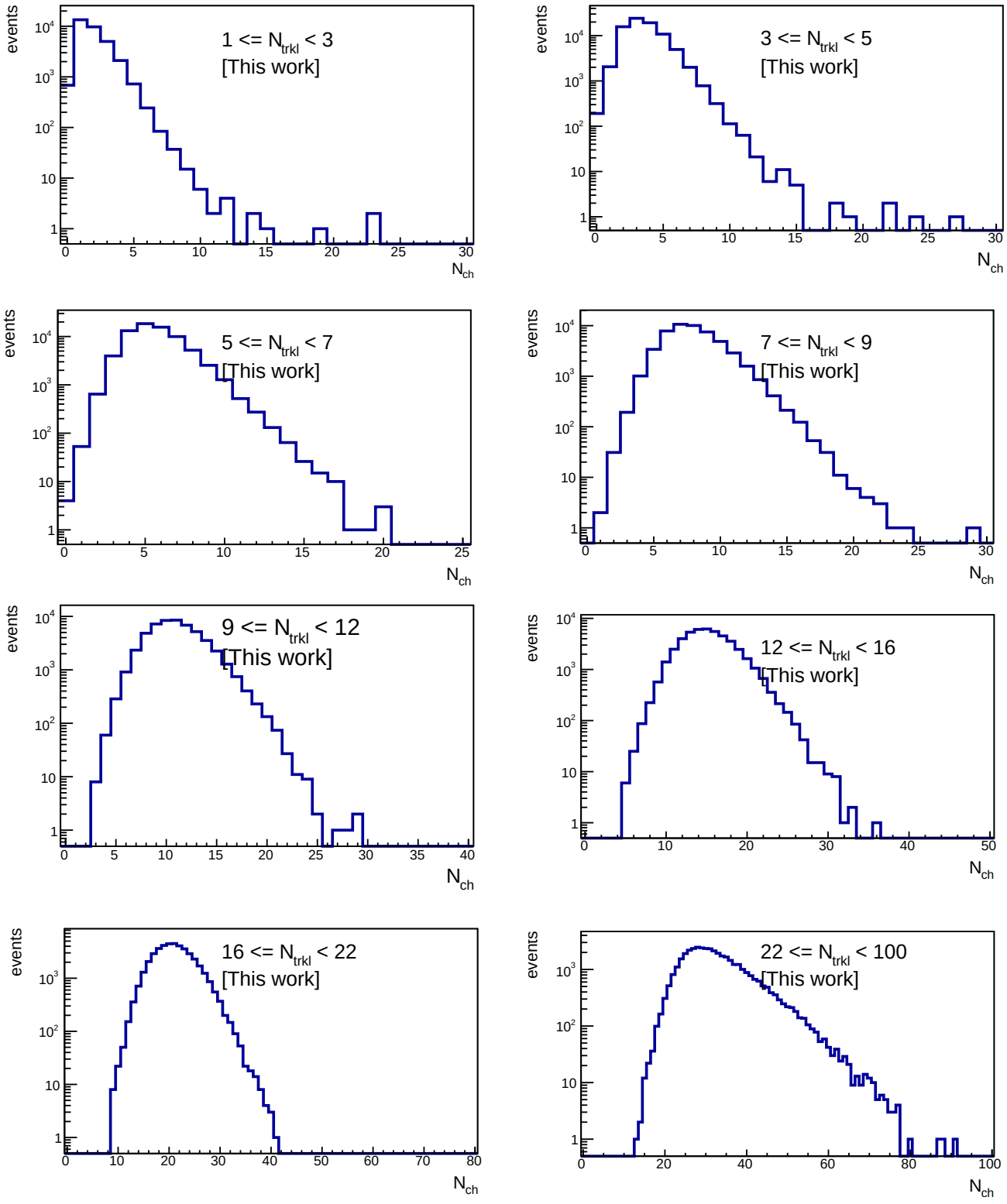

Fig. 3.16 Mean of N_{ch} distribution in N_{trkl} intervals anchored to the LHC15n data sample

- $\langle dN_{ch}/d\eta \rangle$ is the mean charged-particle density,
- α_i is the SPD efficiency correction factor obtained from Monte Carlo (MC) simulation,
- $\langle N_{trkl}^{corr} \rangle_i$ is the mean number of tracklets in the ith multiplicity bin and
- $\Delta\eta$ is equal to 2 since the kinematic region where only charged particles are considered is $|\eta| < 1$.

To obtain the relative multiplicity, the corrected MB tracklet distribution obtained in section 3.3.1.1 is utilized. The distribution is divided into 9 bins, similar to those used to obtain the α factor as described in 3.3.1.1. The mean number of corrected tracklets is determined for each bin i. The value of the mean charged-particle density ($\langle dN_{ch}/d\eta \rangle$) is defined as [131]:

$$\langle dN_{ch}/d\eta \rangle = \frac{\langle N_{trkl}^{corr} \rangle \cdot \langle \alpha \rangle}{\Delta\eta} \tag{3.10}$$

where $\langle \alpha \rangle$ is α_{global} as deteremined in 3.3.1.1 and N_{trkl}^{corr} is the mean number of corrected tracklets over the entire tracklet distribution. The value of $\langle dN_{ch}/d\eta \rangle$ is determined by the ALICE central multiplicity group for MB at $\sqrt{s} = 5.02$ TeV in pp collisions for INEL>0 and $|\eta| < 1$, and is given as 5.70 +0.08 −0.06 [56].

A summary of the values of $\frac{dN_{ch}}{d\eta}$ using method 1 and 2 is shown in Table 3.7. This comparison is shown for the LHC17p+q data samples. For method 1, $\frac{dN_{ch}}{d\eta} = \frac{\langle N_{trkl}^{corr} \rangle_i \cdot \alpha_i}{\Delta\eta}$ where $\langle N_{trkl}^{corr} \rangle_i$ is the corrected mean number of tracklets from data in a specific multiplicity bin i. For method 2, $\frac{dN_{ch}}{d\eta}$ is the mean number of charged particles ($\langle N_{ch} \rangle$) in the respective corrected tracklet intervals (N_{trkl}^{corr}). The comparison for the LHC15n data sample is shown in Table 3.8. The statistical errors quoted in the tables are calculated by adding all the errors in quadrature. For method 1, the statistical error of the α-factor and the mean number of corrected tracklets is added in quadrature; for method 2, the ratio of standard deviation and mean number of tracklets is determined to find the error of the mean.

It is evident that there is a notably large difference between method 1 and 2 for the first multiplicity bin; referring back to Fig. 3.11a and 3.12a, it is observed that the generated multiplicity is lower than the reconstructed SPD tracklets. Since method 1 is dependent on the SPD tracklets and method 2 is dependent on the generated tracklets, the two methods behave differently in the first multiplicity bin as compared to the rest of the bins where the generated multiplicity is greater than the SPD tracklets. Figures 3.11 and 3.12 show as expected that the probability of having low multiplicity is larger with reconstructed tracks as compared to generated tracks. This difference will need to be accounted for when determining the self-normalized yield in the final result, the first multiplicity bin will need to be scaled.

Multiplicity bin	α	$\frac{dN_{ch}}{d\eta}$	
		Method 1	Method 2
1-2	1.17365 ± 0.30164	0.65873 ± 0.30164	0.94847 ± 1.31489
3-4	1.15905 ± 0.18477	1.72378 ± 0.18477	1.82082 ± 0.894613
5-6	1.16534 ± 0.22630	2.8876 ± 0.22630	2.9684 ± 0.652989
7-8	1.19678 ± 0.26785	4.16475 ± 0.26785	4.13796 ± 0.545766
9-11	1.22286 ± 0.20128	5.74319 ± 0.20128	5.61563 ± 0.487128
12-15	1.21745 ± 0.16040	7.78651 ± 0.1604	7.71882 ± 0.424744
16-21	1.19658 ± 0.10747	10.4487 ± 0.10747	10.6479 ± 0.376843
22-41	1.14798 ± 0.02746	14.4951 ± 0.0274601	16.2039 ± 0.432449
42-130	1.1156 ± 0.026194	25.0928 ± 0.028452	27.2589 ± 0.301536

Table 3.7 Comparison of $\frac{dN_{ch}}{d\eta}$ for method 1 and 2 for data samples LHC17p+q.

Multiplicity bin	α	$\frac{dN_{ch}}{d\eta}$	
		Method 1	Method 2
1-2	1.13087±0.453039	0.672166±0.453039	0.976784 ± 1.23492
3-4	1.06481±0.248762	1.59793±0.248762	1.81635 ± 0.822591
5-6	1.12722±0.285686	2.80429±0.285686	2.85957 ± 0.620013
7-8	1.21217±0.321153	4.23619±0.321153	4.00776 ± 0.536382
9-11	1.2166±0.234524	5.74797±0.234524	5.51403 ± 0.477531
12-15	1.22654±0.182449	7.89102±0.182449	7.61777 ± 0.413417
16-21	1.17216±0.121205	10.3888±0.121205	10.5221 ± 0.366122
22-100	1.11196±0.206035	15.1244±0.206035	16.3256 ± 0.48746

Table 3.8 Comparison of $\frac{dN_{ch}}{d\eta}$ for method 1 and 2 for LHC15n data sample.

Another notable difference of up to 10% and 8% for the last two bins, respectively, is seen in Table 3.7. This difference is attributed to the fact that the multiplicity reach of the reconstructed tracklets is less than the generated tracks. As a result, at higher multiplicities, the pseudorapidity density determined with Method 1 will be less than the mean number of generated tracklets for Method 2. This difference is clearly indicated in Fig. 3.11.

For consistency with other analyses, Method 2 will be utilized to obtain the final results. A summary of $\frac{dN_{ch}/d\eta}{\langle dN_{ch}/d\eta \rangle}$ for all the data samples is shown in Table 3.9. The statistical errors quoted in the table are the same as shown in Tables 3.7 and 3.8 since $\langle dN_{ch}/d\eta \rangle$ is only quoted with systematic uncertainties in [56].

The next subsection will be devoted to a discussion on the determination of the self-

LHC17p+q		LHC15n	
Multiplicity bin	$\frac{dN_{ch}/d\eta}{\langle dN_{ch}/d\eta \rangle}$	Multiplicity bin	$\frac{dN_{ch}/d\eta}{\langle dN_{ch}/d\eta \rangle}$
1-2	0.166398 ± 1.31489	1-2	0.171366 ± 1.23492
3-4	0.319442 ± 0.894613	3-4	0.318659 ± 0.822591
5-6	0.520771 ± 0.652989	5-6	0.501679 ± 0.620013
7-8	0.725959 ± 0.545766	7-8	0.703116 ± 0.536382
9-11	0.985199 ± 0.487128	9-11	0.967373 ± 0.477531
12-15	1.35418 ± 0.42744	12-15	1.33645 ± 0.413417
16-21	1.86805 ± 0.376843	16-21	1.84598 ± 0.366122
22-41	2.84279 ± 0.432449	22-100	2.86414 ± 0.487468
42-130	4.78227± 0.301536		

Table 3.9 Multiplicity axis that will be used in the final result for data samples LHC17p+q and LHC15n.

normalized charged-particle multiplicity utilizing the "Official Framework" method.

3.3.2 Official Framework

The "Official Framework" utilizes the absolute yields available from the ALICE central multiplicity group [56]. The multiplicity estimator can be determined using the information available from the ALICE central multiplicity group. The basic criteria used to obtain the absolute yields for the run, event and multiplicity selection are given in a short summary below.

Run Selection

The criteria for the run selection is similar to that discussed in section 3.2.1 with two additional conditions added:

- The following detector is used: SPD.
- A pile-up associated with $\mu < 0.1$ is preferable where μ is the mean value of the Poisson distribution which describes the probability to have n collisions when the beams cross each other, i.e. the average number of visible pp interactions per bunch crossing.

Event Selection

The criteria for the event selection is also similar to that discussed in Section 3.2.2. The events selected satisfied the following conditions:

- Physics selection;
- Events must have at least a SPD-determined primary vertex;
- Events must have a primary vertex located within $|z| < 10$ cm, and;
- Events must not be tagged as pile-up by: AliESDEvent::IsPileupFromSPD().

Multiplicity Selection

The selection criteria mentioned above are standard for pp collisions. In addition to those, the selection on the hadronic activity in the events needs to be applied.

Although there are several methods that can be used for the multiplicity selection, there are two favored methods; the mid-pseudorapidity estimator (SPD estimator) and the V0 amplitude estimator (forward rapidity estimator). The mid-pseudorapidity estimator is used as the reference for the charged-particle multiplicity in the $|\eta| < 1$ region. The V0 amplitude estimator is used for the event classification according to hadronic activity based on the V0 amplitudes.

In this study, the mid-pseudorapidity estimator is used since it allows a wider rapidity gap between the measured charged particles and the multiplicity detectors. However, the V0 amplitude estimator is also considered to show the possible over-bias/overestimation at forward rapidity since the V0 is used in the measurements at forward rapidity, where both the multiplicity and single muons from heavy-flavour decays are measured.

3.3.2.1 Multiplicity Estimation

In this section, the charged-particle multiplicity at midrapidity and forward rapidity is determined.

- **SPD estimator (midrapidity)**
  The pseudorapidity density, $dN_{ch}/d\eta$, is the average number of charged particles produced in an η region. The SPD tracklet multiplicity estimator in pp collisions at $\sqrt{s} = 5.02$ TeV is available from the ALICE central multiplicity group [56]. Using the available pseudorapidity values, the charged-particle multiplicity ($dN_{ch}/d\eta/\langle dN_{ch}/d\eta\rangle$) can be determined. The charged-particle multiplicity is the fraction of the pseudorapidity in a given multiplicity percentile bin to the average/absolute pseudorapidity density.
  In order to find the average/absolute pseudorapidity density, the following expres-

sion can be used:

$$\langle dN_{ch}/d\eta \rangle = \frac{dN_{ch}}{d\eta_{0-100\%}} = \frac{\Sigma(dN_{ch}/d\eta_i)(\Delta x)}{\Sigma \Delta x} \tag{3.11}$$

where Δx is the interval width and i is the multiplicity percentile bin as noted in the SPD estimator shown in Table 3.10. The corresponding systematic uncertainty of the average/absolute pseudorapidity density is determined using the following expression:

$$\Delta\langle dN_{ch}/d\eta \rangle = \Delta\frac{dN_{ch}}{d\eta_{0-100\%}} = \frac{\Sigma(\Delta dN_{ch}/d\eta_i)(\Delta x)}{\Sigma \Delta x} \tag{3.12}$$

where $\Delta dN_{ch}/d\eta_i$ is the corresponding systematic uncertainty also noted in the table.

The average pseudorapidity density is determined as $\langle dN_{ch}/d\eta \rangle = 5.94\ ^{+0.11}_{-0.10}$ and quoted in Table 3.10.

Mult (%)	$\frac{dN_{ch}}{d\eta}$	syst. uncertainty	$\frac{dN_{ch}/d\eta}{\langle dN/d\eta \rangle}$	syst. uncertainty
0-1	25.33	+0.48 -0.44	4.26	+0.16 -0.15
1-5	17.83	+0.31 -0.29	3.00	+0.11 -0.11
5-10	13.94	+0.24 -0.22	2.35	+0.08 -0.08
10-15	11.70	+0.17 -0.16	1.97	+0.07 -0.06
15-20	10.08	+0.15 -0.13	1.70	+0.06 -0.06
20-30	8.24	+0.11 -0.10	1.39	+0.05 -0.05
30-40	6.38	+0.10 -0.09	1.07	+0.04 -0.04
40-50	5.06	+0.10 -0.09	0.85	+0.03 -0.03
50-70	3.55	+0.07 -0.06	0.60	+0.02 -0.02
70-100	1.71	+0.05 -0.05	0.29	+0.01 -0.01
0-100	5.94	+0.11 -0.10		

Table 3.10 Pseudorapidity density $dN/d\eta$ extracted from [56] and the charged-particle multiplicity $\frac{dN_{ch}/d\eta}{\langle dN/d\eta \rangle}$ in pp collisions at $\sqrt{s} = 5.02$ TeV.

The self-normalized charged-particle multiplicity is therefore determined using the expression:

$$\frac{dN_{ch}/d\eta_i}{\langle dN_{ch}/d\eta \rangle} = \frac{dN_{ch}/d\eta_i}{dN_{ch}/d\eta_{0-100\%}} \tag{3.13}$$

The corresponding systematic uncertainty for the self-normalized charged-particle multiplicity is determined using the following expression:

$$\Delta\frac{dN_{ch}/d\eta_i}{\langle dN_{ch}/d\eta \rangle} = \frac{(\frac{dN_{ch}}{d\eta_i} \times \Delta\langle\frac{dN_{ch}}{d\eta}\rangle) + (\langle\frac{dN_{ch}}{d\eta}\rangle \times \Delta\frac{dN_{ch}}{d\eta_i})}{\langle\frac{dN_{ch}}{d\eta}\rangle^2 + \Delta\langle\frac{dN_{ch}}{d\eta}\rangle^2} \tag{3.14}$$

The multiplicity axis (self-normalized charged-particle multiplicity) and corresponding systematic uncertainty are given in column 4 and 5 of Table 3.10. Columns 2 and 3 in the table give the pseudorapidity density and the corresponding systematic uncertainty for the different multiplicity percentile bins.

- **V0M estimator (forward rapidity)**
  The V0M multiplicity estimator table is also available from the ALICE central multiplicity group [56] that contains the pseudorapidity values; there are two multiplicity estimator tables available, one for the LHC17p data sample and another for the LHC15n data sample. Like done for the SPD estimator table, the pseudorapidity density in different multiplicity classes is given as well as the average pseudorapidity density. The self-normalized charged-particle is then determined. Following the steps discussed above, a summary of the charged-particle multiplicity values is given in Table 3.11 for the LHC17p and LHC15n data samples. It should be noted that there is no table available for anchor to the LHC17q data sample.

Mult (%)	$\frac{dN_{ch}/d\eta}{\langle dN/d\eta\rangle}$ (LHC17p)	syst. uncertainty	$\frac{dN_{ch}/d\eta}{\langle dN/d\eta\rangle}$ (LHC15n)	syst. uncertainty
0-1	3.36	+0.06 -0.04	3.34	+0.05 -0.04
1-5	2.64	+0.04 -0.03	2.63	+0.04 -0.03
5-10	2.17	+0.03 -0.03	2.16	+0.03 -0.02
10-15	1.87	+0.03 -0.02	1.86	+0.03 -0.02
15-20	1.66	+0.03 -0.02	1.64	+0.02 -0.02
20-30	1.41	+0.02 -0.02	1.38	+0.02 -0.02
30-40	1.15	+0.02 -0.01	1.13	+0.01 -0.01
40-50	0.95	+0.02 -0.01	0.92	+0.01 -0.01
50-70	0.72	+0.01 -0.01	0.70	+0.01 -0.01
70-100	0.59	+0.01 -0.01	0.43	+0.01 -0.01

Table 3.11 Values of the charged-particle multiplicity ($\frac{dN_{ch}/d\eta}{\langle dN/d\eta\rangle}$) for LHC17p (second column) and LHC15n (fourth column). The corresponding systematic uncertainty is given in the third and fifth columns for LHC17p and LHC15n, respectively.

Two methods were utilized for the multiplicity estimation. The first method is the data-driven method that uses information from the SPD. This method uses the MB trigger to extract information from the SPD to determine the pseudorapidity density. The pseudorapidity density is then converted to a self-normalized charged-particle multiplicity that is then used as the x-axis in the final result of heavy-flavour production as a function of charged-particle multiplicity. The second method is the "Official Framework" method that is based on both the mid- and forward rapidity estimators. The pseudorapidity den-

sity in different multiplicity classes is already available therefore the only step required is to determine the self-normalized charged-particle multiplicity.

In the next section, the method of extracting the heavy-flavour decay muon yield from the event selected data sample will be discussed.

3.4 Heavy-flavour decay muon yield determination

In this section the focus is on extracting the muon yield. Details on the muon track cuts that are applied in the data sample are discussed. The normalization factor responsible for normalizing the MSL and MSH triggered events to MB events is determined. A selection of cuts need to be applied on the data in order to extract the muon yield as discussed in section 3.4.1 and in section 3.4.2, the determination of the normalization factor is discussed. The section is concluded with a discussion on the normalization to inelastic events.

3.4.1 Muon Track Cuts

The muon track cuts applied on the event selected data sample are as follows:

- **Eta Muon Track cut**
  $-4.0 < \eta < -2.5$, the eta cut is used to remove tracks found at and beyond the edge of the muon spectrometer.

- **ThetaAbs Muon Track cut**
  $171^\circ < \theta_{abs} < 178^\circ$, muons passing the high-density region of the front absorber are rejected by applying this cut.

- **MatchLpt(Hpt) and MatchApt Muon Track cut**
  The tracks detected in the muon tracking chambers are matched to those detected in the trigger system. The MatchLpt is used for the MSL trigger, MatchHpt is used for MSH trigger and for the MB trigger, the MatchApt is used.

- **PDCA Muon Track cut**
  This cut is used to remove beam-induced background particles. The distance of closest approach (DCA) of particles produced at the IP follows a Gaussian distribution due to the multiple scatterings in the absober, whereas the particles coming from elsewhere do not. Particles that do not follow the Gaussian distribution are eliminated. The tracks with $p\times$DCA greater than 6σ are rejected, where p is the momentum of the track [156]. The effectiveness of this cut as well as the other mentioned cuts is illustrated in Fig. 3.17, Fig. 3.17a is a 2D distribution of the

momentum (p) and DCA before any of the muon track cuts were applied and Fig. 3.17b shows the 2D distribution after the application of all the track cuts.

Figure 3.18 shows the evolution of the p_{T} distribution of the MSL and MSH triggers for LHC17p+q data samples as each muon track cut discussed above is applied. The data-points with the circle (N_trks) is the total number of muon tracks before the application of muon track cuts. The square, upward triangle, downward triangle and open diamond points are the eta, thetaAbs, matchLpt (Hpt) and PDCA cut distributions, respectively. Similar trends are observed in the LHC15n data samples, which can be found in Ref. [49].

3.4.1.1 Muon yields in different multiplicity bins

The muon yields extracted in section 3.4 are now plotted in different multiplicity bins according to the multiplicity bins shown in Table 3.9. Figures 3.19 and 3.20 show the muon yields in different multiplicity bins for the MSL (Fig. 3.19a and 3.20a) and MSH (Fig.3.19b and 3.20b) trigger for the LHC17p+q and LHC15n data samples, respectively.

The muon yields are also plotted in different multiplicity percentile bins according to the SPD estimator given in Table 3.10. Since the V0M estimator has the same multiplicity percentile bins as the SPD estimator, the muon yields in the multiplicity percentile bins are the same. Figures C.1 and C.2 in Appendix C.0.1 show the muon yields in different multiplicity percentile bins for the MSL and MSH trigger for the LHC17p+q and LHC15n data samples, respectively.

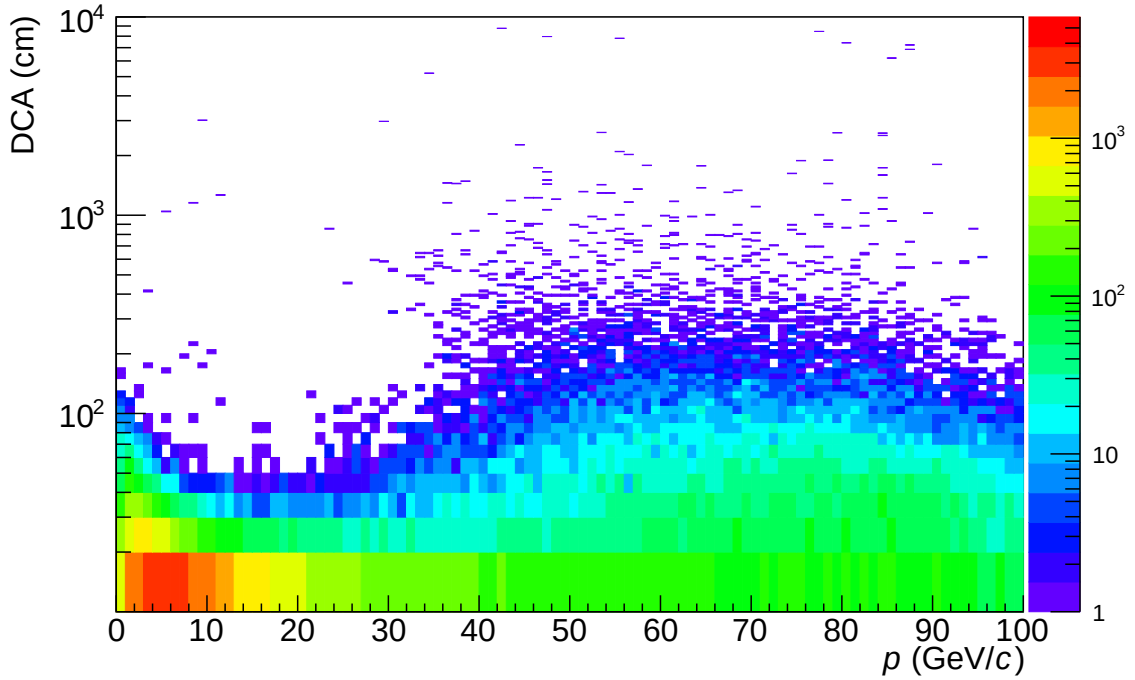

(a) Distribution of DCA vs momentum of muons measured in pp collisions at $\sqrt{s} = 5.02$ TeV before muon track cuts are applied.

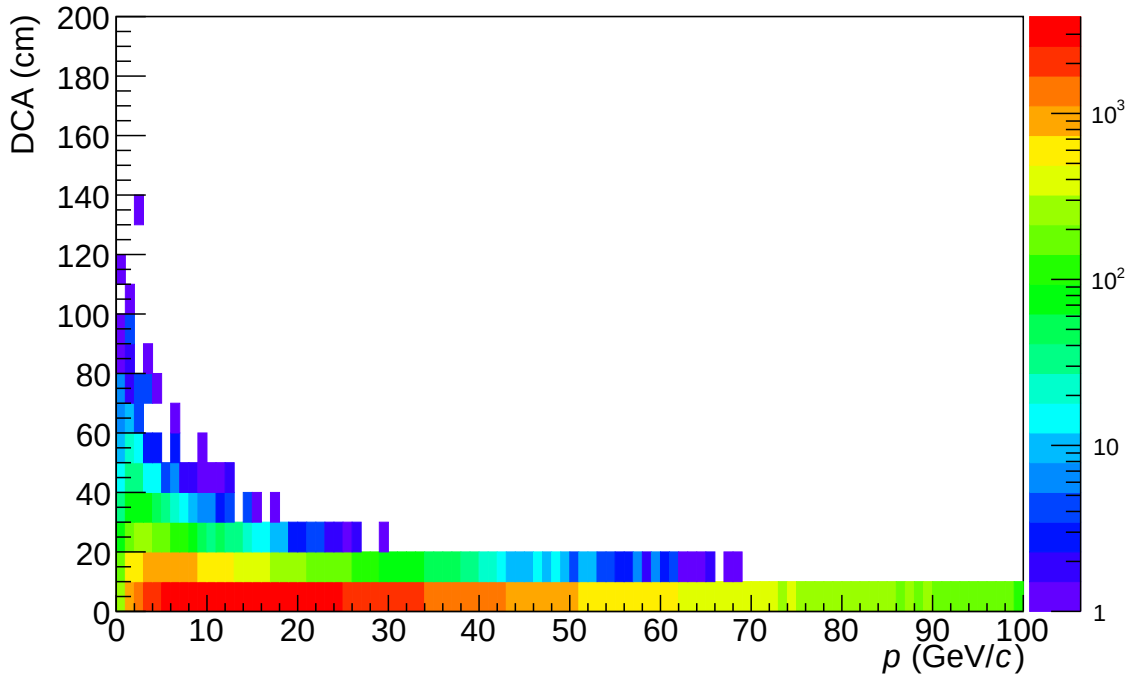

(b) Distribution of DCA vs momentum of muons measured in pp collisions at $\sqrt{s} = 5.02$ TeV after all muon track cuts are applied.

Fig. 3.17 DCA vs momentum of muons measured in pp collisions at $\sqrt{s} = 5.02$ TeV. The distributions before (3.17a) and after (3.17b) all muon track cuts are applied.

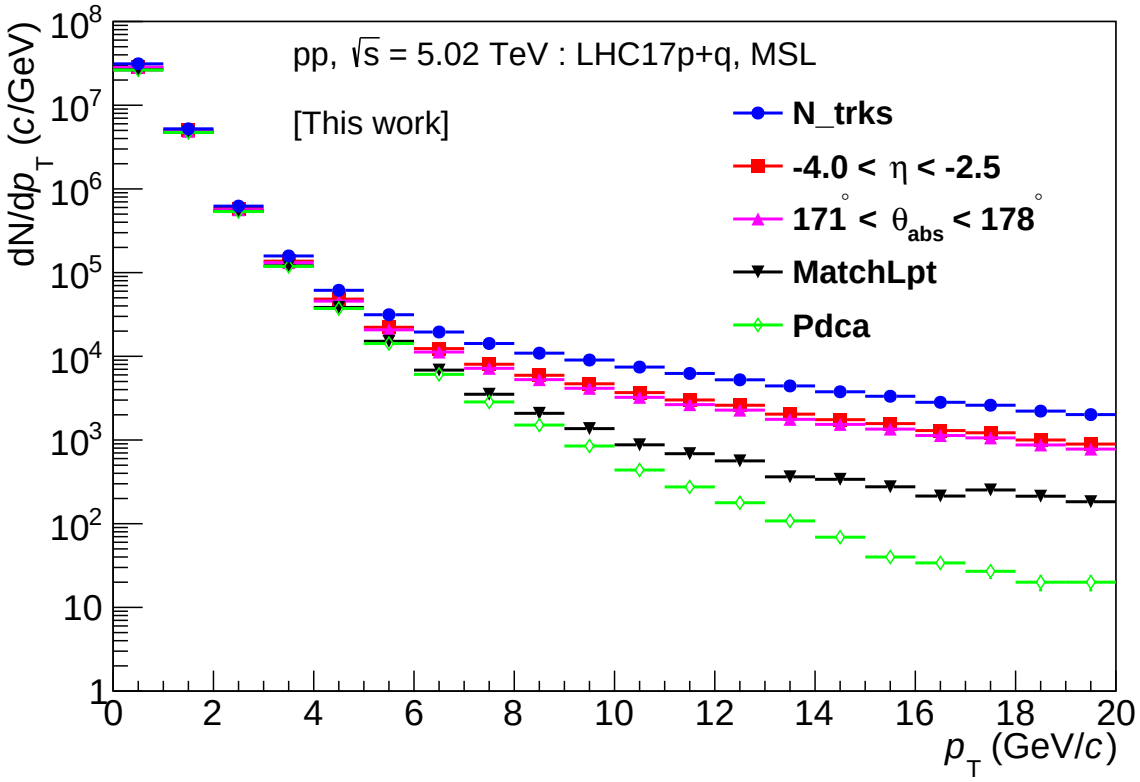

(a) MSL p_{T} distribution for LHC17p+q.

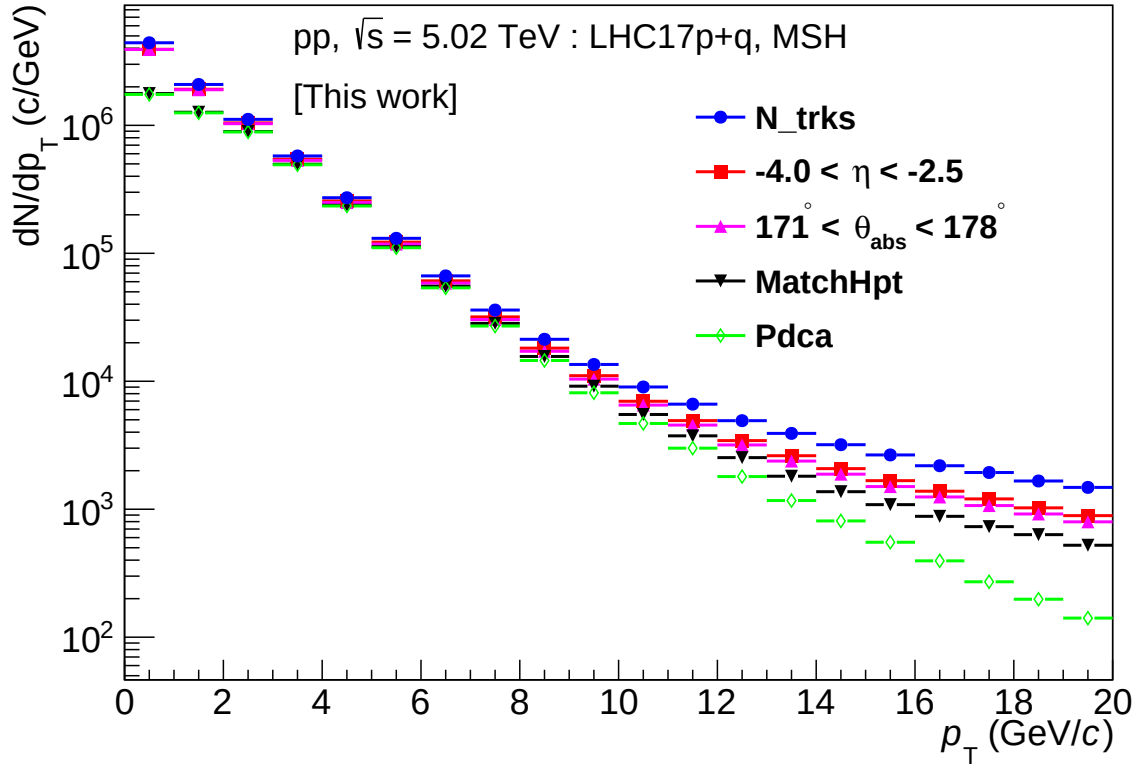

(b) MSH p_{T} distribution for LHC17p+q.

Fig. 3.18 Evolution of MSL (3.18a) and MSH (3.18b) p_{T} distributions after each muon track cut.

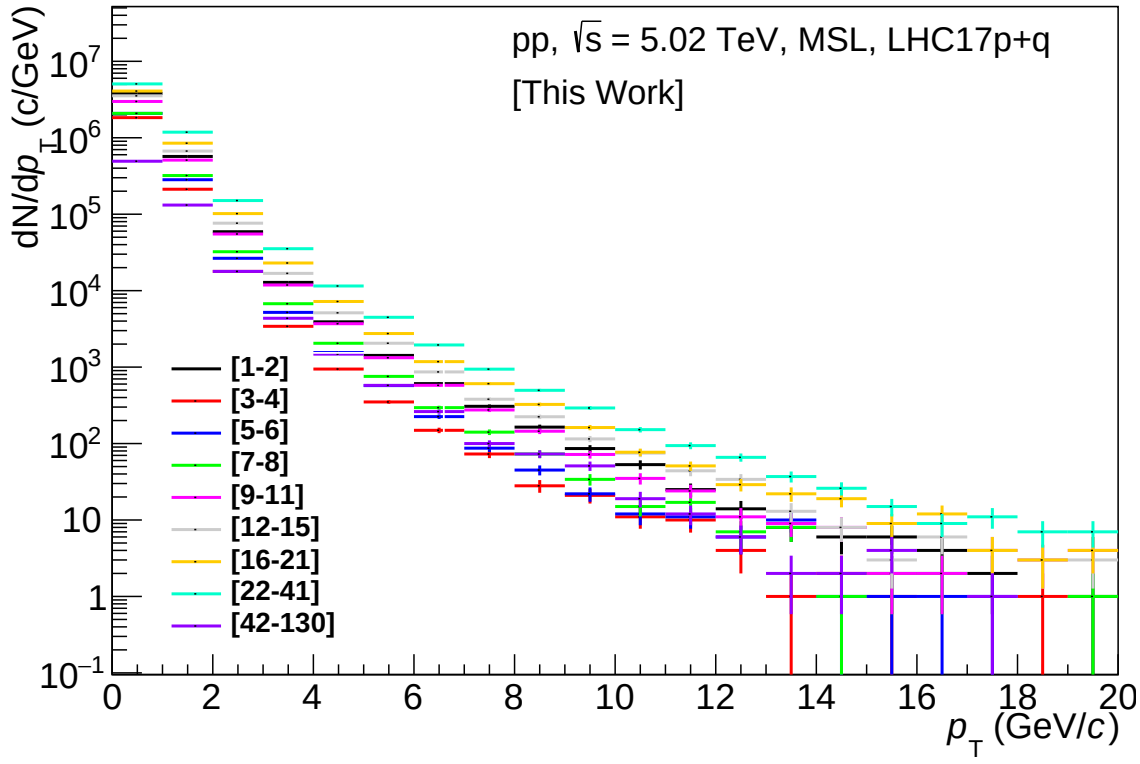

(a) p_{T} distribution in different multiplicity bins for MSL trigger.

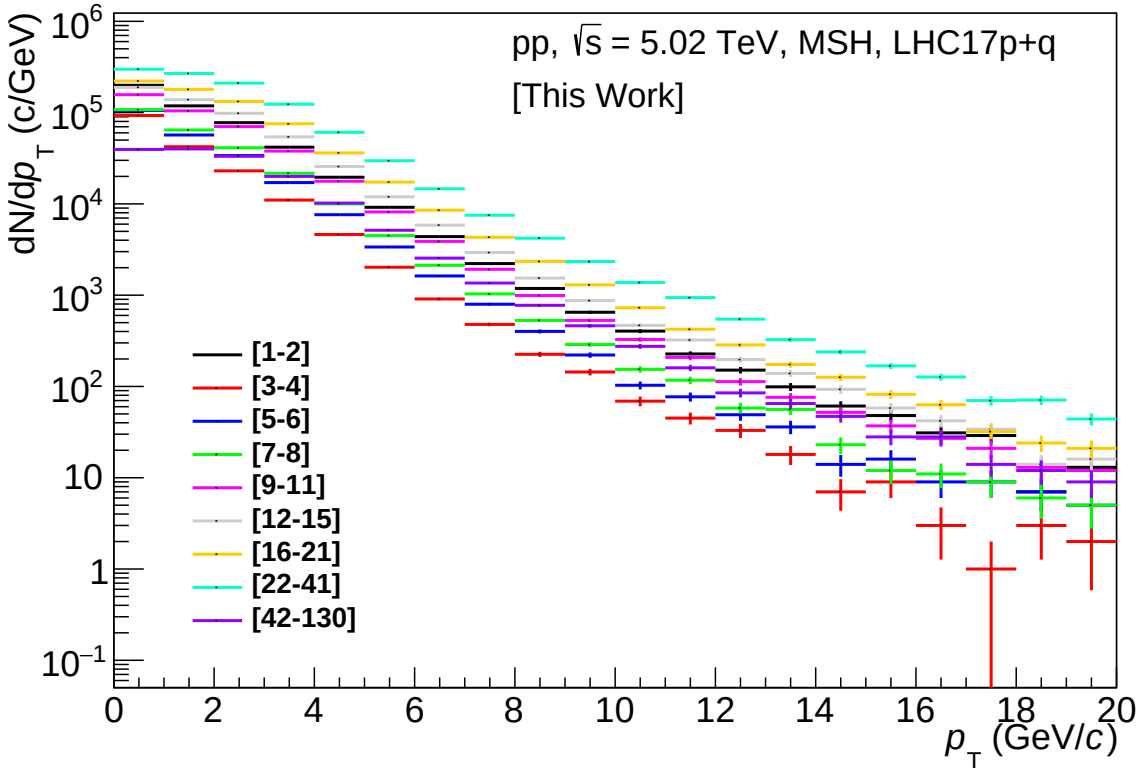

(b) p_{T} distribution in different multiplicity bins for MSH trigger.

Fig. 3.19 Muon yields in different multiplicity bins for MSL (3.19a) and MSH (3.19b) triggers for LHC17p+q data sample. The horizontal lines represent the bin width and the vertical lines represent the statistical errors.

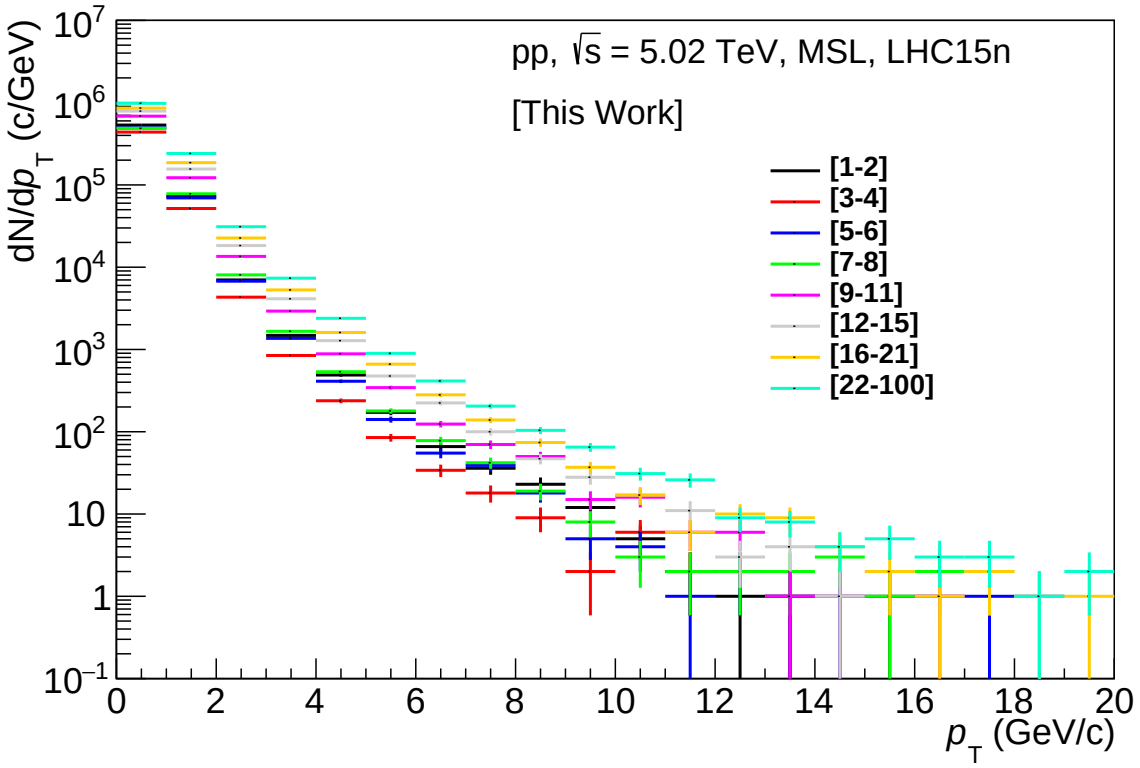

(a) p_{T} distribution in different multiplicity bins for MSL trigger.

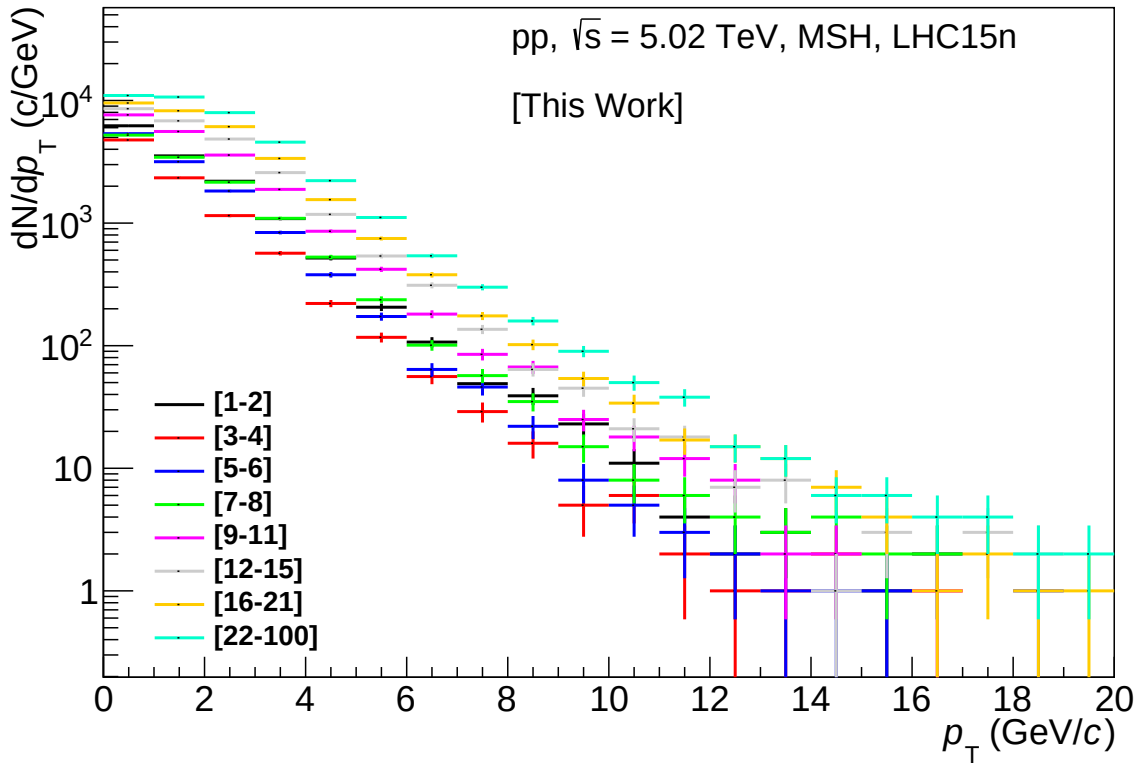

(b) p_{T} distribution in different multiplicity bins for MSH trigger.

Fig. 3.20 Muon yields in different multiplicity bins for MSL (3.20a) and MSH (3.20b) triggers for LHC15n data sample. The horizontal lines represent the bin width and the vertical lines represent the statistical errors.

3.4.2 Normalization Factor

The normalization factor, F_{norm} is the factor required to obtain the minimum bias equivalent sample of muon triggered events. Hence, it is the fraction of single low or high p_{T} muons within the minimum bias events. This factor is needed to determine the integrated luminosity. To find this normalization factor, two methods are used: the offline and online (scaler) method. In the offline method, one applies the muon trigger condition on minimum-bias events. Both these methods have been utilized in other single muon studies in pp [152, 157] , p-Pb [131, 152] and Pb-Pb [158] analyses. The online method is determined by using the expression given in the equation 3.15 while offline method makes use of the expression given in equation 3.20 .

3.4.2.1 Scaler Method (Online Method)

The scaler method relies on the L0b trigger input (scalers) taken from the OCDB. The factor F_{norm} is calculated using the expression [152, 157, 158]:

$$F^{i}_{norm-onl}MSL(MSH) = \frac{L0b^{i}_{CINT7} \times purity^{i}_{CINT7} \times F^{i}_{pile-up}}{L0b^{i}_{MSL(MSH)} \times purity^{i}_{MSL(MSH)}} \tag{3.15}$$

where

- i is the run number, F_{norm} is determined per run.
- $L0b_{CINT}$, $L0b_{MSL}$ and $L0b_{MSH}$ are the scaler (trigger rate) values recorded at L0b level for CINT7, MSL and MSH triggers, respectively.
- $purity^{i}_{MSL(MSH)}$ is the purity factor associated with the MSL(MSH) trigger and is computed as the ratio of physics selected events to the total number of events.
- The $F^{i}_{pile-up}$ is the correction factor associated with the V0 MB trigger (CINT7).

The $\mathrm{F}^{i}_{pile-up}$ factor is required to account for the detector response during data taking. The pile-up factor is defined as:

$$F^{i}_{pile-up} = \frac{\mu^{i}}{(1 - e^{-\mu^{i}})} \tag{3.16}$$

with

$$\mu^{i} = -ln(1 - purity^{i}_{MB} \times \frac{L0bRate^{i}_{MB}}{N^{i}_{colliding} \times f_{LHC}}) \tag{3.17}$$

where:

- $f_{LHC} = 11\ 245$ Hz is the collision frequency of the LHC
- μ^{i} is the mean value of the Poisson distribution which describes the probability to have n collisions per bunch crossing.

- The variable $purity^{i}_{MB}$ is the purity factor (CINT7) associated to the MB trigger and is computed as the ratio of physics selected events to the total number of events.
- $L0bRate^{i}_{MB}$ and $N_{colliding}$ are the rates of number of the minimum-bias events recorded by the L0b counters and the number of interacting bunches, respectively.

The values of μ expressed by equation 3.17 are also available in the run condition table (RCT) on the ALICE Grid [159]. The pile-up factor is typically evaluated for the MB event trigger (CINT7), however, in the case of the LHC15n data sample, the MB event trigger with the T0 (C0TVX) is also used for reasons discussed in detail in [157]. The pile-up correction is still computed using the same procedure for the C0TVX MB trigger, the purity factor for the trigger is considered to be unity as quoted in [157, 160]. A purity factor of unity is used due to the fact that there are no L0a[1] entries for the C0TVX-B-NOPF-CENTNOTRD trigger available during the whole run period, leading to the assumption that 100% of the background events firing the T0 are also firing the V0 [157].

Figure 3.21a shows the purity (CINT7) as a function of run number for the MB trigger and Fig. 3.21b shows the L0b rates for the MB trigger.

Figure 3.22a shows the number of interacting bunches as a function of run number while the pile-up correction factor as a function of run number is shown in Fig. 3.22b.

The final value of the normalization factor is the weighted average of the normalization factors per run number while the statistical uncertainty is used as a weight. The final value is given by [152, 157, 158]:

$$F^{MSL(MSH)}_{norm} = \frac{\Sigma_i F^{MSL(MSH)}_{norm}/(\sigma^2)^{MSL(MSH)}_{stat}}{\Sigma_i 1/(\sigma^2)^{MSL(MSH)}_{stat}} \tag{3.18}$$

The statistical uncertainty is calculated as:

$$[\Delta F^{MSL(MSH)}_{norm}]_{stat} = \sqrt{\frac{1}{\Sigma_i 1/(\sigma^2)^{MSL(MSH)}_{stat}}} \tag{3.19}$$

Figures 3.21 and 3.22b are shown for the LHC17p data sample to show an example of what is observed, results for the LHC15n data sample are available in Ref. [157].

3.4.2.2 Offline Method

The normalization factors for MSL (F^{MSL}_{norm}) and MSH (F^{MSH}_{norm}) triggers using the Offline method are expressed as follows [152, 157, 158]:

$$F^{MSL}_{norm} = \frac{N^{i}_{MB}}{N_{(MB\&\&0MSL)}} \tag{3.20}$$

[1] L0a entries are events taken after a decision from the central trigger processor, CTP.

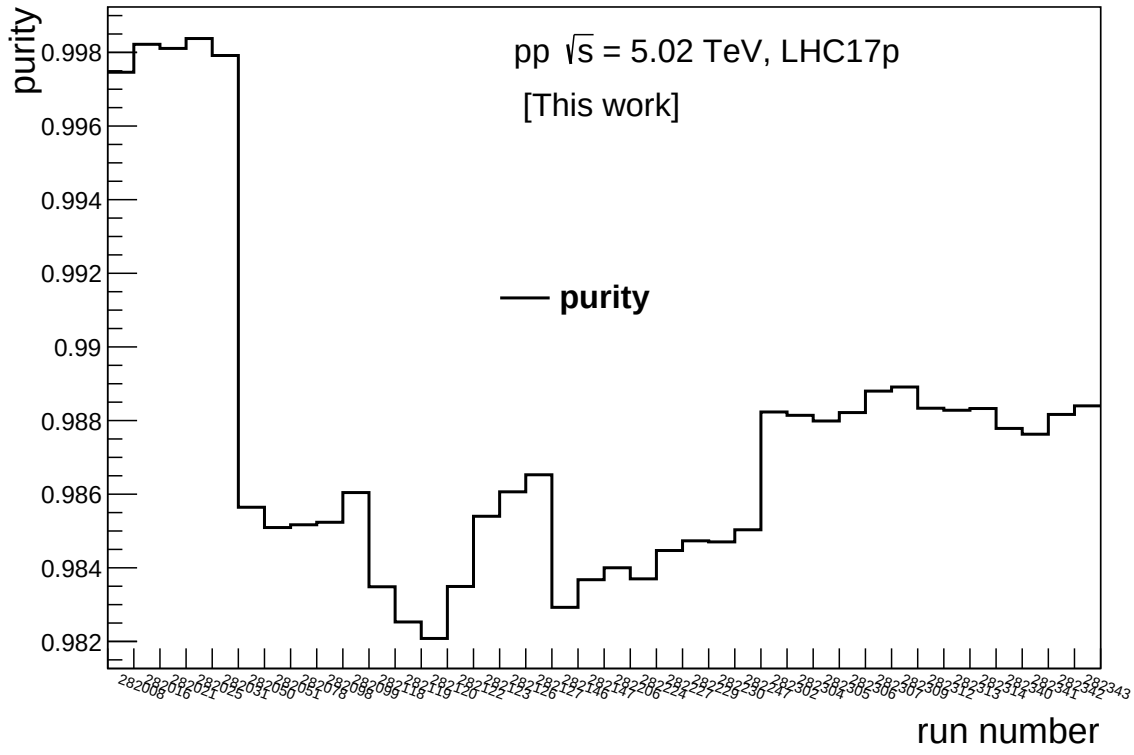

(a) Purity as function of run number.

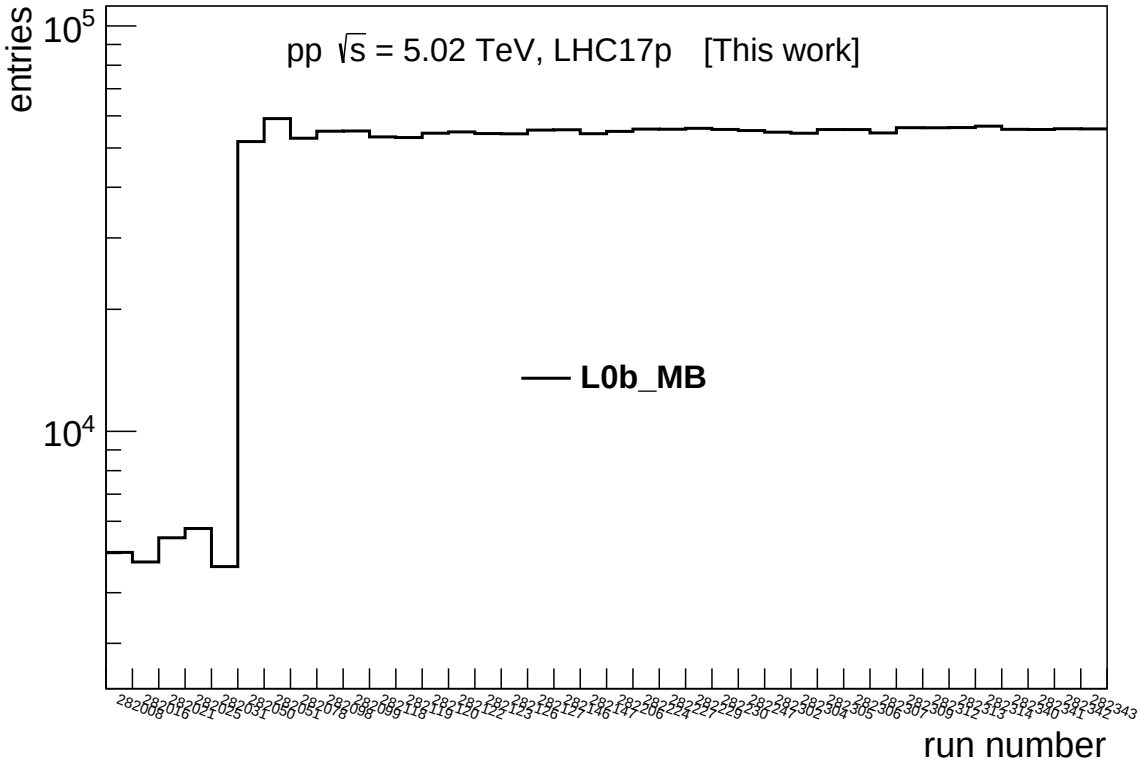

(b) L0brates as a function of run number.

Fig. 3.21 Purity (3.21a) and L0brates (3.21b) as a function of run number.

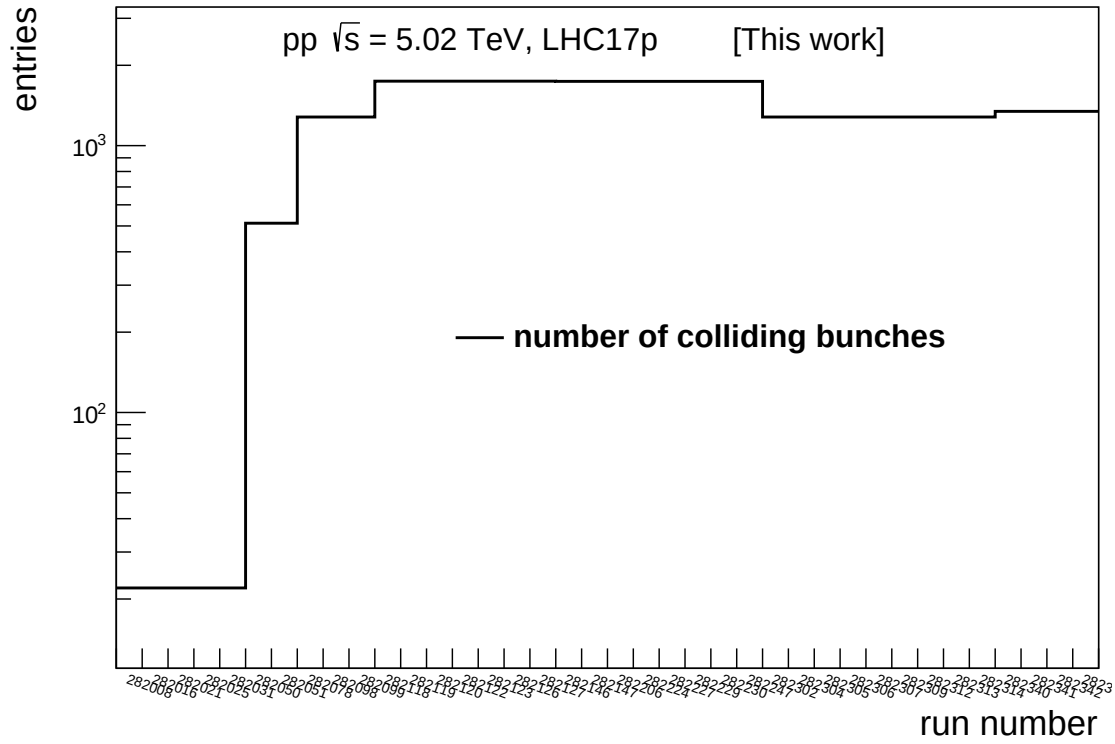

(a) Number of interacting bunches as function of run number.

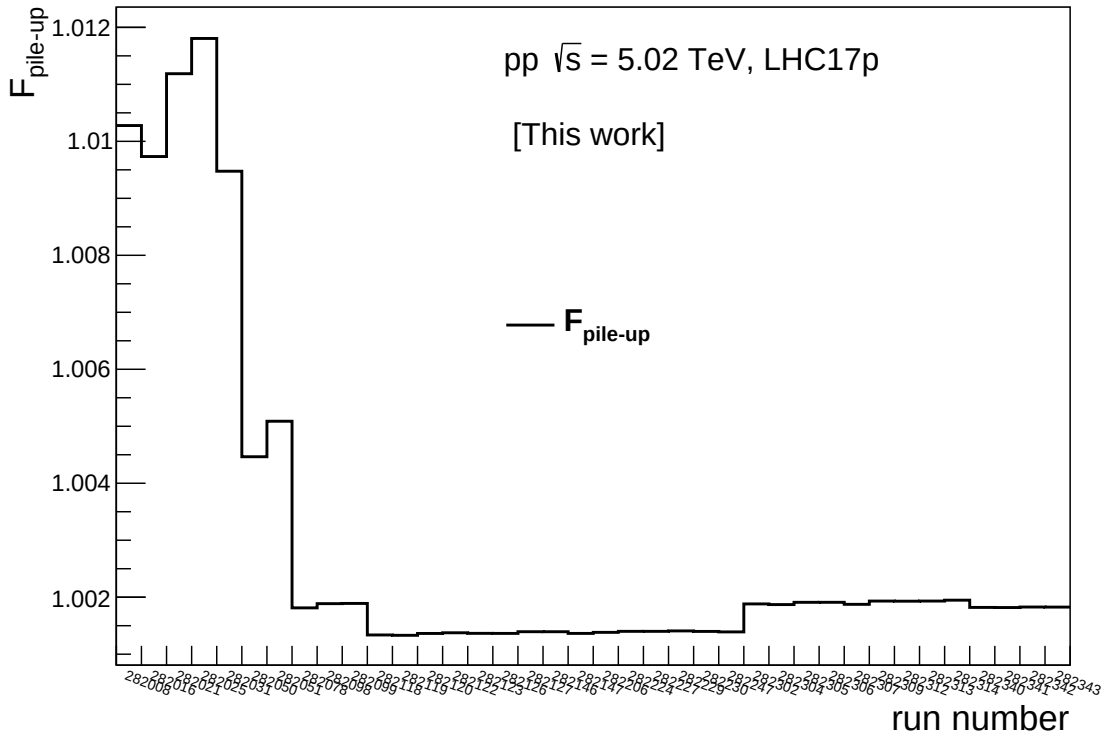

(b) Pile-up as a function of run number.

Fig. 3.22 Number of interacting bunches (3.22a) and Pile-up (3.22b) as function of run number.

and

$$F^{MSH}_{norm} = \frac{N^i_{MB}}{N^i_{MB\&\&0MSL}} \times \frac{N^i_{MSL}}{N^i_{MSL\&\&0MSH}} \tag{3.21}$$

where:

- N^i_{MB} and N^i_{MSL} are the number of MB and MSL events after the offline selection, respectively.
- $N_{MB\&\&0MSL}$ and $N_{MSL\&\&0MSH}$ are the sample of MB events containing a 0MSL input and the sample of MSL events containing a 0MSH input. The CTP trigger input ID for MSL and MSH triggers are 13 for 0MSL and 14 for 0MSH, respectively.

In the offline method, $F^i_{pile-up}$ is not considered in the determination of the normalization factor as it was implemented in the "AddPhysicsSelection" task.

The final value of the normalization factor is the weighted average of the normalization factors per run number for which the statistical uncertainty is used as a weight. The final value is given by [152, 157, 158]:

$$F^{MSL(MSH)}_{norm} = \frac{\Sigma_i F^{MSL(MSH)}_{norm}/(\sigma^2)^{MSL(MSH)}_{stat}}{\Sigma_i 1/(\sigma^2)^{MSL(MSH)}_{stat}} \tag{3.22}$$

The statistical uncertainty is calculated as:

$$[\Delta F^{MSL(MSH)}_{norm}]_{stat} = \sqrt{\frac{1}{\Sigma_i 1/(\sigma^2)^{MSL(MSH)}_{stat}}} \tag{3.23}$$

3.4.2.3 Normalization factor results

Both normalization factors as a function of run number are shown in Fig.3.23 and 3.24 for the LHC17p and q data samples. The red data points show the F_{Norm} values using the offline method and the black data points are obtained with the scaler method. The final weighted values are shown with the blue and green solid lines for offline and scaler methods, respectively. Figures 3.23a and 3.24a show F_{Norm} as a function of the run number for the MSL trigger and figures 3.23b and 3.24b show for the MSH trigger. The same was done for the LHC15n data sample to achieve the final weighted average normalization factor for the MSL and MSH triggers for which the figures are available in Ref. [157].

The final normalization factor values and corresponding statistical errors calculated using the offline and scaler methods for all the data samples are summarized in Table 3.12.

The final scaler method normalization factor values of the LHC15n data sample do not follow the same trend as observed for the LHC17p and q data sample as observed in Table

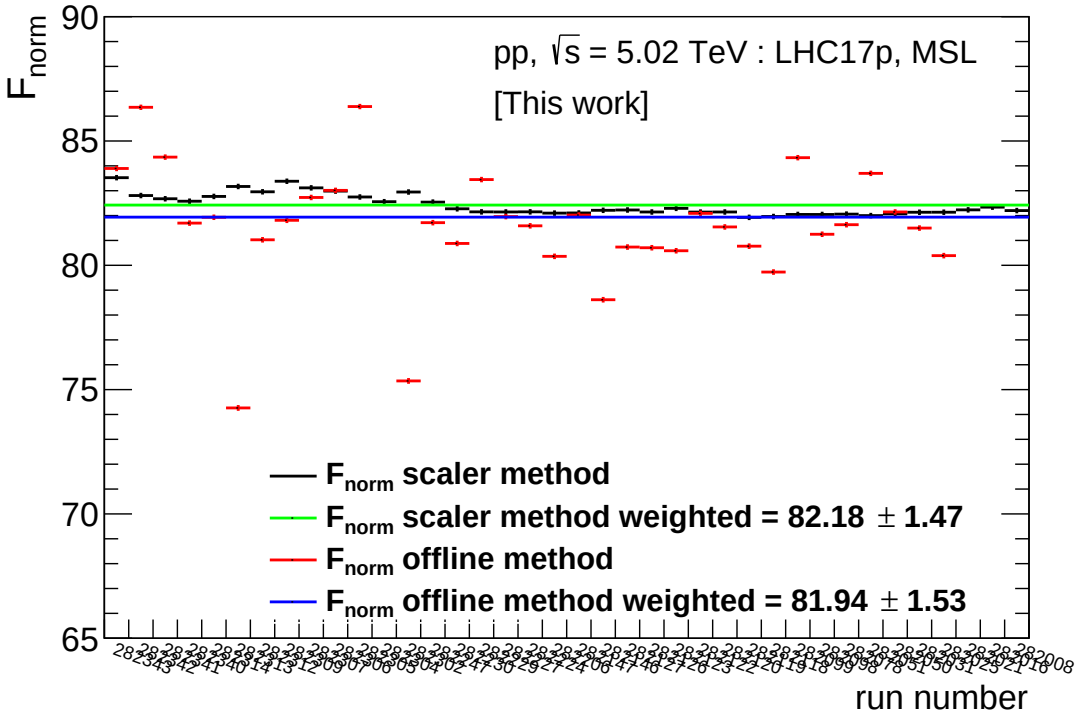

(a) Normalization factors for MSL trigger as a function of run number. Red (black) data points show the offline (scaler) methods.

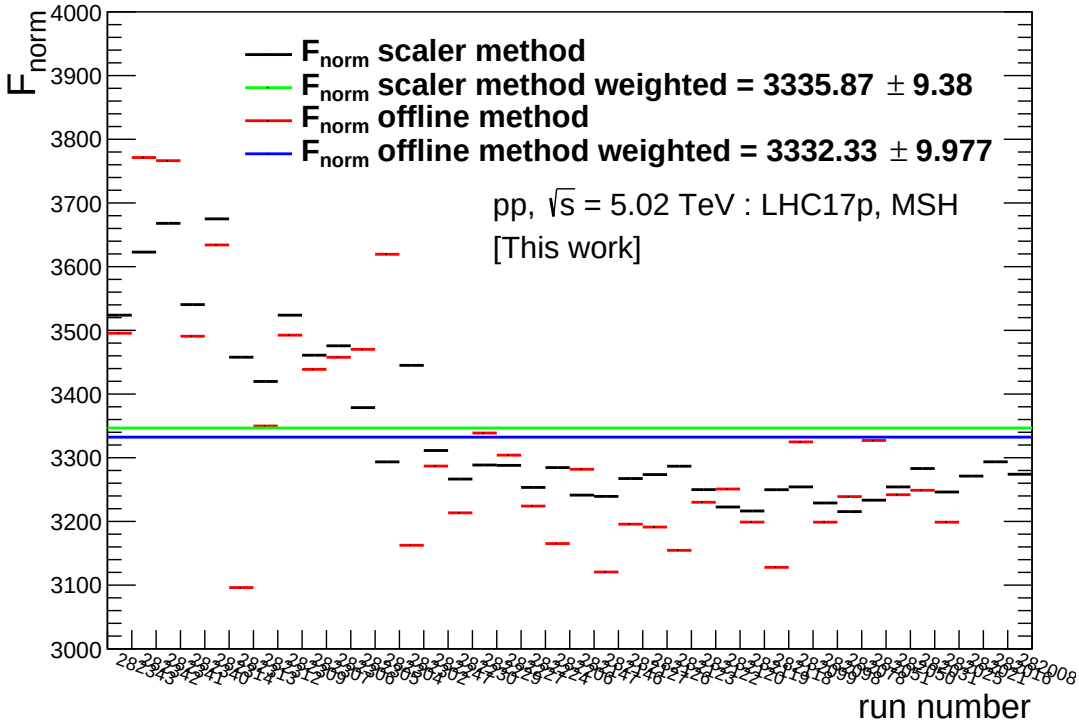

(b) Normalization factors for MSH trigger as a function of run number. Red (black) data points show the offline (scaler) methods.

Fig. 3.23 Normalization factors for MSL (3.23a) and MSH (3.23b) as a function of run number for the LHC17p data sample.

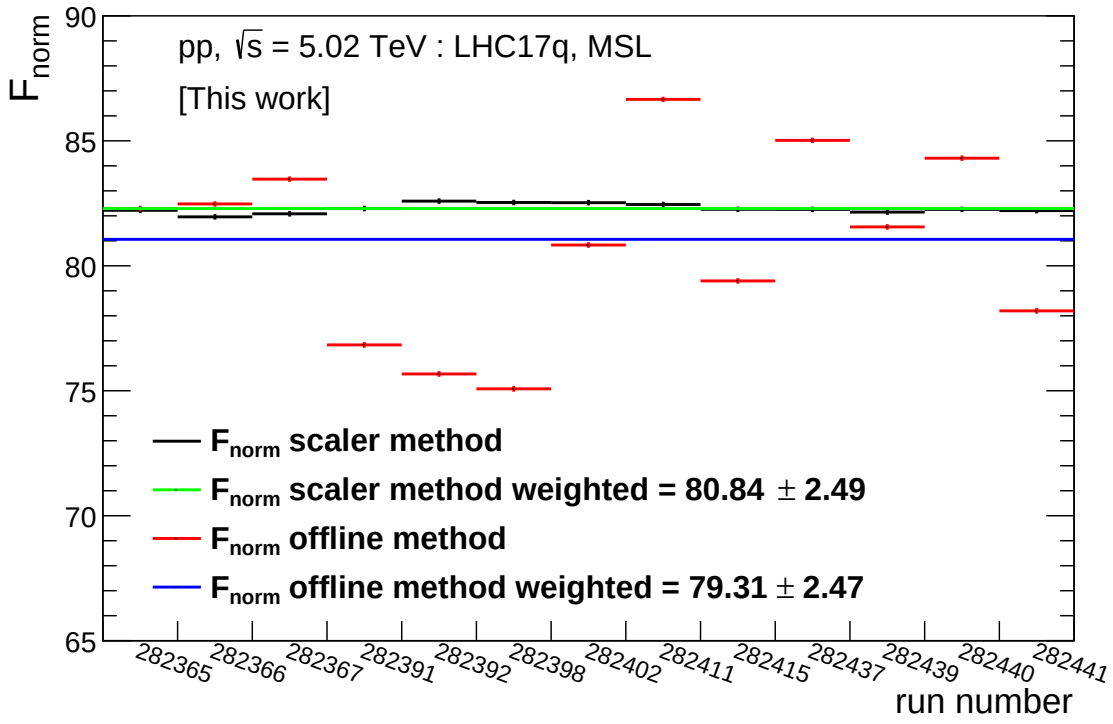

(a) Normalization factors for MSL trigger as a function of run number. Red (black) data points show the offline (scaler) methods.

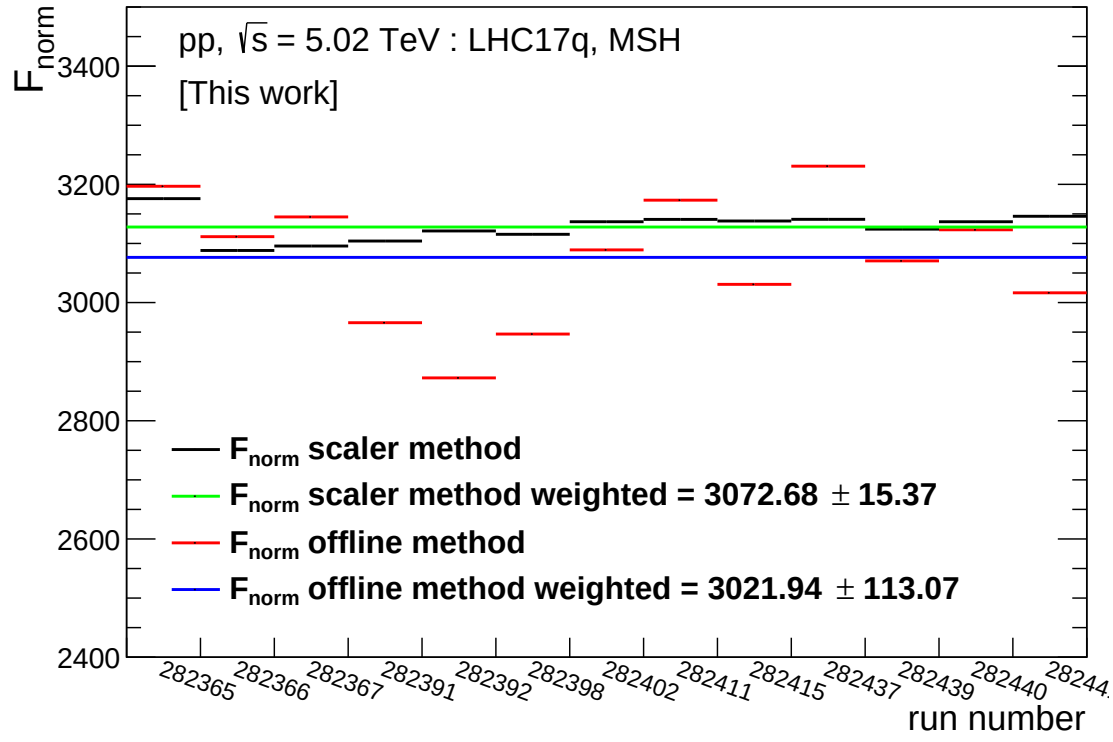

(b) Normalization factors for MSH trigger as a function of run number. Red (black) data points show the offline (scaler) methods.

Fig. 3.24 Normalization factors for MSL (3.24a) and MSH (3.24b) as a function of run number for the LHC17q data sample.

Data sample	Trigger	Scaler Method	Offline Method
LHC17p	MSL	82.18±1.47	81.94 ± 1.53
	MSH	3335.87±9.38	3332.33 ± 9.77
LHC17q	MSL	80.84± 2.49	79.31 ± 2.47
	MSH	3072.68 ± 15.37	3021.94 ± 113.07
LHC15n	MSL	34.58 ±1.18	81.96± 1.81
	MSH	1384.42 ± 7.46	3285.62 ± 11.47

Table 3.12 Normalization factors determined using scaler and offline methods for MSL and MSH data sample.

3.12 while the normalization factors obtained from the offline method are comparable. This difference in the scaler method is attributed to the pile-up factor being evaluated using the T0 (C0TVX) instead of the V0 MB trigger as already mentioned in section 3.4.2.1. Since the results for the LHC15n data sample have already been published [157], the same procedure is followed for consistency.

Since the offline method suffers from a lack of statistics, the statistical uncertainty of the method is higher than that of the scaler method. The difference in statistical uncertainties is clearly observed in the LHC17q data sample. The statistical uncertainty for the MSH trigger is $\sim 0.5\%$ for the scaler method and $\sim 3.7\%$ for the offline method. The normalization factor values obtained using the scaler method will be used to determine the cross-section of muons from heavy-flavour hadron decays while the results obtained from the offline method will be used to determine the normalization factor as a function of multiplicity as discussed later in this thesis.

3.4.2.4 Normalization factor as function of multiplicity

The normalization factor as a function of multiplicity can be determined by making use of the intergrated normalization factor computed in section 3.4.2. This method scales the factor by the number of MB and MSL(H) events as shown in the expression below [131]:

$$F_{norm_i}^{MSL(H)} = F_{norm}^{MSL(H)} \times \frac{N_{MB}^{i}}{N_{MB}} \times \frac{N_{MSL(H)}}{N_{MSL(H)}^{i}} \tag{3.24}$$

$F_{norm_i}^{MSL(H)}$ is the normalization factor per multiplicity percentile bin, $F_{norm}^{MSL(H)}$ is the integrated normalization factor calculated previously. N_{MB}^{i} and N_{MB} are the number of minimum bias events in the multiplicity percentile bin and integrated multiplicity, respectively. $N_{MSL(H)}^{i}$ and $N_{MSL(H)}$ are the numbers of MSL(H) events in the multiplicity bin and integrated multiplicity, respectively.

Table 3.13 shows a summary of the normalization factors as a function of multiplicity for the MSL and MSH triggers, respectively, for each data sample. These values are used in the analysis using the SPD estimator.

For the "Official framework", Tables C.1 and C.2 in Appendix C.0.2 show a summary of the normalization factors as a function of multiplicity for the MSL and MSH triggers, respectively, for each data sample.

3.4.2.5 Luminosity Determination

Luminosity is defined as the interaction rate per unit cross section, it measures how many particles are squeezed through a given space in a given time. The corresponding integrated luminosity [157] is given by:

$$L_{int} = \frac{N_{MSL(MSH)} \times F_{norm}^{MSL/MSH}}{\sigma_{VdM}^{T0}}, \tag{3.25}$$

where σ_{VdM} is the visible cross-section measured in the van der Meer scans either with the T0 or V0 detectors, respectively. The corresponding values are σ_{VdM}^{T0} **= (20.82 ± 0.01) mb** and σ_{VdM}^{V0} = (50.87 ± 0.04) mb [161] for the LHC17p and q data samples and; σ_{VdM}^{T0} **= (21.6 ± 0.4) mb** and σ_{VdM}^{V0} = (51.2 ± 1.2) mb [162] for the LHC15n data sample. The uncertainties quoted are the systematic uncertainties. $N_{MSL(MSH)}$ is the number of events for the MSL(MSH) triggers after the offline selection which are quoted in the tables in appendix A.2. $F_{norm}^{MSL/MSH}$ is the final value of the normalization factor given in Table 3.12.

A summary of the corresponding luminosity values is given in Table 3.14 for both MSL and MSH triggers for the data samples under study. The luminosity values for the LHC15n data sample are in agreement within statistical uncertainties with published results [49]. There is $\sim$ 2.6% and $\sim$ 2.6% difference between data and published data for the MSL and MSH trigger luminosity. These differences can be attributed to the combined differences of the F_{Norm} factors as well as the differences in the $N_{MSL/MSH}$ values that arise from the number of events analysed. The differences in the number of events analyzed is dependent on how many jobs failed during analysis when submitted on the Grid.

In order to normalize the yield to the number of inelastic pp collisions, an inelastic normalization factor is required. In the next subsection, this factor is discussed briefly.

3.4.3 Normalization to inelastic collisions

The integrated muon yield extracted in section 3.4 is the particle yield normalized to the number of MB events, however, MB needs to be scaled to the number of inelastic

Mult. Bin	LHC17p		LHC17q		LHC15n	
	MSL	MSH	MSL	MSH	MSL	MSH
$[1-2]$	38.817 ± 0.862	1765.61 ± 22.130	58.946 ± 2.020	2544.68 ± 101.94	59.849 ± 2.719	2632.18 ± 121.581
$[3-4]$	145.55 ± 3.307	9426.97 ± 99.417	189.049 ± 6.294	9950.98 ± 390.716	124.218 ± 4.472	6634.06 ± 248.395
$[5-6]$	125.477 ± 2.618	7397.85 ± 76.857	144.345 ± 4.839	6917.01 ± 272.608	108.029 ± 3.885	5188.21 ± 192.43
$[7-8]$	111.84 ± 2.354	6014.8 ± 64.309	116.491 ± 3.947	5128.56 ± 203.821	100.225 ± 3.711	4473.16 ± 170.156
$[9-11]$	100.466 ± 2.066	4968.67 ± 47.18	91.723 ± 3.078	3702.98 ± 146.122	85.016 ± 2.890	3444.7 ± 119.485
$[12-15]$	89.161 ± 1.824	3998.59 ± 36.666	73.577 ± 2.473	2756.03 ± 108.873	78.546 ± 2.577	3027.55 ± 101.089
$[16-21]$	76.936 ± 1.572	3058.02 ± 27.664	57.733 ± 1.951	2013.09 ± 79.815	77.763 ± 2.448	2750.38 ± 88.105
$[22-41]$	57.748 ± 1.184	1722.5 ± 15.687	38.567 ± 1.319	1222.77 ± 48.898	$68.763 \pm 2.132^{*}$	$2243.39 \pm 70.453^{*}$ [a]
$[42-130]$	33.221 ± 1.257	487.118 ± 16.751	20.531 ± 1.370	573.323 ± 40.058		

Table 3.13 Normalization factor per multiplicity bin for the different data samples for both the MSL and MSH triggers, used for the data-driven method analysis.

[a] $*$For the LHC15n data sample, the last multiplicity bin is $[21-100]$

Data sample	Trigger	Luminosity (nb^{-1})
LHC17p	MSL	247.19± 1.47
	MSH	1237.55± 9.38
LHC17q	MSL	26.93± 2.49
	MSH	1832.30 ± 15.37
LHC15n	MSL	55.15 ± 1.25
	MSH	106.60 ± 7.47

Table 3.14 Integrated luminosity for MSL and MSH data sample.

collisions. This is achieved by correcting the muon yield with an inelastic normalization factor, F_{inel}, which is the ratio of the V0 visible cross-section to the inelastic cross-section.

The V0 visible cross-section in pp collisions at $\sqrt{s} = 5.02$ TeV can be extracted from the ALICE luminosity determination report [162]. However, ALICE has not measured the inelastic cross-sections in pp collisions yet and as a result, the inelastic cross-section values are adopted from other experiments as discussed in [163]. The inelastic normalization factor in pp collisions at $\sqrt{s} = 5.02$ TeV is:

$$F_{inel} = 0.7573 \pm 0.0190\ (2.51\%)$$

where the value in brackets is the systematic uncertainty of the inelastic normalization factor.

The next section deals with is a discussion on the acceptance times efficiency which is the factor used to correct for the detector inefficiency.

3.5 Acceptance times Efficiency ($A \times \epsilon$)

The acceptance times efficiency ($A \times \epsilon$) correction factor takes into account the detector conditions during the data taking period and a correction factor is determined to correct for the detector inefficiency. Information of the Forward Muon Spectrometer can be accessed from the Offline Calibration Data Base (OCDB). The inefficiency can be caused by for instance missing channels and mis-alignment of the trigger and tracking chambers with respect to the detector.

The GEANT3 transport package [145]; which is a Monte Carlo Transport code used to model the transport of particles through matter; is used for the detector description and the detector response. A run-by-run simulation is done to take into account the condition of the detector over time. The simulated statistics are proportional to the number of muon triggers.

The analysis tasks used in the acceptance times efficiency study can be accessed via https://github.com/alisw/AliPhysics/tree/master/PWG/muondep/AccEffTemplates

The $A \times \epsilon$ factor is defined as:

$$A \times \epsilon = \frac{\text{reconstructed events}}{\text{generated events}} \tag{3.26}$$

In this study, FONLL is used in two different ways:

- To ascertain the shape of the p_{T}- and η-distributions with the MC used to determine $A \times \epsilon$ and;
- To obtain the charm and beauty differential cross-sections for comparison with the experimental results.

The next section is a discussion of the FONLL parameterizations and how these are used to ascertain the shape of the p_{T}- and η-distributions.

3.5.1 FONLL Parameterizations

FONLL has already been discussed in more detail in Chapter 1. In this study, there are three contributions that are considered towards calculating the single muon inclusive differential cross-section, namely:

- b $\rightarrow \mu$ with branching ratio of 10.86%
- b $\rightarrow D \rightarrow \mu$ with branching ratio of 9.66%
- c $\rightarrow \mu$ with branching ratio of 10.33%

The CTEQ6.6 PDFs was used for these contributions, these are the only available PDFs for pp collisions at $\sqrt{s} = 5.03$ TeV. Figures 3.25a and 3.25b show the differential cross-sections for the transverse momentum and η of the various contributions and their sum (black data points), respectively.

The total differential cross-sections are then fitted with the following functions:

$$p_0 e^{x(p_1(1-e^{p_2 x}+p_3)} x^{-p_4}(p_5 + x p_6 + x^2 p_7) \tag{3.27}$$

for the transverse momentum, and

$$p_0 + x^2 p_1 + x^4 p_2 + x^6 p_3 + x^8 p_4 \tag{3.28}$$

for η, where p_i are free parameters and x is the variable. The fits are shown in Fig. 3.26; for the MSL trigger, the fit is from 2-20 GeV/c while the MSH trigger is fitted from 4-20

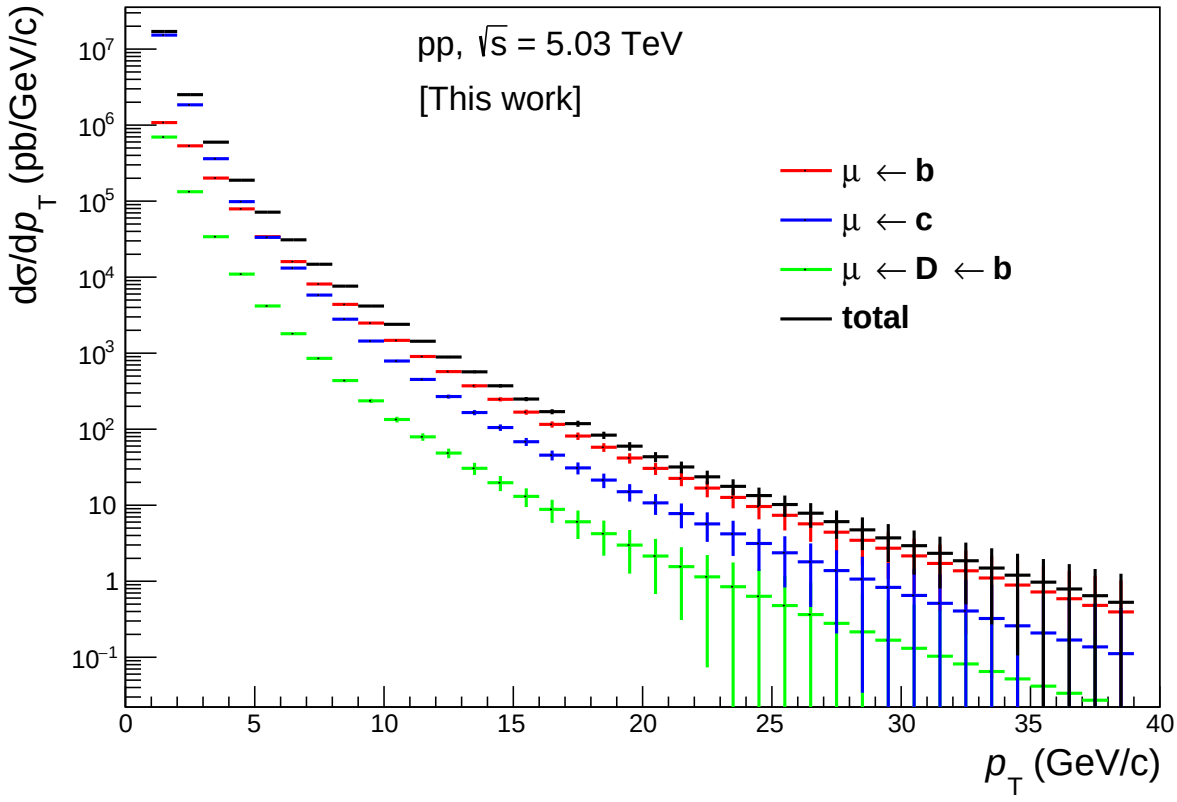

(a) p_{T} Cross-sections obtained from FONLL simulations.

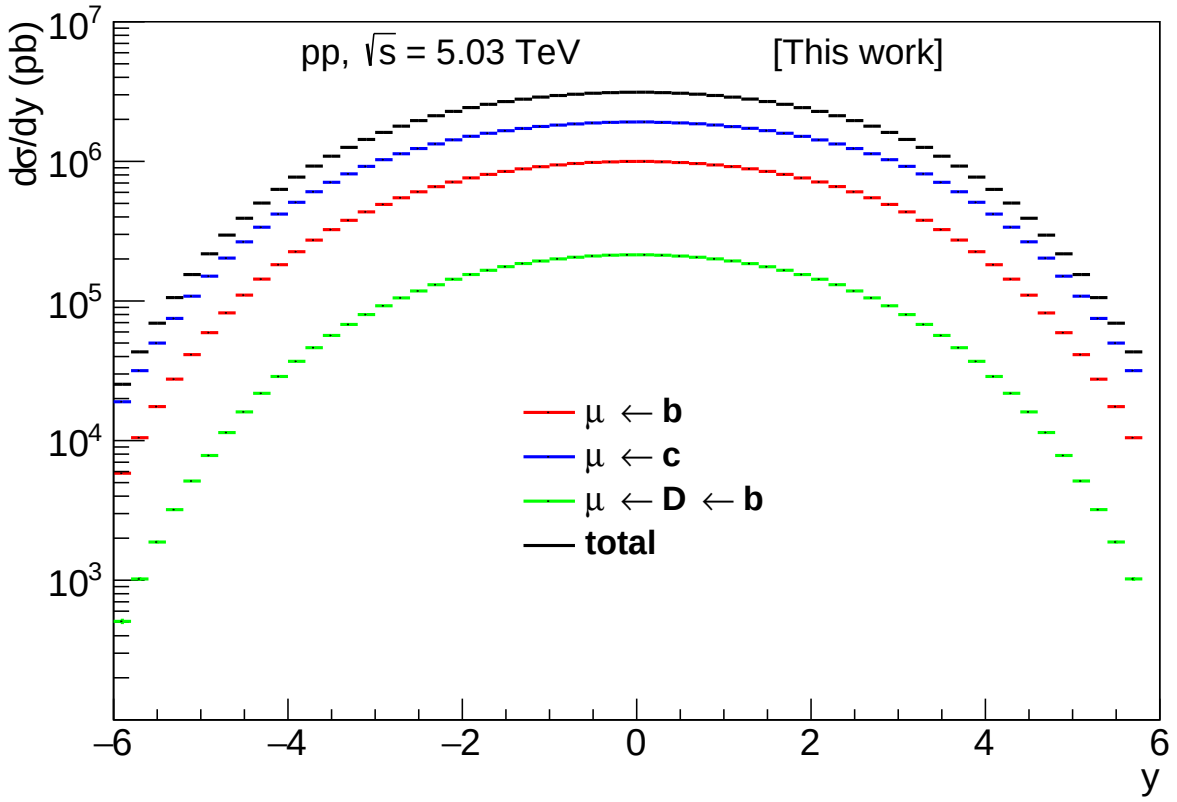

(b) Rapidity cross-sections obtained from FONLL simulations.

Fig. 3.25 Differential p_{T} (3.25a) and rapidity (3.25b) cross-sections from FONLL simulations.

GeV/c. The choice of $p_{\mathrm{T}} > 2$ GeV/c for the MSL trigger is attributed to the fact that since there is a high contribution from primary charged pion and kaon (hadron) decay muons for $p_{\mathrm{T}} < 2$ GeV/c (will be discussed in the next section), the region of interest is 2-20 GeV/c. Since the MSH trigger has a p_{T} threshold of 4.2 GeV/c, only muons with $p_{\mathrm{T}} > 4.2$ GeV/c are picked up by this trigger. These fits are used as the input to generate muons that would be detected in an ideal detector with no inefficiencies.

The reconstructed and generated data obtained from the MC simulation as shown in Fig. 3.27 are then used to determine the $A \times \epsilon$ factor using equation 3.26. Figure 3.27a shows the reconstructed and generated MC data as a function of p_{T} for both the MSL and MSH triggers. Figure 3.27b shows the $A \times \epsilon$ as a function of p_{T} for MSL (blue data points) and MSH (red data points) triggers for the LHC17p data sample.

Due to the larger statistical uncertainties at high p_{T} for both MSL and MSH triggers slight fluctuations are observed. To overcome this, a new MC simulation is done with new p_{T} ranges for both MSL and MSH triggers. The MSL trigger p_{T} range changed from $2-20$ GeV/c to $4-20$ GeV/c while the MSH trigger p_{T} range changed from $4-20$ GeV/c to $6-20$ GeV/c, this is shown in Fig. 3.28. This change in p_{T} introduced effectively more statistics, allowing for the statistical uncertainty to decrease.

To further decrease the uncertainty, the bin width at high p_{T} was increased, allowing for the bins to have more statistics. The two MC simulations were combined for both MSH and MSH triggers to ensure the MSL trigger still starts at $p_{\mathrm{T}} = 2$ GeV/c and the MSH trigger starts at 4 GeV/c. Figure 3.28 shows the changes in the statistical error evolution as the different changes were implemented. The blue line shows the final statistical error evolution. These changes were applied to all the data samples as they all suffered from a lack of statistics at high p_{T} (> 8 GeV/c).

A summary of how the statistical uncertainty decreased at high p_{T} is shown in Table 3.15 for all the data samples. In the "before" column the statistical uncertainties at high p_{T} are listed while the "after" column quotes the statistical uncertainties after the above mentioned changes were applied.

The $A \times \epsilon$ factor is extracted in different pseudorapidity intervals as shown in Fig. 3.29. Figures 3.29a and 3.29b show the $A \times \epsilon$ as a function of p_{T} for the MSL trigger and MSH trigger, respectively. This is done to observe the consistency of the fraction of reconstructed and generated events at different pseudorapidity intervals as well as to check for "edge effects" at the boundaries of the muon spectrometer acceptance. No clear trend is observed between the two triggers and/or the pseudorapidity intervals.

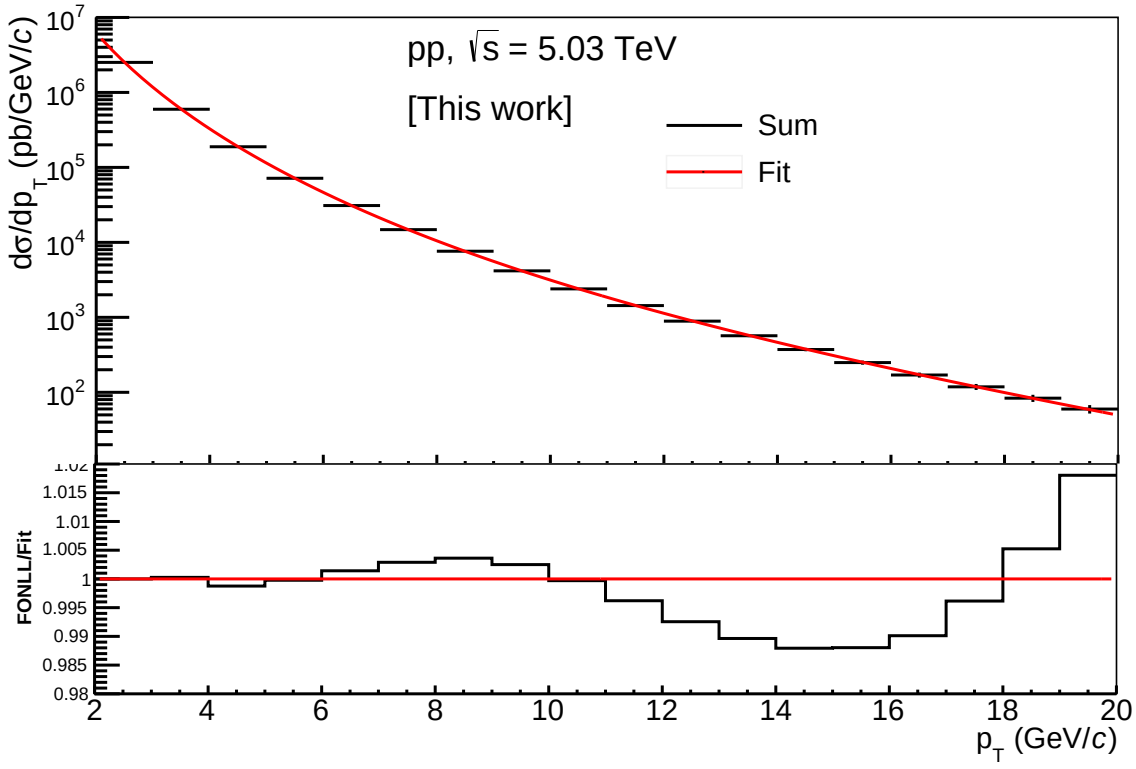

(a) Fitted p_{T}-differential cross-section and ratio plot of the fit and p_{T}-differential cross-section.

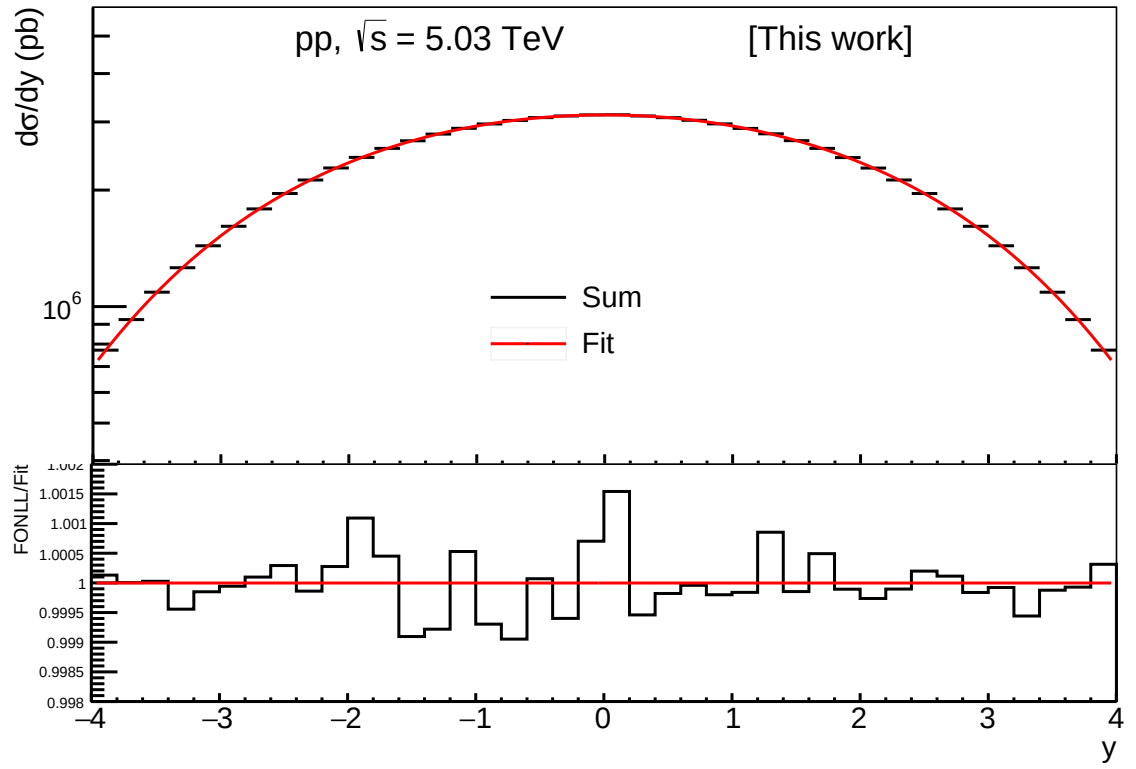

(b) Fitted rapidity-differential cross-section and ratio plot of the fit and rapidity-differential cross-section.

Fig. 3.26 p_{T}-differential (3.26a) and η (3.26b) cross-sections fitted with functions expressed by equation 3.27 and 3.28, respectively.

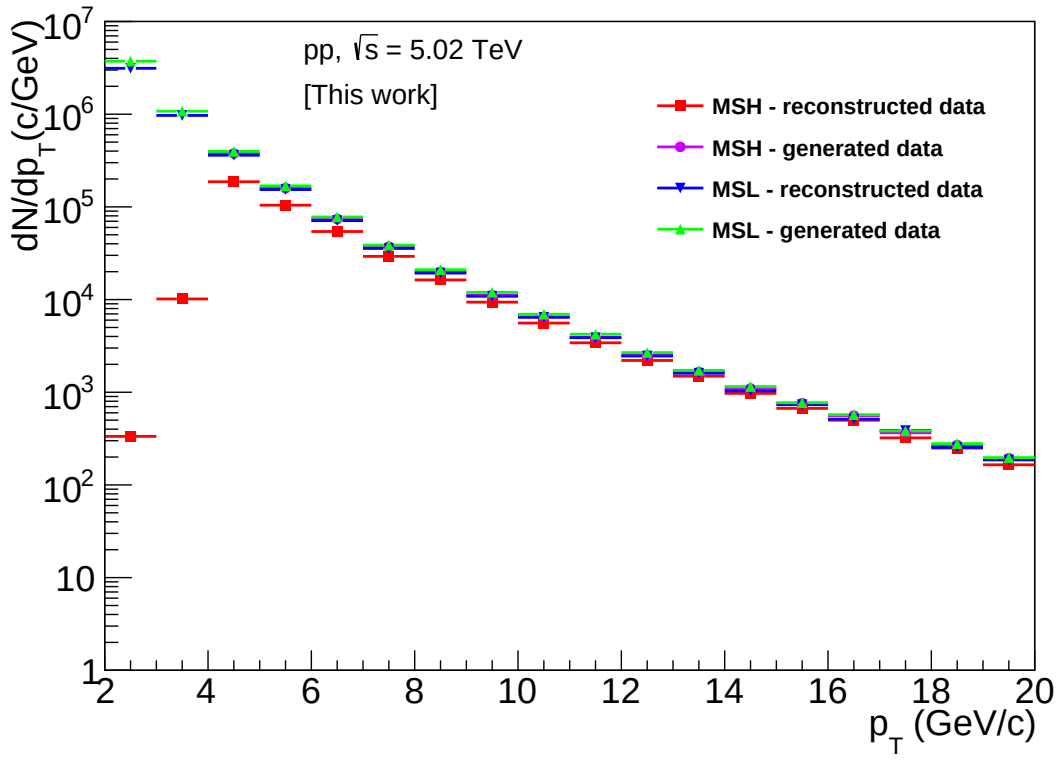

(a) Reconstructed and generated MC data as a function of p_{T} for MSL and MSH triggers.

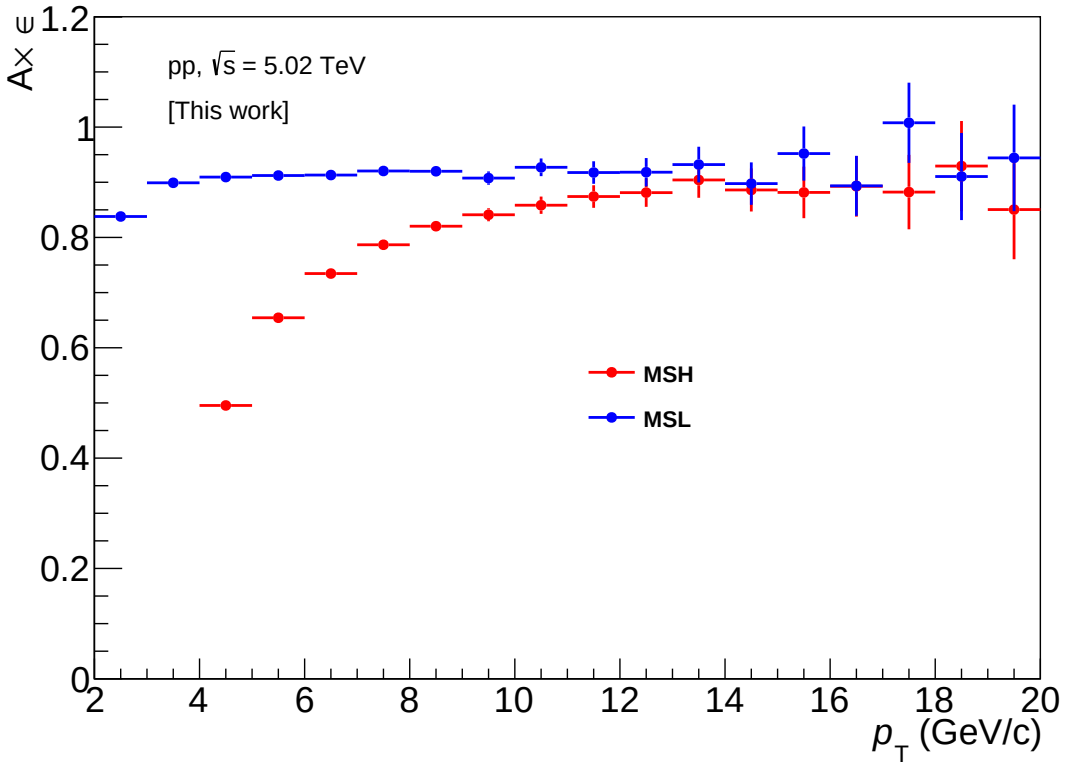

(b) $A \times \epsilon$ as a function of p_{T} for MSL and MSH triggers. The error bars are the statistical uncertainties.

Fig. 3.27 Reconstructed and generated yields (3.27a) and $A \times \epsilon$ (3.27b) as a function of p_{T} for MSL and MSH triggers.

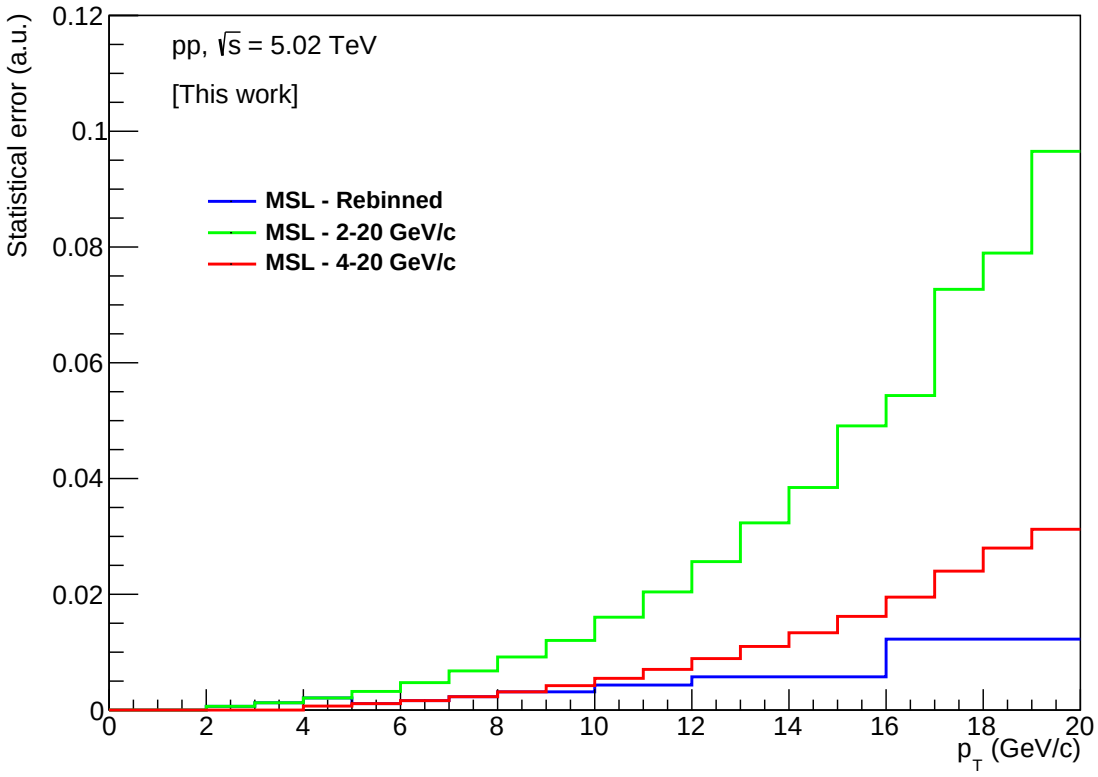

(a) Statistical error evolution for the MSL trigger.

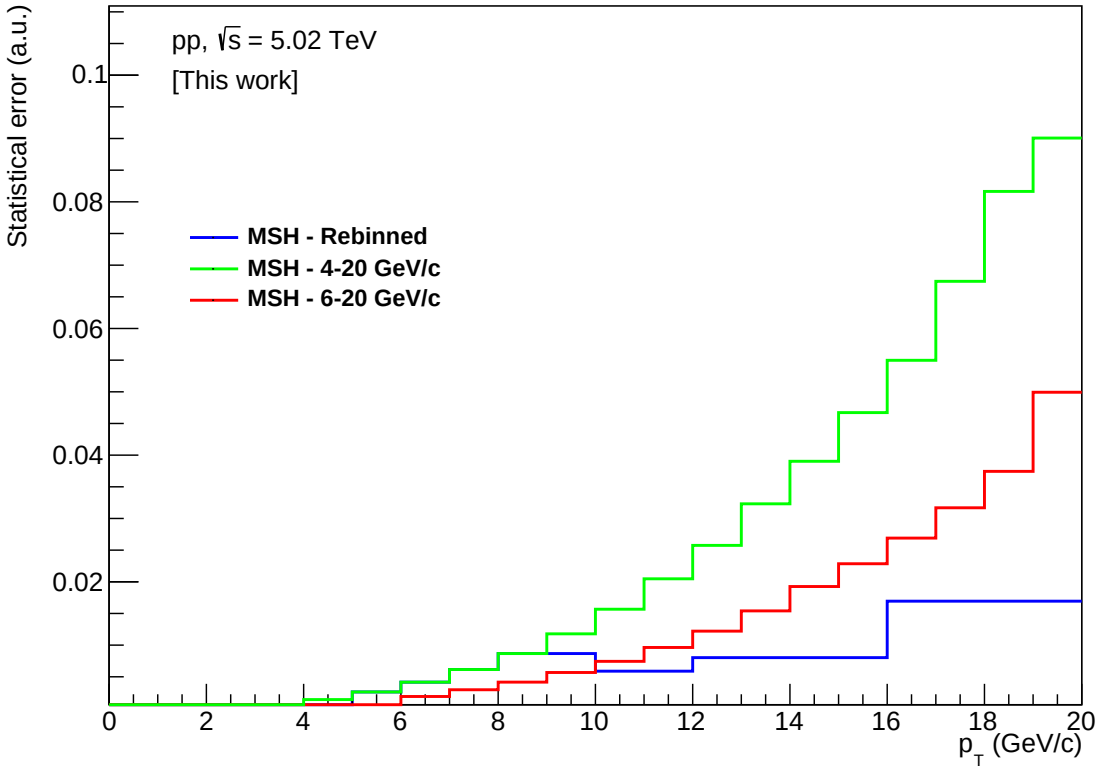

(b) Statistical error evolution for the MSH trigger.

Fig. 3.28 Statistical error evolution for the MSL trigger (3.28a) and MSH trigger (3.28b) for LHC17p data sample.

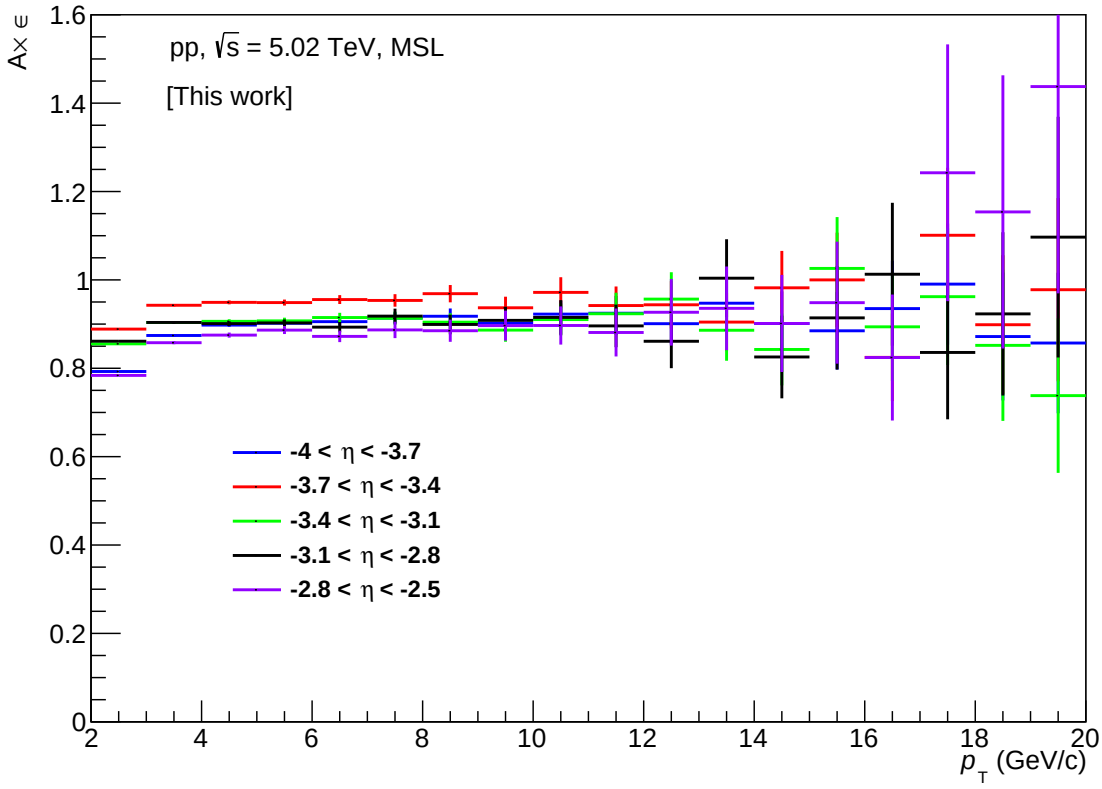

(a) $A \times \epsilon$ as a function of p_{T} in different η bins for the MSL trigger.

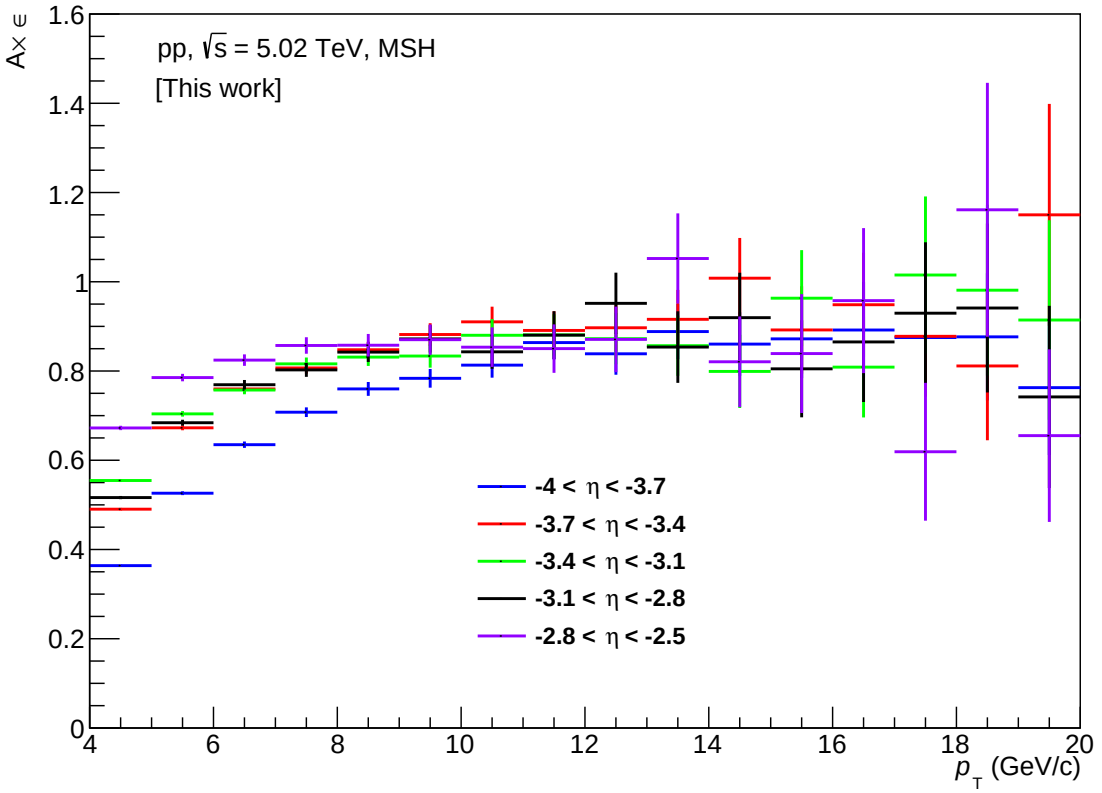

(b) $A \times \epsilon$ as a function of p_{T} in different η bins for the MSH trigger.

Fig. 3.29 $A \times \epsilon$ as a function of p_{T} in different η bins for MSL (3.29a) and MSH (3.29b).

Data sample		Before	After
LHC17p	MSL	10%	1.5%
	MSH	5%	1.8%
LHC17q	MSL	9%	3.8%
	MSH	3.8%	1.6%
LHC15n	MSL	13%	1.5%
	MSH	9%	3.5%

Table 3.15 Summary of the statistical uncertainties at $p_{\mathrm{T}} = 20$ GeV/c.

3.5.2 Final results of $A \times \epsilon$

The final values of $A \times \epsilon$ shown in Fig. 3.30 and Fig. 3.31a and 3.31b showing the corresponding 2D plots of $A \times \epsilon$ as a function of p_{T} and η, are used to correct the measured number of muons to obtain the actual number of muons produced for the LHC17p data samples. Similarly, the final values of $A \times \epsilon$ for the LHC17q and LHC15n data samples is shown in Fig. D.1 in Appendix D. For the MSL trigger, $A \times \epsilon$ saturates at around 90% at high p_{T} ($p_{\mathrm{T}} > 10$ GeV/c). For the MSH trigger, $A \times \epsilon$ saturates at around 85% at high p_{T} ($p_{\mathrm{T}} > 12$ GeV/c). A similar trend is observed in the LHC17q data sample. For the LHC15n data sample, $A \times \epsilon$ saturates at around 90% and 89% for the MSL and MSH triggers, respectively.

3.5.3 $A \times \epsilon$ as a function of multiplicity

The $A \times \epsilon$ as a function of multiplicity needs to also be taken into account. To account for the multiplicity dependence of the $A \times \epsilon$ correction factor, the correction factor is studied as a function of multiplicity. Two production cycles - LHC16e and LHC16e-plus anchored to the LHC15o run period in Pb-Pb collisions at $\sqrt{s_{NN}} = 5.02$ TeV - are exploited using a simulation based method based on the embedding technique [164] .

The embedding technique involves embedding a single muon in each of the MB events for 80% of the chunks. In the case of the two production cycles utilized in this study, one muon is embedded in each MB event for 80% of the chunks of the 137 runs, about 10M muons are reconstructed. The muon input shapes are obtained from a parameterization of the p_{T}- and y-distributions using FONLL as discussed above. The $A \times \epsilon$ is extracted by applying a weight proportional to the number of MSL/MSH triggered events in each run. This is done to take into account the evolution of the detector efficiency with time.

To avoid introducing any bias, only muons in real data are embedded. The $A \times \epsilon$ is studied as a function of corrected number of tracklets in $|\eta| < 1$. Figure 3.32a shows the multiplicity dependence of $A \times \epsilon$, the number of corrected tracklet multiplicity is shown

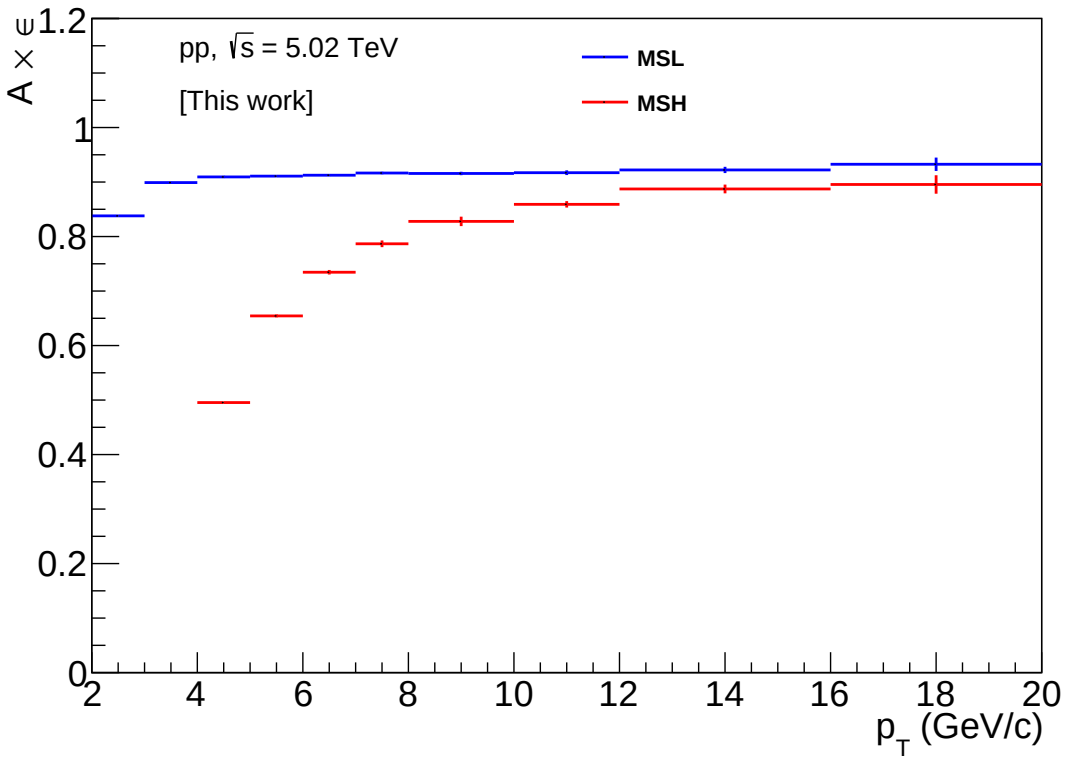

Fig. 3.30 $A \times \epsilon$ for MSL and MSH triggers as a function of p_{T} for the LHC17p data sample. The vertical lines are the statistical uncertainties associated with the results.

up to 300 in Pb-Pb collisions at $\sqrt{s_{NN}} = 5.02$ TeV. In this study, a maximum of ~ 130 corrected tracklets is achieved. It is observed that the $A \times \epsilon$ is constant in this corrected tracklet range. It can therefore be concluded that the $A \times \epsilon$ in pp collisions will be constant too.

It is however important to note that the $A \times \epsilon$ varies at low multiplicities, especially the first bin which is scaled by 0.85 at low p_{T}. This is well observed in Fig. 3.32b where at low multiplicity, the points fluctuate and thereafter remain constant at 0.31 for higher multiplicities.

In the next section, a look into how all the correction factors thus far affect the muon yield and inclusive differential cross-section is shown.

3.6 Corrected inclusive muon yield

The inclusive differential cross-section can be determined taking into account the steps discussed in the previous section. The inclusive differential cross-section is expressed as [157]:

$$\frac{d\sigma_{\mu\pm\leftarrow HF}}{dp_{\mathrm{T}}} = \frac{d\sigma_{tot}^{\mu\pm\leftarrow HF}/dp_{\mathrm{T}}dy - d\sigma_{bckg}^{\mu\pm\leftarrow HF}/dp_{\mathrm{T}}dy}{A \times \epsilon \cdot F_{norm} \cdot N_{MSL/MSH}} \cdot \sigma_{MB} \tag{3.29}$$

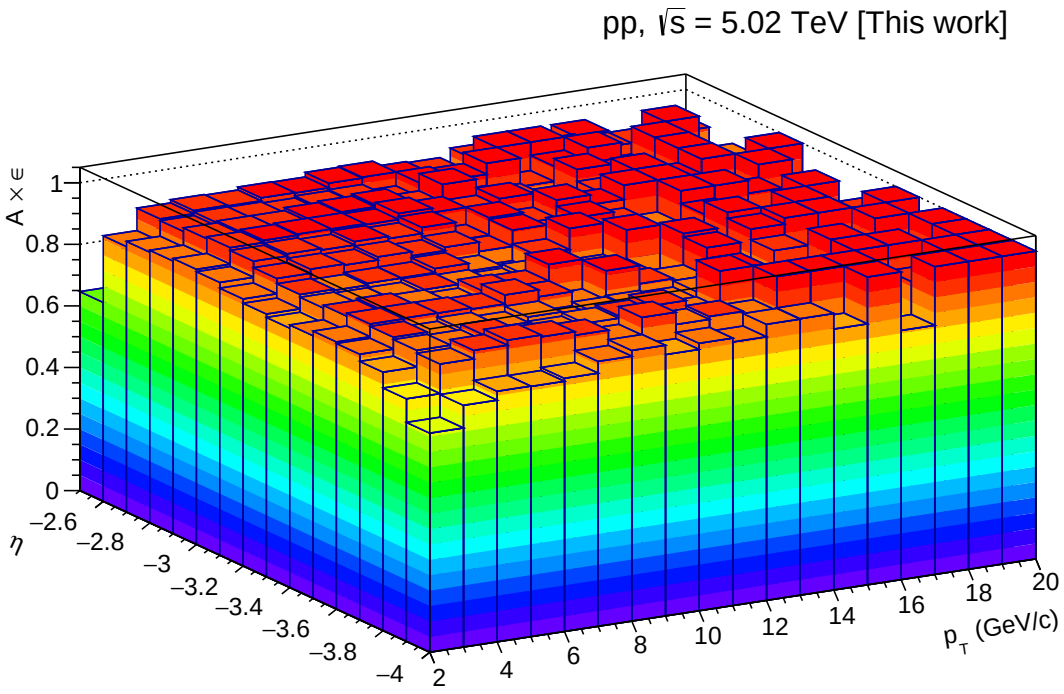

(a) $A \times \epsilon$ as a function of p_{T} in different η bins for the MSL trigger.

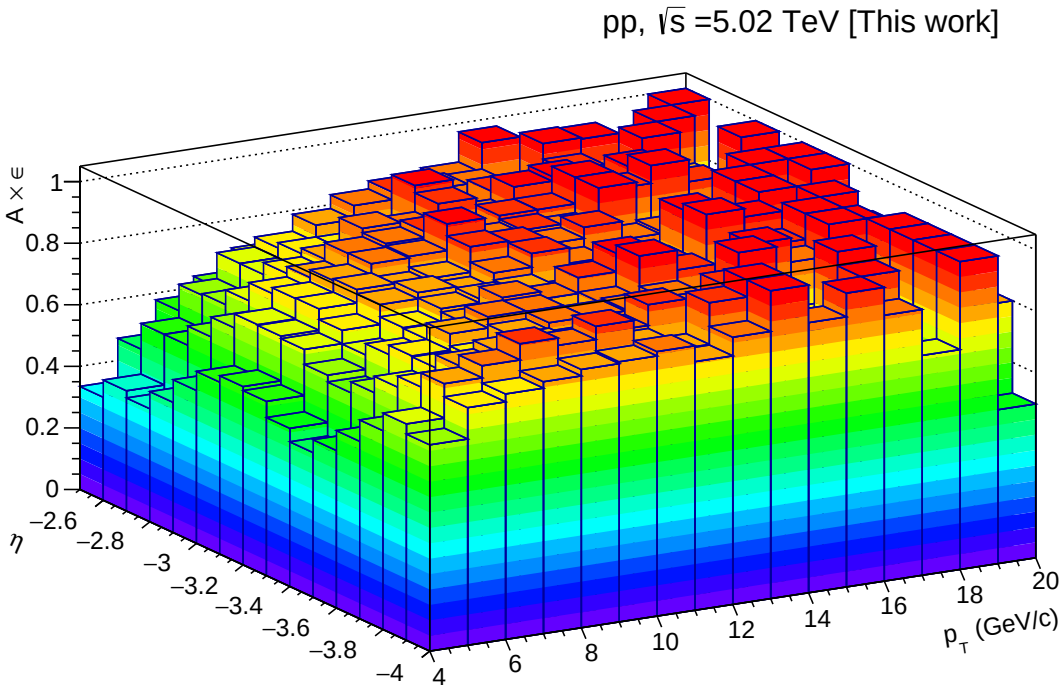

(b) $A \times \epsilon$ as a function of p_{T} in different η bins for the MSH trigger.

Fig. 3.31 2D Distribution of the $A \times \epsilon$ as a function of p_{T} and η for MSL (3.31a) and MSH (3.31b).

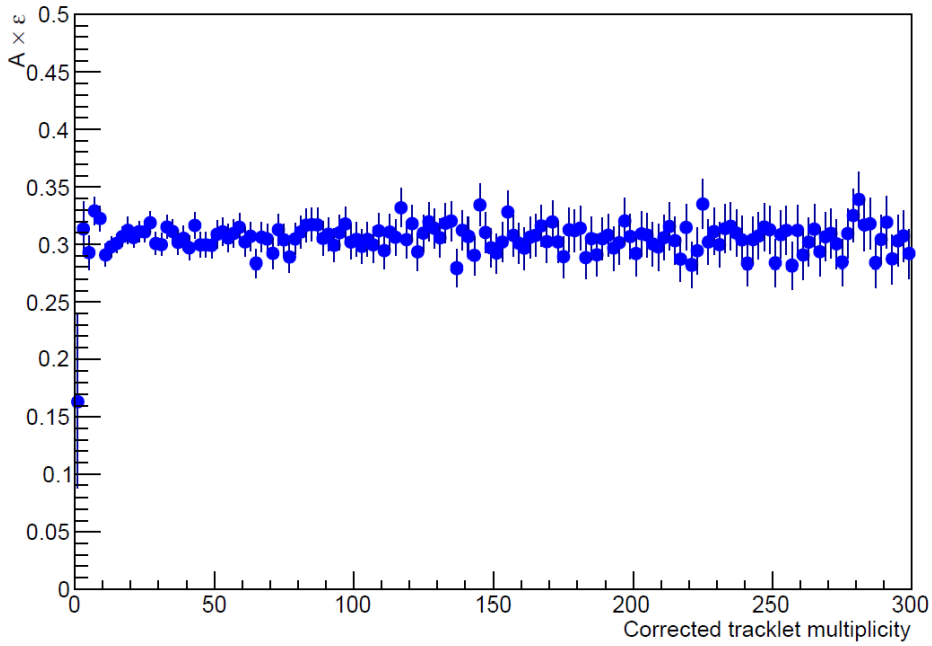

(a) $A \times \epsilon$ as a function of corrected SPD tracklet multiplicity from embedding production.

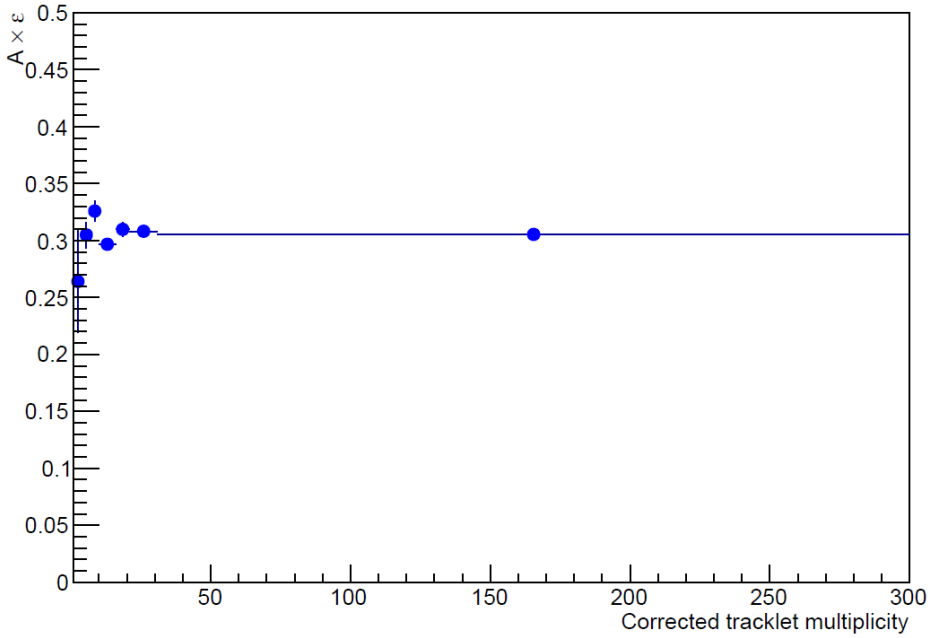

(b) $A \times \epsilon$ as a function of corrected SPD tracklet multiplicity from embedding production illustrating the fluctuations at low multiplicities and consistent at 0.31 for corrected tracklet multiplicity > 30.

Fig. 3.32 $A \times \epsilon$ as a function of corrected SPD tracklet multiplicity from embedding production.

where $A \times \epsilon$ is the acceptance times efficiency, F_{norm} is the normalization factor, $N_{MSL/MSH}$ are the number of MSL/MSH events and σ_{MB} is the visible cross-section measured in the van der Meer scans for the T0 detector.

Before determining the inclusive differential cross-section, a comparison of the p_{T}-distributions for the MSL and MSH triggered events is made. The inclusive muon yield distributions shown in section 3.4 are corrected for with $A \times \epsilon$ and normalized to the equivalent number of MB events in MSL and MSH triggered events. The ratio of the MSL triggered events to the MSH triggered events is expected to be unity. The F_{norm} and $N_{MSL/MSH}$ values used for this correction are quoted in Table 3.16. A bin-by-bin correction of the $A \times \epsilon$ is performed.

Data sample	LHC17p	LHC17q	LHC15n
σ_{MB}	20.82±0.01 mb	20.82±0.01 mb	21.6±0.4 mb
N_{MSL}	5.452467×10^7	6 099 882	3.1603659×10^7
N_{MSH}	6 808 855	1.08007×10^7	1.495153×10^7
F_{Norm}^{MSL}	82.18 ± 1.53	80.84 ± 2.49	34.75 ± 1.18
F_{Norm}^{MSH}	3319.65 ± 9.39	3072.68 ± 15.37	1390.81 ± 7.46

Table 3.16 Summary of the F_{norm}, $N_{MSL/MSH}$ and σ_{MB}

Figure 3.33a shows the comparison of the p_{T}-distributions for the MSL and MSH triggered events after normalization to MB events and $A \times \epsilon$ correction. To better view the comparison, the ratio of the MSL to MSH distribution is determined. This ratio is shown in Fig. 3.33b and deviates from unity at high-p_{T} ($p_{\mathrm{T}} > 16$) by 8%.

The inclusive differential cross-section is obtained by considering both the MSL and MSH inclusive differential cross-sections where the MSL inclusive differential cross-section is considered from 2-7 GeV/c while the MSH inclusive differential cross-section is considered from 8 GeV/c. The overall inclusive differential cross-section is obtained by multiplying the p_{T}-distributions for the MSL and MSH triggered events shown in Fig. 3.33a with the visible cross-section measured in the van der Meer scans for the T0 detector.

Figure 3.34 shows the inclusive differential cross-section for the combined data samples. It is important to note that the inclusive differential cross-section shown in Fig. 3.34 is a cross section of all the muon sources as measured by the muon spectrometer. In order to determine the inclusive differential cross-section from heavy flavour decay, the predominant muon source contributions need to be comprehensively studied and removed, these are indicated by the red term in equation 3.44. The next section focuses on the different muon sources and their contribution to the inclusive differential cross-section.

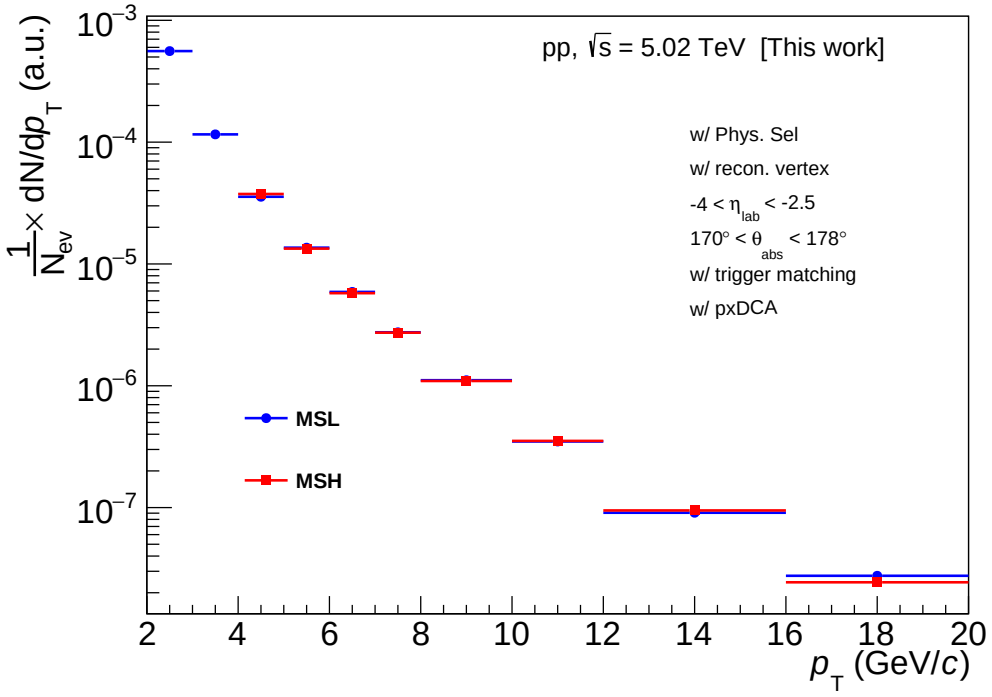

(a) Comparison of the p_{T}-distributions for the MSL and MSH triggered events normalized to MB events and corrected for $A \times \epsilon$ for the combined data samples.

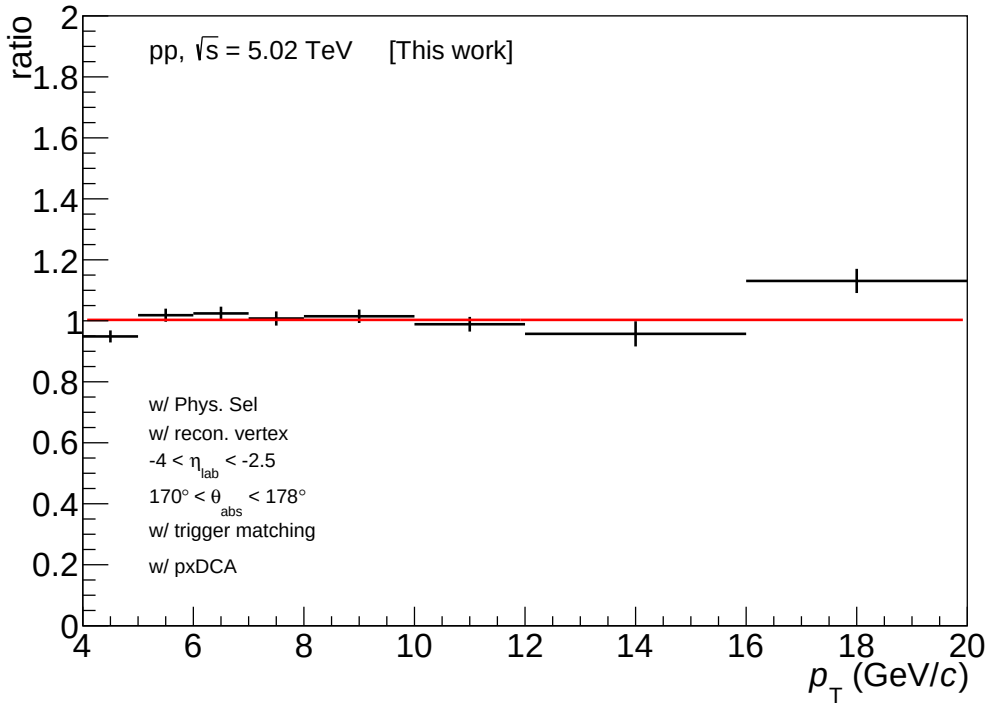

(b) Ratio of the p_{T}-distributions for the MSL and MSH triggered events.

Fig. 3.33 Comparison of the p_{T}-distributions (3.33a) and ratio (3.33b) of the MSL and MSH triggered events.

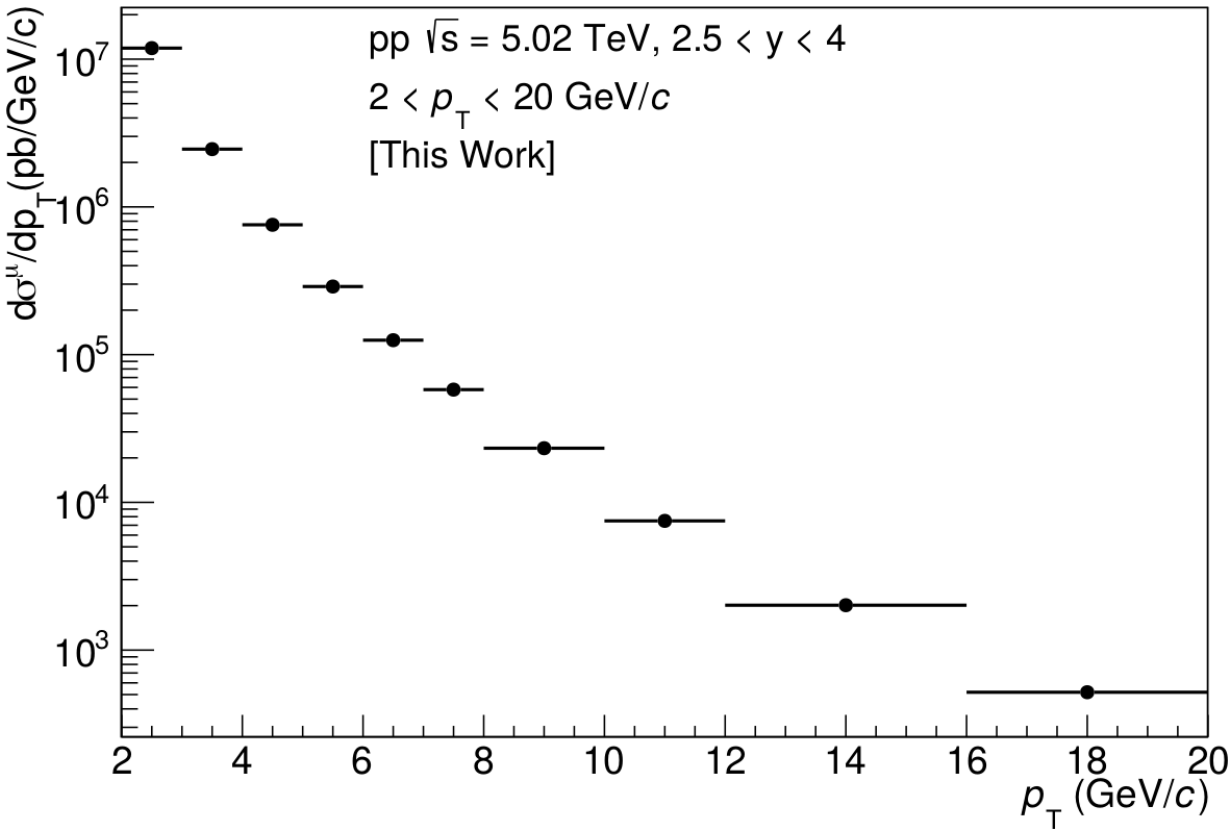

Fig. 3.34 Differential inclusive single muon cross-section. Statistical errors are smaller than the symbols.

3.7 Background Subtraction

In this study, the p_{T} region of interest is $2 < p_{\mathrm{T}} < 20$ GeV/c. This region is chosen since this is where HF decay muons dominate. There are four contributions in the p_{T} region of interest which are considered in the background subtraction in this analysis.

- The main background contribution at low/intermediate p_{T} is from primary charged pion and kaon decays;
- In the region $2 < p_T < 5$ GeV/c, the contribution of secondary muons (primary charged pions and kaons) produced inside the front absorber via the interactions of light hadrons with the absorber material;
- At high p_{T} ($p_T >\sim 14/15$ GeV/c) the main source of background is from W/Z/γ^*-decay muons;
- The contribution from decay muons of J/ψ is small over the whole p_{T} range compared to the other contributions [157].

In this section, these contributions will be discussed in detail.

3.7.1 Contributions of muons from primary charged pion and kaon decays

As already mentioned, single decay muons from primary charged π and K are the main contributions at low/intermediate p_{T}. Since these contributions are even larger at $p_{\mathrm{T}} <$ 2 GeV/c, the p_{T} region of interest is $2 < p_{\mathrm{T}} < 20$ GeV/c in the present HF studies. The strategy implemented in this analysis has already been used in other analyses [49, 158]. The strategy involves using published ALICE measurements of primary charged pion and kaon decays at midrapidity extrapolated to forward rapidity as inputs. The strategy is implemented and extensively discussed in detail in [49, 157] for pp collisions at $\sqrt{s} = 5.02$ TeV and upon which this current study is based.

The contribution of muons from primary charged π and K is subtracted from the inclusive muon yield according to the expression:

$$\frac{dN_{pp}^{\mu\rightarrow HF}}{dp_T} = \frac{dN_{pp}^{incl\mu}}{dp_T} - \frac{dN_{pp}^{\mu\rightarrow K,\pi}}{dp_T} \tag{3.30}$$

The muon background contribution and the corresponding estimated background fraction from primary charged π and K is presented. The background fraction is determined using the expression:

$$\text{fraction} = \frac{\mu \leftarrow \pi/K}{\text{inclusive } \mu} \tag{3.31}$$

where $\mu \leftarrow \pi/K$ is the inclusive p_{T} distribution of single decay muons of charged π and K and inclusive μ is the inclusive μ distribution from experimental data that were corrected for by the $A \times \epsilon$ correction factor and normalized to minimum bias events. The muon background contribution from primary charged pions and kaons, as well as the corresponding fraction are shown in Fig. 3.35a and 3.35b, respectively. A comparison of Fig. 3.35b with simulations by means of PYTHIA8 [63] obtained results can be found in the Appendix E.1 figure E.1b.

The total muon background fraction from both primary charged π and K decays in the acceptance of the muon spectrometer goes up to $\sim 39\%$ at $p_{\mathrm{T}} = 2$ GeV/c and decreases with p_{T} down to $\sim 4\%$ at $p_{\mathrm{T}} = 20$ GeV/c as quoted in [49]. In this study however, the total muon background fraction from both primary charged π and K decays in the acceptance of the muon spectrometer goes up to $\sim 47\%$ at $p_{\mathrm{T}} = 2$ GeV/c and decreases with p_{T} down to $\sim 4\%$ at $p_{\mathrm{T}} = 20$ GeV/c. The differences are a result of using different bin widths. For the multiplicity results it is necessary to take care of this contribution as

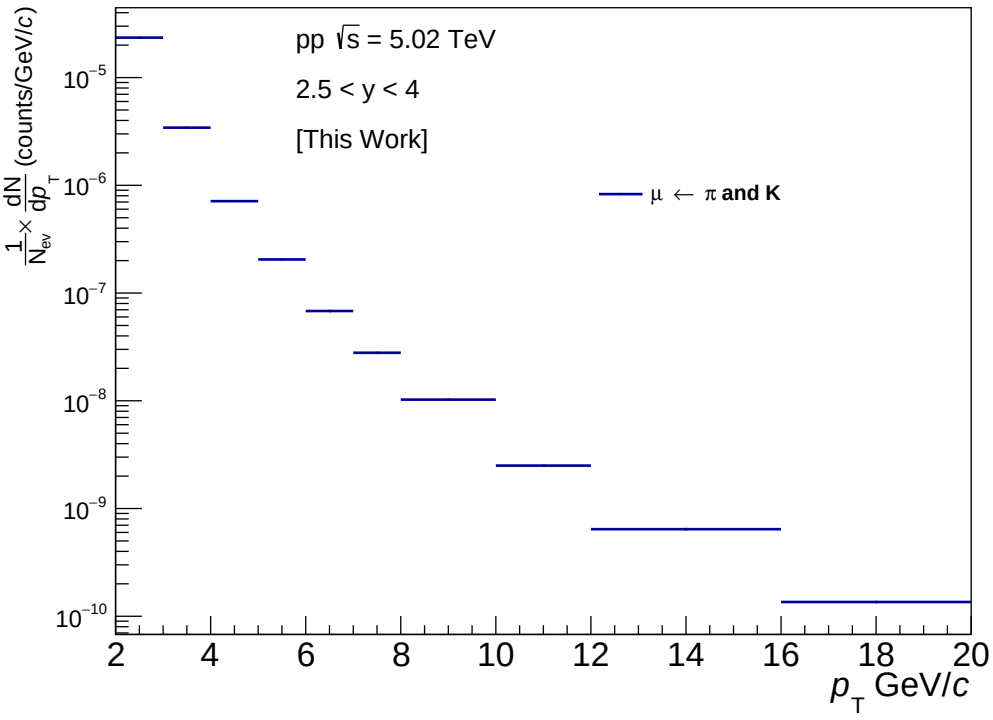

(a) Inclusive p_{T} distribution of single decay muons of charged π and K at forward rapidity in pp collisions at $\sqrt{s} = 5.02$ TeV.

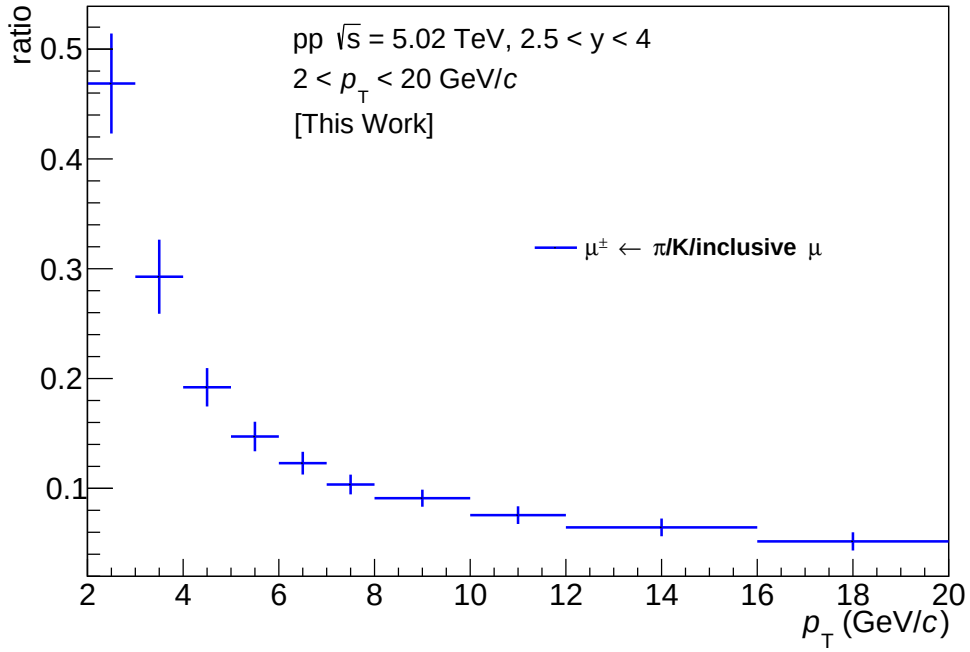

(b) Background fraction of single decay muons from primary charged π and K at forward rapidity in pp collisions at $\sqrt{s} = 5.02$ TeV.

Fig. 3.35 Inclusive p_{T} distribution (3.35a) and background fraction (3.35b) of single decay muons from primary charged π and K at forward rapidity in pp collisions at $\sqrt{s}$ = 5.02 TeV.

a function of multiplicity. The next subsection is a discussion on the primary pion and kaon contribution as a function of multiplicity.

3.7.1.1 Muon contribution from pion and kaon decays as a function of multiplicity

Since the final result is also presented as the heavy-flavour production as a function of charged-particle multiplicity, the primary charged π and K hadron decay muon contribution needs to be extracted in different multiplicity bins and/or percentile bins for the two multiplicity measurements. For this analysis, the inputs are only available at $\sqrt{s} = 7$ TeV [165] as a function of multiplicity and not at $\sqrt{s} = 5.02$ TeV. An extra step is therefore added to the strategy described above to account for the center-of-mass energy differences.

Input spectra:

The input spectra of the primary charged π and K used in this study are extracted from Ref. [165]. Figure 3.36 shows the p_{T} distribution spectra of primary charged π (left) and K (right) measured at midrapidity ($|y| < 0.9$) in different multiplicity classes in pp collisions at $\sqrt{s} = 7$ TeV up to 20 GeV/c. The error bars are the total uncertainties summed in quadrature.

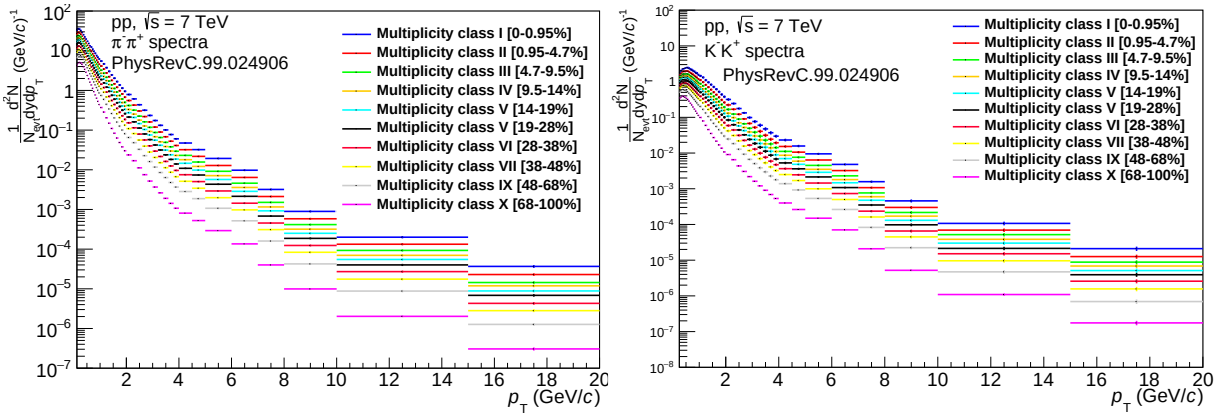

Fig. 3.36 p_{T} distributions of primary charged π (left) and K (right) decays in different multiplicity classes in pp collisions at $\sqrt{s} = 7$ TeV measured at midrapidity [165].

Energy scaling:

The energy scaling factor can be determined using the pseudorapidity density ($dN_{ch}/d\eta$) distributions at $\sqrt{s} = 5.02$ and 7 TeV. This factor is determined using the following expression:

$$F_{energy} = \frac{(dNch/d\eta)_{7TeV}}{(dN_{ch}/d\eta)_{5.02TeV}} = \frac{(1/N_{evt} \cdot d^2N/dydp_T)^{\pi,K}_{7TeV}}{(1/N_{evt} \cdot d^2N/dydp_T)^{\pi,K}_{5.02TeV}} \tag{3.32}$$

where F_{energy} is the scaling factor, $(dNch/d\eta)$ is the pseudorapidity denstiy distribution at $\sqrt{s} = 5.02$ and 7 TeV, $(1/N_{evt} \cdot d^2N/dydp_T)^{\pi,K}$ is the double differential yield at $\sqrt{s} = 5.02$ and 7 TeV. The validity of this method of determining the scaling factor.

Published data of the pseudorapidity density $(dN_{ch}/d\eta)$ distributions at $\sqrt{s} = 5.02$ and 7 TeV [166] are used to determine the scaling factor, this is achieved by taking the ratio of the 7 TeV distribution with the 5.02 TeV distributions. To obtain a single value of the scaling and not as a function of η, the ratio is fitted with a pol0 function. The scaling factor is determined to be $F_{energy} = 1.08334 \pm 0.343954$. This value is used to divide the input spectra shown in Fig. 3.36 to obtain the scaled input distributions. Figure 3.37 shows the pseudorapidity density $(dN_{ch}/d\eta)$ distributions at $\sqrt{s} = 5.02$ and 7 TeV (left) and the ratio (right).

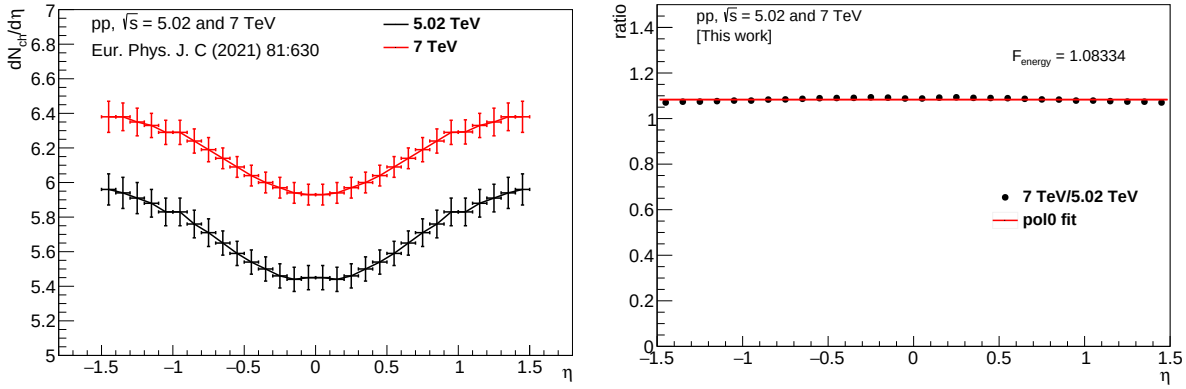

Fig. 3.37 Pseudorapidity density $(dN_{ch}/d\eta)$ distributions at $\sqrt{s} = 5.02$ and 7 TeV [166] (left) and the ratio (right)

Extrapolation of π and K spectra to high p_{T}:
The same procedure described in [49, 157] for the extrapolation is followed here where the p_{T}-distribution of the input spectra of the primary charged π and K are extrapolated to higher p_{T}, up to 40 GeV/c. The distributions are fitted 1000 times with a power-law function:

$$f(p_{\mathrm{T}}) = \frac{a}{(b^2 + p_{\mathrm{T}}^2)^c} \tag{3.33}$$

where a, b, c are free parameters. After which the statistical and systematic uncertainties are added in quadrature while results with $\chi^2/\mathrm{ndf} > 1.5$ are discarded. This has to be done for each multiplicity class for both the π and K scaled spectra. Figures 3.38 and 3.39 show the extrapolated distributions for the primary charged π and K, respectively. To save space, all 10 multiplicity class distributions are shown in one figure. Sub-figures **a) - j)** show the multiplicity starting from multiplicity class I and increasing in numeric order.

The same procedure followed to obtain the extrapolation factor from midrapidity to for-

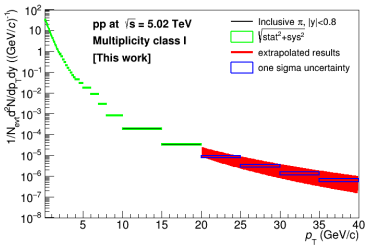

(a) Multiplicity class I

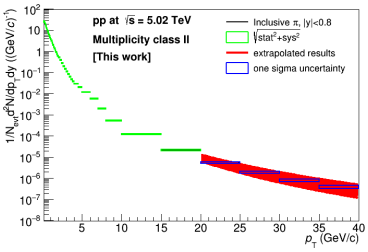

(b) Multiplicity class II

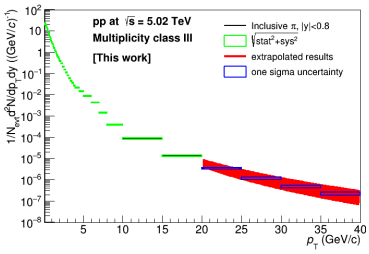

(c) Multiplicity class III

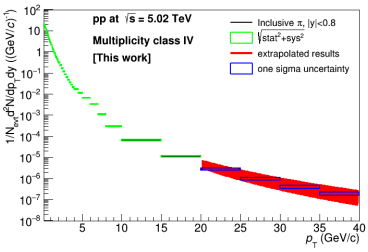

(d) Multiplicity class IV

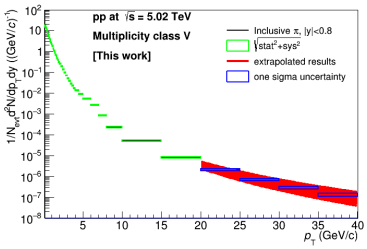

(e) Multiplicity class V

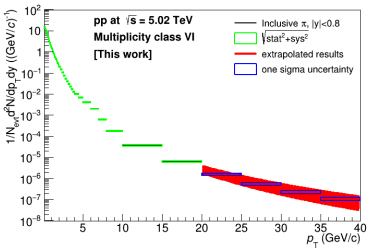

(f) Multiplicity class VI

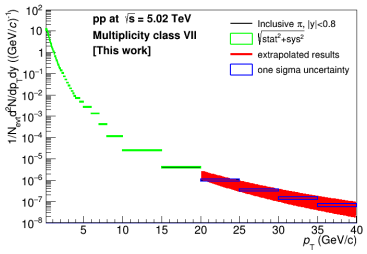

(g) Multiplicity class VII

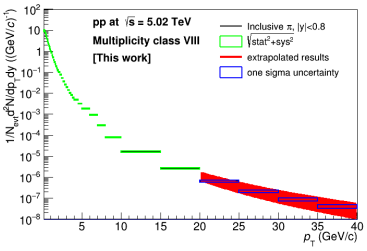

(h) Multiplicity class VIII

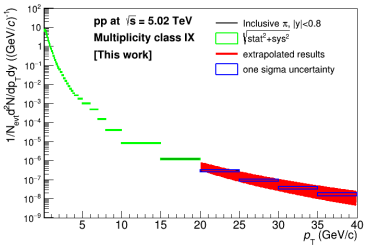

(i) Multiplicity class IX

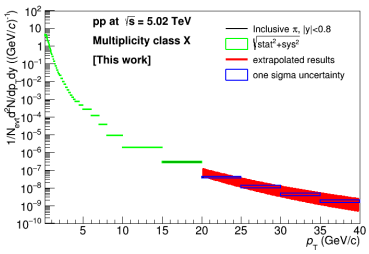

(j) Multiplicity class X

Fig. 3.38 Extrapolated p_{T} distributions of primary charged pion decays in different multiplicity classes in pp collisions at $\sqrt{s} = 5.02$ TeV measured at midrapidity.

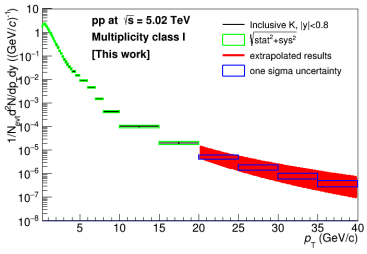

(a) Multiplicity class I

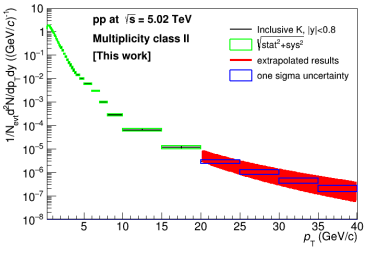

(b) Multiplicity class II

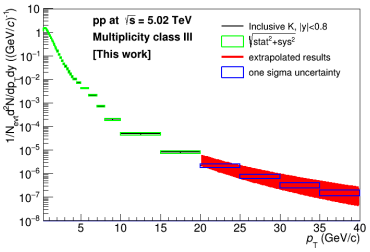

(c) Multiplicity class III

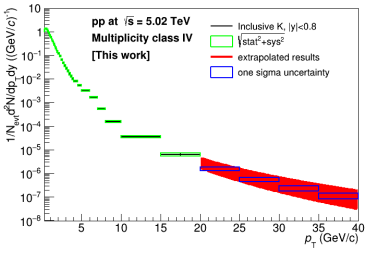

(d) Multiplicity class IV

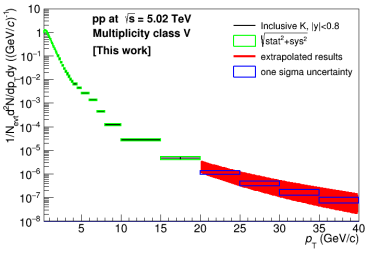

(e) Multiplicity class V

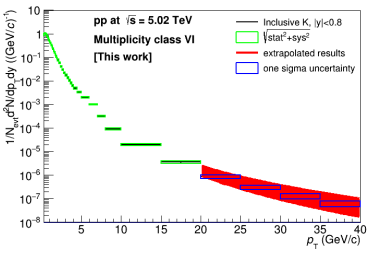

(f) Multiplicity class VI

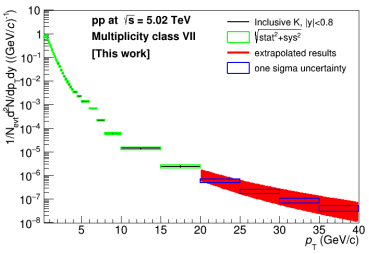

(g) Multiplicity class VII

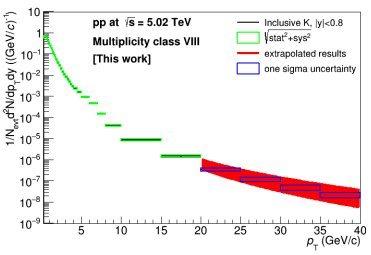

(h) Multiplicity class VIII

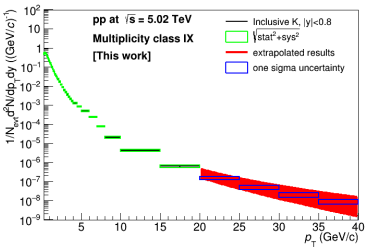

(i) Multiplicity class IX

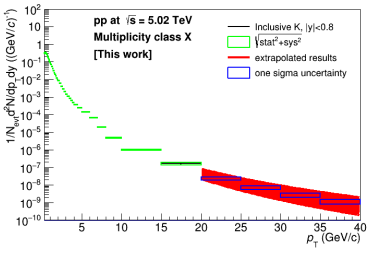

(j) Multiplicity class X

Fig. 3.39 Extrapolated p_{T} distributions of primary charged kaon decays in different multiplicity classes in pp collisions at $\sqrt{s} = 5.02$ TeV measured at midrapidity.

ward rapidity described in [49, 157] is followed for the respective multiplicity percentile bins.

The corresponding estimated muon background fraction from primary charged π and K is shown in Fig. 3.40. The muon background fraction is determined using the expression:

$$\text{fraction} = \frac{(\mu \leftarrow \pi/K)_i}{\text{inclusive } \mu} \tag{3.34}$$

where $\mu \leftarrow \pi/K$ is the muon p_{T}-distribution of the primary charged π and K per multiplicity percentile bin i and inclusive μ is the inclusive μ distribution from experimental data that are normalized to minimum bias events.

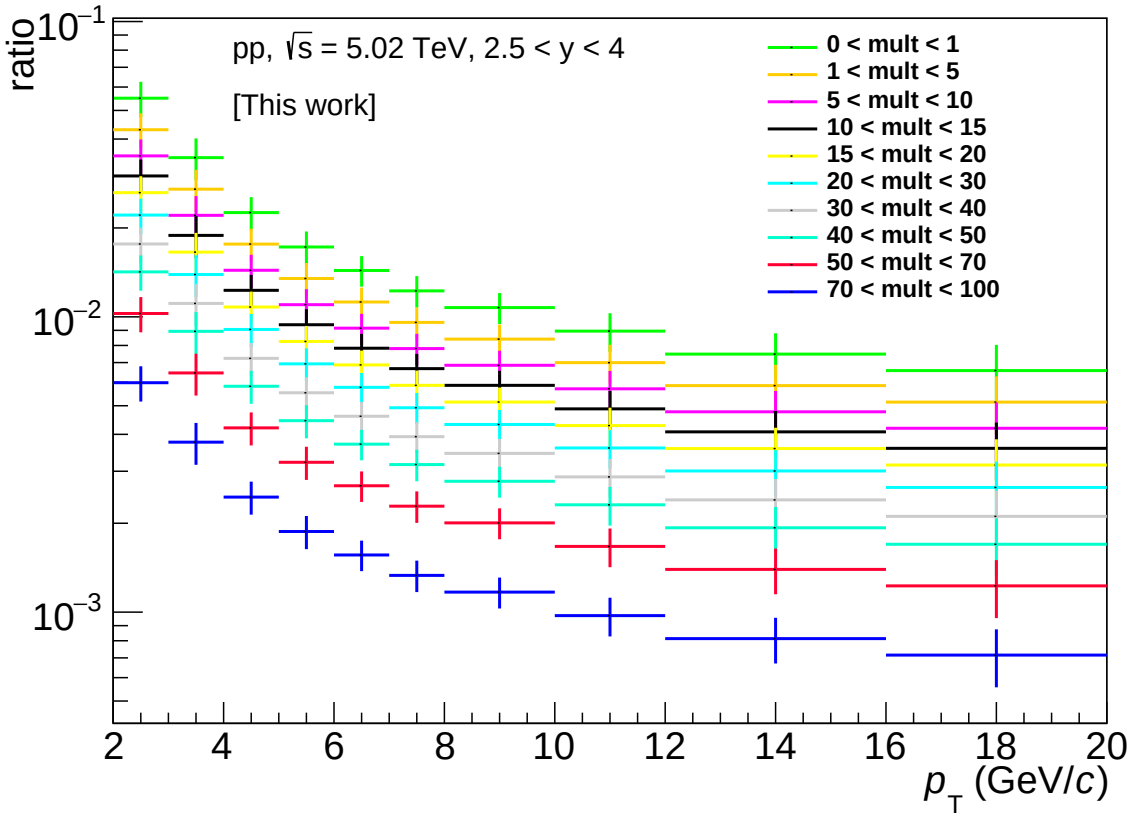

Fig. 3.40 Estimated background fraction in different multiplicity percentile bins of primary charged π and K at forward rapidity in pp collisions at $\sqrt{s} = 5.02$ TeV.

The muon background fraction decreases with an increase in multiplicity percentile bin, this is expected as the charged particle multiplicity also decreases with an increase in multiplicity percentile bin. The next section will focus on the contribution from secondary muons.

3.7.2 Contribution from secondary decay muons

The contribution of muons coming from the decay of secondary light hadrons (charged π and K) that are a result of the interaction between the light-charged hadrons and the absorber material needs to be accounted for. These muons contribute mainly in the p_{T} region $2 < p_{\mathrm{T}} < 5$ GeV/c. Monte Carlo simulations are used to estimate this contribution with the GEANT3 [145] transport code. The MC productions considered in this thesis are summarized in Table 3.17. For the LHC17p and q data samples, a general purpose MC

MC Production	Event Generator	Number of events	Data set Anchored to
LHC16f1a	PYTHIA6 (Perugia2011)	107 274 000	LHC15n
LHC16f1b	PHOJET	106 761 000	LHC15n
LHC18j2_fast	PYTHIA8 (Monash2013)	587 147 200	LHC17p+q
LHC20a2	EPOS	27 555 000	LHC17p+q

Table 3.17 Summary of MC productions

production using PYTHIA8 event generator [63] is used to estimate the contribution of secondary decay muons. The p_{T}-distribution of the various muon sources using PYTHIA8 is shown in Fig. 3.41a; just like the inclusive muon yield, the contribution decreases as a function of p_{T}. For the LHC15n data sample, there are two MC Muon productions available for analysis to estimate the contribution of secondary decay muons. A similar p_{T}-dependence trend of the contribution is observed for the LHC15n data sample,the results are available in Ref. [49]. Both data samples have two MC productions available which are utilized when determining the systematic uncertainty which will be discussed later in the chapter.

The contribution from the secondary decay muons is subtracted from the inclusive muon yield according to the expression:

$$\frac{dN_{pp}^{\mu\rightarrow HF}}{dp_T} = \frac{dN_{pp}^{incl\mu}}{dp_T} - \frac{dN_{pp}^{\mu\rightarrow sec.\pi/K}}{dp_T} \tag{3.35}$$

The background fraction is determined using the following expression:

$$\text{fraction} = \frac{\mu \leftarrow sec.\pi/K}{\text{all } \mu} \tag{3.36}$$

The background fraction of the secondary decay muons for integrated multiplicity is shown in Fig. 3.41b. The contribution has a maximum of $\sim 3\%$ at $p_{\mathrm{T}} = 2$ GeV/c and decreases as p_{T} increases. Above $p_{\mathrm{T}} = 5$ GeV/c, the contribution is negligible. This confirms the statement made earlier that the secondary muons only contribute in the p_{T} region $2 < p_{\mathrm{T}} < 5$ GeV/c.

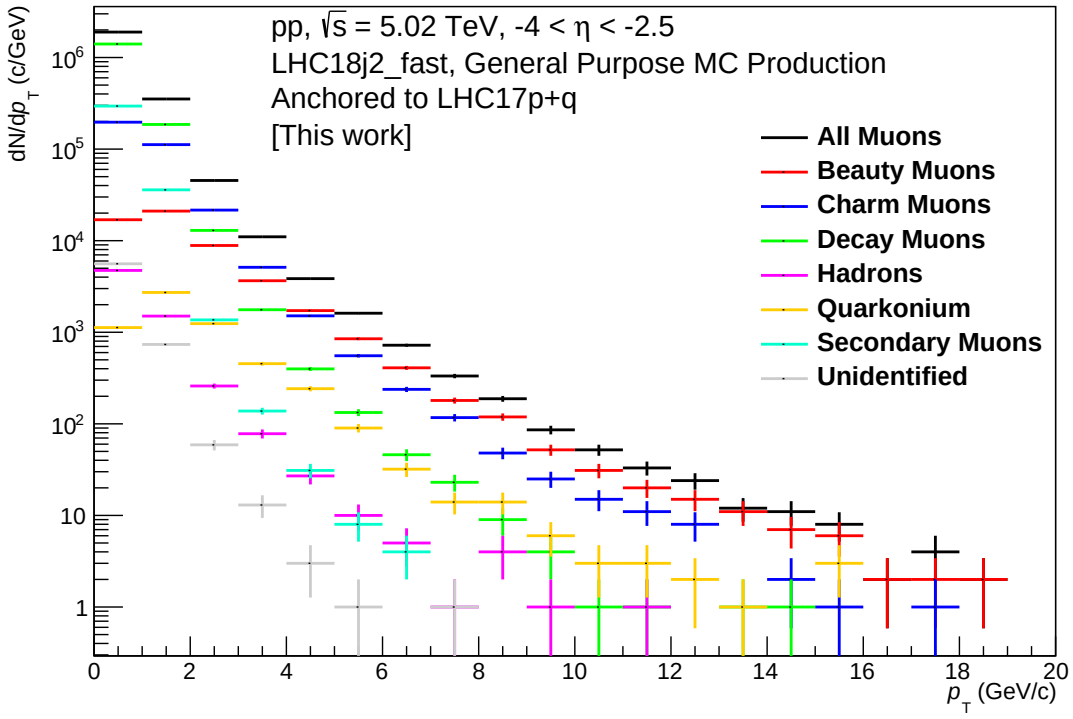

(a) p_{T} distributions of single decay muons from various sources.

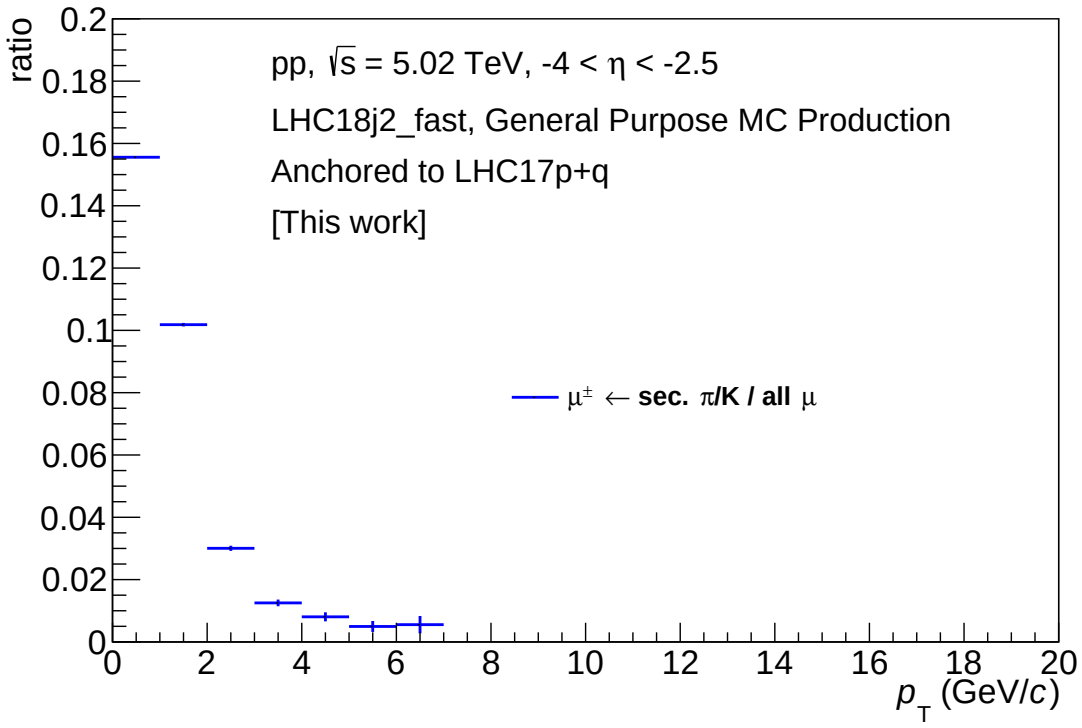

(b) Background fraction of the secondary decay muons.

Fig. 3.41 p_{T} distributions of single decay muons from various sources (3.41a) and background fraction of secondary decay muons (3.41b) associated with the LHC17p and q data sample.

The fraction of the secondary decay muons and the primary π and K determined in section 3.7.1 can also be determined. It is mentioned in Ref. [49, 157] that this fraction is p_{T} independent, however the contribution is relatively higher ($\sim 10\%$) in the p_{T} region of interest.

Next, the secondary decay muon contribution in different multiplicity bins will be discussed.

3.7.2.1 Contribution from secondary decay muons as a function of multiplicity

Since the final result includes also the heavy-flavour production as a function of charged-particle multiplicity, the secondary decay muon contribution is extracted in different multiplicity bins and/or percentile bins for the two multiplicity measurements. The background fraction is determined using the following expression:

$$\text{fraction} = \frac{\mu \leftarrow sec.\pi_i/K_i,}{\text{all } \mu_i} \tag{3.37}$$

where i represents the different multiplicity bins and/or percentile bins.

The same MC production used to determine the distributions for integrated multiplicity are used to find the p_{T}-distribution of the various muon sources in different multiplicity and/or percentile bins. The background fraction as a function of p_{T} in different multiplicity bins is determined thereafter. Figure 3.42 shows the background fraction for the multiplicity bins determined using the data-driven method discussed in section 3.3.1. Figure 3.42a shows the background fraction associated with the LHC17p and q data sample while Fig. 3.42b shows the background fraction associated with the LHC15n data sample.

For the LHC17p and q data samples, the background fraction across all the multiplicity bins is less than $\sim 4\%$ mainly in the region $2 < p_{\mathrm{T}} < 5$ GeV/c where the secondary muons contribute significantly. For the LHC15n data sample, the background fraction for all the multiplicity bins is less than $\sim 4\%$ in the region $2 < p_{\mathrm{T}} < 5$ GeV/c except for the first multiplicity bin [1-2] where the contribution peaks at $\sim 7\%$ and decreases thereafter. The differences in the background contributions for the two MC productions can be possibly attributed to the statistics, the MC production anchored to the LHC17p and q has a factor of 5 times more statistics than the production anchored to the LHC15n data sample.

The background fraction as a function of p_{T} in different multiplicity percentile bins for the "Official Framework" multiplicity estimation discussed in section 3.3.2 is shown in Fig. E.2 in Appendix E.2.

After the subtraction of the contributions from primary charged π/K and the secondary

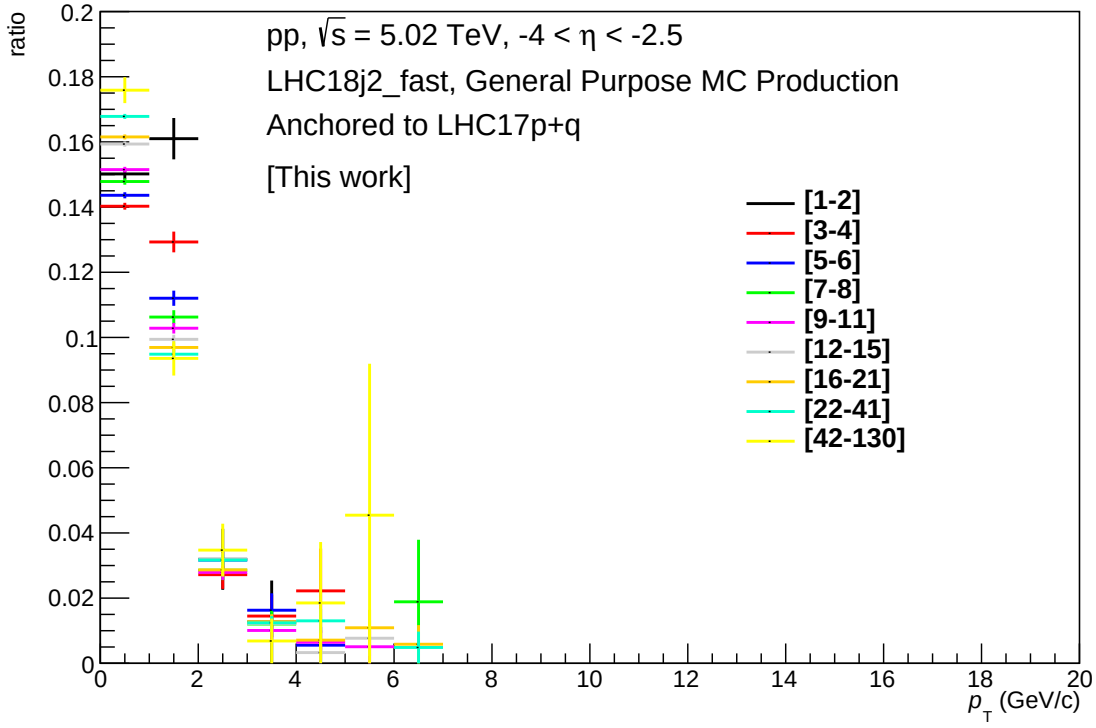

(a) Background fractions of the secondary muons in different multiplicity bins.

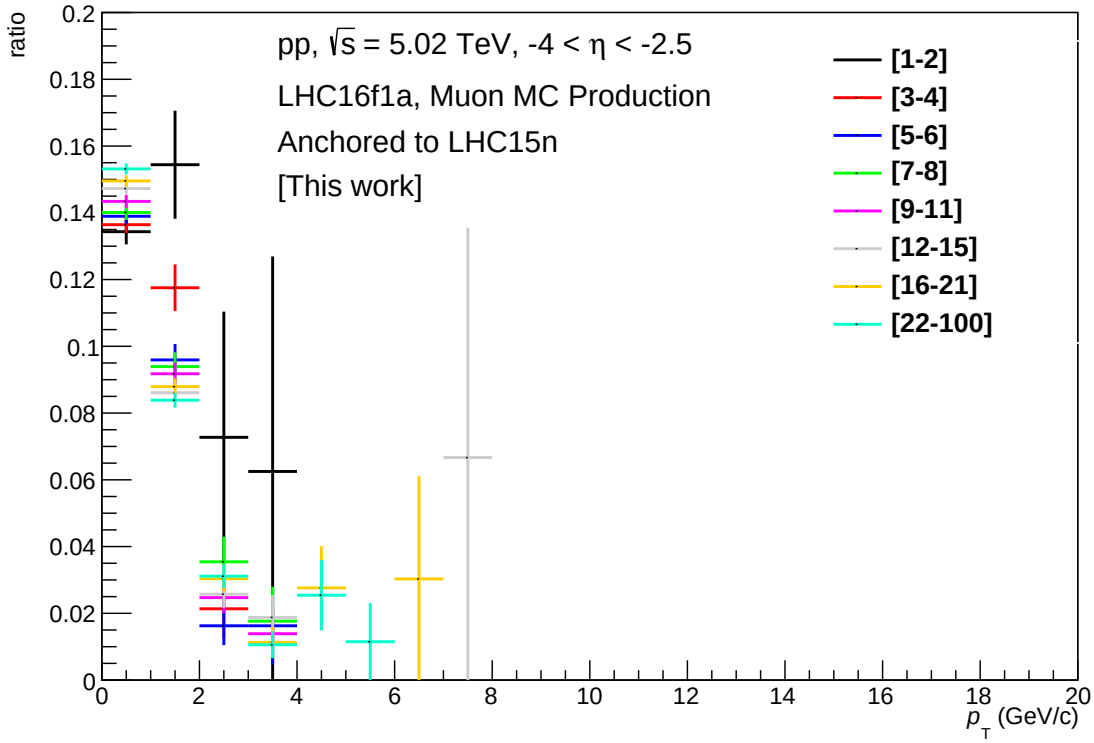

(b) Background fractions of the secondary muons in different multiplicity bins.

Fig. 3.42 Background fractions of secondary muons in different multiplicity bins associated with the LHC17p and q (3.42a) and LHC15n (3.42b) data samples.

decay muon contributions from the muon yield, the yield is then converted into a cross-section according to equation 3.44 to then account for the remaining two background contributions; W and Z/γ^*-decay muons and J/ψ decay muons.

3.7.3 Contribution from W and Z/γ^*-decay muons

The contribution from the weak bosons ($W/Z/\gamma^*$) can be estimated through simulations using the POWHEG event generator [167]. The POWHEG (**P**ositive **W**eight **H**ardest **E**mission **Generator**) method is developed to overcome the problem of negative weighted events. The method is developed in such a way that it generates the hardest radiation first by using a technique that yields positive weighted events only using the exact NLO matrix elements [168]. The CT10 Parton Distribution Functions [169] are included in the event generator.

In this thesis, a contribution from W and Z/γ^* to the inclusive total single muon p_{T}- and η-differential cross-section is considered and needs to be accounted for. At high $p_{\mathrm{T}} >\sim 14$ GeV/c the main source of background is from W and Z/γ^*-decay muons [49]. Following the procedure described in Ref. [170]:

1. Run POWHEG simulations interfaced with PYTHIA;
2. Analyze the output of the simulations, applying the full event selection and muon track cuts to the $\frac{dN}{dp_T}$;
3. Scale the resulting distribution by a factor $\frac{\sigma_{4\pi}}{nTrials}$ where $\sigma_{4\pi}$ is the total POWHEG cross-section of the process and $nTrials$ is the total number of events generated by POWHEG before the application of any selection.

Following the procedure above, the simulations for W^+, W^- and Z/γ are done separately. The total POWHEG cross-section for the process and $nTrials$ can be extracted from a pyxsec_hists.root file that is generated when a POWHEG simulation is ran. The total POWHEG cross-section and $nTrials$ for each process is summarized in Table 3.18.

Process	Cross-section ($\sigma_{4\pi}$ mb)	$nTrials$	
		LHC17p+q	LHC15n
W^+	4.15×10^{-6}	3 025 549	218 907
W^-	2.73×10^{-6}	3 025 506	253 615
Z/γ^*	1.51×10^{-6}	2 981 064	249 754

Table 3.18 Summary of the total POWHEG cross-section values and $nTrials$ for each process.

The contribution from W and Z/γ^*-decay muons is subtracted from the inclusive muon cross section according to the expression:

$$\frac{d^2\sigma^{\mu^{\pm}\to HF}}{dp_T} = \frac{d^2\sigma^{\mu^{\pm}}}{dp_T} - \frac{d^2\sigma^{\mu\to W/Z/\gamma^*}}{dp_T} \tag{3.38}$$

The differential cross-section for each process is shown in Fig. 3.43, for illustration purposes, only the LHC17p and q data sample cross-section for each process is shown. The cross-section for each process for the LHC15n data sample is available in Ref. [49]. The sum of the different processes is taken to obtain the total contribution of the electroweak bosons. The total differential single-muon cross-section of electroweak boson decay is shown in Fig. 3.44a together with the inclusive muon differential cross-section for the LHC17p and q data samples.

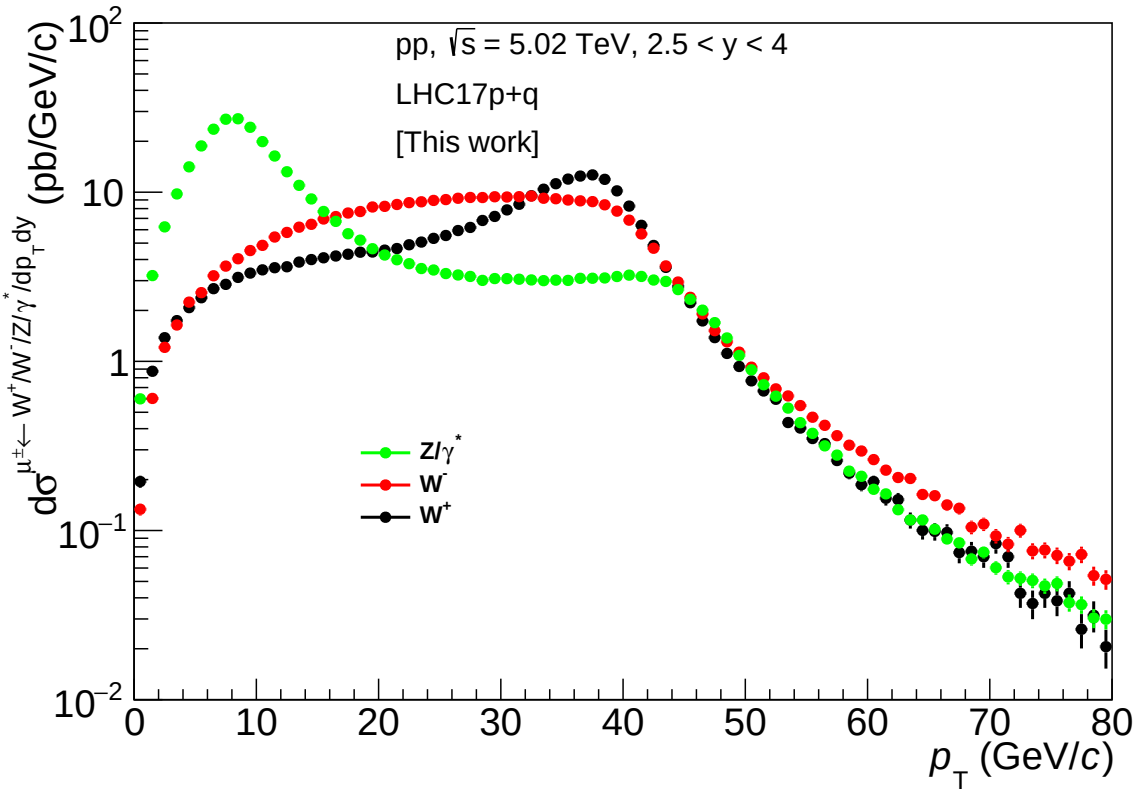

Fig. 3.43 Cross-sections for each decay process using POWHEG simulations.

The background fraction is determined using the following expression:

$$\text{fraction} = \frac{\mu \leftarrow W/Z\gamma}{\mu \text{ inclusive}} \tag{3.39}$$

The background fraction for the integrated multiplicity associated with the LHC17p and q data samples is shown in Fig. 3.44b and this contribution is small ($\sim 1\%$) up to $p_{\mathrm{T}} = 12$ GeV/c and reaches a maximum of $\sim 9\%$ at high p_{T}. The total differential single-muon

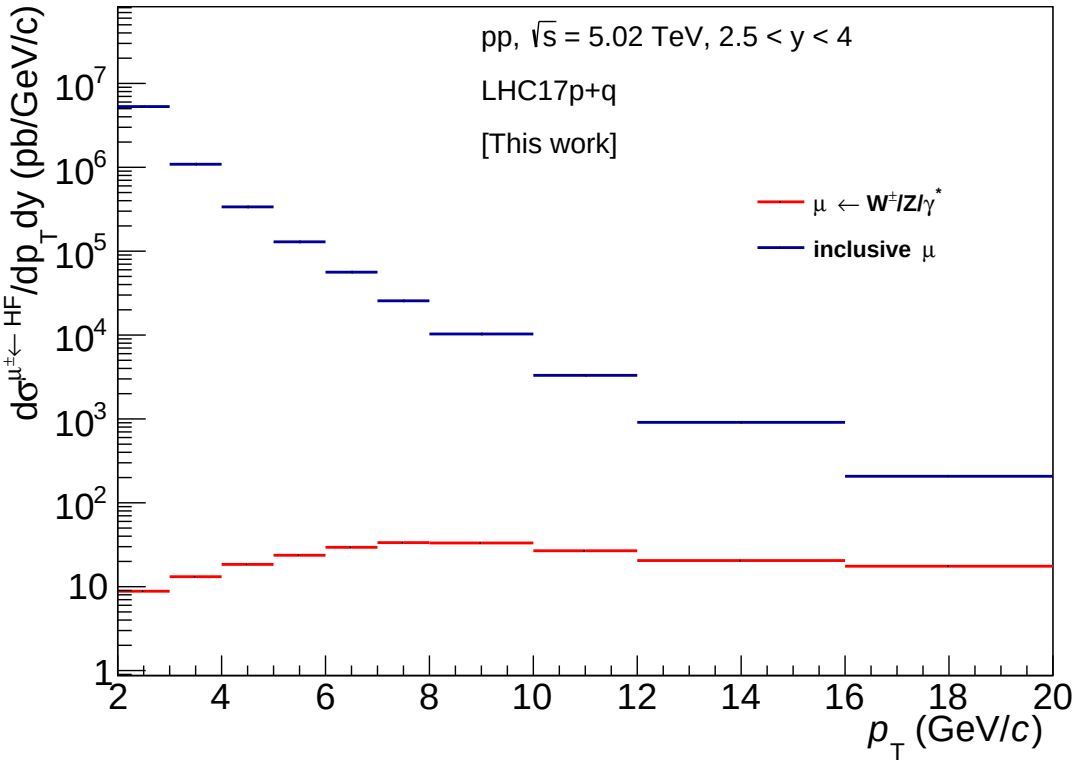

(a) Differential cross-sections of inclusive muons and electroweak boson single-muon decay.

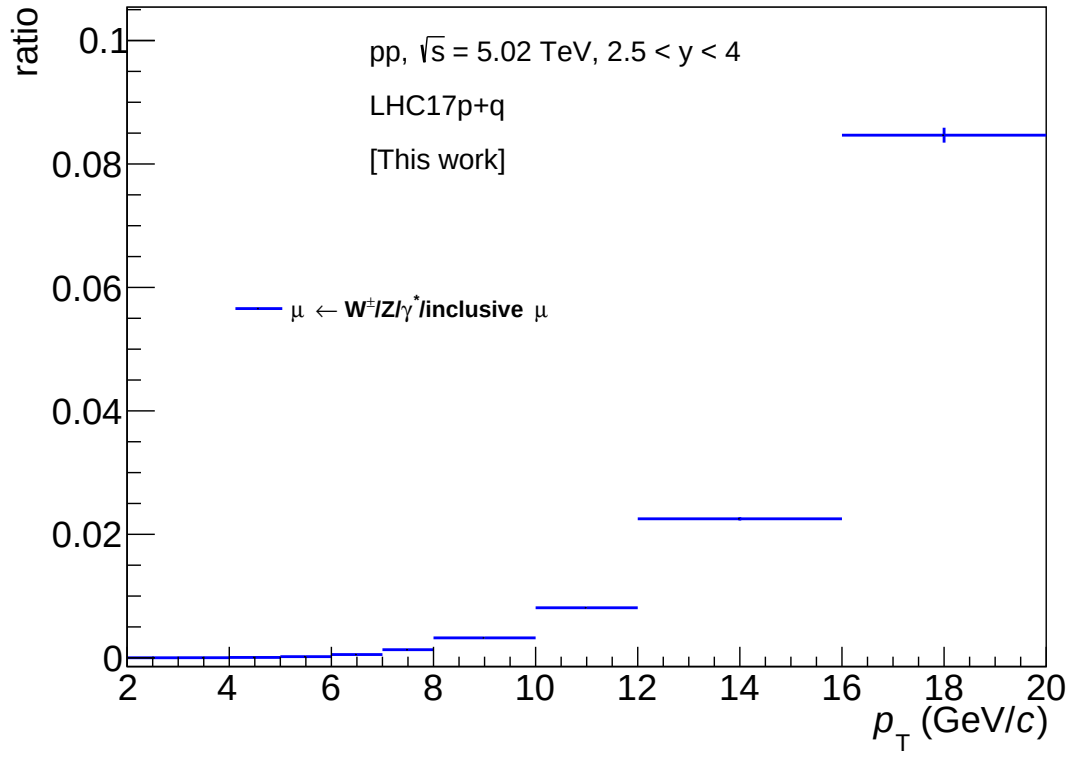

(b) Background fraction of electroweak boson decays.

Fig. 3.44 Differential cross-sections of inclusive muons and electroweak boson single-muon decay (3.44a) and background fraction of electroweak bosons decays (3.44b) for the LHC17p and q data samples.

cross-section electroweak boson decay is shown in Appendix E.3 in Fig. E.3 together with the inclusive muon differential cross-section for the LHC15n data sample. The background fraction for the integrated multiplicity is also shown in Fig. E.3. This contribution is also small ($\sim 1\%$) up to $p_{\mathrm{T}} = 14$ GeV/c and reaches a maximum of $\sim 6\%$ at high p_{T}.

Since the final result is also presented as the heavy-flavour production yield vs charged-particle multiplicity, the electroweak boson contribution needs to be extracted in different multiplicity bins and/or percentile bins for the two multiplicity measurements. However, since no measurements for electroweak boson production yields vs charged-particle multiplicity are available, the background fraction will not be determined in multiplicity bins. For the background fraction in different multiplicity bins, the W and Z/γ^* background fraction up to $p_{\mathrm{T}} = 12$ GeV/c for the LHC17p and q data samples and $p_{\mathrm{T}} = 14$ GeV/c for the LHC15n data sample, is considered, respectively, as it is below $\sim 2\%$.

3.7.4 Contribution from J/ψ

In this thesis, a contribution from J/ψ single muon decay to the inclusive total single muon p_{T}- and η-differential cross-section needs to be accounted for. The contribution is very small as compared to the other contributions already discussed. However, single muons from the decay of J/ψ contribute over the whole p_{T} range of interest. The J/ψ decay-muon contribution can be determined by making use of the following steps:

1. Generation of J/ψ with a uniform p_{T}- and y-distribution using fast detector simulations;
2. Force J/ψ to decay into dimuon using PYTHIA decayer;
3. Weigh the muons decaying from J/ψ according to the extrapolated p_{T}- and y-distributions of J/ψ;
4. Correct the p_{T}-distribution of the muons with the branching ratio (5.961%) for the decay of J/ψ to dimuon.

In this study, p_{T}- and y-distributions of J/ψ in pp collisions at $\sqrt{s} = 5.02$ TeV obtained from [171] are used to weigh the generated uniform p_{T}- and y-distributions of J/ψ. These distributions are shown in Fig. 3.45, on the left is the p_{T}- and on the right is the y-distribution. The error bars are the total uncertainties summed in quadrature.

The p_{T}-distribution is extrapolated to 40 GeV/c. The extrapolation is done by fitting the Levy-Tsallis distribution [157]:

$$f(p_T) = norm \times p_T \times [\frac{1 + (m_T - m_0)}{n \times T}]^{-n} \tag{3.40}$$

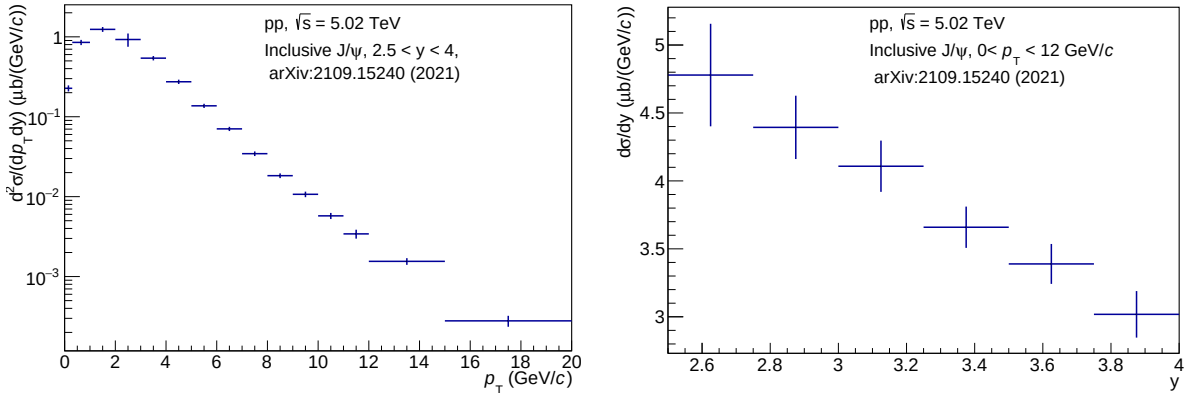

Fig. 3.45 p_{T}- (left) and (right) y-cross-sections of J/ψ in pp collisions at $\sqrt{s} = 5.02$ TeV obtained from [171].

where m_0 is the rest mass of J/ψ, $m_T = \sqrt{p_T^2 + m_0^2}$ and $norm$, n, T are free parameters. The y distribution is extrapolated to $-6 < y < 6$. The extrapolation is done by fitting a Gaussian function.

The distributions from the extrapolations are shown in Fig. 3.46 and are used to weigh the uniform p_{T}- and y-distributions of J/ψ to obtain the cross-section in the muon spectrometer acceptance range ($2.5 < y < 4.0$). The p_{T}-distribution of the muons is also corrected with the branching ratio (5.961%) for the decay of J/ψ to a dimuon.

The contribution from J/ψ-decay muons is subtracted from the inclusive muon cross section according to the expression:

$$\frac{d^2\sigma^{\mu^{\pm}\rightarrow HF}}{dp_T} = \frac{d^2\sigma^{\mu^{\pm}}}{dp_T} - \frac{d^2\sigma^{\mu\rightarrow J/\Psi}}{dp_{\mathrm{T}}} \tag{3.41}$$

Figure 3.47a shows the differential J/ψ and inclusive muon cross-sections for the LHC17p and q data samples. To determine the background fraction of the J/ψ, the ratio of the differential J/ψ cross-section and inclusive muon cross-section is determined, i.e.

$$\text{fraction} = \frac{\mu \leftarrow J/\psi}{\mu \text{ inclusive}} \tag{3.42}$$

The background is shown in Fig. 3.47b. The background fraction reaches a maximum of $\sim 4.6\%$ at $p_{\mathrm{T}} = 6$ GeV/c and decreases to $\sim 2\%$ at high p_{T}.

Figure E.4 in Appendix E.4 shows the differential J/ψ and inclusive muon cross-section on the top for the LHC15n data sample. The background fraction is also shown in Fig. E.4. The background fraction reaches a maximum of $\sim 4.6\%$ at $p_{\mathrm{T}} = 6$ GeV/c and decreases to $\sim 2\%$ at high p_{T}.

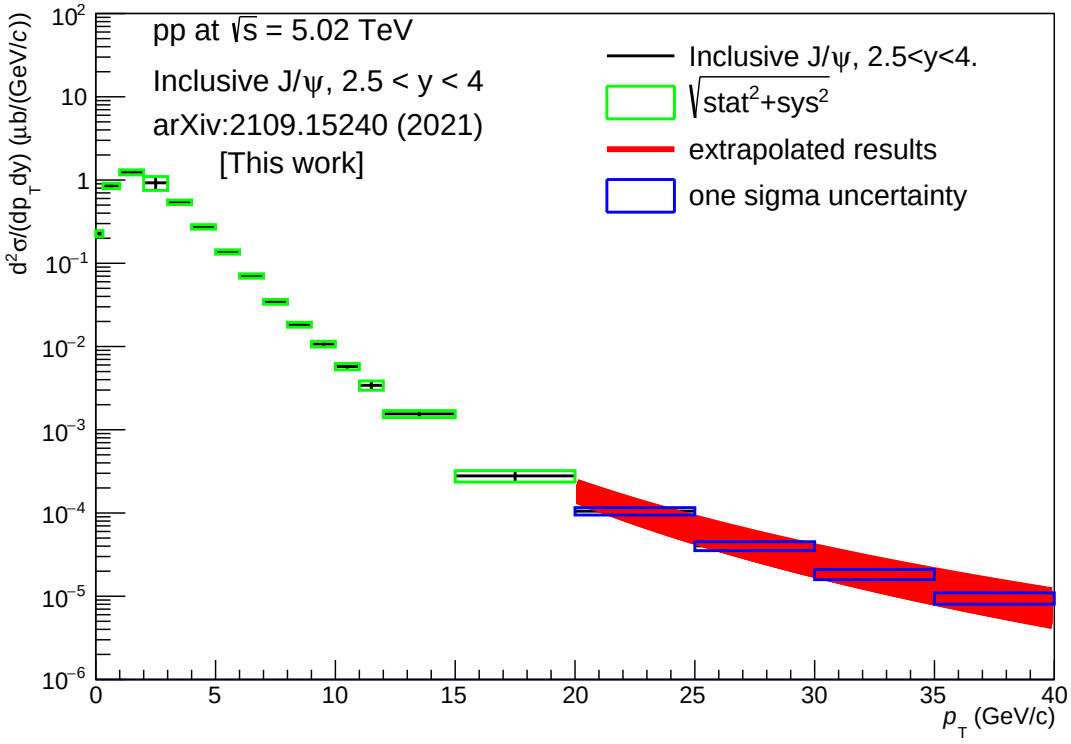

(a) Extrapolated differential p_{T} cross-section of J/ψ in pp collisions.

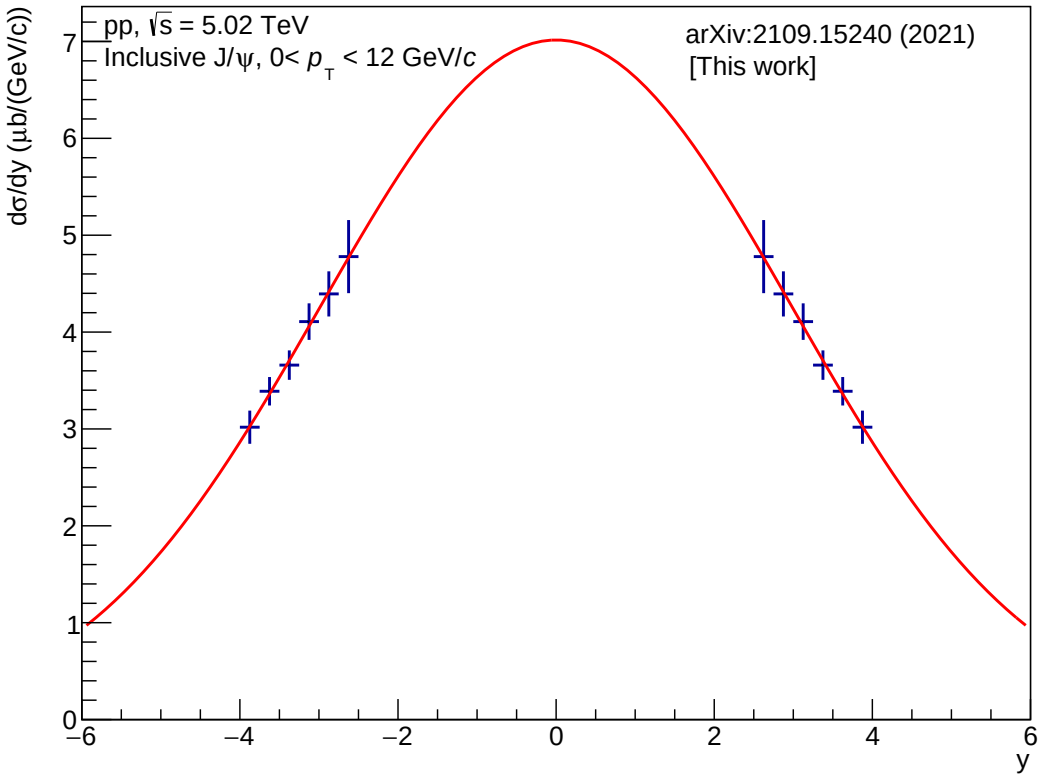

(b) Extrapolated differential y cross-section of J/ψ in pp collisions.

Fig. 3.46 Extrapolated p_{T} (3.46a) and (3.46b) y cross-section of J/ψ in pp collisions at $\sqrt{s} = 5.02$ TeV obtained from [171]. The error bars are the statistical and systematic uncertainties added in quadrature.

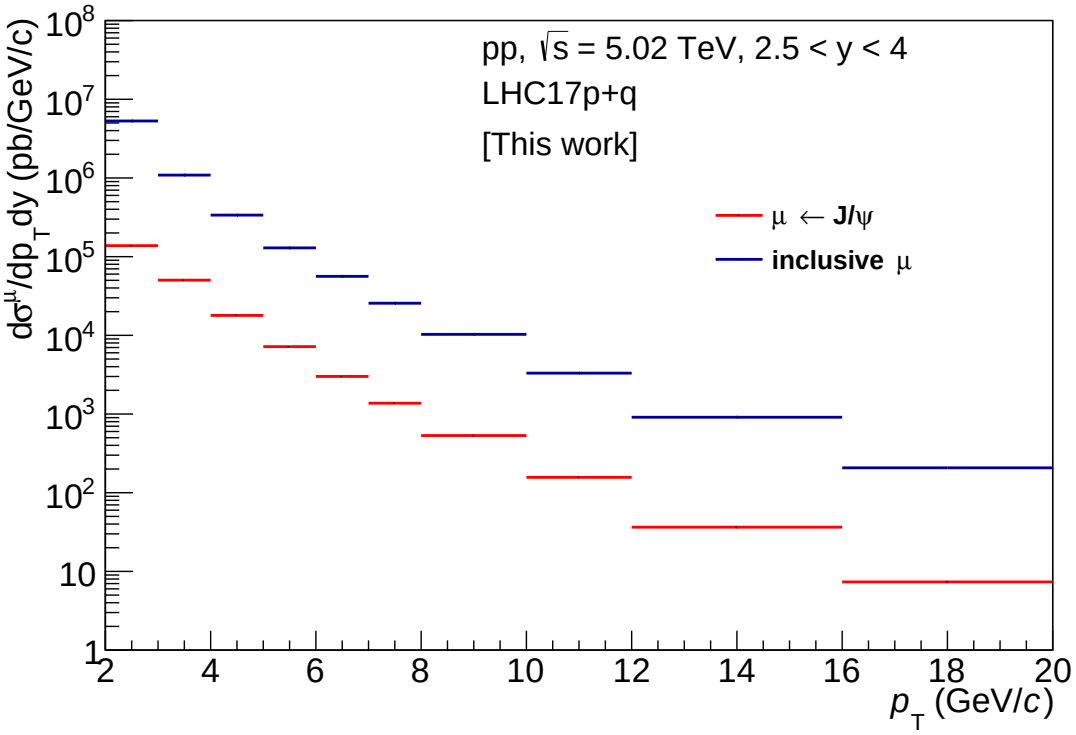

(a) Differential cross-section distributions of the inclusive muons and J/ψ dimuon differential cross-section in pp collisions at $\sqrt{s} = 5.02$ TeV.

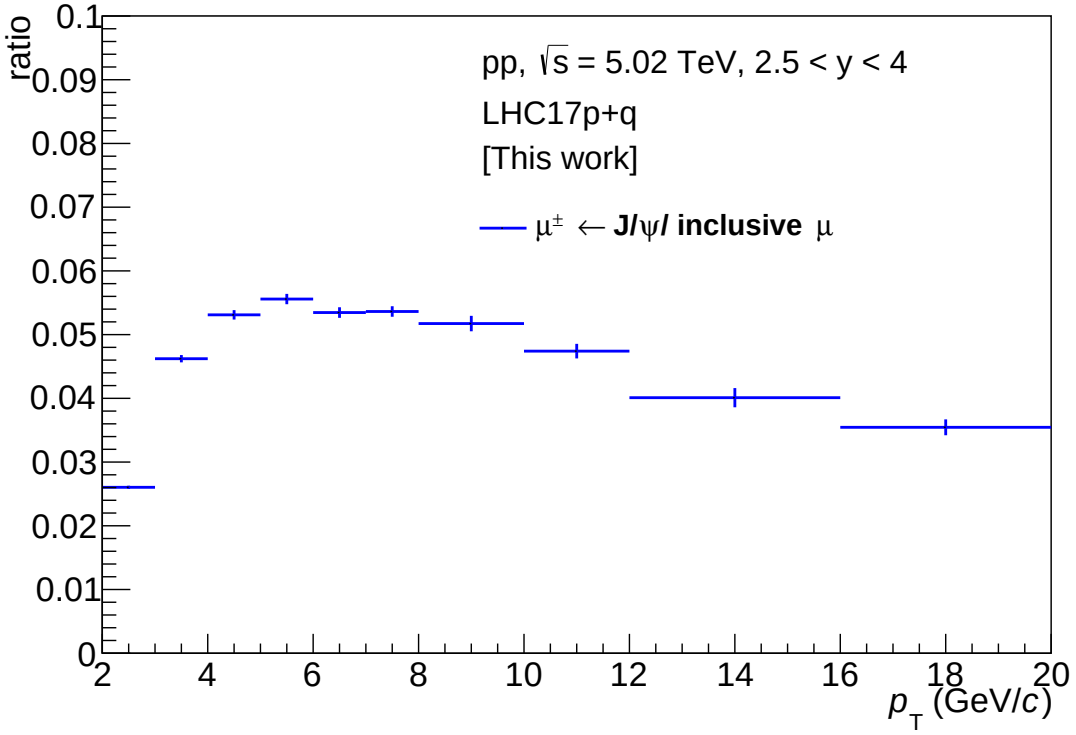

(b) Background fraction of J/ψ.

Fig. 3.47 Differential cross-section distributions of the inclusive muons and J/ψ dimuon differential cross-section (3.47a) and background fraction of J/ψ (3.47b) in pp collisions at $\sqrt{s} = 5.02$ TeV for the LHC17p and q data samples.

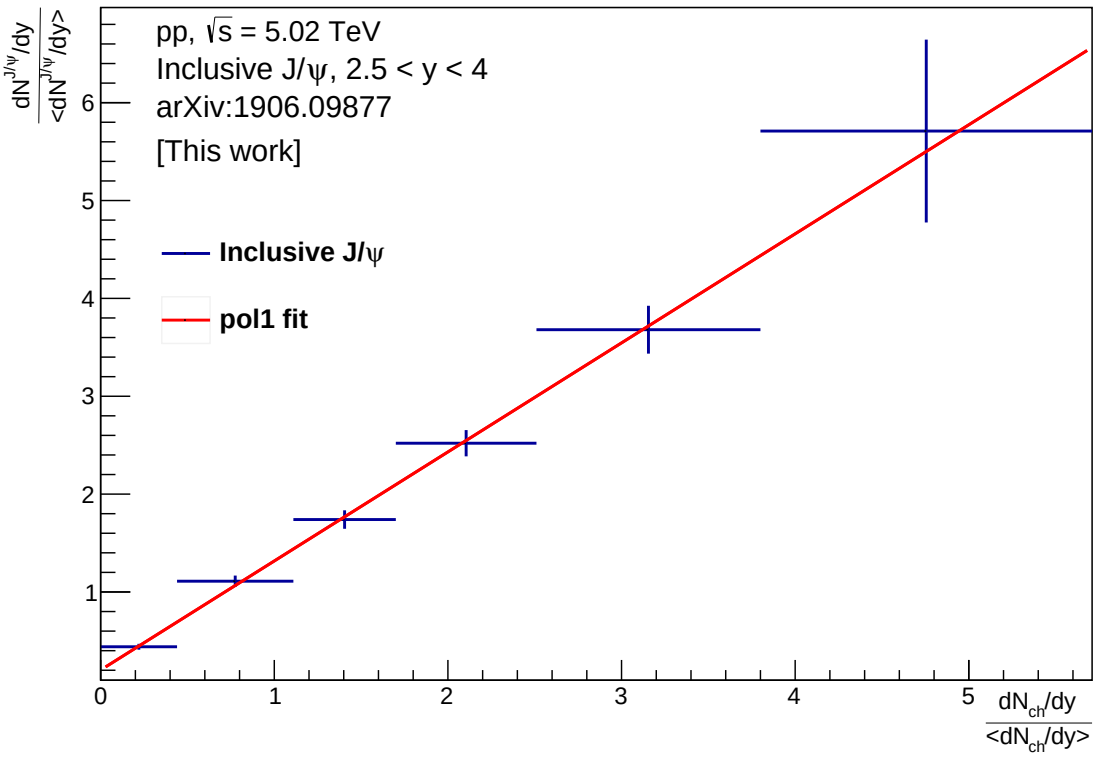

Fig. 3.48 The relative J/ψ yield as a function of the relative charged-particle density measured at forward rapidity in pp collisions at $\sqrt{s} = 5.02$ TeV [172]. The red solid line is the pol1 fit.

3.7.4.1 Contribution from J/ψ as a function of multiplicity

The J/ψ muon contribution needs to be extracted in different multiplicity bins and/or percentile bins for the two multiplicity measurements. The J/ψ production cross-section is not available as a function of multiplicity, however, there are published results of the self-normalized J/ψ production as a function of charged-particle multiplicity [172]. The published data are used to determine the self-normalized J/ψ production in the charged-particle multiplicity bins/axis required for this analysis.

The input of the self-normalized J/ψ yield vs charged-particle multiplicity used in this study is shown in Fig. 3.48. The error bars are the total uncertainties summed in quadrature. To obtain the self-normalized J/ψ yield in the desired charged-particle multiplicity bin/axis, the data points in Fig. 3.48 are fitted with a pol1 function expressed as:

$$f(x) = p_0 + p_1 x \tag{3.43}$$

where p_0 and p_1 are free parameters.

The results of the self-normalized J/ψ yield in the respective charged-particle multiplicity bins of interest in this study are shown in Tables 3.19 and E.1 (available in Appendix E.1) for the data-driven method and "Official Framework", respectively. The errors shown in

the table are calculated by summing the errors of the free parameters from the fit and charged-particle multiplicity in quadrature. For the data-driven method, the statistical errors as shown in Table 3.9 are negligible hence the statistical error is the same for the tables. For the "Official Framework" method, the charged-particle multiplicity consists of only the systematic uncertainty and therefore only the errors of the free parameters are considered for the statistical error.

LHC17p+q		LHC15n	
$\frac{dN_{ch}/d\eta}{\langle dN/d\eta \rangle}$	J/ψ self-normalized yield	$\frac{dN_{ch}/d\eta}{\langle dN/d\eta \rangle}$	J/ψ self-normalized yield
0.166398	0.02311 ± 0.0036	0.171366	0.02344 ± 0.0036
0.319442	0.03328 ± 0.0036	0.318659	0.03323 ± 0.0036
0.520771	0.04665 ± 0.0036	0.501679	0.04538 ± 0.0036
0.725959	0.06028 ± 0.0036	0.703116	0.05876 ± 0.0036
0.985199	0.07750 ± 0.0036	0.967373	0.07614 ± 0.0036
1.35418	0.10201 ± 0.0036	1.33645	0.10083 ± 0.0036
1.86805	0.13614 ± 0.0036	1.844598	0.13468 ± 0.0036
2.84279	0.20089 ± 0.0036	2.86414	0.20231 ± 0.0036
4.78227	0.32972 ± 0.0036		

Table 3.19 Self-normalized J/ψ yields as a function of charged-particle multiplicity for the data-driven method.

3.8 Systematic Uncertainties

This section will be a discussion on all the systematic uncertainties considered in the analysis.

The systematic uncertainty for the muon tracking efficiency is estimated by comparing the single-muon tracking efficiency in data and that of simulations. The systematic uncertainty is 0.5% [49]. This value is independent of p_{T} and y.

The systematic uncertainty for the muon trigger efficiency is determined by using the trigger response function. This is achieved by varying the efficiency of each local board by its uncertainty in the simulation after which the $A \times \epsilon$ is obtained and compared with the default trigger efficiencies. A detailed description of the procedure is discussed in Ref. [49]. The corresponding values for the MSL and MSH triggers are given as 1% and 3%, respectively [49].

The muon trigger-tracking systematic uncertainty is dependent on the χ^2 cut as discussed in other analyses [49, 131, 153]. The χ^2 cut is used to define the matching between the reconstructed tracks in the tracking chambers with the trigger tracklets. For the single muon analysis, the systematic uncertainty amounts to 0.5% as quoted in [49, 131].

The systematic uncertainty on mis-alignment of the muon chambers is estimated by utilizing Monte Carlo simulations that models the tracker response of the muon spectrometer with a parameterization of the tracking chamber resolution and systematic mis-alignment effects. The tracking chamber resolution is measured using the residual distance between the reconstructed tracks and their associated clusters. The systematic mis-alignment effects are determined by comparing the reconstructed tracks p_{T}-distribution of the positive and negative muons. The curvature of these distributions are opposite in the dipole magnetic field and therefore making them sensitive to mis-alignment. The parameterization is tuned either on data or on the full Monte Carlo simulation. A comparison of the heavy-flavour decay muon p_{T}-differential distributions obtained with the two parameterizations gives an estimation of the systematic uncertainty. The systematic uncertainty is negligible for $p_{\mathrm{T}} < 7$ GeV/c and then increases to about 15% in the interval $18 < p_{\mathrm{T}} < 20$ GeV/c. This procedure is discussed in detail in [49, 83, 157].

The total systematic uncertainty on the normalization to the MB σ^{T0}_{VdM} cros-section is 1.8% and σ^{T0}_{VdM} is 2.09% for the LHC17p+q and LHC15n data samples, respectively. These values contain contributions from the measurement of the T0 trigger cross-section determined by using the Van der Meer scan technique and the stability of the T0 trigger during data taking. More details on the determination of the total systematic uncertainty is discussed in [161, 162]. The systematic uncertainty on the inelastic normalization factor

is 2.51%.

The systematic uncertainty on all the background contributions is considered. For each contribution, a systematic uncertainty is associated with it.

1. **Primary charged pion and kaon:** The systematic uncertainty from the single-muon decay of primary charged π and K ranges from about 11% to 24% as a function of p_{T} [49]. The various contributions considered for the systematic uncertainties include:

   - Midrapidity inputs + p_{T} extrapolation π and K - these are uncertainties from the inputs of published data as well as from the extrapolation procedure to high p_{T}.
   - Rapidity extrapolation π and K - these uncertainties are from considering the different MC productions available for the extraction of the rapidity distributions.The systematic uncertainty is estimated by making a comparison of the different MC productions.
   - Absorber effect - the systematic uncertainties are determined by considering the π and K background contribution when applying the sharp cut and when considering the absorber effect during the weighing of the fast simulations. The systematic uncertainties are estimated by making a comparison of the different π and K background contributions when considering the absorber effect and applying the sharp cut.
   - p_{T} dependent rapidity extrapolation π and K - the systematic uncertainties are determined by considering different color reconnection options in the pythia simulations used for the rapidity distributions.

   The total systematics uncertainties are added in quadrature to obtain the decay muon uncertainty of π and K.

2. **Secondary muons:** The systematic uncertainty from the secondary decay muons is estimated from the comparison of the MC productions available for the LHC17p+q and LHC15n data samples. A comparison between PYTHIA8 [63] and EPOS [67] is made for the LHC17p+q data samples. This leads to a relative systematic uncertainty of about 4.8%. A comparison between PYTHIA6 [173] and PHOJET [174] is made for the LHC15n data samples. This leads to a relative systematic uncertainty of about 1.6%.

3. **Electroweak bosons:** The systematic uncertainty from the electroweak boson decays is estimated from the comparison of the W production cross-section as given

Source	vs. p_{T}	
	LHC17p+q	LHC15n
Tracking efficiency	0.5%	
Trigger efficiency	1% MSL and 3% MSH	
Matching efficiency	0.5%	
Resolution and alignment	0-15% (negligible for $p_{\mathrm{T}} < 7$ GeV/c)	
σ^{T0}_{VdM}	1.8%	2.09%
F_{norm} MSL(MSH)	1.9% (1.7%)	2.8% (0.7%)
$W/Z/\gamma^*$ decay muons	8%; (7%)	8%; (7%)
J/ψ decay muons	1.9%	1.9%
Secondary decay muons	4.8%	1.6%
$\pi(K)$ decay muons	$1-4.4$%	$1-4.4$%
Total uncertainty	**up to** 11%	**up to** 11%

Table 3.20 Systematic uncertainties considered in the measurement of muons from heavy-flavour decays in $2.5 < y < 4$.

by POWHEG when using different PDFs. CT10 and CTEQ6L PDFs were used for this comparison. This leads to a systematic uncertainty of about 8%; (7%) for muons from W (Z/γ) decays.

4. **J/ψ:** The systematic uncertainty on the J/ψ cross-section is quoted as 1.9% in [171].

The systematic uncertainty of the normalization factor is determined using the scaler and offline methods. The difference between the two methods is considered to be the systematic uncertainty on the normalization factor. For the LHC17p+q data sample, the systematic uncertainty of the normalization factor is 1.9% (1.7%) for the MSL(MSH) trigger. For the LHC17p+q data sample, the systematic uncertainty of the normalization factor is 2.8% (0.7%) for the MSL(MSH) trigger.

A summary of the systematic uncertainties considered in the measurement of muons from heavy-flavour decays in $2.5 < y < 4$ is given in Table 3.20. Systematic uncertainties can either be correlated or uncorrelated. The uncorrelated systematic uncertainties, account for detection efficiencies, alignment and background subtraction. These systematic uncertainties are added in quadrature to obtain the total systematic uncertainty as shown in Table 3.20.

The systematic uncertainty on the measurement of the multiplicity dependence of muons from heavy-flavour production is considered. A summary of the systematic uncertainties considered is shown in Table 3.21. The total systematic uncertainty is the quadratic sum

Source	vs. p_{T}
Multiplicity axis	up to 7%
F_{inel}	2.51%
$W/Z/\gamma^*$ decay muons	up to 2%
J/ψ decay muons	1.52%
Secondary decay muons	up to 15%
$\pi(K)$ decay muons	up to 5%
Total uncertainty	**up to** 18%

Table 3.21 Systematic uncertainties considered in the measurement of muons from heavy-flavour decays as a function of charged-particle multiplicity.

of the sources listed in Table 3.21.

3.9 Heavy-flavour decay differential cross-section

The inclusive differential cross-section shown in section 3.9 included muons from various muon sources. Section 3.41 disscussed contributions from different background sources, the background contribution is removed from the inclusive differential cross-section. The inclusive heavy-flavour differential cross-section is expressed as [157]:

$$\frac{d\sigma_{\mu^{\pm}\leftarrow HF}}{dp_{\mathrm{T}}} = \frac{d\sigma_{tot}^{\mu^{\pm}\leftarrow HF}/dp_{\mathrm{T}}dy - d\sigma_{bckg}^{\mu^{\pm}\leftarrow HF}/dp_{\mathrm{T}}dy}{A \times \epsilon \cdot F_{norm} \cdot N_{MSL/MSH}} \cdot \sigma_{MB} \tag{3.44}$$

Figure 3.49 shows a comparison of the inclusive differential single muon cross-section (red data points) and the heavy-flavour decay muon differential cross-section (black data points). The boxes are the total systematic uncertainties as discussed in section 3.8. This comparison shows the contribution of the different background sources towards the inclusive differential cross-section. In the bottom panel of Fig. 3.49 is the ratio of the inclusive differential single muon cross-section and heavy-flavour decay muon differential cross-section.

In the next chapter, the final results will be discussed. The heavy-flavour differential cross-section obtained from this study will be shown and compared with theoretical model and published measurements. The final result of the self-normalized heavy-flavour yield vs charged-particle multiplicity will also be shown and compared with available results in the heavy flavour sector.

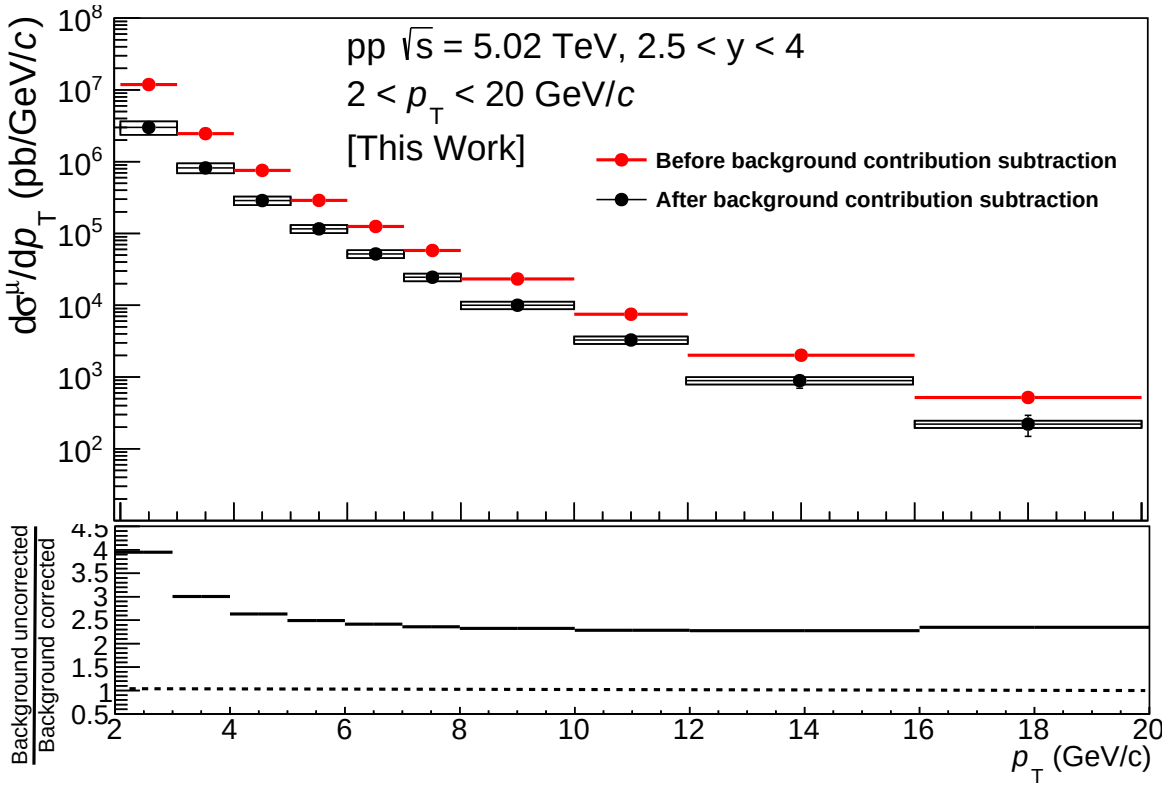

Fig. 3.49 Inclusive differential single muon cross-section and heavy-flavour decay muon differential cross-section (top panel). Ratio of the inclusive differential single muon cross-section and heavy-flavour decay muon differential cross-section (bottom panel). The boxes are the systematic uncertainties.

CHAPTER 4

Discussion of results

The aim of this study is to determine the heavy-flavour decay muon differential cross-section as well as the differential measurement of the heavy-flavour decay muon yield as a function of the charged-particle multiplicity in pp collisions at $\sqrt{s} = 5.02$ TeV from data taken in 2015 and 2017 during Run 2. This chapter is divided into two sections; the first section is devoted to a discussion of the heavy-flavour decay muon differential cross-section while the second section will cover the differential measurement of the heavy-flavour decay muon yield as a function of the charged-particle multiplicity. These measurements will be compared with published measurements from other studies in pp and p-Pb collisions at different center-of-mass energies.

4.1 Heavy-flavour decay muon differential production cross-section

The heavy-flavour single muon decay p_{T}- and η-differential cross-sections will be compared with published data at the same center-of-mass energy as well as at $\sqrt{s} = 7$ TeV and theoretical models based on pQCD calculations.

The inclusive p_{T}-differential cross-section is defined in this way:

$$\frac{d\sigma_{\mu^{\pm}\leftarrow HF}}{dp_T} = \frac{dN_{tot}^{\mu^{\pm}\leftarrow HF} - dN_{bckg}^{\mu^{\pm}\leftarrow HF}}{A \times \epsilon \cdot F_{norm} \cdot N_{MSL/MSH}} \cdot \sigma_{MB} \tag{4.1}$$

where $dN_{tot}^{\mu\pm\leftarrow HF}$ is the inclusive muon yield, $dN_{bckg}^{\mu\pm\leftarrow HF}$ is the total background contribution, $A \times \epsilon$ is the acceptance times efficiency factor, F_{norm} is the normalization factor, $N_{MSL/MSH}$ are the number of MSL/MSH events and σ_{MB} is the visible cross-section measured in the van der Meer scans for the T0 detector.

The inclusive heavy-flavour decay muon differential cross-section is measured as a function of p_{T} in the range 2-20 GeV/c and integrated over the muon spectrometer acceptance ($2.5 < y < 4$). As initially discussed in section 3.9, the inclusive heavy-flavour decay muon differential cross-section is obtained by considering both the MSL and MSH inclusive heavy-flavour decay muon differential cross-sections. For the p_{T} range 2-7 GeV/c, the MSL inclusive heavy-flavour decay muon differential cross-section is considered while for the p_{T} range 8-20 GeV/c, the MSH inclusive heavy-flavour decay muon differential cross-section is considered.

Figure 4.1a shows the inclusive p_{T}-differential cross-section of muons from heavy-flavour at $\sqrt{s} = 5.02$ TeV and it is observed that it decreases with an increase in p_{T}. This trend is expected as reported in other analyses [49, 152, 158]. The black data points are the final result obtained from this analysis study, the boxes around the data points represent the systematic uncertainties. The vertical lines are statistical errors obtained from adding the errors contributing to the inclusive heavy-flavour decay muon differential cross-section in quadrature.

The experimental results are compared to calculations performed with the theoretical model FONLL [175]. The red curve represents the total heavy-flavour contribution where the solid curve represents the central values and the dashed curve is the systematic uncertainty. The theoretical systematic uncertainties are from scales, masses and PDFs combined quadratically. The data and FONLL calculations follow the same trend. In the bottom panel is the ratio of the experimental data to FONLL.

The blue, green and teal solid curves and their corresponding dashed curves are the different production cross-sections for $c \to \mu$, $b \to \mu$ and $b \to D \to \mu$, respectively. The solid curves are the central values and the dashed curves are the systematic uncertainty. At $p_{\mathrm{T}} < 4$ GeV/c, the charm quark dominates as observed from the blue curves; at $p_{\mathrm{T}} > 4$ GeV/c, there is an overlap where the bottom quarks start to dominate as indicated by the green curves. The indirect decay of the bottom quark to the muon via a charm hadron is also considered in the total muon cross-section from heavy-flavour muon decays and is represented by the teal curve. The data and theoretical model are in agreement within systematic uncertainties.

The inclusive heavy-flavour decay muon p_{T}-differential cross-section is also studied as a function of the pseudorapidity (η) as shown in Fig. 4.1b. The result is integrated over

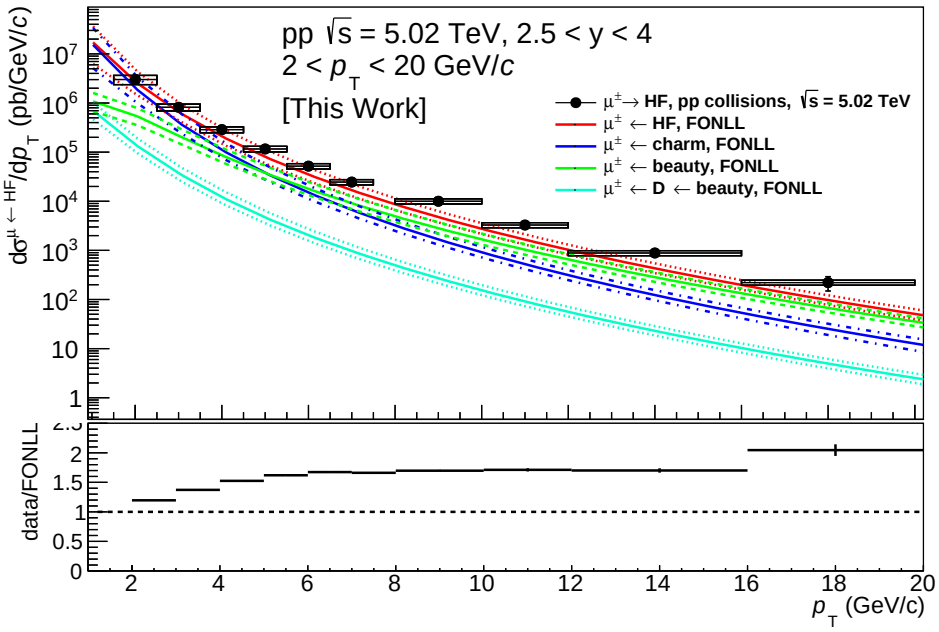

(a) Inclusive p_{T}-differential cross-section in pp collisions at $\sqrt{s} = 5.02$ TeV compared with theoretical calculations from FONLL [175] (top panel). Ratio of the experimental data to FONLL is shown in the bottom panel.

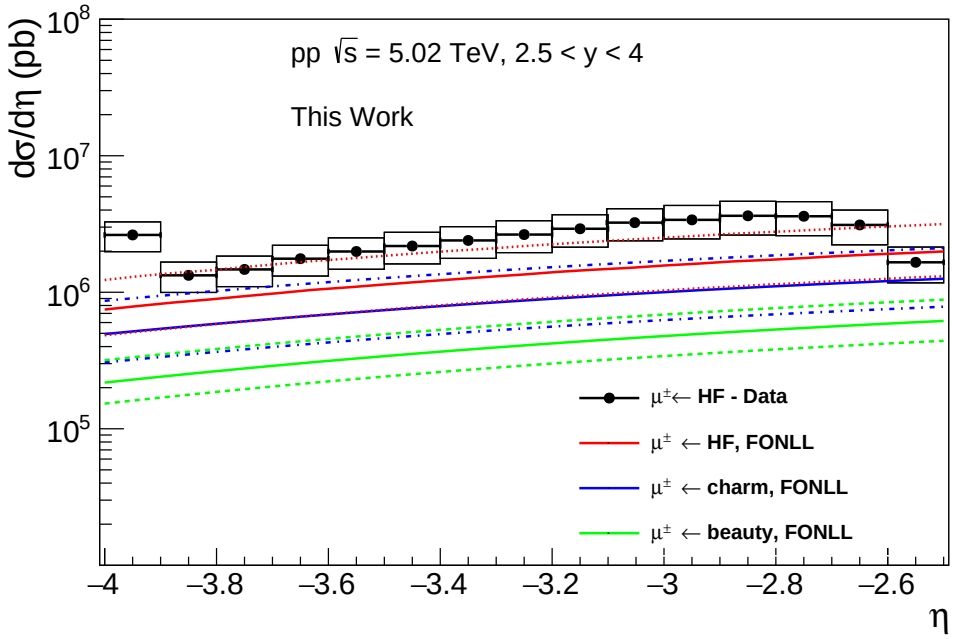

(b) Inclusive η-differential cross-section for integrated p_{T} ($2 < p_{\mathrm{T}} < 20$ GeV/c) in pp collisions at $\sqrt{s} = 5.02$ TeV compared with theoretical calculations from FONLL [175].

Fig. 4.1 Inclusive p_{T}- (4.1a) and η-differential (4.1b) cross-section in pp collisions at $\sqrt{s}$ = 5.02 TeV compared with theoretical calculations from FONLL [175], the solid curves are the central values and the dotted curves are the systematic uncertainty. The vertical lines and boxes around the data points represent the systematic uncertainties.

$2 < p_{\mathrm{T}} < 20$ GeV/c for the muon spectrometer acceptance. The result is compared to FONLL calculations with the total cross-section from heavy-flavour represented by the red curves, the solid curve being the central values and the dashed curves being the systematic uncertainty. It is observed that the charm quark dominates over the entire pseudorapidity range which is consistent with published measurements of heavy-flavour decay muon production at forward rapidity in pp collisions at $\sqrt{s} = 5.02$ TeV [49] and 7 TeV [176].

The inclusive heavy-flavour decay muon p_{T}-differential cross-section is measured in five sub-rapidity intervals in the range $-4 < \eta < -2.5$, each interval has a width $\Delta 3$. The inclusive p_{T}-differential cross-section is compared to FONLL predictions. Figure 4.2 shows the inclusive p_{T}-differential cross-section measured in five sub-rapidity intervals.

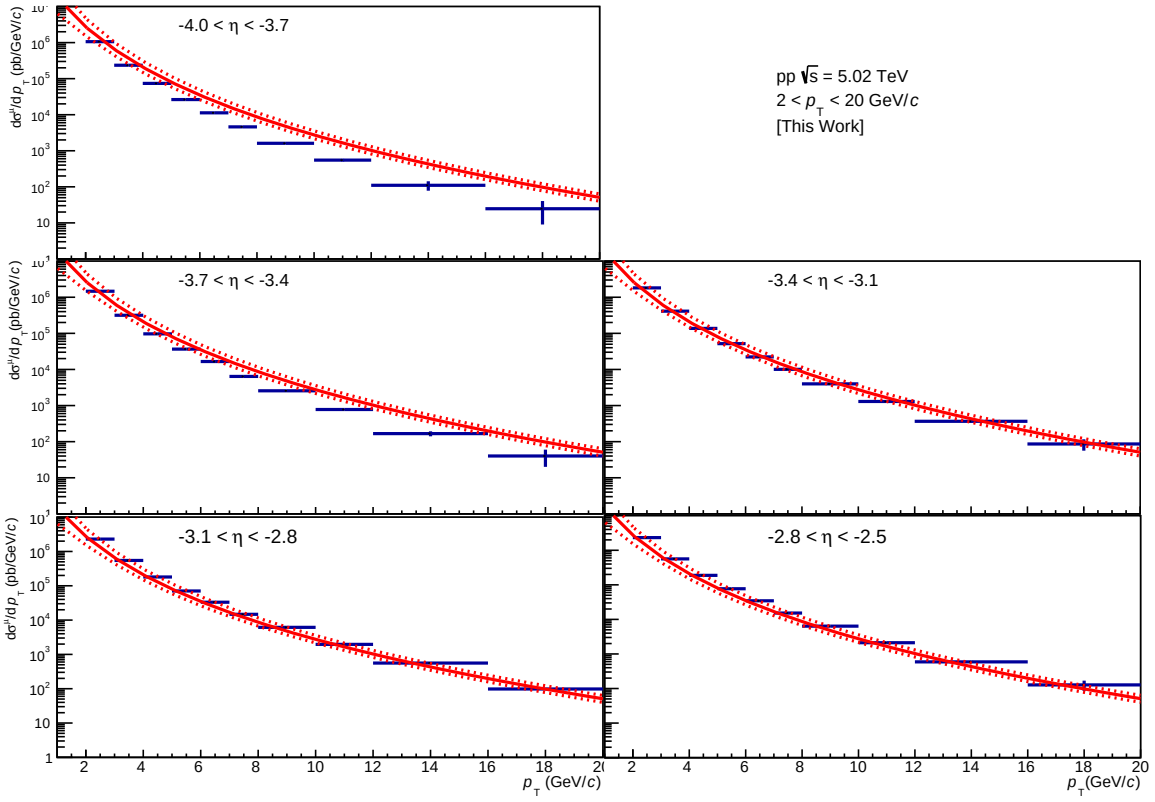

Fig. 4.2 Heavy-flavour decay muon production cross-section in pp collisions at $\sqrt{s} = 5.02$ TeV in different η intervals compared with theoretical calculations from FONLL [175]. The horizontal lines are the bin width and the vertical lines are statistical errors.

From Fig. 4.2, it is observed that the FONLL predictions describe the data within uncertainties for the most of the η intervals except the interval $-4 < \eta < -3.7$ where FONLL describes the data at low p_{T} but overestimates the data at $p_{\mathrm{T}} > 4$ GeV/c. To clearly observe the inclusive p_{T}-differential cross-section dependence on η, the ratio of the inclusive p_{T}-differential cross-sections with the total differential cross-section from FONLL is

determined. The corresponding ratios of the measurements to FONLL are shown in Fig. 4.3.

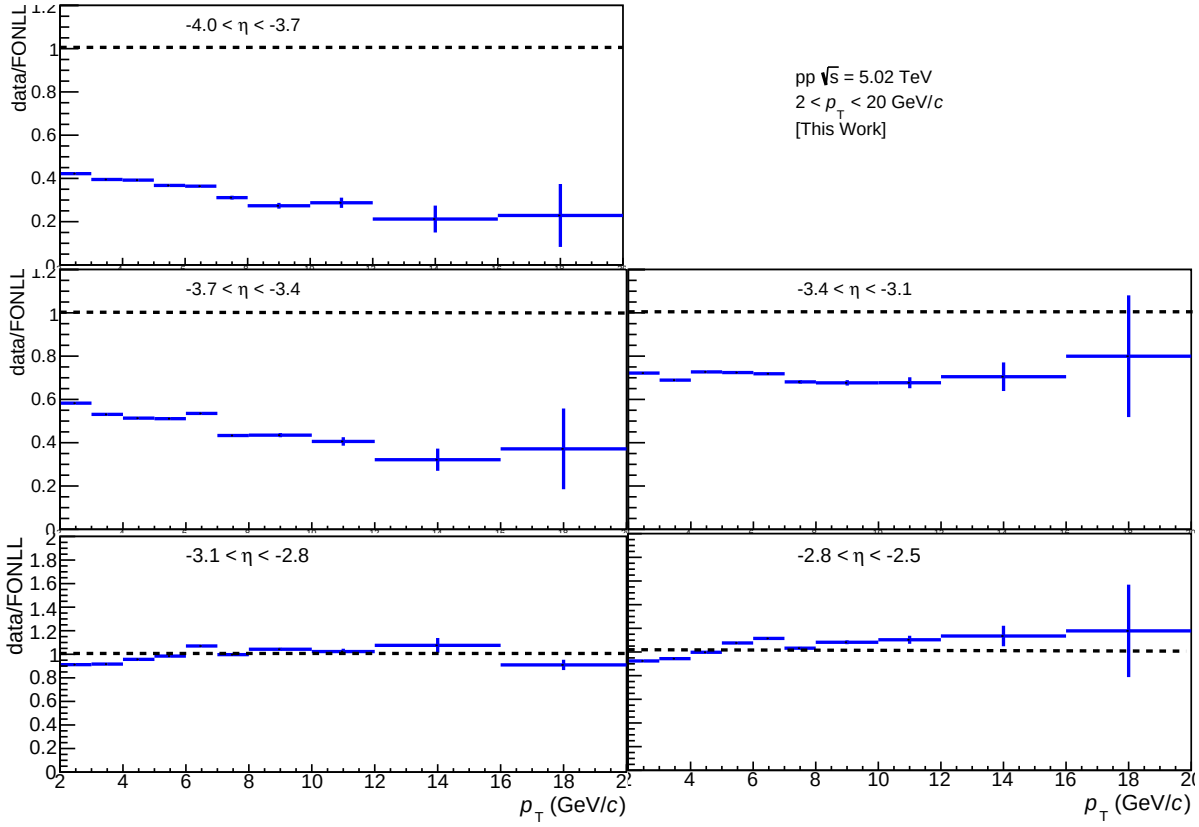

Fig. 4.3 Ratio of the heavy-flavour decay muon production cross-section and theoretical calculations from FONLL [175] in pp collisions at $\sqrt{s} = 5.02$ TeV in different η intervals. The horizontal lines are the bin width and the vertical lines are statistical errors obtained by adding the errors of the distributions in quadrature.

A comparison of the inclusive differential cross-section of this study with other measurements is discussed in the next section.

4.1.1 Comparison with other measurements in pp collisions

The main aim of determining the inclusive heavy-flavour decay muon differential cross-section in this study was to improve the statistics of already published data [49] of the heavy-flavour decay muon production cross-section in pp collisions at $\sqrt{s} = 5.02$ TeV. The comparison between the measurements in this thesis and the published data is shown in Fig. 4.4a, the ratio between the results is shown in the bottom panel. The published data and results show that there is a difference of up to 19% at low-p_{T} ($p_{\mathrm{T}} = 2$ GeV/c). The horizontal lines are the bin width and the vertical lines are statistical errors obtained by adding the errors of the distributions in quadrature. It can be noted that results in this

study were achieved with more recent published data for the background contributions as well as utilized MC productions with better statistics as compared to the published data. This could account for the differences in the inclusive heavy-flavour decay muon differential cross-sections.

As done in [49], the inclusive differential heavy-flavour decay muon cross-section measurement is compared with similar measurement in pp collisions at $\sqrt{s} = 7$ TeV [176]. Figure 4.4b shows the comparison where the green data points are those of the 7 TeV measurements from Run 1 data and the black data points are results from this current study at 5.02 TeV. From the comparison, a difference in the cross-sections is observed where the 7 TeV measurements lie above the 5.02 TeV measurements. This is expected as the heavy-flavour decay muon differential cross-section increases with center-of-mass energy as discussed in section 1.2.2.

Like in [49], a similar also observation made here is the difference in p_{T} reach of both measurements. The Run 1 measurements [176] lacked statistics and this is clearly observed from the results where the p_{T} range from 2 to 12 GeV/c. A ratio of the 7 TeV measurement with the 5.02 TeV measurement is taken and shown in the bottom panel of Fig. 4.4b. The ratio increases smoothly with an increase in p_{T} from about 1.8 ($p_{\mathrm{T}} = 2$ GeV/c) up to 2.5 ($p_{\mathrm{T}} = 12$ GeV/c) as observed in [49].

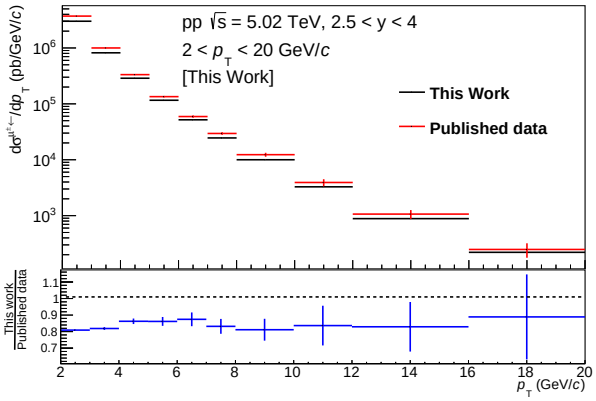

(a) Comparison of this work with published work in pp collisions at $\sqrt{s} = 5.02$ TeV [49].

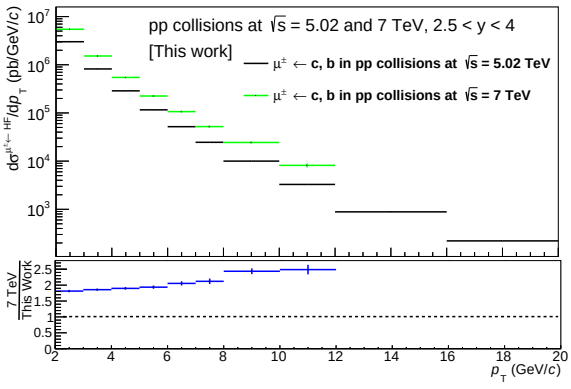

(b) Comparison of this work and measurments as $\sqrt{s} = 7$ TeV [176] in pp collisions.

Fig. 4.4 Comparison of the heavy-flavour decay muon production cross-section in pp collisions at $\sqrt{s} = 5.02$ with published data [49] (4.4a) and 7 TeV [176] (4.4b). The bottom panels show the ratios of the comparison in the top panel. The vertical lines are statistical uncertainties.

In the next section, results of the self-normalized yield as a function of charged-particle multiplicity will be shown.

4.2 Self-normalized yield as a function of charged-particle multiplicity

The aim of this work is to study the correlation of the differential heavy-quark decay muon yield and the charged-particle multiplicity. This is achieved by finding the self-normalized yield as a function of charged-particle multiplicity. The self-normalized yield is defined as [131]:

$$\frac{dN/d\eta}{\langle dN/d\eta \rangle} = \frac{N_{tot}(1 - f^{BKG})}{F_{norm} \cdot N_{MSL(H)}} \cdot \langle \frac{F_{norm} \cdot N_{MSL(H)} \cdot A \times \epsilon}{N_{tot}(1 - f^{BKG}) \cdot F_{inel}} \rangle \tag{4.2}$$

where N_{tot} is the total number of muons in the multiplicity bin, f^{BKG} is the background fraction that is estimated in section 3.41, F_{norm} is the normalization factor per multiplicity bin as discussed in section 3.4.2.4 and $N_{MSL/MSH}$ are the number of MSL/MSH events per multiplicity bin. All the quantities indicated by $\langle\rangle$ are integrated over multiplicity. It is important to note that the integrated multiplicity term is corrected for by the $A \times \epsilon$ that is determined in Chapter 3 in section 3.5. F_{inel} is the ratio of the V0 visible cross-section measured in the van der Meer scans and the inelastic cross-section, $F_{inel} = 0.7574 \pm 0.0190$. This factor is necessary to normalize the yield to the number of inelastic pp collisions. As already mentioned above, the inclusive heavy-flavour decay muon p_{T}-differential cross-section is measured as a function of p_{T} in the range 2-20 GeV/c and integrated over the muon spectrometer acceptance. The total number of muons and number of MSL/MSH events per multiplicity bin are also taken in the p_{T} range 2-20 GeV/c. The results of the self-normalized yield as obtained with equation 4.2 for the different multiplicity estimation methods is given in Table 4.1. It should be noted that the p_{T}-integrated self-normalized yield is determined using the MSL sample as the yield is dominated by low-p_{T} muons.

In Chapter 3, two methods that can be used for the analysis of multiplicity are discussed; the "Official Framework" method developed by the ALICE central multiplicity analysis group and the data-driven method. A comparison of the results obtained from these two methods is shown in this section.

The section will commence with a comparison of the results of the self-normalized yield vs charged-particle multiplicity obtained from this study employing both the "Official Framework" and data driven techniques. These will be compared to other heavy-flavour measurements at mid- and forward rapidity for different collision systems and center-of-mass energies.

Data-driven method		SPD estimator		V0M estimator	
$\frac{dN_{ch}/d\eta}{\langle dN_{ch}/d\eta\rangle}$	$\frac{dN^{\mu\leftarrow HF}/d\eta}{\langle dN^{\mu\leftarrow HF}/d\eta\rangle}$	$\frac{dN_{ch}/d\eta}{\langle dN_{ch}/d\eta\rangle}$	$\frac{dN^{\mu\leftarrow HF}/d\eta}{\langle dN^{\mu\leftarrow HF}/d\eta\rangle}$	$\frac{dN_{ch}/d\eta}{\langle dN_{ch}/d\eta\rangle}$	$\frac{dN^{\mu\leftarrow HF}/d\eta}{\langle dN^{\mu\leftarrow HF}/d\eta\rangle}$
0.166398 ± 1.31489	0.2325	0.29	0.2643	0.51	0.2399
0.319442 ± 0.894613	0.4721	0.60	0.7118	0.71	0.8342
0.520771 ± 0.652989	0.7507	0.85	1.2013	0.94	0.9433
0.725959 ± 0.545766	1.0152	1.07	1.5405	1.14	1.4626
0.985199 ± 0.487128	1.4108	1.39	1.8298	1.40	1.8868
1.35418 ± 0.42744	1.8173	1.70	2.1373	1.65	2.2134
1.86805 ± 0.376843	2.2524	1.97	2.3150	1.87	2.5479
2.84279 ± 0.432449	3.2217	2.35	2.6554	2.17	2.9149
4.78227± 0.301536	5.4285	3.00	2.9274	2.65	3.4048
		4.26	3.2496	3.35	3.6123

Table 4.1 Self-normalized charged-particle multiplicity and self-normalized yield for the different multiplicity estimation methods.

4.2.1 Self-normalized yield as a function of self-normalized charged-particle multiplicity

The data-driven method utilizes tracklets measured in the SPD at midrapidity to determine the multiplicity estimator. The multiplicity estimator is discussed in Chapter 3 in subsection 3.3.1.

The mid-pseudorapidity estimator is used as the reference for the charged-particle multiplicity in the $|\eta| < 1$ region while the V0 amplitude estimator is used for the event classification according to hadronic activity based on the V0 amplitudes. For the "Official Framework" multiplicity estimation, the two methods are compared.

The determination of self-normalized charged-particle multiplicity, used as the x-axis in the final result, is discussed in Chapter 3 in subsection 3.3.2. Unlike in the data-driven method where multiple steps are followed to obtain the multiplicity axis, the pseudorapidity density in different multiplicity classes is already available for use with only the requirement to determine the self-normalized charged-particle multiplicity.

The multiplicity dependence of the heavy-flavour yield in pp collisions at $\sqrt{s} = 5.02$ TeV is shown in Fig. 4.5. The correlation between the multiplicity and heavy-flavour yield is compared to a linear function, y=x, shown by the solid magenta line. The square boxes are the systematic uncertainties. An approximately faster than linear increase within uncertainties is observed from the results. The increasing trend of the self-normalized yield is visible, where the data points lie above the solid line. This trend is consistent

with what is observed in other heavy-flavour measurements which will be demonstrated later in the section.

To better assess deviations from the linear behavior, the ratio between the the heavy-flavour yield and self-normalized charged-particle multiplicity is taken and shown in the bottom panel of Fig. 4.5. It can be noted that the ratio lies above 1 for the data-driven method (blue data points) over the full multiplicity range. This is an indication that the differential heavy-flavour decay muon scales slightly faster than linear with the underlying event activity in the presence of a rapidity gap between the forward rapidity ($-4 < \eta < -2.5$) at which the heavy-flavour yield is measured and midrapidity ($|\eta| < 1$) at which the charged-particle multiplicity is measured.

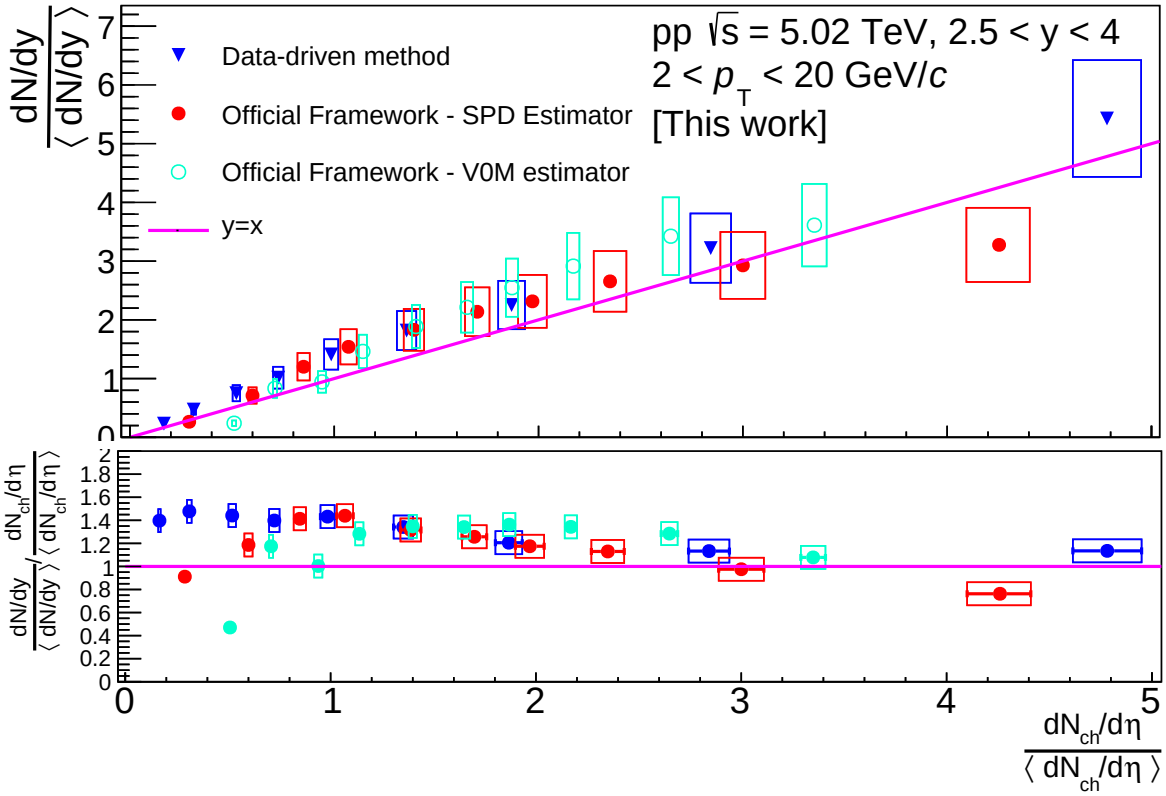

Fig. 4.5 Comparison of the self-normalized yield as a function of charged-particle multiplicity using the data-driven method, SPD and V0M estimators of the "Official Framework" method. Ratio between the the heavy-flavour yield and self-normalized charged-particle multiplicity. The solid line is y=x and the boxes represent the systematic uncertainties.

Figure 4.5 also shows a comparison of the data-driven method and the "Official Framework" method SPD and V0M multiplicity estimators. All the methods are in agreement at low charged-particle multiplicities; moving to higher multiplicities, both the SPD and V0M estimators of the "Official Framework" tend to deviate from the linear trend with a

possibility of saturating at higher charged-particle multiplicity ($(dN_{ch}/d\eta)/\langle dN_{ch}/d\eta\rangle \sim 3$). The data-driven method allows for a somewhat higher charged-particle multiplicity reach as compared to the "Official Framework" method.

A comparison is also made between the V0M and SPD estimators. The V0M estimator increases faster than the SPD estimator within systematic uncertainties. This confirms what was discussed in Chapter 1 section 1.4 of no possible auto-correlation bias that arises from multiplicity selection [75]. Auto-correlation bias arises when the additional particles produced with heavy-flavour particles increase the multiplicity and as a result, the multiplicity is shifted to high values and therefore resulting in a stronger than linear increase of the differential heavy-flavour decay muon with multiplicity.

The differences between the data-driven and "Official Framework" can be attributed to the correction of the SPD efficiency not taken into account. In Chapter 3, a correction of the SPD tracklets is made in order to obtain a uniform distribution of the average tracklets as a function of the z-vertex (Fig. 3.5 and 3.7). This correction is not made in the "Official Framework" multiplicity estimation. Another difference between the two methods is SPD pile-up; in the data-driven method, the SPD pile-up is accounted for by correcting for the SPD efficiency while in the "Official Framework" method, the contamination from in-bunch pile-up events was removed offline which involved excluding events with multiple vertices reconstructed in the SPD according to [56].

A comparison of results from this study obtained with the data-driven method and "Official Framework" method using the SPD estimator with other heavy-flavour measurements at midrapidity are shown in the next sections.

4.2.2 Comparison with other heavy-flavour measurements at mid- and forward rapidity in pp collisions

The self-normalized yield as a function of charged-particle multiplicity can also be studied in different p_{T} bins. This is done to observe if there is a p_{T} dependence of the self-normalized yield as a function of charged-particle multiplicity. The p_{T} range is sliced into 6 bins. The MSL sample is used for the low-p_{T} bins (2 - 4 and 4 - 6 GeV/c) while the MSH sample is used for the high-p_{T} bins (6 - 20 GeV/c). The results are shown in Fig. 4.6, there is an increasing trend in the different p_{T}-bins. At low charged-particle multiplicities, the MSL sample yields dominates while at high charged-particle multiplicities, the MSH sample yields dominate, more specifically, the p_{T} interval $14 < p_{\mathrm{T}} < 20$ GeV/c.

The low-p_{T} intervals (2-6 GeV/c) that utilizes the MSL triggered events sample displays a faster than linear increase while the high-p_{T} intervals (6-20 GeV/c) that utilizes the MSH triggered events sample displays a less than linear increase except at the highest multi-

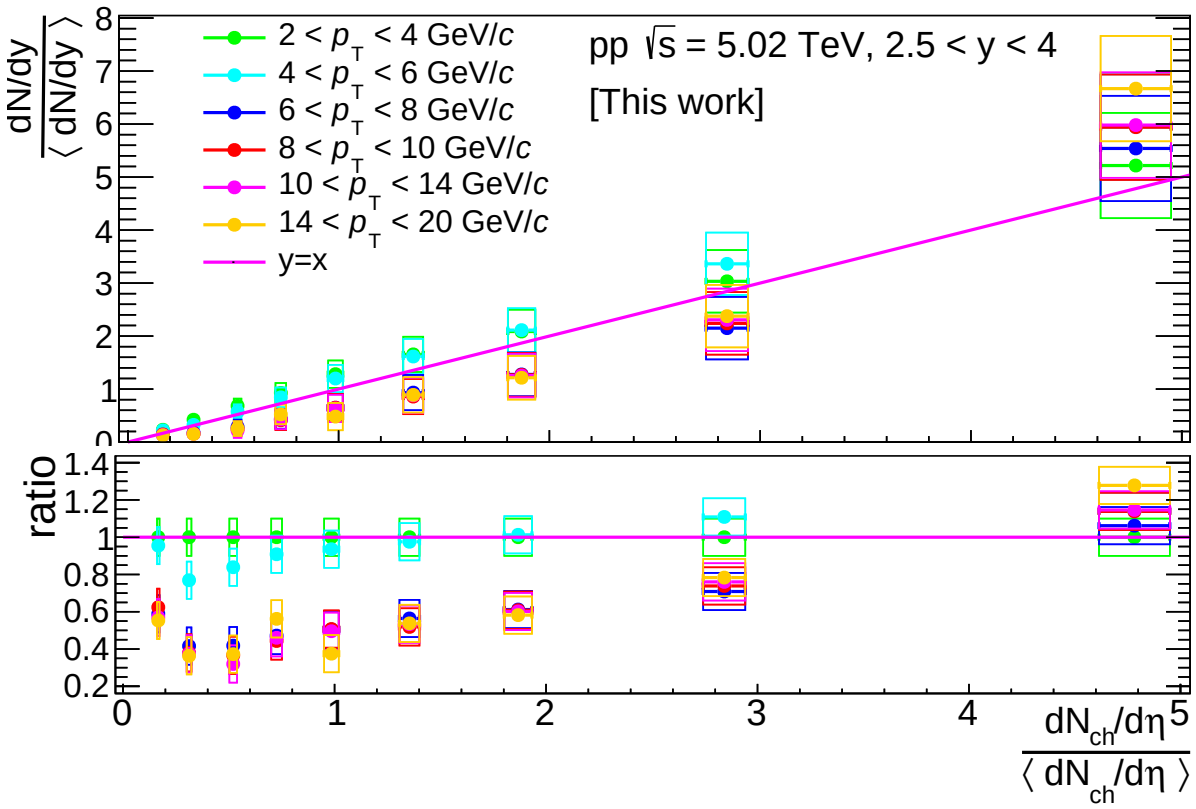

Fig. 4.6 Self-normalized yield as a function of charged-particle multiplicity in different p_{T} intervals. The solid line is y=x and the boxes represent the systematic uncertainties (top panel). Ratio of the relative muon yields in p_{T} intervals as a function of the relative charged-particle multiplicity, p_{T} interval $2 < p_{\mathrm{T}} < 4$ GeV/c is chosen as reference. The horizontal solid line represents unity and the boxes represent the systematic uncertainties (bottom panel).

plicity. This confirms the choice of using the MSL triggered event sample to determine the self-normalized yield for integrated p_{T}.

The ratio of the relative muon yields in p_{T} intervals shown in Fig. 4.6 as a function of the relative charged-particle multiplicity is determined and shown in the bottom panel of Fig. 4.6 where p_{T} interval $2 < p_{\mathrm{T}} < 4$ GeV/c is chosen as reference. The dashed magenta line indicates unity and also the ratio of the first p_{T} interval itself is shown by the green data points. The low-p_{T} intervals (2-6 GeV/c) are in agreement within uncertainties. The high-p_{T} intervals (6-20 GeV/c) are less than the reference interval except at the last charged-particle multiplicity bin where the ratio is above 1.

A further comparison between the MSL and MSH triggered events sample in the common p_{T} range is made for the self-normalized yield as a function of charged-particle multiplicity. Two p_{T} ranges were chosen - low- p_{T} (2-4 GeV/c) and high-p_{T} (14-20 GeV/c); the low-p_{T}

range is chosen to further justify the choice in using the MSL triggered events sample for the determination of the self-normalized yield as a function of charged-particle multiplicity. Figure 4.7 shows the comparisons of the MSL and MSH triggers in a common p_{T} range; on the left is a comparison in the low-p_{T} range and on the right the high-p_{T} range. It is observed in the low-p_{T} range that the MSL trigger rises faster than the MSH trigger. In the high-p_{T} range, the MSL and MSH triggers are comparable at low multiplicities and the MSH trigger dominates at the highest multiplicity. It is also observed that both MSL and MSH triggers contain more low-p_{T} muons than high-p_{T}.

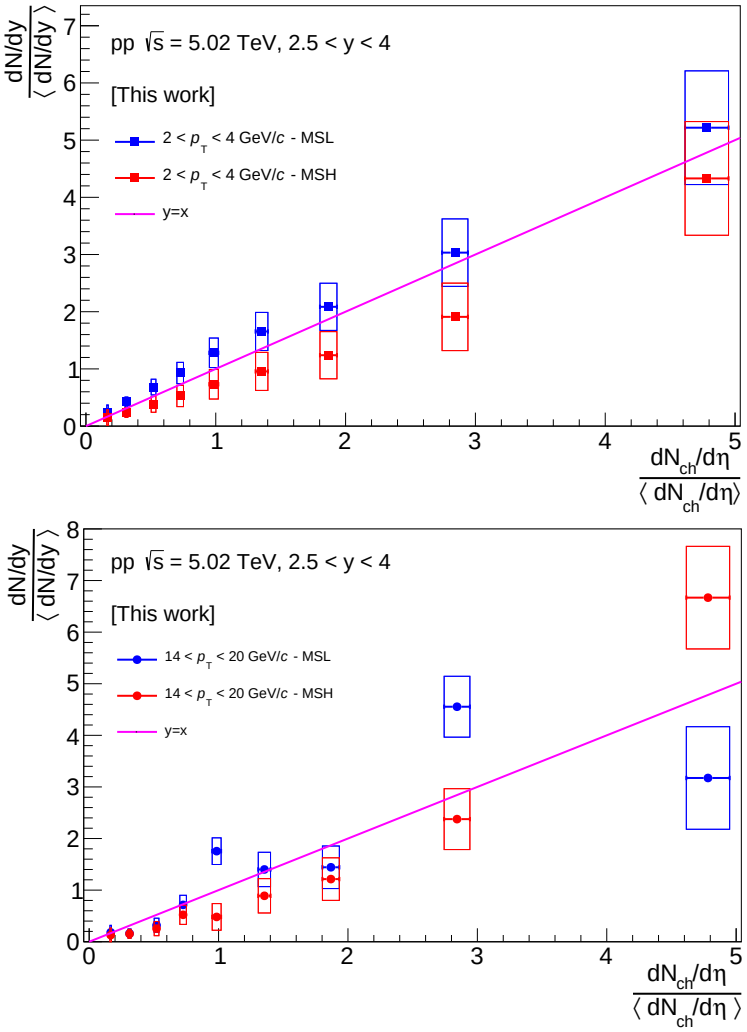

Fig. 4.7 Self-normalized yield as a function of charged-particle multiplicity in two different p_{T} intervals. The solid line is y=x and the boxes represent the systematic uncertainties. Top: low-p_{T} interval $2 < p_{\mathrm{T}} < 4$ GeV/c. Bottom: high-p_{T} interval $14 < p_{\mathrm{T}} < 20$ GeV/c

The p_{T}-dependence of the differential measurement of the heavy-flavour decay muon yield as a function of the charged-particle multiplicity is necessary when making comparisons with measurements at midrapidity. A comparison of the differential heavy-flavour decay

via the single muon decay channel in the p_{T} range $2 < p_{\mathrm{T}} < 4$ GeV/c at forward rapidity is made with the measurements of the average D-meson [71] and J/ψ [177] via the hadronic and semi-leptonic decay channel at midrapidity, respectively.

The comparison is between D-meson, J/ψ and inclusive measurements from this study. It is important to note that this comparison involves three different processes in which the decay muons are measured; **1.)** in the case of the D-meson, composed of a charm and light anti-quark, only charm quarks decaying to light hadrons (pion and koans) are measured via the hadronic decay channel while **2.)** in the case of J/ψ, composed of a charm and anti-charm, there is a 5.961% probability that it will decay into a dimuon pair via the muonic (or electronic) decay channel and **3.)** in this inclusive measurements, muons from both the charm and beauty quark decays are measured. D-meson and J/ψ measurements are exclusive measurements as these only exclusively measure light hadrons (pions and kaons) and muons from the charm quark, respectively.

A comparison is made between J/ψ measurements via the muonic decay channel [172] and heavy-flavour decay muon measurements in pp collisions at $\sqrt{s} = 5.02$ TeV at forward rapidity. This comparison plays a key role in understanding the heavy-flavour decay muons measured directly from charm and beauty quarks before undergoing the hadronization process compared to decay muons from heavy-flavoured particles where the charm and beauty quarks have hadronized.

Figure 4.8 shows the self-normalized yields of J/ψ [172] and this study of heavy-quarks as a function of charged-particle multiplicity in pp collisions at $\sqrt{s} = 5.02$ TeV measured at forward rapidity using both techniques: data-driven method (blue) and the SPD estimator of the "Official Framework" (red). Overall, the results from this study and those from J/ψ are compatible at low charged-particle multiplicity ($(dN_{ch}/d\eta)/\langle dN_{ch}/d\eta\rangle \sim 3$). There is an approximately linear increase for the J/ψ measurements while results from this study show an approximately faster than linear increase.

A comparison of the self-normalized yield as a function of charged-particle multiplicity for the average D-meson [71] (orange data points) and J/ψ [177] (green data points) measurements at midrapidity and at forward rapidity for this study (blue and red data points) are shown in Fig. 4.9. The solid line is a y=x and the square boxes are the systematic uncertainties. Similarly, it is observed that the results are compatible at low charged-particle multiplicity ($(dN_{ch}/d\eta)/\langle dN_{ch}/d\eta\rangle \sim 3$).

There is an approximately faster than linear increase in both the midrapidity and forward rapidity measurements. It is also noted that the results at midrapidity increases faster than the measurements at forward rapidity at higher multiplicities (> 3), the increase seems to depend on the rapidity gap between the rapidity used in the particle-yield mea-

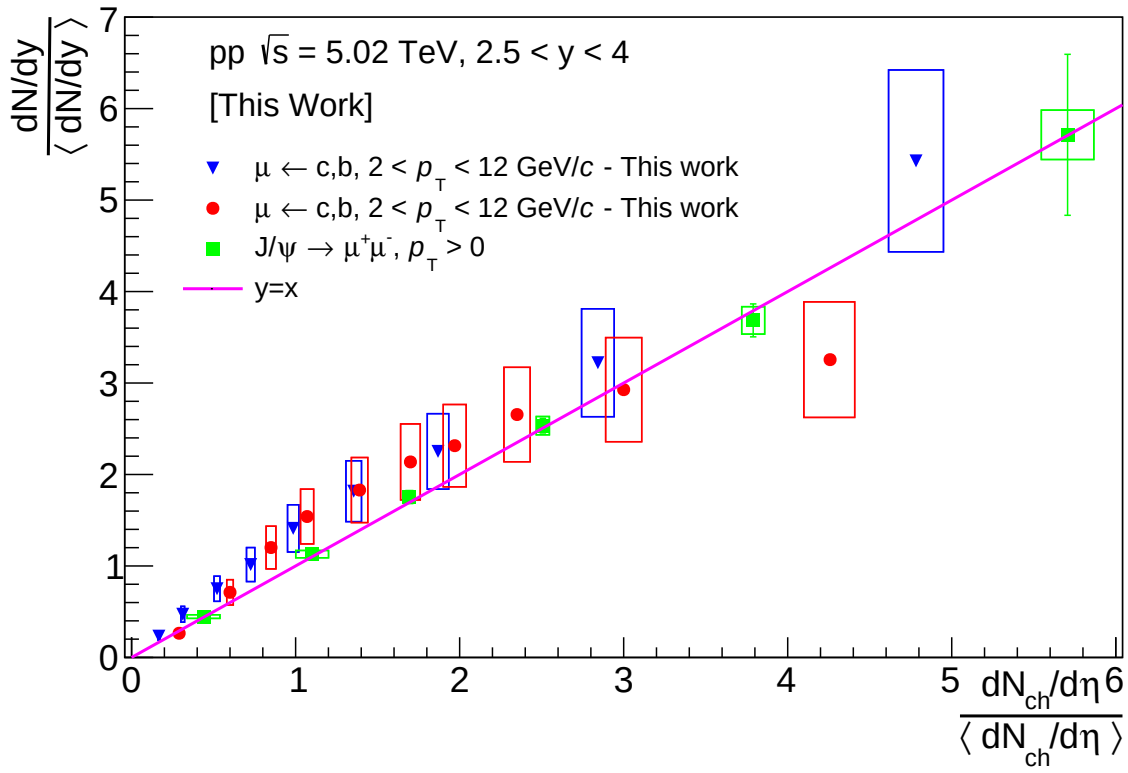

Fig. 4.8 Comparison of J/ψ (green data points) [172] and the differential heavy-flavour (red and blue data points) muon decay as a function of charged-particle multiplicity in pp collisions at $\sqrt{s} = 5.02$ at forward rapidity. The solid line is y=x and the boxes represent the systematic uncertainties.

surement and the multiplicity measurement one. The stronger than linear heavy-flavour relative yields with charged-particle multiplicity measurements in D-meson and J/ψ measurements are qualitatively consistent with calculations that include MPI contributions to the particle production. Auto-correlation bias arises when the additional particles produced with heavy-flavour particles increase the multiplicity and as a result, the multiplicity is shifted to high values and therefore resulting in a stronger than linear increase of the differential heavy-flavour decay with multiplicity. These differences can therefore be attributed to possible auto-correlation bias that arises from the same rapidity region (midrapidity) of the multiplicity selection and the particle production measurement as well as the contribution of MPIs to the particle production.

This chapter is concluded with a comparison of differential heavy-flavour measurements vs charged-particle multiplicity performed in the pp collision system with the p-Pb collision system.

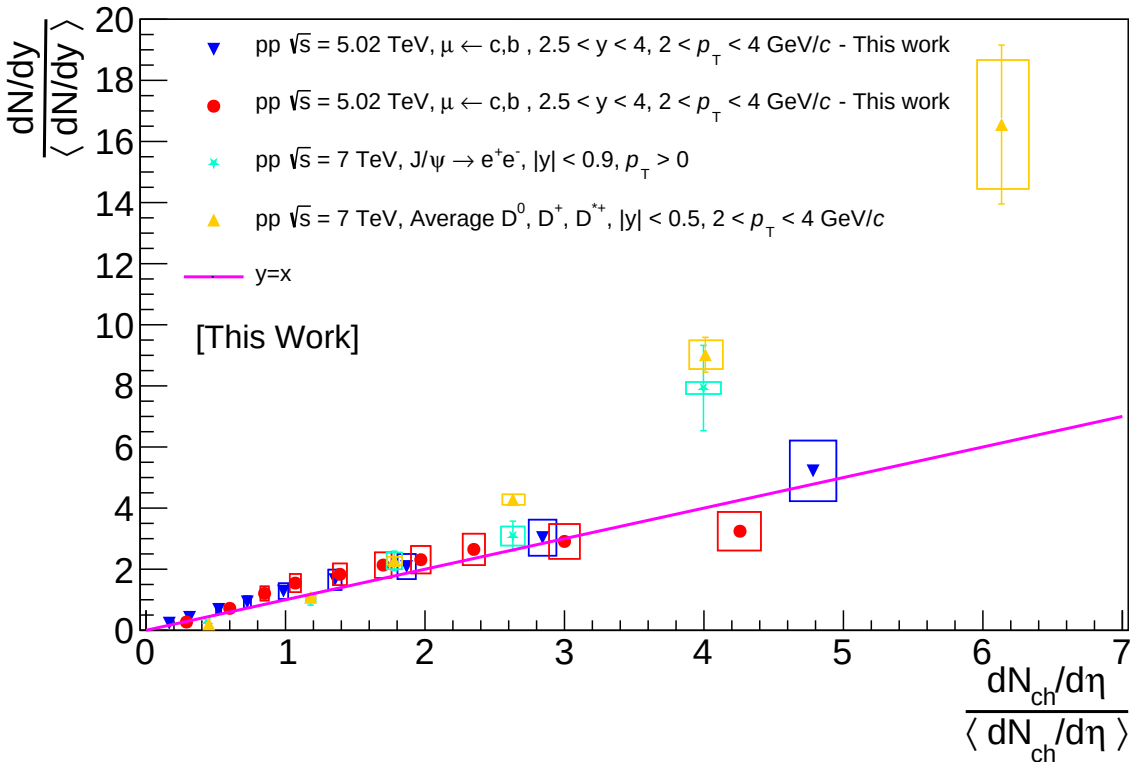

Fig. 4.9 Self-normalized yield as a function of charged-particle multiplicity measured in midrapidity for the average D-meson [71] and J/ψ [177] measurements and at forward rapidity for this study. The solid line is y=x and the boxes represent the systematic uncertainties.

4.2.3 Comparison of pp and p-Pb measurements

The final comparison made is between the pp and p-Pb colliding system at the center-of-mass energy of 5.02 TeV. This comparison is made between mid- and forward rapidity measurements for the average D-meson measurements [78] and relative J/ψ measurements [79] in p-Pb with the inclusive measurement of this study. In this comparison the p_{T} range $2 < p_{\mathrm{T}} < 4$ GeV/c in pp is considered.

In a p-Pb collision system, the production of heavy quarks can be influenced by the dense environment found within the Pb nucleus. This effect is known as cold nuclear matter (CNM) effects [51, 52]. The production of heavy-flavour hadrons at all the stages of their formation are affected by these effects. As a result, the initial condition of the collision may be affected by the presence of the Pb nucleus in a p-Pb collision which can possibly account for the differences in the measurements [78]. The comparison between measurements in p-Pb and this study will shed light on how the correlation between particle production and multiplicity is influenced by the collision geometry. The multiplicity of the produced particles is expected to be dependent on the number of nucleons that are overlapping in

the collision region, this implies that the multiplicity would be dependent on the collision geometry.

Figure 4.10 shows the comparison of the average D-meson measurements [78] (orange data points) and J/ψ measurements [79] (green data points) in p-Pb at $\sqrt{s_{NN}} = 5.02$ TeV and the differential heavy-flavour decay muon (blue and red data points) in pp at $\sqrt{s} = 5.02$ TeV as a function of charged-particle multiplicity at midrapidity and forward rapidity (this work), respectively. The solid line is y=x and the boxes represent the systematic uncertainties. All the measurements show an approximately faster than linear increase. The results from this study and those from the D-meson and J/ψ are compatible at low charged-particle multiplicity ($(dN_{ch}/d\eta)/\langle dN_{ch}/d\eta\rangle \sim 3$). However, it is noted that the average D-meson and J/ψ measurements increase faster at higher multiplicities as compared to the measurements in this study.

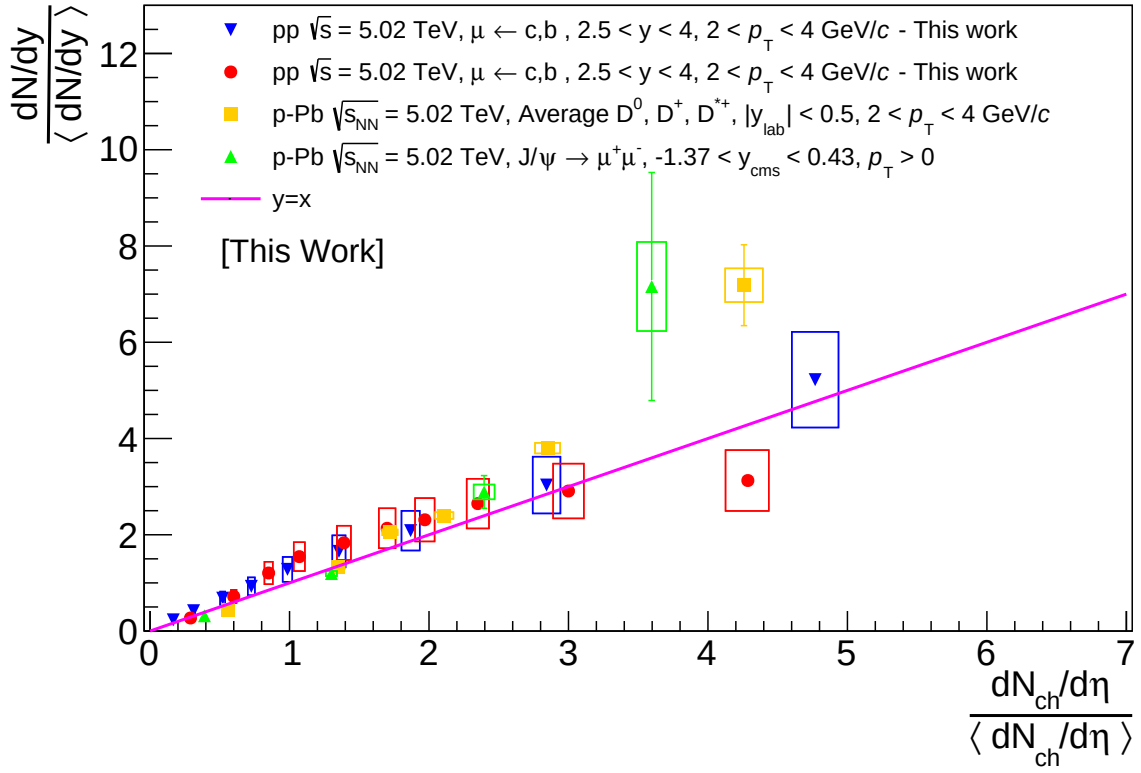

Fig. 4.10 Comparison of average D-meson [78] and relative J/ψ [79] measurements in p-Pb at $\sqrt{s_{NN}} = 5.02$ TeV and the differential heavy-flavour muon decay in pp at $\sqrt{s} = 5.02$ TeV as a function of charged-particle multiplicity at midrapidity and forward rapidity, as indicated. The solid line is y=x and the boxes represent the systematic uncertainties.

Two similar comparisons were discussed in Chapter 1: **1)** a comparison of p-Pb data at $\sqrt{s_{NN}} = 5.02$ TeV with pp at $\sqrt{s} = 7$ TeV results of the relative D-meson yield as function of charged-particle multiplicity [78] and **2)** a comparison of relative J/ψ measurement on

the relative charged-particle multiplicity is compared to measurements for prompt D-meson at midrapidity in p-Pb collisions at $\sqrt{s_{NN}} = 5.02$ TeV in [79] at midrapidity. In both comparisons, the measurements increase stronger than linear. It was also observed in the comparison between the relative D-meson yield as function of charged-particle multiplicity in p-Pb data at $\sqrt{s_{NN}} = 5.02$ TeV with pp at $\sqrt{s} = 7$ TeV that the D-meson measurements in pp collisions increase faster than in p-Pb collisions. It should however be noted that in the comparison of D-meson yields, both collision systems were D-meson measurements unlike in this study where a comparison is made between inclusive measurements and the D-meson.

The final chapter will conclude this thesis followed with an outlook of this study and related measurements.

CHAPTER 5

Conclusion and outlook

In this thesis, the inclusive heavy-flavour decay muon p_{T}- and η-differential cross-sections were measured. This was done with the aim of improving the statistics of already published inclusive heavy-flavour decay muon differential cross-section in pp collisions at $\sqrt{s}$ = 5.02 TeV. The statistics were improved by considering also the reference data taken in 2017 in addition to the 2015 data in pp collisions at $\sqrt{s} = 5.02$ TeV. The total integrated luminosity during the 2015 data-taking period was ~ 100 nb^{-1} in pp collisions at $\sqrt{s}$ = 5.02 TeV; and ~ 1.3 pb^{-1} considering the 2017 data-taking period at the same $\sqrt{s}$. To add to the published inclusive heavy-flavour decay muon differential cross-section, a new observable: heavy-flavour decay muon yield as a function of the charged-particle multiplicity was also measured and the obtained results were presented in this study. This measurement is the first for the inclusive heavy-flavour decay muon measurements at forward rapidity in pp collisions at $\sqrt{s} = 5$ TeV. These measurements play an important role in acting as a baseline for p-Pb and Pb-Pb collision systems at $\sqrt{s} = 5.02$ TeV.

5.1 Conclusion

The inclusive heavy-flavour decay muon differential cross-section was measured as a function of p_{T} in the range 2-20 GeV/c and integrated over the muon spectrometer acceptance ($2.5 < y < 4$). The experimental data were compared with the theoretical model FONLL where it was observed that at $p_{\mathrm{T}} < 6$ GeV/c, the measured data are consistently close

to the upper band of the FONLL prediction. The central values of FONLL predictions systematically underestimate the measured heavy-flavour decay muon differential cross-section. This is consistent to what was reported in the published heavy-flavour decay muon analyses in pp collisions at at $\sqrt{s} = 5.02$ TeV where the FONLL predictions underestimates the experimental data. Similar observations were made in studies of heavy-flavour particles in pp collisions at at $\sqrt{s} = 2.76$, 5.02 and 7 TeV in ALICE. At low p_{T}, $2 < p_{\mathrm{T}} < 4$ GeV/c, the dominant process is the charm decay ($c \rightarrow \mu$, BR $\approx 10.33\%$) while from mid- to high p_{T}, $4 < p_{\mathrm{T}} < 20$ GeV/c, the dominant process is the direct beauty decay ($b \rightarrow \mu$, BR $\approx 10.86\%$). The indirect beauty decay ($b \rightarrow D \rightarrow \mu$, BR $\approx 9.66\%$) is consistently less over the p_{T} range.

FONLL calculations include the non-perturbative fragmentation function tuned on e^+e^- data and assumes that all charm and beauty quarks fragments only into open heavy-flavour hadrons and their decay into final-state leptons. Leptons from charm- and beauty-hadron decays are controlled by measuring the decay spectra and their corresponding branching ratios. Furthermore, FONLL uncertainties include various choices for the charm and beauty quark masses, the factorization and renormalization scales, and the uncertainty on the PDFs. It should be noted that the FONLL predictions utilize the CTEQ6.6 PDFs, these are the only PDFs available for FONLL calculations in pp collisions at $\sqrt{s} = 5.03$ TeV. These PDFs are obtained by global analysis of hard scattering data in the framework of general-mass perturbative QCD and are employed to study theoretical predictions and their uncertainties for significant processes at the Fermilab Tevatron and CERN's Large Hadron Collider.

The inclusive heavy-flavour decay muon differential cross-section was also measured as a function of η in the p_{T} range 2-20 GeV/c. A comparison with the theoretical model FONLL showed FONLL predictions describe the data within uncertainties. The comparison of the inclusive heavy-flavour decay muon differential cross-section in different η intervals with FONLL showed that the predictions describe the data within uncertainties for most of the η intervals except the interval $-4 < \eta < -3.7$ where FONLL describes the data at low p_{T} but overestimates the data at $p_{\mathrm{T}} > 4$ GeV/c. In contrast, in other pp collisions studies at $\sqrt{s} = 2.76$, 5.02 and 7 TeV at forward rapidity in ALICE, it was found that FONLL calculations provided an overall good description of the data over the entire p_{T} range for all the η intervals. Further investigations will need to be performed to understand the differences in this study.

A comparison of the inclusive heavy-flavour decay muon p_{T}-differential cross-section results obtained in this study with published data in pp collisions at $\sqrt{s} = 5.02$ TeV was made. A ratio between this work and the published data indicates a difference of up to 19% at low-p_{T} ($p_{\mathrm{T}} = 2$ GeV/c). A smooth increase with an increase in p_{T} from a factor of

about 0.81 ($p_{\mathrm{T}} = 2$ GeV/c) up to 0.88 ($p_{\mathrm{T}} = 20$ GeV/c) was observed. These differences can be attributed to the utilization of different data for the subtraction of the background contribution whereby in this study more recent published data were utilized as well as available MC productions with more statistics. The same p_{T} reach as the published data was achieved despite the increase of statistics in this study. This could be due to the W and Z/γ^* contribution towards high-p_{T} ($p_{\mathrm{T}} > 20$) which increases significantly with p_{T} thereby limiting the extension of the p_{T} reach beyond 20 GeV/c where it is under control.

Similarly to the pp collisions at $\sqrt{s} = 5.02$ TeV publication, a comparison of the inclusive differential cross-section of heavy-flavour decay muons as a function of p_{T} in pp collisions at $\sqrt{s} = 5.02$ TeV and 7 TeV was also made. A difference in the inclusive differential cross-sections was observed where the 7 TeV measurements lie above the 5.02 TeV measurements as expected from literature, and a higher p_{T} reach of up to $p_{\mathrm{T}} = 20$ GeV/c was achieved in this study. The ratio of the 7 TeV measurement with the 5.02 TeV measurement showed a smooth increase with an increase in p_{T} from a factor of about 1.8 ($p_{\mathrm{T}} = 2$ GeV/c) up to 2.5 ($p_{\mathrm{T}} = 12$ GeV/c). The energy dependence of the differential cross-section is confirmed, that is, the production of charm and beauty quarks increases with center-of-mass energy in pp collisions.

These inclusive differential cross-section measurements in pp collisions at $\sqrt{s} = 5.02$ TeV act as a reference for measurements of the nuclear modification factor, essential for the study of the effects of the hot and dense matter, the quark-gluon plasma (QGP), in Pb-Pb collisions at the same center-of-mass energy. In p-Pb collisions at the same center-of-mass energy, these pp measurements serve as a baseline for the investigation of cold nuclear matter effects (CNM), useful to disentangle initial and final state effects.

A new observable in pp collisions at $\sqrt{s} = 5.02$ TeV, the differential heavy-quark decay muon yield as a function of the charged-particle multiplicity, was also investigated with an aim to test the contribution towards understanding:

- The interplay between soft and hard partonic interactions,
- Events that contain MPIs are expected to have higher multiplicity, and
- The role of the collision geometry as well as the final-state effects.

The interplay between soft and hard processes was studied by analyzing the differential heavy-flavour decay muon yield as a function of charged-particle multiplicity. The event multiplicity (soft processes), determined by the number of charged-particles produced at midrapidity while the hard processes were accessed by measuring the heavy-flavour decay muon yield at forward rapidity in pp collisions at $\sqrt{s} = 5.02$ TeV. At forward rapidity an approximately faster than linear increase of the heavy-flavour yield as a function of

charged-particle multiplicity was observed. This trend is an indication that the differential heavy-flavour decay muon yield scales slightly faster than linear with the underlying event activity in the presence of a rapidity gap between the heavy-flavour measurements at forward rapidity ($2.5 < y < 4$) and the charged-particle multiplicity measured at midrapidity ($|y| < 1$). The underlying event activity are the additional interactions that are not associated with the initial hard scattering process, this includes multiple parton-parton interactions (MPIs).

Two methods were utilized for the multiplicity estimation; the data-driven method and the "Official Framework"; which consists of both the midrapidity (SPD) and forward rapidity (V0M) estimators. The results from both methods were in agreement within systematic uncertainties at low multiplicities. A comparison of the "Official Framework" SPD and V0M estimators was also made, the measurements were in agreement. The agreement of the results implies that there are no auto-correlation effects that arise from multiplicity selection. It is important to note that heavy-flavour particles are produced together with other particles like charm-anticharm pairs ($c \rightarrow D,\ \bar{c} \rightarrow \text{jet} \rightarrow \text{jet fragmentation}$) and decay daughters ($B \rightarrow J/\psi + \text{x}$). The additional particles increase the multiplicity, shifting the multiplicity distribution towards higher values thus resulting in a stronger than linear increase of differential heavy-flavour decay with multiplicity. These effects are known as auto-correlation effects. It was also observed that at high multiplicities, the V0M estimator increases faster than the SPD estimators. However, since the "Official Framework" does not correct for the SPD efficiency in the multiplicity estimation method, the measurements appear to be saturating at high multiplicities. For this reason, the data-driven method measurement would be the preferred method for comprehensive and complete multiplicity measurements for this kind of study.

A comparison between the measurements in this study and those of J/ψ measurements via the muonic decay channel as a function of charged-particle multiplicity at forward rapidity in pp collisions at $\sqrt{s} = 5.02$ TeV was made. This comparison plays a key role in understanding how the hadronization process affects the differential heavy-flavour decay muon as well as allowing for indirect comparisons to theoretical models. The measurements are compatible at low charged-particle multiplicity (< 3) where an approximately linear increase for the J/ψ measurements is observed while results from this study show an approximately faster than linear increase. The compatibility of the measurements indicates that hadronization mechanisms do not influence particle production. Moreover, one can draw conclusions from J/ψ measurements being well described at low charged-particle multiplicity (< 3) by the percolation string model. A similar trend is exhibited by results from this study, it can therefore be concluded that the percolation string model, which estimates the influence of color charge exchange during the interaction, is expected to describe the differential heavy-flavour decay muon yield as a function of charged-particle

multiplicity measurements well at low multiplicity (< 3).

Heavy-flavour production vs charged-particle multiplicity measurements can also contribute towards understanding how events containing MPIs have higher multiplicities. Particle production can be dependent on the total charged-particle multiplicity due to several interactions that occur at parton level in a collision. In the case of the production of heavy quarks, the production can be affected by MPIs in head-on collisions that may occur between two partons of incoming protons. These interactions occur at small distances with a large momentum transfer and as a result, the final state particles are produced at large angles with respect to the beam line and thus creating massive particles with high p_{T}. To extract information on the relative contributions of individual processes to the total production, a comparison with D-meson and J/ψ measurements as a function of charged-particle multiplicity at mid-rapidity in pp at $\sqrt{s} = 7$ TeV was made. The measurements differ in the sense that the D-meson (open charm) was measured exclusively via a hadronic decay channel at midrapidity, J/ψ (charm-anticharm) was measured exclusively via the electronic decay channel at midrapidity and heavy-flavour decay muons were measured inclusively by summing decay muons from charm and beauty quarks at forward rapidity. An approximately faster than linear increase was globally observed in the measurements, however, at charged-particle multiplicities > 3 the midrapidity measurements (D-meson and J/ψ) have a stronger increase than the forward rapidity measurements (heavy-flavour decay muon). Furthermore, these differences depend on the rapidity gap between the rapidity used in the particle-yield measurement and that of the multiplicity measurement one. These differences are attributed to the possible auto-correlation bias that arises from the same rapidity region (midrapidity $|y| < 1$) of the multiplicity selection and the particle production measurement of the D-meson and J/ψ.

The stronger than linear trend observed in D-meson and J/ψ measurements is quantitatively described by calculations that include MPI contributions, such as PYTHIA 8.157 calculations which describes heavy-flavour production via four main mechanisms: (*i*) initial hard process, (*ii*) hard processes in MPI produced via the same mechanisms as the initial hard process from subsequent interactions, (*iii*) gluon splitting from hard process and (*iv*) initial or final state radiation (ISR/FSR). In the case of the D-messon, the main contributions come via the hard process in MPI and ISR/FSR, suggesting that the origin of charm quarks is from gluons that split into a $c\overline{c}$ pair which contributes to the heavy-flavour production. For the ISR/FSR process, the initial gluon originated from initial or final state radiation. It can therefore be concluded that measurements from this study at forward rapidity contain only events with a small number of MPI contribution over the entire multiplicity interval as compared to the D-meson and J/ψ measurements at midrapidity where at low multiplicity intervals, only events with a small number of MPI contribute while high multiplicity events are dominated by a large number of MPI as

observed in the results.

In small systems, measurements in pp collisions provide a baseline for p-Pb. Morever, a similar comparison with D-meson, J/ψ measurements and heavy-flavour decay muons as a function of charged-particle multiplicity was made at mid-rapidity in p-Pb collisions at $\sqrt{s} = 5.02$ TeV and were compared with the forward rapidity measurements. A similar observation is made as discussed above where an approximately faster than linear increase is observed in the measurements, however, at charged-particle multiplicities > 3 the midrapidity measurements have a stronger increase than the forward rapidity measurement. A comparison of p-Pb data at $\sqrt{s_{NN}} = 5.02$ TeV with pp at $\sqrt{s} = 7$ TeV results of the relative D-meson yield as function of charged-particle multiplicity was made, this allowed for a more direct comparison between pp and p-Pb measurements since the comparison is between the same species (D-mesons). The trend observed showed that the pp measurements increase faster than the p-Pb measurements. The initial condition of the collision may be affected by the presence of the Pb nucleus in a p-Pb collision, i.e. the number of nucleons that are overlapping in the collision region and thus on the collisions centrality (geometry of the collision). Additionally, multiple binary nucleon-nucleon interactions can also affect the initial conditions of the p-Pb collision. As a result, this can possibly account for the differences in the measurements as the p-Pb collision follows a hydrodynamic expansion as described by EPOS calculations that include viscous hydrodynamic evolution. Other possible factors that can explain the stronger than linear increase of the p-Pb measurements include short distance gluon-radiation and contributions from MPIs. In this study, however, it cannot be strictly concluded that the presence of the Pb nucleus affects the initial condition. To gain a better understanding, measurements of heavy-flavour decay muons as a function of charged-particle multiplicity in p-Pb collisions at $\sqrt{s} = 5.02$ TeV at forward rapidity will be required to make a direct comparison.

In summary, the heavy-flavour vs charged-particle multiplicity measurements contribute towards understanding:

- The interplay between soft and hard partonic interactions:
  The differential heavy-flavour decay scales sightly faster than linear with the underlying event activity in the presence of a rapidity gap between the heavy-flavour measurements at forward rapidity ($2.5 < y < 4$) and the charged-particle multiplicity measured at midrapidity ($|y| < 1$).

- Events that contain MPIs are expected to have higher multiplicity as compared to events that do not contain MPIs:
  The stronger than linear trend observed in D-meson and J/ψ measurements is quantitatively described by calculations that include MPI contributions. Measurements from this study display an approximately faster than linear increase, therefore it

can be concluded that only events with a small number of MPI contribute over the entire multiplicity interval.

- The role of the collision geometry as well as the final-state effect:
  The multiplicity of the produced particles is expected to be dependent on the number of nucleons that are overlapping in the collision region. The comparison between relative D-meson and J/ψ measurements in p-Pb collisions and inclusive heavy-flavour measurements provides further insight into understanding the role of the collision geometry as well as the final-state effect. A direct comparison between inclusive heavy-flavour measurements in pp and p-Pb collisions at the same collision energy is required.

In this work, the experimental measurements of the inclusive heavy-flavour p_{T}- and η-differential cross sections as well as the heavy-flavour decay muon yield as a function of the charged-particle multiplicity in pp collisions at center-of-mass energy of 5.02 TeV were presented. These results were compared to available published experimental results at forward and midrapidity both in pp and p-Pb collisions. Furthermore, this study is a first for the inclusive measurements of heavy-flavour decay muons as a function of charged-particle multiplicity at this energy at forward rapidity as well as in Run 2. A comparison with theoretical calculations like EPOS and PYTHIA is vital in order to further improve the understanding of the production mechanism of heavy-flavor quarks in pp collisions, in particular at forward rapidity, and their correlation to the charged-particle multiplicity.

5.2 Outlook

It is anticipated to employ the most recent available data in pp collisions at $\sqrt{s} = 5.02$ TeV for background studies in order to reduce the systematic uncertainties, in particular, concerning the contribution of the pion/kaon dominating the low p_{T} region of the differential cross section. Moreover, it is worth investigating, utilizing the latest available MC, the contribution of the resolution and alignment of the muon spectrometer component which could account for the uncertainties impacting the high p_{T} region of the distribution. A comparison between the measured heavy-flavour decay muon yield vs charged-particle multiplicity and theoretical model calculations is also anticipated. It is also important to mention that results from this study will be compared with results from ongoing similar analyses at $\sqrt{s} = 8$ and 13 TeV in pp collisions as well as with ongoing multiplicity studies in p-Pb collisions at forward rapidity. This will allow for a more comprehensive study of the energy dependence of the differential heavy-quark decay muon as a function of charged-particle multiplicity in small-system collisions.

During Run 1 and 2, the muon spectrometer setup did not allow for a separation of

the measurement of open charm and beauty components due to limitations in the mass resolution as well as the lack of detectors close to the interaction vertex. To overcome these challenges, as part of the ALICE Upgrade programme, the muon spectrometer underwent an upgrade during the long shutdown (LS2) to introduce the Muon Forward Tracker (MFT), a silicon pixel detector. The MFT was added to the muon spectrometer with the idea to match the extrapolated muon tracks from the tracking chambers after the front absorber with clusters measured by the MFT planes in front of the absorber.

The matching of the muon tracks and the MFT clusters will result in the muon tracks gaining enough pointing accuracy; this will provide a reliable measurement of the offset of the muon tracks with respect to the interaction vertex. This enhancement on the measurement of muon tracks will allow for the possibility to disentangle open charm and beauty production in the analysis of single muons.

Run 3 offers new physics also in terms of the measurement of heavy-flavour decays exclusively at forward rapidity. These measurements will refine current inclusive measurements at forward rapidity and allow for direct comparisons with midrapidity measurements.

Bibliography

[1] Tasnuva Chowdhury. Study of Υ production as a function of charged-particle multiplicity in proton-proton collisions at $\sqrt{s} = 13$ TeV with ALICE at the LHC. http://cds.cern.ch/record/2691433, 2019. Presented 05 Jul 2019.

[2] Pseudorapidity. https://en.wikipedia.org/wiki/Pseudorapidity. Accessed: 2021-06-17.

[3] Center of mass energy. https://www.encyclopedia.com/science/encyclopedias-almanacs-transcripts-and-maps/energy-center-mass. Accessed: 2021-06-17.

[4] Definition of the ALICE Coordinate System and basic rules for sub-detector components numbering. http://personalpages.to.infn.it/~tosello/EngMeet/NamingConventions/ALICE-INT-2003-038.pdf. Accessed: 2021-08-10.

[5] Costanza Cavicchioli. Development and Commissioning of the Pixel Trigger System for the ALICE experiment at the CERN Large Hadron Collider. https://www.researchgate.net/figure/ALICE-coordinate-system_fig11_241772043, 01 2010.

[6] Tom Kibble. The Standard Model of Particle Physics. *European Review*, 23, 12 2014.

[7] Brian R Martin. *Nuclear and Particle Physics*. Wiley, 2006.

[8] Standard Model of Elementary Particles. https://commons.wikimedia.org/wiki/File:Standard_Model_of_Elementary_Particles_Anti.svg. Accessed: 2022-06-15.

[9] Douglas Giancoli. *Elementary particles*, chapter 32, pages 915–945.

[10] Kenneth S. Schmitz. Chapter 1 - Philosophy of Science. In Kenneth S. Schmitz, editor, *Physical Chemistry*, pages 183–367. Elsevier, Boston, 2018.

[11] Günther Dissertori. *The Determination of the Strong Coupling Constant*, chapter Chapter 6, pages 113–128.

[12] Siegfried Bethke and Peter Zerwas. Schwache starke wechselwirkung – die asymptotische freiheit der quarks. *Physik Journal*, 3(12):31–35, 2004.

[13] Phys Org. The 2004 Nobel Prize in Physics. https://phys.org/news/2004-10-nobel-prize-physics.html. Accessed: 2022-04-09.

[14] nLab. Renormlization group flow. https://ncatlab.org/nlab/show/renormalization%20group%20flow. Accessed: 2022-04-09.

[15] Alexandre Deur, Stanley J. Brodsky, and Guy F. de Téramond. The QCD running coupling. *Progress in Particle and Nuclear Physics*, 90:1–74, Sep 2016.

[16] Damien M Pierce. The strong coupling constant in grand unified theories. https://www.slac.stanford.edu/pubs/slacpubs/7250/slac-pub-7403.pdf, August 1996.

[17] DESY: Coupling constant for strong interactions. https://cds.cern.ch/record/1730521, Apr 1980.

[18] T. Wengler. Determination of the strong coupling constant at LEP. http://dx.doi.org/10.1142/9789812706706_0104, Jan 2007.

[19] Aida X. El-Khadra, George Hockney, Andreas S. Kronfeld, and Paul B. Mackenzie. A Determination of the strong coupling constant from the charmonium spectrum. *Phys. Rev. Lett.*, 69:729–732, 1992.

[20] Peskin and Schroeder. *An Introduction to Quantum Field Theory*. CRC Press, 2018.

[21] Manuel Mussini. Measurement of low p_T D^0 meson production cross section at CDF II. 10.2172/1016881, 02 2022.

[22] Edward Shuryak. Lectures on nonperturbative QCD (Nonperturbative Topological Phenomena in QCD and Related Theories). https://arxiv.org/abs/1812.01509, 2018.

[23] Stanley J. Brodsky and Leonardo Di Giustino. Setting the Renormalization Scale in QCD: The Principle of Maximum Conformality. 10.1103/PhysRevD.86.085026, 2012.

[24] Karl Jakobs. Physics at the LHC - From Standard Model measurements to Searches for New Physics 2011 European School of High-Energy Physics. pages 309–358. 53 p, Jul 2012. Comments: 53 pages, 42 figures, to be published in the proceedings of ESHEP 2011. arXiv:1206.7024v1 [hep-ex] 29 Jun 2012.

[25] E L Berger. Heavy quark production in hadron collisions. https://cds.cern.ch/record/179163, Jun 1987.

[26] M.J. Tannenbaum. From Bjorken Scaling to pQCD–Experimental techniques from pp collisions of the 1970's with application to au+au collisions at RHIC. *Nuclear Physics A*, 749:219–228, mar 2005.

[27] Jonathan Pumplin, Daniel Robert Stump, Joey Huston, Hung-Liang Lai, Pavel Nadolsky, and Wu-Ki Tung. New generation of parton distributions with uncertainties from global QCD analysis. *Journal of High Energy Physics*, 2002(07):012–012, Jul 2002.

[28] Jonathan Pumplin, Daniel Robert Stump, Joey Huston, Hung-Liang Lai, Pavel Nadolsky, and Wu-Ki Tung. New Generation of Parton Distributions with Uncertainties from Global QCD Analysis. *Journal of High Energy Physics*, 2002(07):012–012, Jul 2002.

[29] Rabah Abdul Khalek, Jacob J. Ethier, and Juan Rojo. Nuclear Parton Distributions from Neural Networks. *Acta Phys. Polon. Supp.*, 12(4):927, 2019.

[30] A M Cooper-Sarkar. HERAPDF fits including f_2(charm) data. 10.48550/ARXIV.1006.4471, 2010.

[31] A. D. Martin, W. J. Stirling, R. S. Thorne, and G. Watt. Parton distributions for the LHC. *The European Physical Journal C*, Jul 2009.

[32] P.L. McGaughey, E. Quack, P.V. Ruuskanen, R. Vogt, and X.-N. Wang. Heavy quark production in pp collisions. http://dx.doi.org/10.1142/S0217751X95001431, Aug 1995. International Journal of Modern Physics A.

[33] M Tanabashi, PD Grp, K Hagiwara, K Hikasa, Katsumasa Nakamura, Y Sumino, F Takahashi, J Tanaka, K Agashe, Giulio Aielli, Claude Amsler, Mario Antonelli, DM Asner, Howard Baer, S Banerjee, RM Barnett, T Basaglia, Christian Bauer, J. Beatty, and P Schaffner. Review of Particle Physics: Particle Data Group. *Physical Review D*, 98, 08 2018.

[34] Marina Artuso, Brian Meadows, and Alexey A. Petrov. Charm Meson Decays. *Annual Review of Nuclear and Particle Science*, 58(1):249–291, Nov 2008.

[35] Elena Bruna. Heavy-flavour production and multiplicity dependence in pp and p-Pb collisions with ALICE. https://indico.cern.ch/event/279518/contributions/634859/attachments/511877/706477/ebruna_LHCP14.pdf. Accessed: 2022-06-17.

[36] Timothy Gershon and Matthew Needham. Heavy flavour physics at the lhc. https://www.sciencedirect.com/science/article/pii/S1631070515000717, 2015. Highlights of the LHC run 1 / Rẽsultats marquants de la premiẽre pẽriode d'exploitation du GCH.

[37] Matteo Cacciari, Stefano Frixione, Nicolas Houdeau, Michelangelo L. Mangano, Paolo Nason, and Giovanni Ridolfi. Theoretical predictions for charm and bottom production at the LHC. *Journal of High Energy Physics*, oct 2012.

[38] V. Del Duca and G. Heinrich. NLO and NNLO Calculations. https://arxiv.org/abs/hep-ph/0604120, 5 2000. 1st Les Houches Workshop on Physics at TeV Colliders. arXiv:hep-ph/0604120.

[39] Matteo Cacciari and Mario Greco. Large-p⊥ hadroproduction of heavy quarks. https://doi.org/10.1016%2F0550-3213%2894%2990515-0, jun 1994. doi: 10.1016/0550-3213(94)90515-0.

[40] FONLL Heavy Quark Production. http://www.lpthe.jussieu.fr/~cacciari/fonll/fonllform.html. Accessed: 2021-12-22.

[41] ALICE Collaboration. Charm-quark fragmentation fractions and production cross section at 4 midrapidity in pp collisions at the LHC. https://journals.aps.org/prd/abstract/10.1103/PhysRevD.105.L011103, May 2021". Phys. Rev. D 105 (2022) L011103,.

[42] ALICE Collaboration. Measurement of beauty and charm production in pp collisions at $\sqrt{s} = 5.02$ TeV via non-prompt and prompt D mesons. *Journal of High Energy Physics*, 2021(5), May 2021.

[43] CDF Collaboration. Measurement of the b-hadron production cross section using decays to $\mu^- D^0 x$ final states in $p\bar{p}$ collisions at $\sqrt{s} = 1.96$ TeV. *Phys. Rev. D*, 79:092003, May 2009.

[44] PHENIX Collaboration. Heavy-quark production in $p + p$ and energy loss and flow of heavy quarks in au + au collisions at $\sqrt{s_{NN}} = 200$ gev. *Phys. Rev. C*, 84:044905, Oct 2011.

[45] STAR Collaboration. Measurements of D^0 and D^* production in p+p collisions at $\sqrt{s} = 200$ GeV. *Phys. Rev. D*, 86:072013, Oct 2012.

[46] X Zhang. Study of heavy flavours from muons measured with the ALICE detector in proton-proton and heavy-ion collisions at the CERN-LHC. PhD Thesis, Clermont-Ferrand U., 2012.

[47] Nicola Carrer and Andrea Dainese. Charm and beauty production at LHC. https://arxiv.org/abs/hep-ph/0311225, 2003.

[48] ALICE Collaboration. Measurement of electrons from semileptonic heavy-flavor hadron decays in pp collisions at $\sqrt{s}$=7 TeV. *Phys. Rev. D*, 86:112007, Dec 2012.

[49] The ALICE collaboration., S. Acharya, D. Adamová, and et al. Production of muons from heavy-flavour hadron decays in pp collisions at $\sqrt{s} = 5.02$ TeV. https://doi.org/10.1007/JHEP09(2019)008. J. High Energy Physics 2019, 8 (2019).

[50] ALICE Collaboration. Reference cross section measurements with ALICE in pp and Pb-Pb collisions at LHC. http://cds.cern.ch/record/1552160, May 2013. Comments: An updated version of proceedings contribution for workshop "LHC Lumi Days 2012", 29 Feb. (2012) at CERN. 11 pages, 8 figures.

[51] Baoyi Chen, Tiecheng Guo, Yunpeng Liu, and Pengfei Zhuang. Cold and hot nuclear matter effects on charmonium production in p+Pb collisions at LHC energy. *Physics Letters B*, 765:323–327, 2017.

[52] STAR Collaboration. Measurement of cold nuclear matter effects for inclusive J/ψ in p+Au collisions at $\sqrt{s_{NN}} = 200$ GeV. *Physics Letters B*, 825:136865, 2022.

[53] Boris Hippolyte. Relativistic Heavy Ions collisions at CERN. http://www.nupecc.org/presentations/hippo_mar17.pdf, March 2017.

[54] Collisions of charged particles. https://ocw.mit.edu/courses/nuclear-engineering/22-105-electromagnetic-interactions-fall-2005/readings/chap6.pdf. Accessed: 2022-03-01.

[55] ALICE Collaboration. The ALICE definition of primary particles. https://cds.cern.ch/record/2270008/files/cds.pdf, 2017. ALICE-PUBLIC-2017-005.

[56] Shreyasi Acharya et al. Pseudorapidity distributions of charged particles as a function of mid- and forward rapidity multiplicities in pp collisions at $\sqrt{s} = 5.02$, 7 and 13 TeV. *Eur. Phys. J. C*, 81(7):630, 2021.

[57] Cristiano Brenner Mariotto, M.Beatriz Gay Ducati, and G. Ingelman. Soft and Hard QCD in Charmonium Production. arXiv:hep-ph/0206254v1, 25 Jun 2002.

[58] Maria Nicassio. Study of global observables in p-p and A-A collisions with ALICE at LHC. https://inspirehep.net/files/5b2477ddfe64457392fde9e13b3a1ec3. Tesi di Dottorato, CERN-THESIS-2010-258 25/03/2010.

[59] Armando Bermúdez Martínez. Studies on the definition of inelastic non-single diffractive events. https://www.desy.de/2011summerstudents/2014/reports/bermudez_armando.pdf. pages 1-14.

[60] Proceedings, 1st International Workshop on Multiple Partonic Interactions at the LHC (MPI08): Perugia, Italy, October 27-31, 2008, 2009. 10.3204/PUBDB-2017-128830.

[61] Torbjörn Sjöstrand and Maria van Zijl. A multiple interaction model for the event structure in hadron collisions. *Phys. Rev. D*, 36:2019, 1987.

[62] S. Porteboeuf and R. Granier de Cassagnac. J/ψ yield vs. multiplicity in proton-proton collisions at the LHC, 2011. arXiv:1012.0719v1 [hep-ex], 3 Dec 2010.

[63] Torbjörn Sjöstrand, Stefan Ask, Jesper R. Christiansen, Richard Corke, Nishita Desai, Philip Ilten, Stephen Mrenna, Stefan Prestel, Christine O. Rasmussen, and Peter Z. Skands. An introduction to PYTHIA 8.2. *Computer Physics Communications*, 191:159–177, Jun 2015.

[64] J. M. Butterworth, J. R. Forshaw, and M. H. Seymour. Multiparton interactions in photoproduction at HERA. *Zeitschrift für Physik C: Particles and Fields*, 72(4):637–646, dec 1996.

[65] T Gleisberg, S Hoeche, F Krauss, A Schaelicke, S Schumann, and J Winter. SHERPA 1. , a proof-of-concept version. *Journal of High Energy Physics*, 2004(02):056–056, feb 2004.

[66] International Masterclasses Hands on Particle Physics. https://atlas.physicsmasterclasses.org/en/zpath_protoncollisions.htm. Accessed: 2022-06-12.

[67] T. Pierog and K. Werner. EPOS Model and Ultra High Energy Cosmic Rays. https://doi.org/10.48550/arXiv.0905.1198, Dec 2009. Nuclear Physics B - Proceedings Supplements,arXiv:0905.1198 [hep-ph].

[68] F. Ambroglini, P. Bartalini, L. Fano, and D. Treleani. Minimum Bias, Underlying Events and Multiple Interactions. http://moby.mib.infn.it/~nason/mcws/Proceedings/MBeUE.pdf. Accessed: 2022-04-10.

[69] H.J. Drescher, M. Hladik, S. Ostapchenko, T. Pierog, and K. Werner. Parton-based Gribov−Regge theory. https://doi.org/10.1016%2Fs0370-1573%2800%2900122-8, sep 2001. doi 10.1016/s0370-1573(00)00122-8.

[70] Shreyasi Acharya. Study of heavy-flavour hadron decay electrons as a function of charged-particle multiplicity in pp collisions at $\sqrt{s}$ = 13 TeV with ALICE. *PoS*, LHCP2018:044, 2018.

[71] ALICE Collaboration". Measurement of charm and beauty production at central rapidity versus charged-particle multiplicity in proton-proton collisions at $\sqrt{s}$=7 TeV. http://dx.doi.org/10.1007/JHEP09(2015)148, Sep 2015.

[72] ALICE Collaboration. J/ψ production as a function of charged particle multiplicity in pp collisions at s =7 TeV. *Physics Letters B*, 712(3):165 – 175, 2012.

[73] LHCb Collaboration. Observation of double charm production involving open charm in pp collisions at $\sqrt{s}$ = 7 TeV. *Journal of High Energy Physics*, 2012(6), jun 2012.

[74] S. Chatrchyan, V. et al. Khachatryan, and CMS Collaboration. Jet and underlying event properties as a function of charged-particle multiplicity in proton–proton collisions at $\sqrt{s}$ = 7 TeV. *Eur. Phys. J. C 73, 2674*, 2013.

[75] ALICE Collaboration. Forward rapidity J/ψ production as a function of charged-particle multiplicity in pp collisions at $\sqrt{s}$ = 5.02 and 13 TeV. https://arxiv.org/abs/2112.09433, 2021. arXiv, doi: 10.48550/ARXIV.2112.09433.

[76] ALICE Collaboration. Measurement of charm and beauty production at central rapidity versus charged-particle multiplicity in proton-proton collisions at $\sqrt{s}$ = 7 TeV. *Journal of High Energy Physics*, 148(09), Sep 2015.

[77] ALICE Collaboration. Enhanced production of multi-strange hadrons in high-multiplicity proton–proton collisions. *Nature Physics*, 13(6):535–539, Apr 2017.

[78] ALICE Collaboration. Measurement of D-meson production versus multiplicity in p-Pb collisions at $\sqrt{s_{NN}}$ = 5.02 TeV. *Journal of High Energy Physics, 10.1007/JHEP08(2016)078*, 2016(8), Aug 2016.

[79] ALICE Collaboration. J/ψ production as a function of charged-particle pseudo-rapidity density in p–Pb collisions at $\sqrt{s_{NN}}$ = 5.02 TeV. *Physics Letters B*, 776, 2018.

[80] Rainer Schicker. Overview of ALICE results in pp, pA and AA collisions. *EPJ Web of Conferences*, 138:01021, 2017.

[81] Betty Abelev et al. Heavy flavour decay muon production at forward rapidity in proton-proton collisions at $\sqrt{s} = 7$ TeV. *Phys. Lett. B*, 708:265–275, 2012.

[82] P.A. Zyla et al. Review of Particle Physics. *PTEP*, 2020(8):083C01, 2020. and 2021 update.

[83] P Janus (2018). Measurement of W and Z Boson Production in 5 TeV pp, p+Pb and Pb+Pb Collisions with the ATLAS Detector. https://doi.org/10.18502/ken.v3i1.1765. KnE Energy, 3(1), 345-351.

[84] LHC at International Masterclasses. https://atlas.physicsmasterclasses.org/en/index.htm. Accessed: 2022-03-05.

[85] Zaida Conesa Del Valle. Performance of the ALICE muon spectrometer. Weak boson production and measurement in heavy-ion collisions at LHC. https://inis.iaea.org/collection/NCLCollectionStore/_Public/39/107/39107530.pdf. Accessed: 2022-03-06.

[86] Werner Herr and B Muratori. Concept of luminosity. https://cds.cern.ch/record/941318, 2006. 10.5170/CERN-2006-002.361.

[87] G. Apollinari, O. Brüning, T. Nakamoto, and Lucio Rossi. Chapter 1: High Luminosity Large Hadron Collider HL-LHC. High Luminosity Large Hadron Collider HL-LHC. *CERN Yellow Report*, pages 1–19. 21 p, May 2017. 21 pages, chapter in High-Luminosity Large Hadron Collider (HL-LHC) : Preliminary Design Report.

[88] The Large Hadron Collider. https://home.cern/science/accelerators/large-hadron-collider. Accessed: 2022-01-31.

[89] CERN. Facts and figures about the LHC. https://home.cern/resources/faqs/facts-and-figures-about-lhc, 2020.

[90] Lyndon Evans. The Large Hadron Collider. *Philosophical Transactions of the Royal Society A: Mathematical, Physical and Engineering Sciences*, 370(1961):831–858, 2012.

[91] CERN's accelerator complex. https://home.cern/science/accelerators/accelerator-complex. Accessed: 2021-06-18.

[92] G. Iadarola et al. Detailed Studies of Beam Induced Scrubbing in the CERN-SPS. In *Proc. 6th International Particle Accelerator Conference (IPAC'15), Richmond, VA, USA, May 3-8, 2015*, number 6 in International Particle Accelerator Conference, pages 3908–3910, Geneva, Switzerland, June 2015. JACoW. https://doi.org/10.18429/JACoW-IPAC2015-THPF091.

[93] RF cavities. https://www.lhc-closer.es/taking_a_closer_look_at_lhc/0.rf_cavities. Accessed: 2022-02-25.

[94] ATLAS. https://home.cern/science/experiments/atlas. Accessed: 2022-01-31.

[95] ALICE. https://home.cern/science/experiments/alice. Accessed: 2022-01-31.

[96] CMS. https://home.cern/science/experiments/cms. Accessed: 2022-01-31.

[97] The Large Hadron Collider beauty. https://home.cern/science/experiments/lhcb. Accessed: 2022-01-31.

[98] Facts and figures about the LHC. https://home.cern/resources/faqs/facts-and-figures-about-lhc. Accessed: 2022-02-11.

[99] The ALICE Collaboration, K Aamodt, A Abrahantes Quintana, R Achenbach, S Acounis, and D Adamová. The ALICE experiment at the CERN LHC. https://doi.org/10.1088/1748-0221/3/08/s08002, Aug 2008.

[100] Magnets and Detectors II. https://www.lhc-closer.es/taking_a_closer_look_at_lhc/0.magnets___detectors_ii. Accessed: 2022-02-07.

[101] C. Fabjan and J. Schukraft. The story of ALICE: Building the dedicated heavy ion detector at LHC, 2011. arXiv, 1101.1257.

[102] 3D ALICE Schematic RUN2 - with description. https://alice-figure.web.cern.ch/node/11218. Accessed: 2022-02-01.

[103] S Acharya et al. Production of light-flavor hadrons in pp collisions at $\sqrt{s}$=7 and $\sqrt{s} = 13$ TeV. *The European Physical Journal C*, 81(3), Mar 2021.

[104] Costanza Cavicchioli. Detector performance of the ALICE silicon pixel detector. *Nucl. Instrum. Meth. A*, 628:77–80, 2011.

[105] Ganda Panjaitan, Kemas Lhaksmana, Esa Prakasa, and L Musa. Detecting the position of the sealring and the edge on the sensor chip. *Journal of Physics: Conference Series*, 1192:012063, 03 2019.

[106] The ALICE collaboration. Performance of the ALICE VZERO system. *Journal of Instrumentation*, 8(10):P10016–P10016, oct 2013.

[107] Buckets and Bunches. https://www.lhc-closer.es/taking_a_closer_look_at_lhc/0.buckets_and_bunches. Accessed: 2022-02-02.

[108] ALICE Collaboration. *ALICE forward detectors: FMD, TO and VO: Technical Design Report*. Technical design report. ALICE. CERN, Geneva, 2004. Submitted on 10 Sep 2004.

[109] A Morsch and ALICE Collaboration. The ALICE forward muon spectrometer at the LHC. 10.1016/S0375-9474(98)00404-7, Aug 1998.

[110] ALICE Collaboration. The ALICE experiment at the CERN LHC. https://iopscience.iop.org/article/10.1088/1748-0221/3/08/S08002., 2008. JINST 3 S08002.

[111] Azhgirey I, Baishev I, and Talanov V. Machine induced background in the low luminosity insertions of the LHC. https://accelconf.web.cern.ch/e02/PAPERS/MOPLE044.pdf, 2002. Accessed: 2022-02-23.

[112] Aurelien Muller. Installation of the station 2 of the ALICE muon tracking chambers. http://cds.cern.ch/record/1070588, Jul 2007.

[113] J Castillo. Alignment of the ALICE MUON spectrometer. https://cds.cern.ch/record/1047110, 2007.

[114] Sanjoy Pal. Characterizations of cathode pad chamber as tracking detector for Muon Spectrometer of ALICE. https://cds.cern.ch/record/1453791/files/CERN-THESIS-2008-170.pdf. PhD Thesis, November 2008.

[115] Dimuon Forward Spectrometer: Tracking chambers. https://twiki.cern.ch/twiki/pub/ALICE/MuonTracking/spectro.png. Accessed: 2021-12-18.

[116] Conesa Del Valle Zaida. Performance of the ALICE muon spectrometer. Weak boson production and measurement in heavy-ion collisions at LHC. https://tel.archives-ouvertes.fr/tel-00198703/file/thesis.pdf, July 2007. Université de Nantes ; Universitat Autónoma de Barcelona.

[117] V. Blobel. Software alignment for tracking detectors. *Nuclear Inst. and Methods in Physics Research, A*, 566(1):5–13, 2006.

[118] C Kleinwort. H1 alignement experience. https://cds.cern.ch/record/1047100, 2007.

[119] J Y Grossiord, Kakoyan V, and Tieulent R. The geometry monitoring system of the ALICE Dimuon Spectrometer: Simulation results. Technical report, CERN, Geneva, 2005. ALICE-INT-2005-020, CERN-ALICE-INT-2005-020.

[120] L. Terlizzi. The ALICE Muon IDentifier (MID). https://doi.org/10.1088/1748-0221/15/10/C10031, Oct 2020, arXiv:2005.00285 [physics.ins-det]. Journal of Instrumentation, 2020 JINST 15 C10031.

[121] Francesco Bossù, Martino Gagliardi, Massimiliano Marchisone, and ALICE Collaboration. Performance of the RPC-based ALICE muon trigger system at the LHC. 11th Workshop on Resistive Plate Chambers and Related Detectors, Frascati (Rome), Italy, 5 - 10 Feb 2012, PoS RPC2012 (2012) pp.059, JINST 7 (2012) pp.T12002, 10.1088/1748-0221/7/12/T12002.

[122] Stefan Rossegger. Upgrade of the alice inner tracking system. *Nuclear Instruments and Methods in Physics Research Section A: Accelerators, Spectrometers, Detectors and Associated Equipment*, 731:40–46, Dec 2013.

[123] The Time Projection Chamber. https://alice-tpc.web.cern.ch/index.php/content/alice-detector-control-system. Accessed: 2021-12-18.

[124] Christian Wolfgang Fabjan, L Jirdén, V Lindestruth, Lodovico Riccati, D Rorich, Pierre Van de Vyvre, O Villalobos Baillie, and Hans de Groot. ALICE trigger data-acquisition high-level trigger and control system: Technical Design Report. https://cds.cern.ch/record/684651, 2004.

[125] O Villalobos Baillie, D Evans, S Fedor, G T Jones, P Jovanovic, A Jusko, I Králik, R Lietava, L Sándor, and J Urbán. The ALICE Central Trigger Processor. https://cds.cern.ch/record/921038, 2005.

[126] Performance of the ALICE experiment at the CERN LHC. *International Journal of Modern Physics A*, 29(24):1430044, Sep 2014.

[127] F. Carena, W. Carena, S. Chapeland, V. Chibante Barroso, F. Costa, E. Dénes, R. Divià, U. Fuchs, A. Grigore, T. Kiss, G. Simonetti, C. Soós, A. Telesca, P. Vande Vyvre, and B. von Haller. The alice data acquisition system. *Nuclear Instruments and Methods in Physics Research Section A: Accelerators, Spectrometers, Detectors and Associated Equipment*, 741:130–162, 2014.

[128] Heiko Engel, Torsten Alt, and Udo Kebschull and. FPGA based data processing in the ALICE high level trigger in LHC run 2. *Journal of Physics: Conference Series*, 898:032018, oct 2017.

[129] ALICE DCS Monitoring. https://alicedcs.web.cern.ch/monitoring/main.aspx. Accessed: 2021-12-18.

[130] R. Alemany, M. Lamont, and et al. S. Page. Functional specication: LHC mode. https://lhc-commissioning.web.cern.ch/lhc-commissioning/

systems/data-exchange/doc/LHC-OP-ES-0005-10-00.pdf, 2017. LHC-OP-ES-005 rev 1.0.

[131] Sibaliso Mhlanga. Heavy-flavour production at forward rapidity as a function of charged-particle multiplicity with ALICE at the LHC. https://open.uct.ac.za/handle/11427/32293. PhD Thesis, December 2020.

[132] Accelerating: Radiofrequency cavities. https://home.cern/science/engineering/accelerating-radiofrequency-cavities. Accessed: 2022-02-25.

[133] Pulling together: Superconducting electromagnets. https://home.web.cern.ch/science/engineering/pulling-together-superconducting-electromagnets. Accessed: 2022-03-27.

[134] ALICE Collaboration. ALICE dimuon forward spectrometer: Technical Design Report. https://edms.cern.ch/document/470838/1. Technical Design Report ALICE, ALICE-DOC-2004-004 v.1, CERN, 1999.

[135] Pieter Johannes Wynand Du Toit. Analysis of $W^{\pm}$ bosons with ALICE: Effect of alignment on $W^{\pm}$ bosons analysis. http://hdl.handle.net/2263/33312, 2013. MSC Dissertation.

[136] V. Chambert. The electronics of ALICE dimuon tracking chambers. In *Topical Workshop on Electronics for Particle physics*, pages 242–246, 2008.

[137] LHC Page 1. https://op-webtools.web.cern.ch/vistar/vistars.php. Accessed: 2022-02-23.

[138] R Bailey and Paul Collier. Standard Filling Schemes for Various LHC Operation Modes. Technical report, CERN, Geneva, Sep 2003.

[139] F Antinori. Naming scheme for ALICE trigger classes, v.0.1 (draft). https://alice-offline.web.cern.ch/sites/alice-offline.web.cern.ch/files/uploads/trigger/class-naming-01.pdf, 2008. Accessed: 2022-02-23.

[140] Index of /aliqaevs/data. https://aliqaevs.web.cern.ch/aliqaevs/data/lumi_Run2_pp5TeV.pdf. Accessed: 2022-02-10.

[141] François Piuz, W Klempt, L Leistam, J De Groot, and Jürgen Schükraft. *ALICE high-momentum particle identification: Technical Design Report*. Technical design report. ALICE. CERN, Geneva, 1998.

[142] ROOT. https://root.cern/about/. Accessed: 2021-06-30.

[143] S Giani, S Ravndal, and M Maire. GEANT steps into the future. https://cds.cern.ch/record/277970, 1995.

[144] The ALICE offline bible. https://alice-offline.web.cern.ch/sites/alice-offline.web.cern.ch/files/uploads/OfflineBible.pdf. Accessed: 2021-12-27.

[145] S. Agostinelli et al. Geant4—a simulation toolkit. *Nuclear Instruments and Methods in Physics Research Section A: Accelerators, Spectrometers, Detectors and Associated Equipment*, 506(3):250–303, 2003.

[146] Giuseppe Battistoni, Till Boehlen, Francesco Cerutti, Pik Wai Chin, Luigi Salvatore Esposito, Alberto Fassò, Alfredo Ferrari, Anton Lechner, Anton Empl, Andrea Mairani, Alessio Mereghetti, Pablo Garcia Ortega, Johannes Ranft, Stefan Roesler, Paola R. Sala, Vasilis Vlachoudis, and George Smirnov. Overview of the fluka code. *Annals of Nuclear Energy*, 82:10–18, 2015. Joint International Conference on Supercomputing in Nuclear Applications and Monte Carlo 2013, SNA + MC 2013. Pluri- and Trans-disciplinarity, Towards New Modeling and Numerical Simulation Paradigms.

[147] Sjöstrand Torbjörn. The pythia event generator: Past, present and future. *Computer Physics Communications*, 246:106910, Jan 2020.

[148] Xin-Nian Wang and Miklos Gyulassy. hijing: A monte carlo model for multiple jet production in pp, pA, and AA collisions. *Phys. Rev. D*, 44:3501–3516, Dec 1991.

[149] Diego Stocco. *Development of the ALICE Muon Spectrometer: Preparation for data taking and heavy flavor measurement.* PhD thesis, Turin University, 2008.

[150] ALICE data flow. https://indico.cern.ch/event/752367/contributions/3116617/attachments/1704565/2858687/DPG_AnalysisTutorial_20181129.pdf. Accessed: 2021-12-27.

[151] E Bruna, A Dainese, M Masera, and F Prino. Vertex reconstruction for proton-proton collisions in ALICE. https://cds.cern.ch/record/1225497, Nov 2009.

[152] Jana Crkovska. Study of the J/ψ production in pp collisions at $\sqrt{s}$ = 5.02 TeV and of the J/ψ production multiplicity dependence in p-pb collisions at $\sqrt{s_{NN}}$ = 8.16 TeV with ALICE at the LHC. http://cds.cern.ch/record/2651031?ln=en, 2018.

[153] D. Adamová et al. J/ψ production as a function of charged-particle pseudorapidity density in p-Pb collisions at $\sqrt{s_{NN}} = 5.02$ TeV. *Phys. Lett. B*, 776:91–104, 2018.

[154] MonALISA Repository for ALICE. https://alimonitor.cern.ch/job_details.jsp. Accessed: 2022-04-13.

[155] ALICE Collaboration. Observation of a multiplicity dependence in the p_{t}-differential charm baryon-to-meson ratios in proton–proton collisions at $\sqrt{s}$=13 TeV. *Physics Letters B*, 829:137065, 2022.

[156] ALICE Collaboration. Production of muons from heavy-flavour hadron decays in p-Pb collisions at $\sqrt{s_{NN}} = 5.02$ TeV. *Physics Letters B*, 770:459–472, Jul 2017.

[157] Zuman Zhang. Open heavy-flavour measurements via muons in proton-proton and nucleus-nucleus collisions with the ALICE detector at the CERN-LHC. https://inspirehep.net/literature/1764880, 2018. PhD Thesis. Clermont-Ferrand U.

[158] ALICE Collaboration. Production of muons from heavy-flavour hadron decays at high transverse momentum in Pb–Pb collisions at $\sqrt{s} = 5.02$ and 2.76 TeV. *Physics Letters B*, 820:136558, 2021.

[159] Index of /aliqaevs/data. https://aliqaevs.web.cern.ch/aliqaevs/data/. Accessed: 2021-10-16.

[160] S. Acharya, D. Adamová, M. M. Aggarwal, G. Aglieri Rinella, M. Agnello, N. Agrawal, Z. Ahammed, N. Ahmad, S. U. Ahn, and et al. Energy dependence of forward-rapidity j/ψ and $\psi(2s)$ production in pp collisions at the LHC. *The European Physical Journal C*, 77(6), Jun 2017.

[161] ALICE Collaboration. ALICE 2017 luminosity determination for pp collisions at $\sqrt{s} = 5$ TeV. http://cds.cern.ch/record/2648933, Nov 2018.

[162] ALICE Collaboration. ALICE luminosity determination for pp collisions at $\sqrt{s} = 5$ TeV. https://cds.cern.ch/record/2202638, Jul 2016.

[163] Constantin Loizides, Jason Kamin, and David d'Enterria. Improved Monte Carlo Glauber predictions at present and future nuclear colliders. *Phys. Rev. C*, 97:054910, May 2018.

[164] ALICE Collaboration. Production of muons from heavy-flavour hadron decays at high transverse momentum in Pb–Pb collisions at $\sqrt{s_{NN}} = 5.02$ and 2.76 TeV. *Physics Letters B*, 820(136558), 2021.

[165] S. Acharya and et.al. Multiplicity dependence of light−flavor hadron production in pp collisions at $\sqrt{s} = 7$ TeV. *Phys. Rev. C*, 99:024906, Feb 2019.

[166] S. Acharya and et.al. Pseudorapidity distributions of charged particles as a function of mid- and forward rapidity multiplicities in pp collisions at $\sqrt{s}$ = 5.02, 7 and 13 TeV. *The European Physical Journal C*, 81:1434–6052, July 2021.

[167] Simone Alioli, Paolo Nason, Carlo Oleari, and Emanuele Re. NLO vector-boson production matched with shower in POWHEG. *JHEP*, 07:060, 2008.

[168] Stefano Frixione, Paolo Nason, and Carlo Oleari. Matching NLO QCD computations with parton shower simulations: the POWHEG method. *Journal of High Energy Physics*, 2007(11):070–070, Nov 2007.

[169] Hung-Liang Lai, Marco Guzzi, Joey Huston, Zhao Li, Pavel M. Nadolsky, Jon Pumplin, and C. P. Yuan. New parton distributions for collider physics. *Phys. Rev. D*, 82:074024, 2010.

[170] ALICECollaboration. $W^{\pm}$-boson production in p−Pb collisions at $\sqrt{s_{NN}}$ = 8.16 TeV and Pb-Pb collisions at $\sqrt{s_{NN}}$ = 5.02 TeV. Apr 2022.

[171] Shreyasi Acharya et al. Inclusive quarkonium production in pp collisions at $\sqrt{s}$ = 5.02 TeV, 9 2021. arXiv 2109.15240 (CERN-EP-2021-197).

[172] Anisa Khatun. J/ψ production as a function of charged-particle multiplicity in pp collisions at $\sqrt{s}$ = 5.02 TeV with ALICE. https://arxiv.org/abs/1906.09877, 2019. 10.48550/ARXIV.1906.09877.

[173] Sjöstrand Torbjörn, Stephen Mrenna, and Peter Skands. PYTHIA 6.4 physics and manual. *Journal of High Energy Physics*, 2006(05):026–026, may 2006.

[174] Fritz W. Bopp, R. Engel, and J. Ranft. Rapidity gaps and the PHOJET Monte Carlo. In *LAFEX International School on High-Energy Physics (LISHEP 98) Session A: Particle Physics for High School Teachers - Session B: Advanced School in HEP - Session C: Workshop on Diffractive Physics*, pages 729–741, 3 1998.

[175] Matteo Cacciari, Mario Greco, and Paolo Nason. The pt spectrum in heavy-flavour hadroproduction. *Journal of High Energy Physics*, 1998(05):007–007, May 1998.

[176] ALICE Collaboration. Heavy flavour decay muon production at forward rapidity in proton−proton collisions at $\sqrt{s}$ = 7 TeV. *Physics Letters B*, 708(3-5):265–275, Feb 2012.

[177] ALICE Collaboration. J/ψ production as a function of charged particle multiplicity in pp collisions at $\sqrt{s}$ = 7 TeV. *Physics Letters B*, 712(03), 2012.

[178] MonALISA Repository for ALICE. p-p, 5.02 TeV - General-purpose Monte Carlo production anchored to LHC17p and LHC17q (extension), FAST, ALIROOT-8017. https://alimonitor.cern.ch/job_events.jsp?timesel=0&owner=aliprod&filter_run=282008:282367&filter_jobtype=p-p%2C+5.02+TeV+-+General-purpose+Monte+Carlo+production+anchored+to+LHC17p+and+LHC17q+%28extension%29%2C+FAST%2C+ALIROOT-8017.

[179] Miniature X-Ray Source. https://www.amptek.com/-/media/ametekamptek/documents/products/specs/retired/mini-x-specifications.pdf?la=en&revision=44d1bf74-727c-47f4-a48f-db08b834ad1e&hash=B472DC6F13E807295EF6344EA53A9733. Accessed: 2022-05-26.

Appendices

APPENDIX A

Data Selection

A.1 Run Lists

- **LHC17p**
  282343, 282342, 282341, 282340, 282314, 282313, 282312, 282309, 282307, 282306, 282305, 282304,282302, 282247, 282230, 282229, 282227, 282224, 282206, 282147, 282146, 282127, 282126, 282123, 282122, 282120, 282119, 282118, 282099, 282098, 282078, 282051, 282050, 282031, 282025, 282021, 282016, 282008

- **LHC17q**
  282441, 282440, 282439, 282437, 282415, 282411, 282402, 282398, 282392, 282391, 282367, 282366, 282365

- **LHC15n**
  244340, 244343, 244351, 244355, 244359, 244364, 244377, 244411, 244416, 244418, 244421, 244453, 244480, 244481, 244482, 244483, 244484, 244531, 244540, 244542, 244617, 244619, 244626, 244627, 244628

A.2 Event Selection

Evolution of the events as each event cut is applied as discussed in 3.2.2 is shown in the tables below for each data sample.

Selection	MB	MSH	MSL
All events	1.1177425×10^9	1.127348×10^9	1.1083×10^9
Physics	4.528605×10^8	4.567168×10^8	4.490011×10^8
Trigger	1.08620×10^8	7 615 005	6.10355×10^7
G. Vertex	9 522 946	6 808 855	5.452467×10^7

Table A.1 Summary of LHC17p event selection

Selection	MB	MSH	MSL
All events	1.391944×10^8	1.391944×10^8	1.342669×10^8
Physics	9.66904×10^7	9.669004×10^7	9.272026×10^7
Trigger	1 806 226	1.195998×10^7	6 468 174
G. Vertex	1 607 112	1.08007×10^7	5 862 042

Table A.2 Summary of LHC17q event selection

Selection	MB	MSH	MSL
All events	1.782717×10^8	1.770734×10^8	1.769229×10^8
Physics	1.638556×10^8	1.627511×10^8	1.62617×10^8
Trigger	537 306	1 619 922	3.390503×10^7
G. Vertex	485 210	1 495 153	3.138087×10^7

Table A.3 Summary of LHC15n event selection

APPENDIX B

Multiplicity Estimation

B.0.1 Optimization of the reference value.

A study of the choice of reference value is given for which the methodology followed here was utilized in other analyses.

While a Poissonian distribution is utilized in the correction of the multiplicity, the reference value $\langle N_{trkl}(ref)\rangle$ has to be chosen in such a way that the resolution of the SPD is preserved. The Poissonian distribution introduces additional dispersion to the events that are reconstructed away from the reference value. To determine the best reference value for the multiplicity correction, a comparison of the two reference values discussed in section 3.3.1.1 is made as a function of z-vertex.

The MC productions introduced in section 3.3.1.1 are utilized to determine the best reference value. Figures B.1 and B.2 shown in this section are for the MC production (LHC20a2) anchored to the LHC17p and q data samples. The correlation between the corrected number of tracklets and the generated charged particles is determined over 8 bins according to the z-position with each bin being 2.5 cm wide covering the z-range from -10 to +10 cm. The correlation factor for each bin is determined. The correlation factor is expected to be similar for all the bins since the dispersion of the tracklets is expected to be consistent along the SPD vertex. This procedure is done for both the minimum and maximum reference values.

Figure B.1 shows the correlation between the corrected number of tracklets and the generated charged particles for the different bins using the maximum reference value for correction. The bottom right panel shows the correlation factor for all 8 bins. It is shown that the dispersion is not the same for each bin.

Figure B.2 shows the correlation between the corrected number of tracklets and the generated charged particles for the different bins using the minimum reference value for correction. The bottom right panel shows the correlation factor for all 8 bins. It is shown that the dispersion is similar for each bin.

As observed in Fig. B.1 at the bottom right panel, the dispersion for the maximum correction varies between 1 and 3%. The greatest difference is in the first bin for $-10 < v_z < -7.5$. The dispersion decreases from 3% to 1% over the zv_z range from -10 to 10 cm . This variation is determined by fitting a pol0 function to the data points and determining how each point varies relative to the fit. The same was done for the minimum correction shown in Fig. B.2 at the bottom right panel. The dispersion for the minimum correction is similar to within a $\sim 1\%$ variation. For this study, the systematic uncertainty of the data-driven method can be determined.

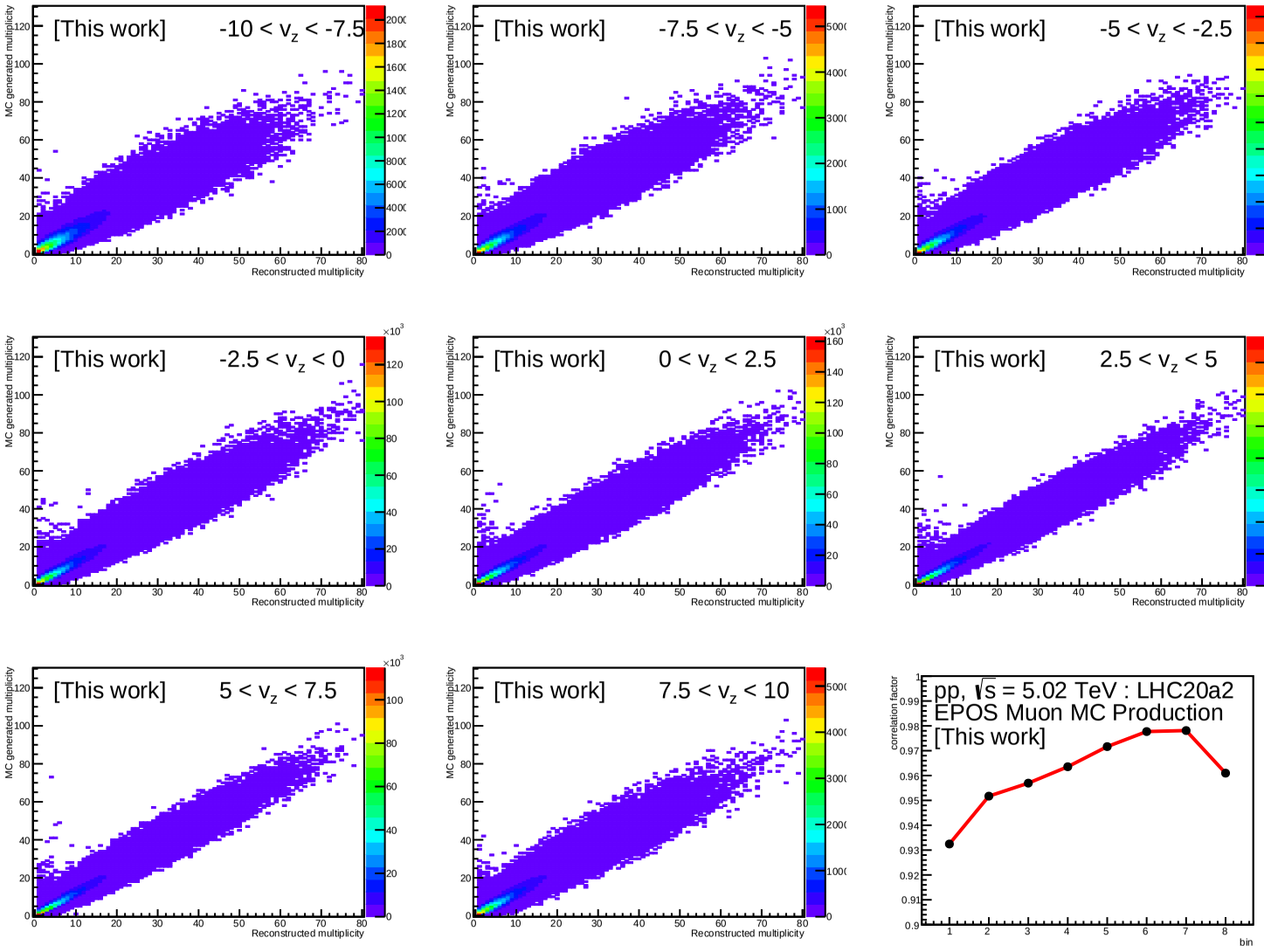

Fig. B.1 Correlation between the corrected number of tracklets and the generated charged particles for the different bins, bottom right panel shows the correlation factor for all 8 bins anchored to the LHC17p and q data samples.

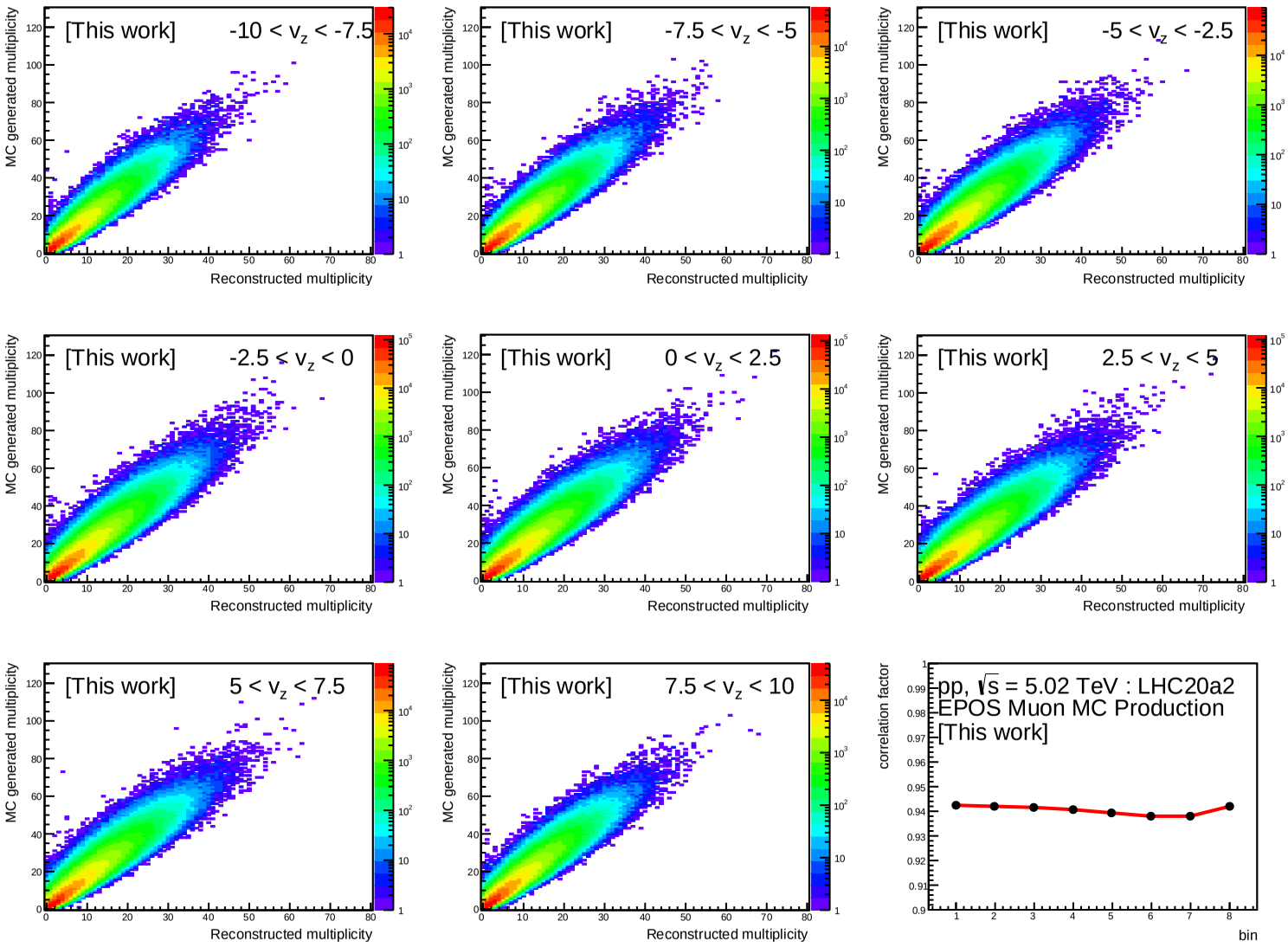

Fig. B.2 Correlation between the corrected number of tracklets and the generated charged particles for the different bins, bottom right panel shows the correlation factor for all 8 bins anchored to the LHC17p and q data samples.

APPENDIX C

Muon Yield

C.0.1 Muon yield in different multiplicity percentile bins

The muon yield extracted in section 3.4 is now plotted in different multiplicity percentile bins according to the SPD estimator given in Table 3.10. Since the V0M estimator has the same multiplicity percentile bins as the SPD estimator, the muon yield in the multiplicity percentile bins is the same. Figure C.1, **??**, C.2 shows the muon yield in different multiplicity percentile bins for the MSL (top) and MSH (bottom) trigger for the LHC17p+q and LHC15n data samples, respectively.

C.0.2 Normalization factor

Tables C.1 and C.2 in Appendix C.0.2 shows a summary of the normalization factor as a function of multiplicity for the MSL and MSH triggers respectively for each data sample, respectively.

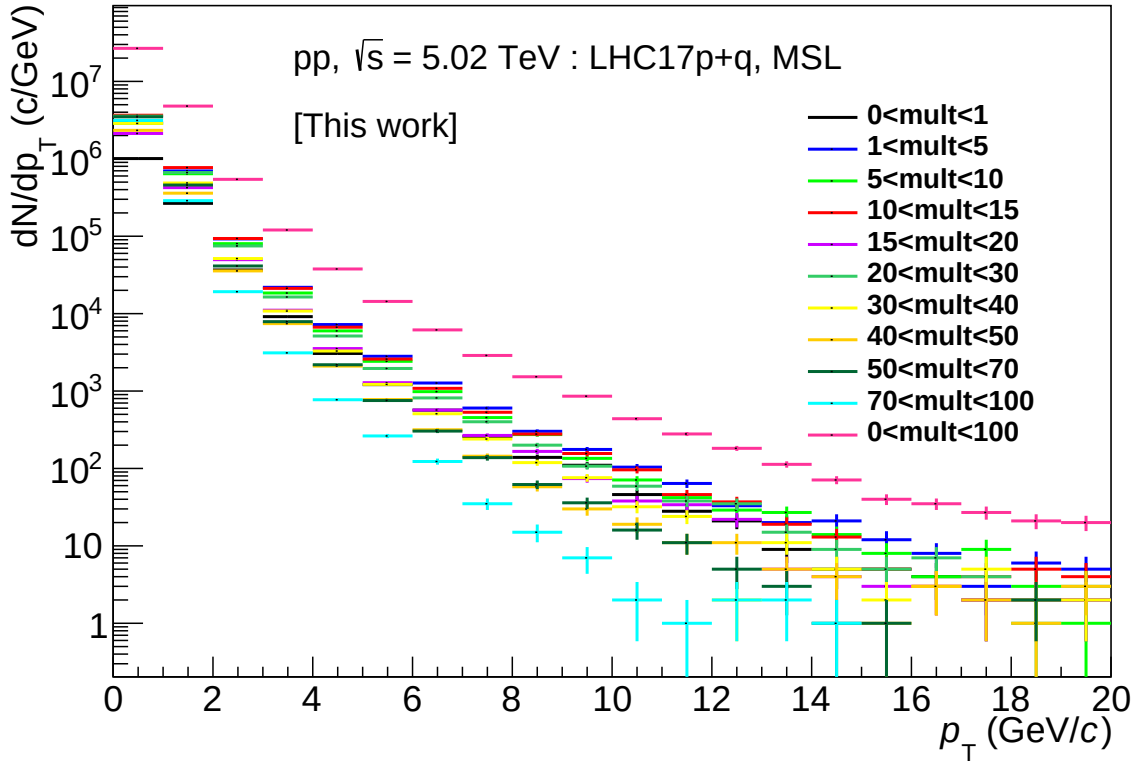

(a) MSL p_{T} distribution in different multiplicity percentile bins.

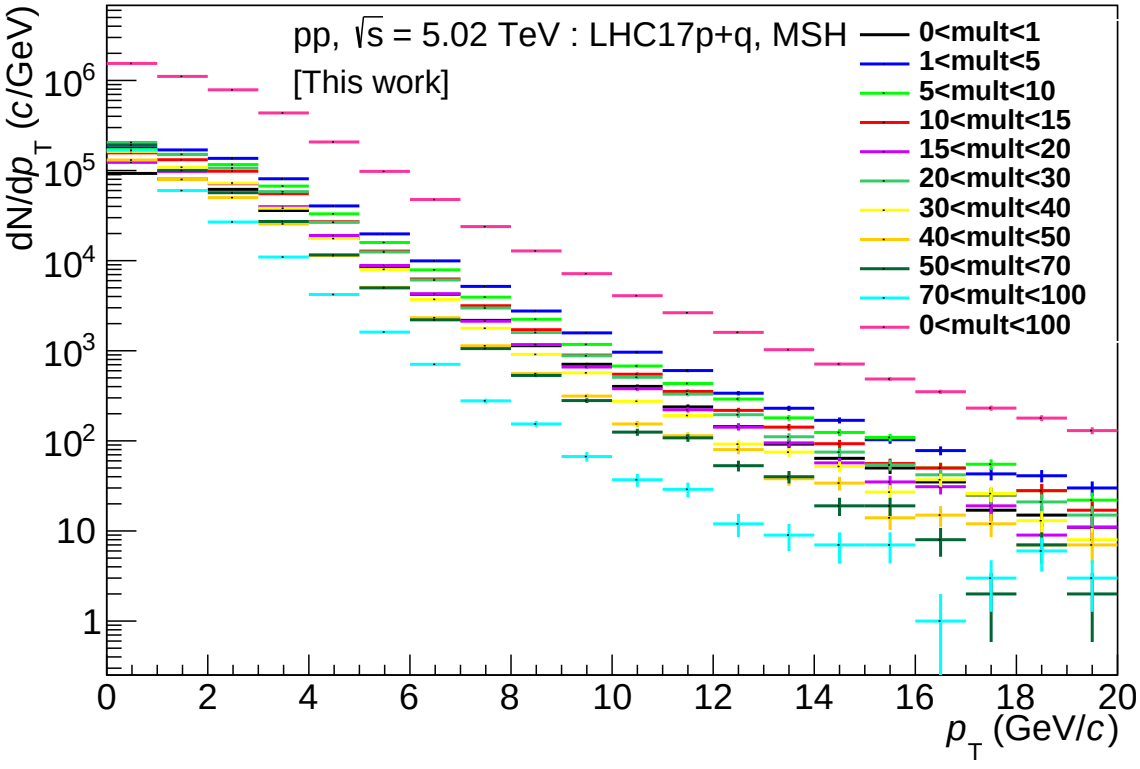

(b) MSH p_{T} distribution in different multiplicity percentile bins.

Fig. C.1 MSL (top) and MSH (bottom) p_{T} distribution in different multiplicity percentile bins for LHC17p+q.

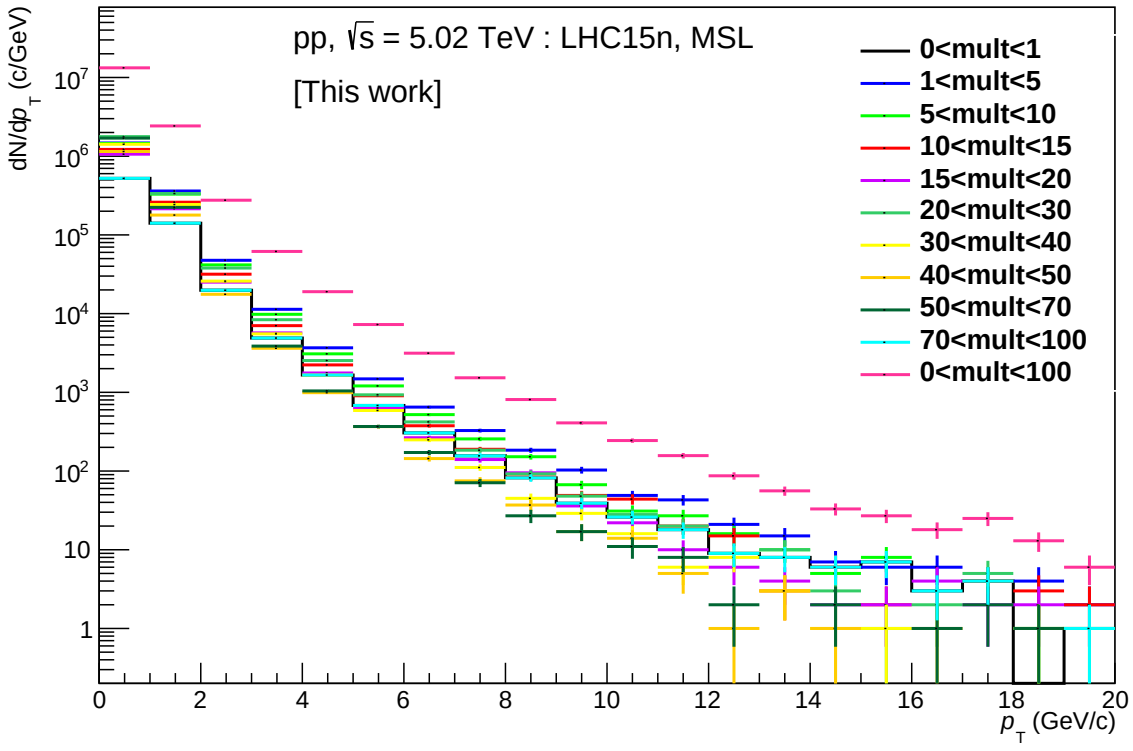

(a) MSL p_{T} distribution in different multiplicity percentile bins.

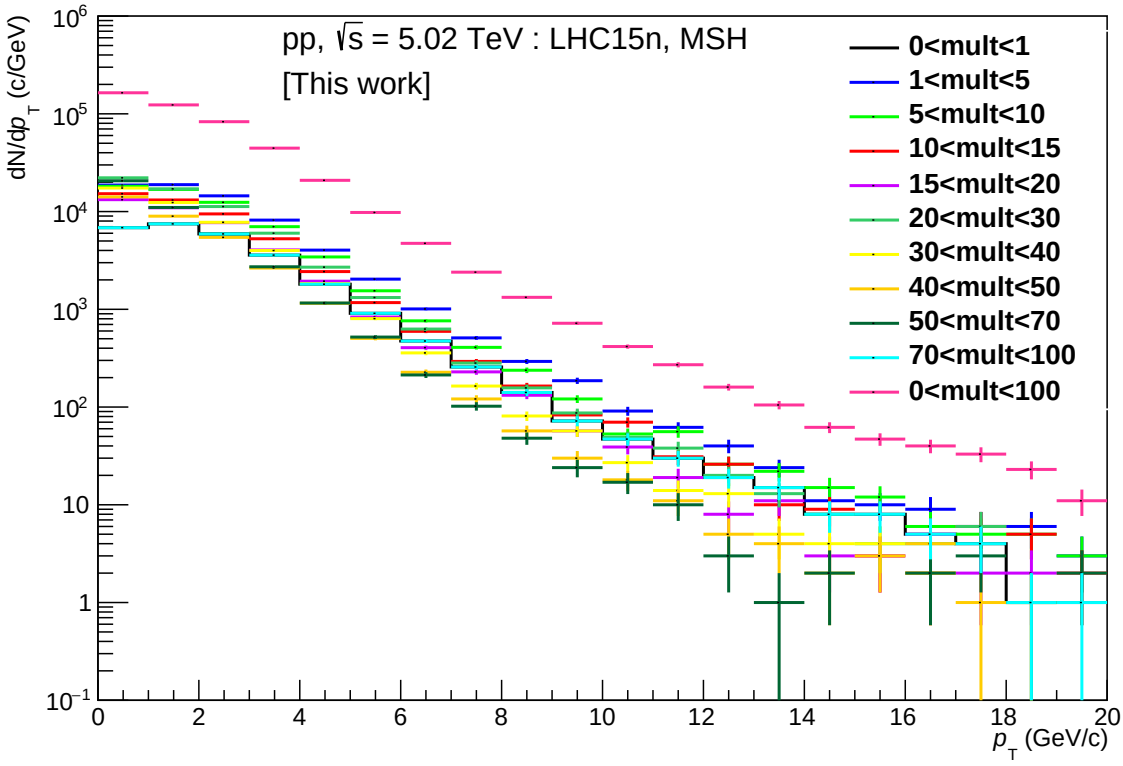

(b) MSH p_{T} distribution in different multiplicity percentile bins.

Fig. C.2 MSL (top) and MSH (bottom) p_{T} distribution in different multiplicity percentile bins for LHC15n.

Multiplicity Percentile	LHC17p		LHC17q		LHC15n	
	MSL	MSH	MSL	MSH	MSL	MSH
0-1	64.39 ± 1.59	1973.79 ± 32.98	47.09 ± 1.89	1353.46 ± 61.11	58.24 ± 4.19	1808.34 ± 124.52
1-5	66.95 ± 1.40	2200.14 ± 21.85	46.45 ± 1.61	1447.73 ± 58.43	71.06 ± 3.03	2330.91 ± 85.96
5-10	69.43 ± 1.44	2414.43 ± 23.52	52.88 ± 1.81	1719.58 ± 68.72	66.68 ± 2.89	2313.31 ± 87.27
10-15	70.46 ± 1.48	2558.82 ± 26.51	56.70 ± 1.95	1942.56 ± 78.14	74.41 ± 3.28	2689.77 ± 103.92
15-20	72.21 ± 1.53	2705.96 ± 29.38	62.05 ± 2.15	2191.13 ± 88.39	70.68 ± 3.33	2661.9 ± 111.88
20-30	77.45 ± 1.57	3054.23 ± 26.02	65.42 ± 2.18	2467.81 ± 96.83	76.22 ± 2.94	2977.66 ± 95.56
30-40	80.14 ± 1.64	3350.73 ± 30.76	78.14 ± 2.60	2966.07 ± 116.19	72.14 ± 3.03	2991.99 ± 108.36
40-50	84.65 ± 1.73	3768.46 ± 37.00	85.96 ± 2.90	3704.82 ± 146.59	85.44 ± 3.64	3766.56 ± 139.45
50-70	93.78 ± 1.92	4573.90 ± 37.12	108.56 ± 3.54	4966.84 ± 191.89	96.44 ± 3.86	4644.58 ± 137.76
70-100	112.56 ± 2.22	6577.92 ± 49.08	149.40 ± 4.82	8588.64 ± 329.79	112.15 ± 3.86	6558.08 ± 177.81

Table C.1 Normalization factor per multiplicity percentile for the different data samples for both the MSL and MSH triggers, used for the SPD estimator analysis.

Multiplicity Percentile	LHC17p		LHC17q		LHC15n	
	MSL	MSH	MSL	MSH	MSL	MSH
0-1	63.29 ± 1.51	1851.13 ± 28.53	41.37 ± 1.67	1112.82 ± 50.39	66.86 ± 4.10	1886.17 ± 108.60
1-5	65.62 ± 1.36	2099.51 ± 19.98	41.68 ± 1.48	1259.36 ± 51.69	62.46 ± 2.67	1950.19 ± 72.15
5-10	66.82 ± 1.38	2302.72 ± 21.97	46.37 ± 1.64	1521.4 ± 62.28	65.33 ± 2.78	2213.17 ± 81.48
10-15	69.90 ± 1.46	2533.46 ± 25.62	51.63 ± 1.84	1779.65 ± 73.44	64.93 ± 2.95	2321.27 ± 93.42
15-20	72.98 ± 1.54	2752.97 ± 29.16	56.56 ± 2.03	2040.25 ± 84.66	70.50 ± 3.29	2627.88± 109.27
20-30	74.65 ± 1.51	2997.69 ± 25.62	64.70 ± 2.19	2465.04 ± 98.01	72.14 ± 2.83	2840.19 ± 93.19
30-40	79.50 ± 1.63	3455.33 ± 31.36	75.72 ± 2.58	3127.34 ± 124.96	78.06 ± 3.22	3320.34 ± 117.34
40-50	86.46 ± 1.79	4030.06 ± 39.36	91.02 ± 3.12	4064.75 ± 162.99	83.91 ± 3.64	3827.19 ± 145.37
50-70	98.70 ± 1.97	5190.68 ± 41.75	117.35 ± 3.87	5896.37 ± 229.93	104.37± 3.78	5402.39 ± 158.93
70-100	127.40 ± 2.53	8316.58 ± 65.73	195.51 ± 6.37	12185.8 ± 471.11	143.12 ± 5.00	9172.55± 255.94

Table C.2 Normalization factor per multiplicity percentile for the different data samples for both the MSL and MSH triggers, used for the V0M estimator analysis.

APPENDIX D

Acceptance times Efficiency ($A \times \epsilon$)

Final results of the $A \times \epsilon$ for the LHC17q (left) and LHC15n data samples is shown in Fig. D.1.

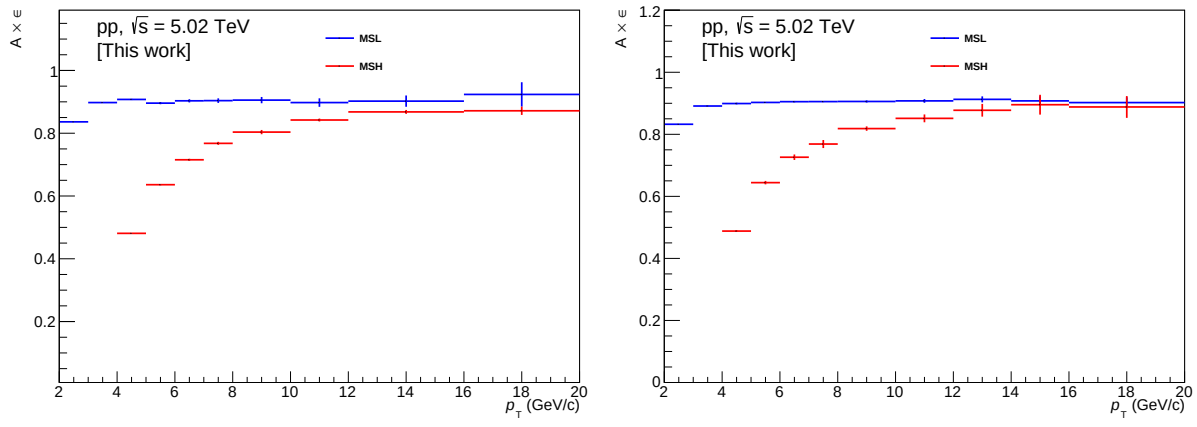

Fig. D.1 $A \times \epsilon$ of MSL and MSH triggers as a function of p_T for LHC17q (left) and LHC15n (right) data samples

APPENDIX E

Background subtraction

E.1 Charged primary pion and kaon

The background fraction as a function of η of single decay muons from primary charged π and K at forward rapidity in pp collisions at $\sqrt{s} = 5.02$ TeV is shown in Fig. E.1a.

A comparison of Fig. 3.35a with PYTHIA8 [178] obtained results, the MC productions lacks statistics at higher p_{T} and also overestimates the determined $\pi + K$ distribution.

E.2 Secondary decay muons

The background fraction as a function of p_{T} in different multiplicity percentile bins; this is associated with the "Official Framework" multiplicity estimation discussed in section 3.3.2. A detailed discussion is given in 3.7.2

E.3 Electroweak Bosons

The total electroweak bosons cross section is shown in the top of Fig. E.3 together with the inclusive muon differential cross section for the LHC15n data sample. The background fraction for the integrated multiplicity is shown in the bottom figure of Fig. E.3.

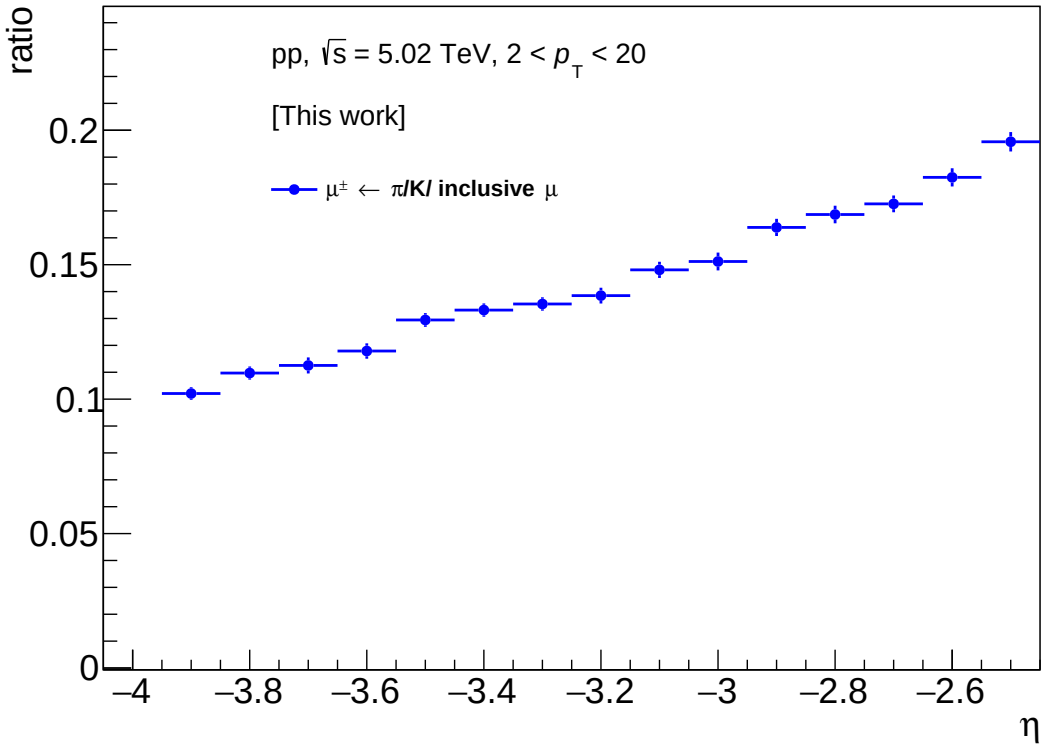

(a) Background fraction as a function of η of single decay muons from primary charged π and K at forward rapidity in pp collisions at $\sqrt{s} = 5.02$ TeV.

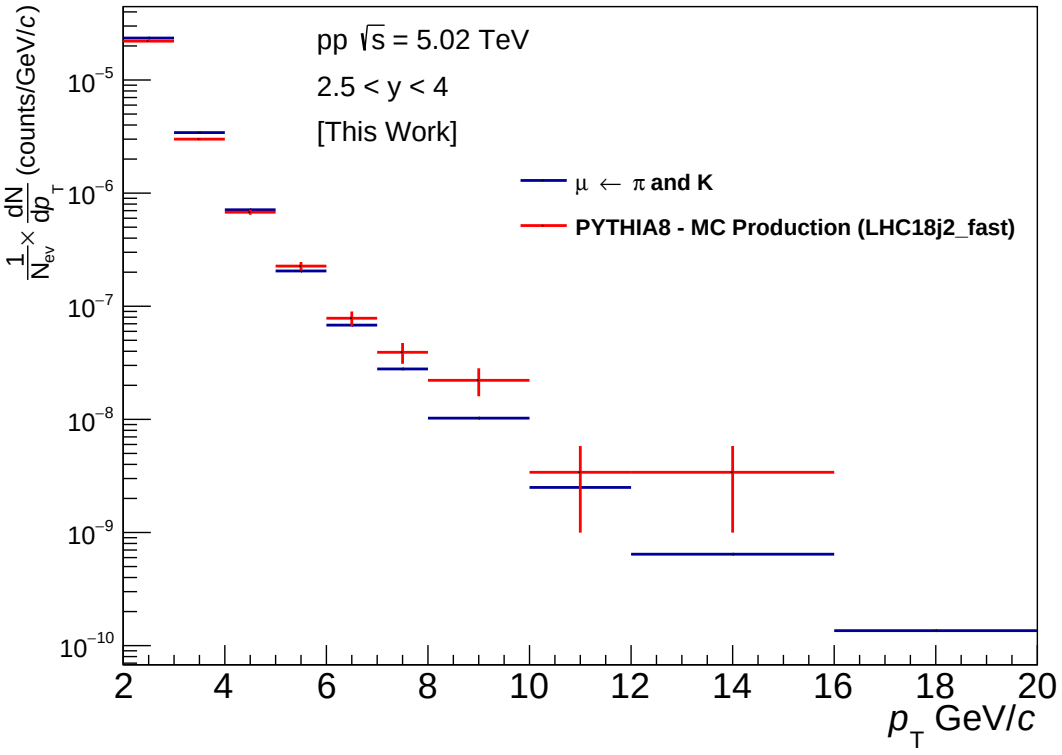

(b) Comparison of $\pi + K$ distributions determined using the improved method that accounts for absorber effects with decay muons distribution from PYTHIA8 [178] based MC production.

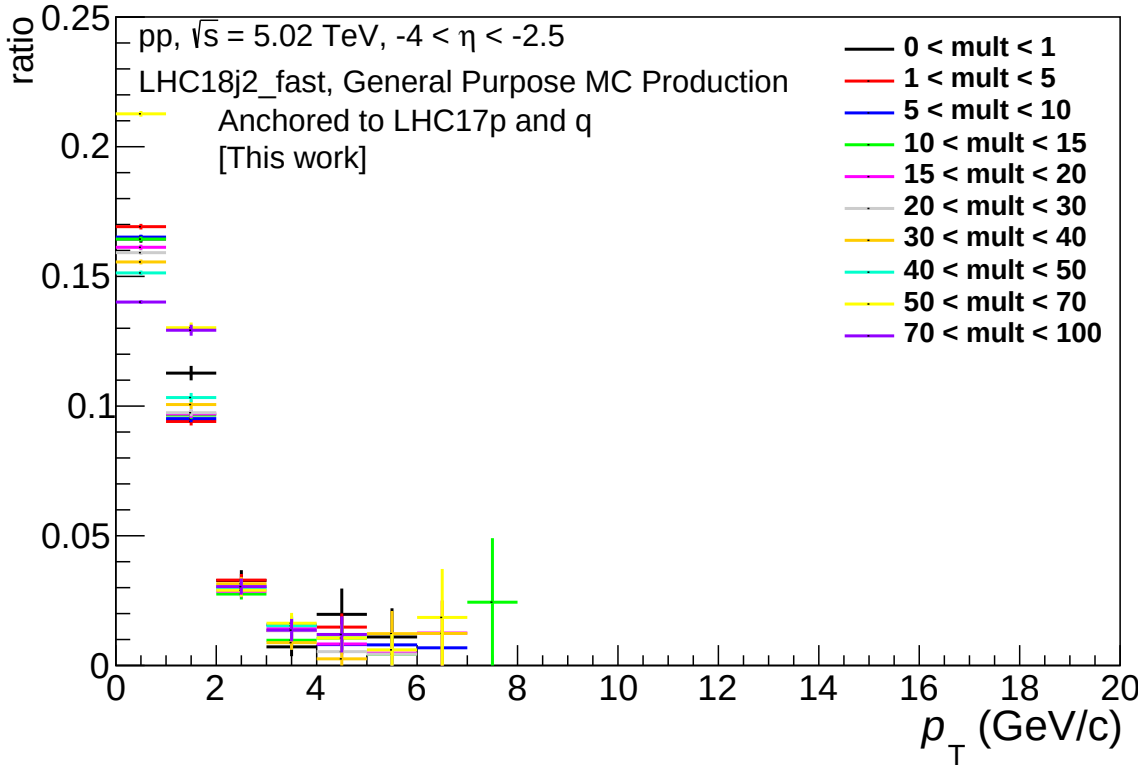

(a) Background fraction of the secondary muons in different multiplicity percentile bins.

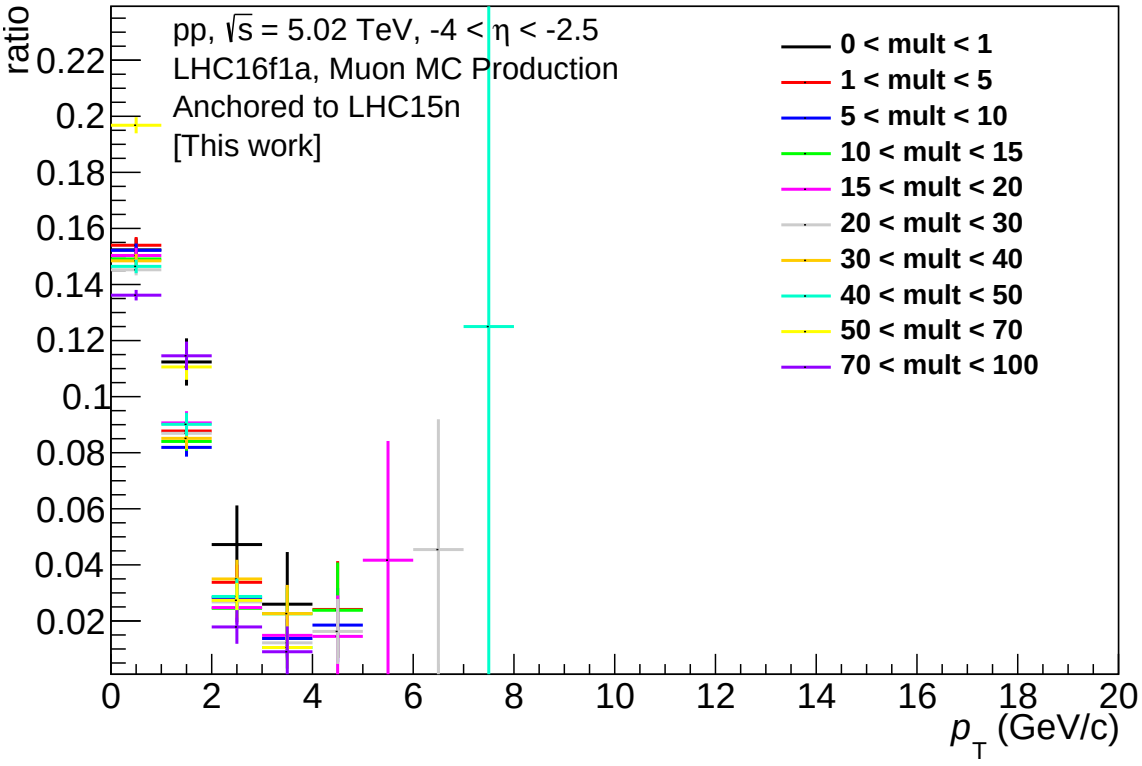

(b) Background fraction of the secondary muons in different multiplicity percentile bins.

Fig. E.2 Background fraction of secondary muons in different multiplicity percentile bins associated with the LHC17p and q (top) and LHC15n (bottom) data samples.

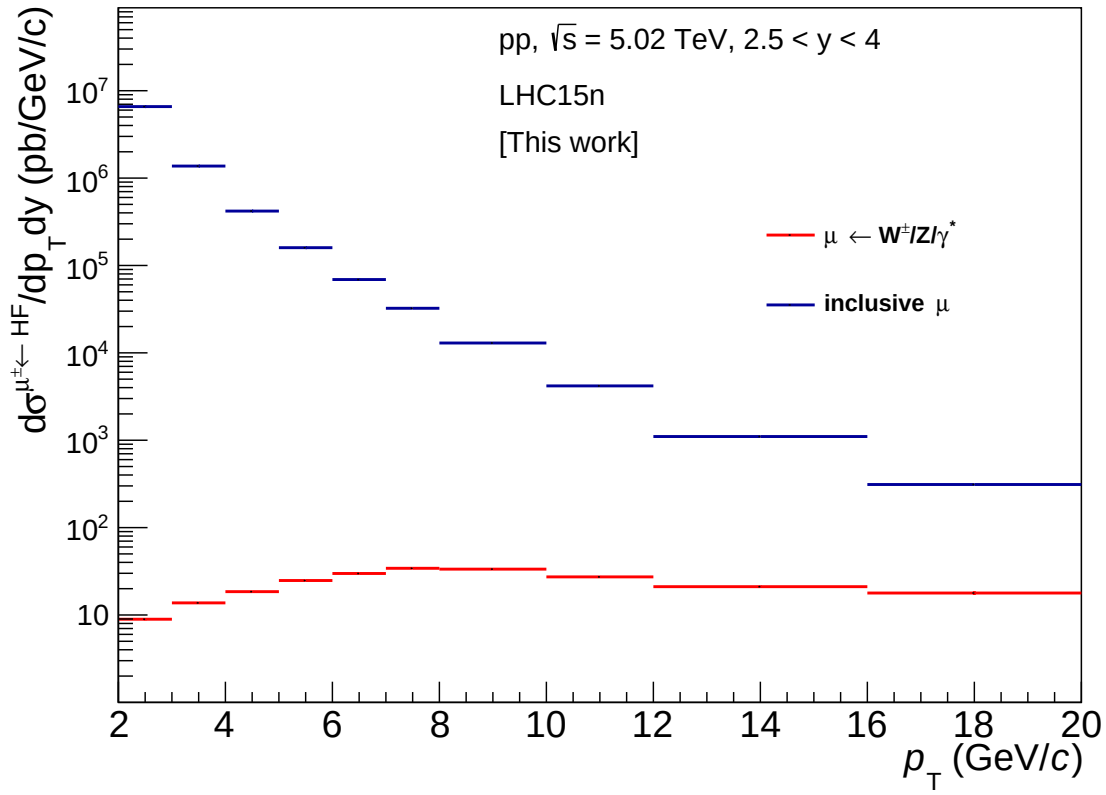

(a) Electroweak bosons and inclusive muon differential cross sections.

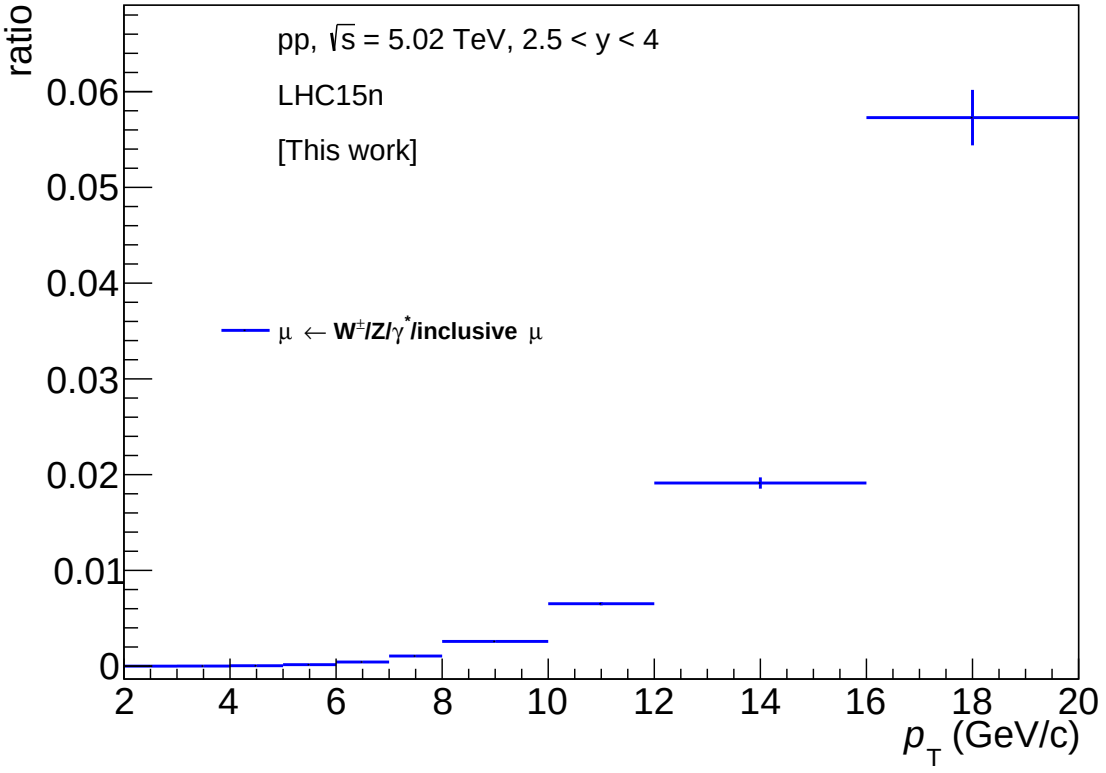

(b) Background fraction of electroweak bosons.

Fig. E.3 Electroweak bosons and inclusive muon differential cross sections (top) and background fraction of electroweak bosons (bottom) for the LHC15n data sample.

E.4 J/ψ background contribution

Figure E.4 shows the J/ψ and inclusive muon cross section on the top for the LHC15n data sample. The background is shown in Fig. E.4 on the bottom.

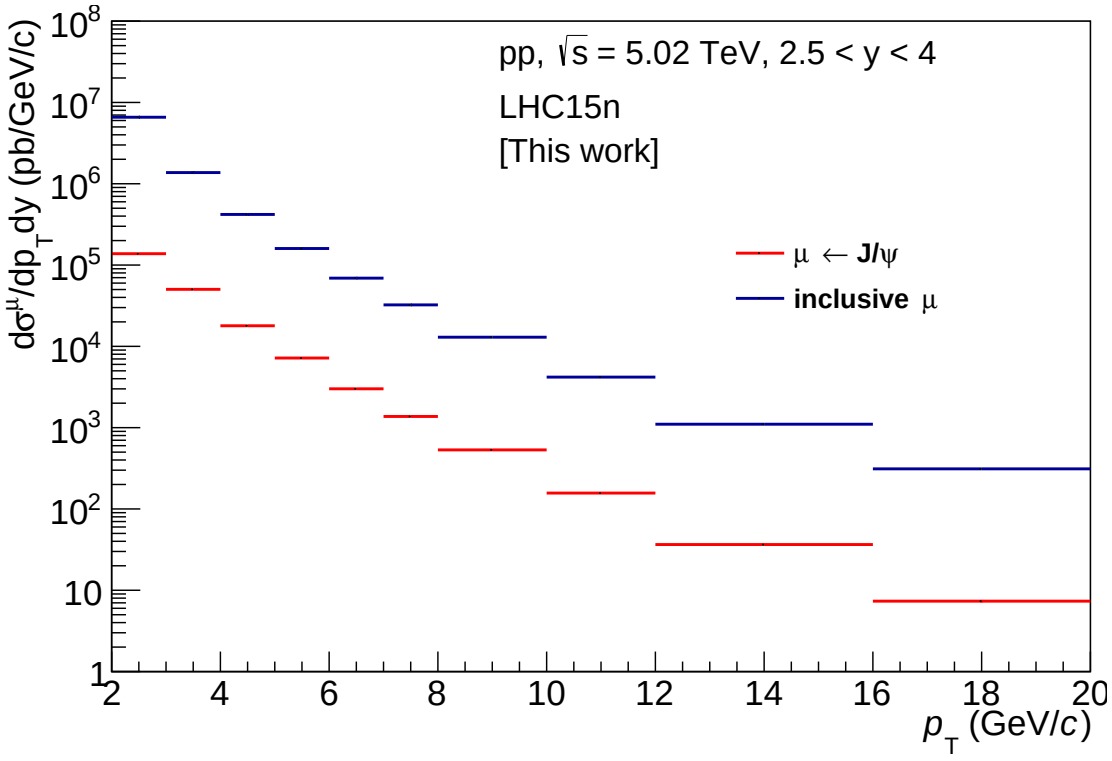

(a) Differential cross section distributions of the inclusive muons and J/ψ.

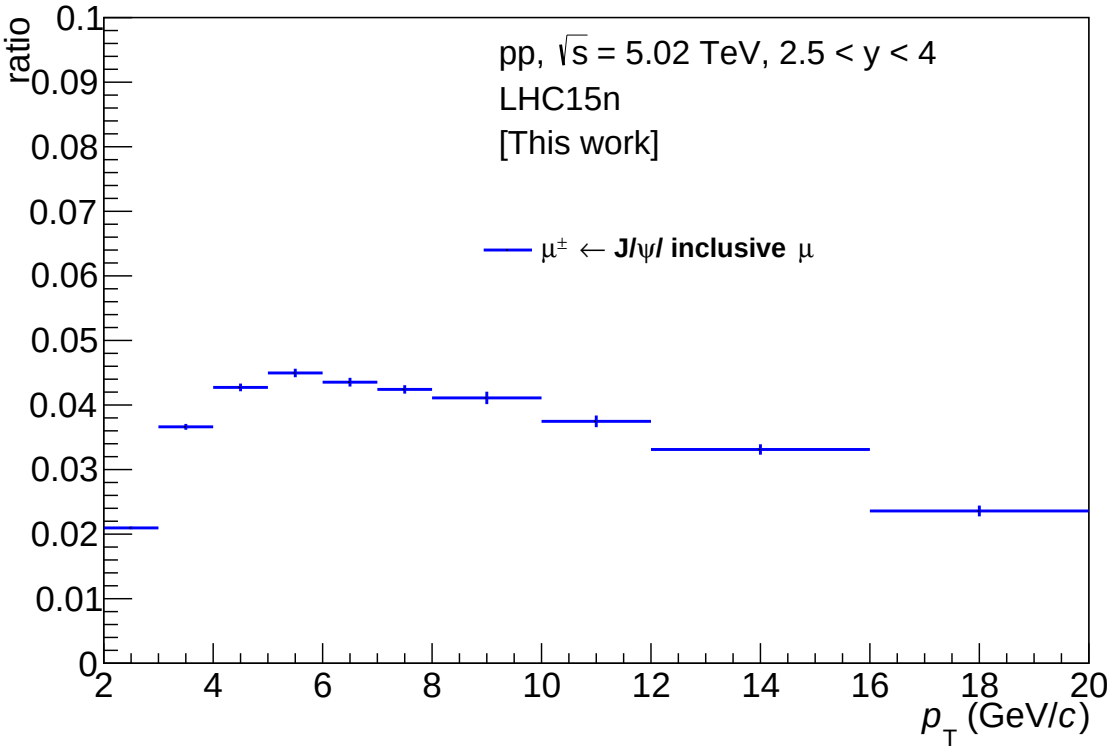

(b) Background fraction of J/ψ.

Fig. E.4 Differential cross section distributions of the inclusive muons and J/ψ (E.4a) and background fraction of J/ψ (E.4b) for the LHC15n data samples.

V0M Estimator				SPD Estimator	
LHC17p		LHC15n		LHC17p and LHC15n	
$\frac{dN_{ch}/d\eta}{\langle dN/d\eta \rangle}$	J/ψ self-normalized yield	$\frac{dN_{ch}/d\eta}{\langle dN/d\eta \rangle}$	J/ψ self-normalized yield	$\frac{dN_{ch}/d\eta}{\langle dN/d\eta \rangle}$	J/ψ self-normalized yield
0.59	0.85975 ± 0.056792	0.43	0.68156 ± 0.056792	0.29	0.52546 ± 0.056792
0.72	1.00461 ± 0.056792	0.70	0.98232 ± 0.056792	0.60	0.870891 ± 0.056792
0.95	1.26090 ± 0.056792	0.92	1.22747 ± 0.056792	0.85	1.14969 ± 0.056792
1.15	1.48376 ± 0.056792	1.13	1.46148 ± 0.056792	1.07	1.39462 ± 0.056792
1.41	1.77348 ± 0.056792	1.38	1.74005 ± 0.056792	1.39	1.75120 ± 0.056792
1.66	2.05205 ± 0.056792	1.64	2.02977 ± 0.056792	1.70	2.09663 ± 0.056792
1.87	2.28606 ± 0.056792	1.86	2.27492 ± 0.056792	1.97	2.39750 ± 0.056792
2.17	2.62036 ± 0.056792	2.16	2.60921 ± 0.056792	2.35	2.82093 ± 0.056792
2.64	3.14408 ± 0.056792	2.63	3.13294 ± 0.056792	3.00	3.54524 ± 0.056792
3.36	3.94639 ± 0.056792	3.34	3.92410 ± 0.056792	4.26	4.94927 ± 0.056792

Table E.1 Self-normalized J/ψ yields as a function of charged particle multiplicity for the V0M and SPD multiplicity estimators for the "Official Framework".

APPENDIX F

Service Work

F.1 Testing of the detection elements

The MCH consists of 5 tracking stations with each station made up of 2 chambers. Stations 1 and 2 are divided into quadrants while stations 3-5 are slats; these slats are the Cathode Pad Chambers (CPC) detector elements of stations 3-5 of the MCH, this was discussed in 2.2.4.4. At the end of Run 2, during the long shutdown (LS2), the slats from stations 3 - 5 that suffered high voltage (HV) trips during Run 2 were removed to be repaired in preparation for Run 3 to be used as spares when required.

Before any repairs were done, tests were performed on the detector elements to identify the problematic areas. The tests constitute of scanning and characterizing the slats using a Mini Amptek X-ray source. In addition to requiring an X-ray source for the tests, a high voltage power supply (HVPS), gas distribution rack, gas bottle filled with $ArCO_2$ and control computer for the X-ray source were required.

For radiation safety reasons, the tests were conducted after hours in the Buffer Zone of ALICE located at Point 2. To avoid radiation exposure, the control computer, HVPS and gas bottle are located outside the buffer zone. This is illustrated in Fig. F.1.

The gas distribution rack is located inside the buffer zone to provide gas to the slat. A plastic pipe is used to connect the rack to the gas bottle. In addition to the pipe connecting the rack and the gas bottle, there are two pipes leaving the rack to connect to

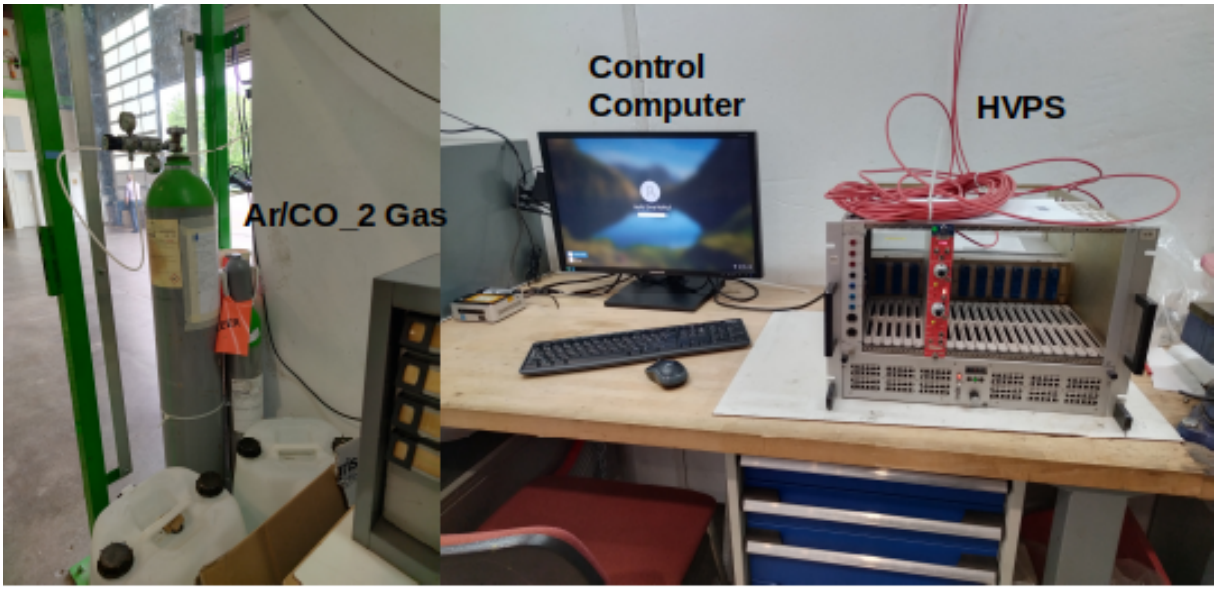

Fig. F.1 Outside the buffer zone where the control PC, gas bottle and HVPS are located.

the slat, one pipe is connected to the inlet and the other to the outlet of the slat to allow gas to continuously flow. This is illustrated in Fig. F.2.

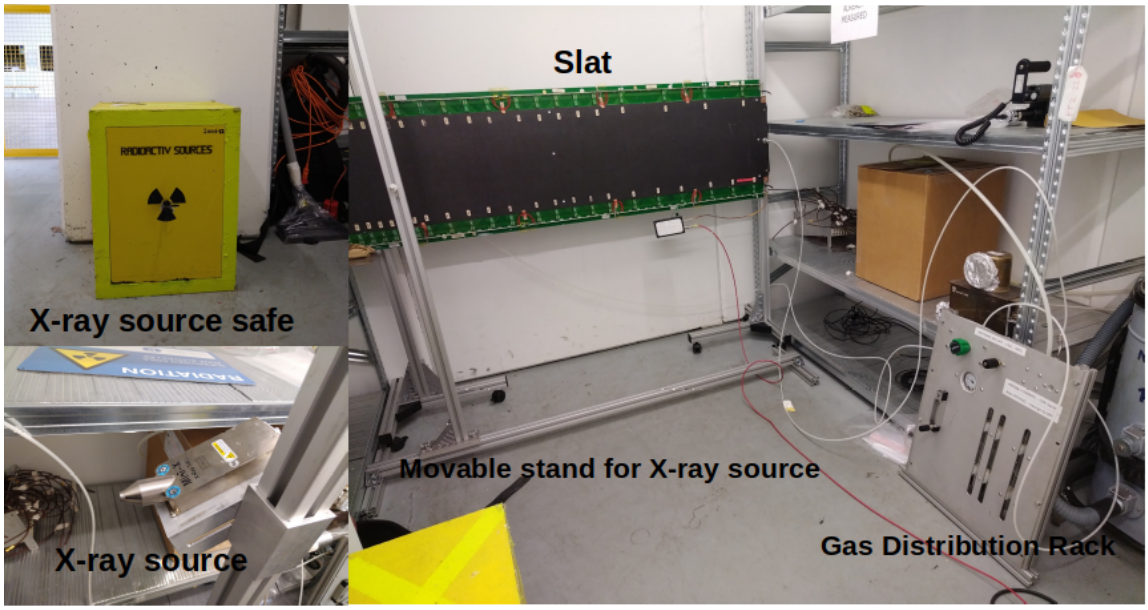

Fig. F.2 Inside the buffer zone where the gas distribution rack, X-ray source and slat are located.

The X-ray source is connected to a movable stand placed ≈ 40 cm away from the slat. The X-ray source system consists of an X-ray tube, a power supply, USB cable to connect to a computer for communication and a connector to an interlock. The X-ray tube provides a grounded anode that simplifies the X-Ray Fluorescence (XRF) process, a variable current

and voltage. The source can have a maximum 80 μA and 50 kV power supply. Silver (Ag) is used as a transmission target with beryllium (Be) as the end window [179]. With its design for continuous use, the Mini-X system is an ideal system for the tests. When the source is not in use, the source is safely stored in a safe inside the buffer zone as shown in Fig. F.2

The X-ray source is operated using the control computer as shown in Fig. F.1. The software is called the Amptex Mini-X controller and it is a USB software interface that allows the user to control the voltage and current of the source. A screenshot of the software is shown in Fig. F.3

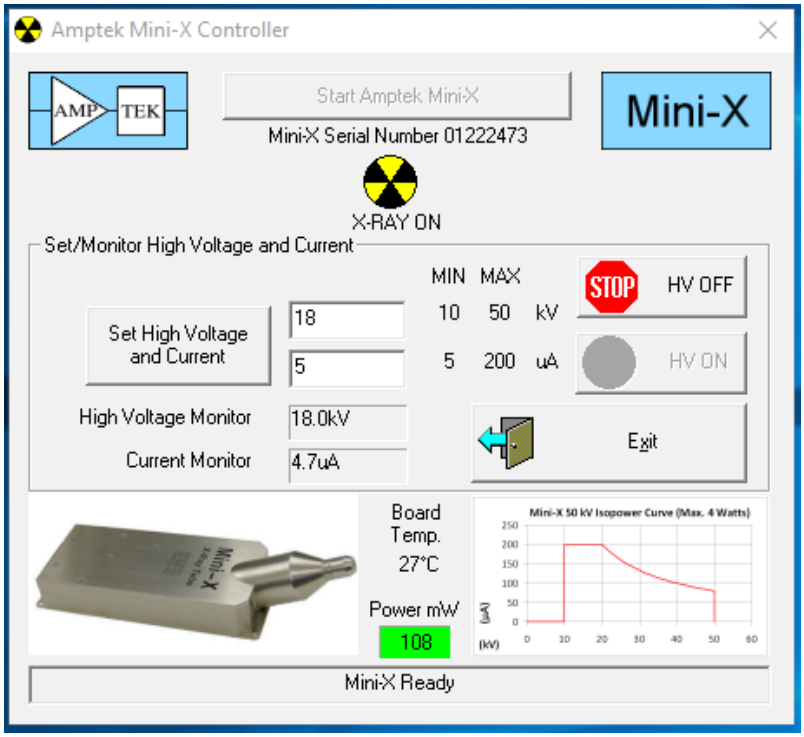

Fig. F.3 Amptex Mini-X controller software used to control the X-ray source safely from outside the buffer zone.

F.1.1 Experimental procedure

Before any tests were performed, the slats were flushed with the gas for a couple of hours. This is done to ensure that there is no humidity in the slat and it also ensures that the slat is only filled with $ArCO_2$. Depending on the size of the slat, the flow rate of the gas is varied between 2-5l per hour.

Once the flushing is completed, the source is then setup and placed 40 cm away from the slat. A distance of 40 cm is chosen as this allows to irradiate/scan an area of a circle with radius 20 cm. Depending on the size of the slat, there can be multiple points that

need to be scanned for the whole slat to be tested. Every point is ≈ 40 cm apart moving horizontally and 10 cm apart moving vertically, this distance is determined by the position of the PCB. Each slat had 3 rows, i. e. top and bottom rows (close to the edges of the slat) and the middle row.

A high voltage of +1700 V is applied to the slat to create an electric field between the two cathode pads. X-rays are then projected onto the slat, as the X-rays travel through the CPC, the $ArCO_2$ gas is ionized and electrons are ejected. The electrons move towards the anode since it is positively charged. As a result of the ionization, there is a charged build-up on the cathodes.

The power of the X-ray source is kept constant at 18 kV. To gauge the stability of the slats at high ionizing fluxes, the intensity of the X-rays is increased by increasing the current in stages starting from 5 μA while monitoring the leakage current recorded by the HVPS module. As the current of the source is increased, the charge from the slat is measured using the HVPS module. The intensity of the X-ray source is increased until the current reading from the slat is between 7.2 and 7.5 μA; this value was chosen as this is the maximum current the slat can withstand without the HVPS tripping. In case of a trip, further investigation is required.

F.1.2 Results and Discussion

A total of 9 slats were tested during the period of May to June 2022. Most of the slats had been tested before in 2019 and had been sent for repairs; however there were some that had never been tested. Figures F.4 and F.5 show one of the slats that was previously tested, repaired and tested again. The green points indicate that the region of the slat is "ok" and the red points indicates that there seems to be a problem with the anode wires in that region of the slat. On the right of both figures, the results of the measurement taken are shown. The 18 kV is the voltage of the source, together with the current applied to increase the intensity of the source. The arrow points to the current measure from the CPC with a comment on the side stating whether the measurement was stable or not.

Measurements in 2019 are shown in Fig. F.4, the slat consists of 2 red points, this indicates that there is a problem on that region of the slat due to the HV trips. The tripping can be a result of either sagging or broken anode wires, the glue used to merged the printed circuit boards (PCBS) has melted and covered the anode wires or there is dust in that region of the slat. These results are used to guide the person responsible for repairs to know where to fix when the slat is opened up.

After repairs, the slat is tested again in 2022 and this is shown in Fig. F.5; as observed, the slat now consists of green points only, which indicates that the repairs were successful

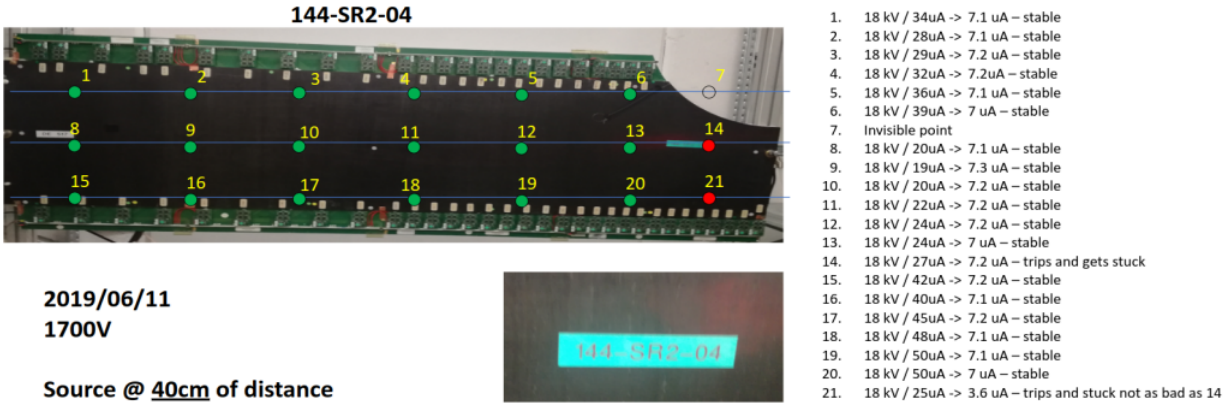

Fig. F.4 Slat 144 SR2 04 measurements when it was tested in 2019

and the slat is ready to be used again. This procedure was done for all the slats. A summary of the overall status of the slats after testing in the period of May-June 2022 is given in Table F.1.

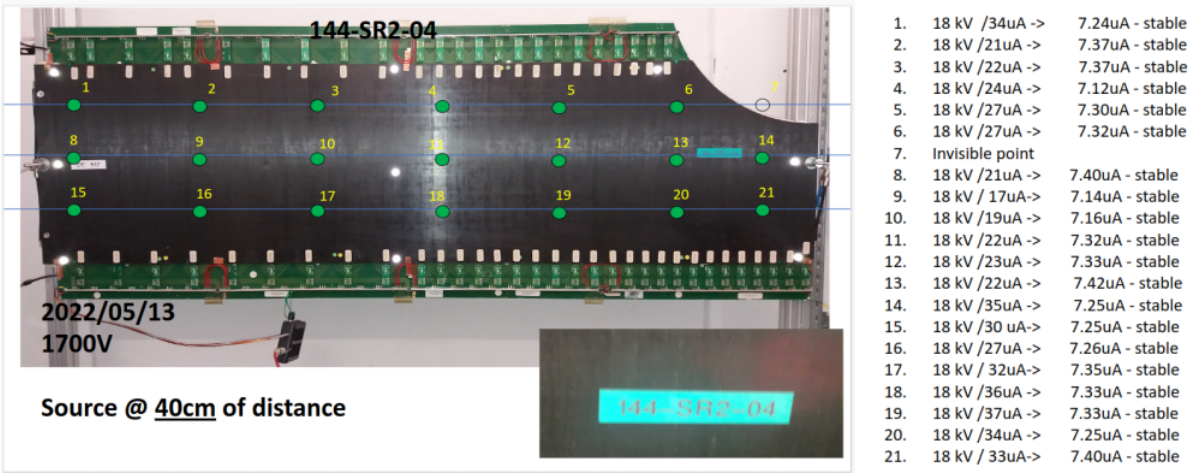

Fig. F.5 Slat 144 SR2 04 measurements when it was tested in 2022

Slat name	Status	Comment
144-SR2-04	Good	No problems
330000 CAG 01	Good	Tripped and recovered within seconds
142-SR1-01	Good	No problems
333000 GAT 13	Good	No problems
112230-NAN-04	Good	No problems
1222330 CAG 02	Good	No problems
112233 NR3-NAN-06	Good	No problems

Table F.1 Summary of all slats tested in the period of the Service Task in May -June 2022.